Synthesis and Application of P4VP Based Block Copolymers from Supercritical CO$_2$

Ryan Larder

Thesis submitted to the University of Nottingham

for the degree of Doctor of Philosophy

June 2021

The University of Nottingham

UNITED KINGDOM · CHINA · MALAYSIA

Declaration

All work presented in this Thesis is the original work of the author, with the exception of results referenced to other sources. It has not been submitted as part of any other degree or professional qualification.

Signed: *R. Larder*

Date: 28/06/2021

Ryan Larder

Acknowledgements

Firstly, I would like to thank my supervisor Steve Howdle for giving me the opportunity to undertake this PhD, and for all his support throughout the course of my time at Nottingham. I would also like to thank the various postdoc supervisors that have made their way through the group for all their advice, assistance and general wisdom. Specifically, I would like to acknowledge Thomas Bennett and Vincenzo Taresco for their role in supervising and guiding me through my PhD journey. I am grateful to them for the many discussions throughout the past few years that have helped to shape both this research and me as a researcher.

I am incredibly lucky to have been able to collaborate with many amazing scientists through the course of this project, without whom this work would not have been possible. Andrea Palumbo, Ullrich Steiner, Jesum Fernandes, Renato Goncalves, Matt Derry, Paul Topham, Iolanda Francolini, Claudia Vuotto and Rob Cavanagh. My thanks to all of you for all your hard work, especially during these more difficult and uncertain times. I am indebted to the support teams in the school of chemistry and the nmRC. In particular, Mark Guyler and Rich Wilson for always coming to the rescue when encountering all manner of technical difficulties. Nikki Westen, Mike Fay and Beth Steer, without them I would surely still be sat desperately trying to operate the instruments that proved essential for this work. Special thanks also go to Sue for providing a constant and necessary supply of tea, but more importantly, for always lending a smile whatever the weather.

I would like to thank all the members of Lab B10, past and present. I have been incredibly lucky to have been part of such a wonderfully supportive group and will miss all the baked goods, coffee breaks and nights at the JA. I am grateful to all those involved in the LDMI DTP and for allowing me to be part of the first cohort of this programme.

Last but not least, I want to thank Bethany for all her love and support both in and out of the lab. Thank you for motivating and encouraging me through the writing up period and COVID lockdowns, I hope to do the same for you as you begin your own PhD journey.

Abstract

In recent years, supercritical carbon dioxide ($scCO_2$) has proven to be an efficient and green medium to produce block copolymer microparticles with internal nanostructures. When conducting controlled radical dispersion polymerisations, the unique physical properties of $scCO_2$ allow for spontaneous self-assembly of the block copolymers within the confines of the stabilised microparticles. This has successfully yielded highly pure hierarchically structured polymers in a single reaction procedure, without the need for any non-renewable or toxic solvents. Moreover, preliminary tests show that when a poly(4-vinylpyridine) (P4VP) block is incorporated into the polymer, the resulting microparticles can be capable of directing the formation of inorganic materials. Selective association of inorganic components to the pyridinyl nitrogen moieties of the P4VP can allow the polymer materials to act as structural templates to fabricate nanoscale functional materials.

However, utilisation of these P4VP based block copolymers in nanofabrication has thus far been underexplored. The main aim of this thesis is to demonstrate the versatility of these block copolymers in templating various functional materials with good control over the end nanoscale morphology. New synthetic strategies were explored to alter both the size and shape of the P4VP templates, allowing the end product to be intricately tailored for its final application. The nanofabrication of several inorganic materials was also studied to prove the breath of possible end applications that these polymeric templates are suitable for.

Specifically, **Chapter 3** demonstrates that simple modifications to the synthesis of P4VP block copolymers in $scCO_2$ allows the size of the templates to be altered. Size modification on both the microscale and nanoscale dimensions were investigated by controlling the size of the microparticles formed in the dispersion polymerisation, and by adjusting the size of the phase separated P4VP domains. In addition, this chapter also studies the nanofabrication of $LiFePO_4$, a common cathode material for rechargeable batteries, by applying the polymer templates in a sol-gel synthetic procedure. The effect of the template microparticle size was investigated by examining the morphology, surface area and electrochemical properties of the fabricated battery materials.

Chapter 4 highlights a new approach to change the shape of the P4VP morphology in scCO$_2$, without needing to alter the ratio of P4VP in the copolymer. Complex P4VP morphologies were obtained by synthesising ABC triblock copolymers in scCO$_2$, allowing the self-assembly dynamics to be controlled by changing the ratio of the other two constituent blocks. These three-phase morphologies were studied through microscopy and X-ray scattering techniques. The new P4VP morphology was then used to template TiO$_2$, an already well-studied inorganic material that has potential application as a photocatalyst. The nanostructure and photocatalytic activity of the triblock templated TiO$_2$ was then studied and compared to an equivalent material templated using the spherical morphology of a simple diblock P4VP copolymer.

Finally, **Chapter 5** details a method to combine both the polymer synthesis and inorganic templating into a single green process in scCO$_2$. Polymerisation of the P4VP block of the copolymer was performed while simultaneously synthesising silver nanoparticles (AgNPs) by thermal degradation of a precursor complex. Chemical association of the silver to the 4VP monomers led to the synthesis of homogeneous composites materials with AgNPs distributed throughout the block copolymer particles. Furthermore, a CO$_2$ extraction procedure was performed on the materials post-synthesis, removing the residual unreacted monomer and precursor to yield clean and non-toxic composites. The cleaned materials were assessed for their potential use in biomedical applications by evaluating their biocompatibility and antimicrobial activity. The composites were also exploited for use as an antimicrobial 'ink' in selective laser sintering (SLS) 3D printing, yielding small solid objects containing an even distribution of AgNPs.

Overall, a number of new strategies are presented to modify the microparticle size, nanoscale dimensions and morphology of P4VP based block copolymers in scCO$_2$. This also includes a method to combine the template synthesis and inorganic structure-directing into one environmentally benign process. The P4VP templates are applied to the fabrication of several functional inorganic materials with multiple end applications investigated. Potential use for the templated materials in both the energy and healthcare sectors proves the value and versatility of these P4VP polymers, with even further applications still to be investigated.

Abbreviations

^{1}H NMR	Proton Nuclear Magnetic Resonance
ABS	Acrylonitrile-Butadiene-Styrene
Ag(hfac)(COD)	(1,5-Cyclooctadiene)(Hexafluoroacetylacetonato)Silver(I)
AgNPs	Silver Nanoparticles
AIBN	2,2'-Azobis(2-Methylpropionitrile)
ATP	Adenosine Triphosphate
ATRP	Atom Transfer Radical Polymerisation
BET	Brunauer–Emmett–Teller
BJH	Barrett-Joyner-Halenda
CRP	Controlled Radical Polymerisation
CV	Coefficient of Variation
CYL	Cylindrical Morphology
D/L_0	Ratio of Confinement Size to Average Polymer Domain Size
DDMAT	2-(Dodecylthiocarbonothioylthio)-2-Methylpropionic Acid
DLS	Dynamic Light Scattering
d_n	Number Average Particle Diameter
D_{P4VP}	Number Average Domain Size of P4VP
dRI	Differential refractive Index
DSC	Differential Scanning Calorimetry
EDXS	Energy-Dispersive X-ray Spectroscopy
EISA	Evaporation Induced Self Assembly
EPDM	Ethylene Propylene Diene Monomer
FDM	Fused Deposition Modelling
FRP	Free-Radical Polymerisation
FTIR	Fourier Transform Infrared
$f_{polymer}$	Volume fraction of polymer

GPC	Gel Permeation Chromatography
GYR	Gyroidal Morphology
HPLC	High-Performance Liquid Chromatography
IJP	Ink Jet Printing
L+S(II)	Spheres in Lamellar Morphology
LAM	Lamellar Morphology
LDH	Lactate Dehydrogenase
MCM	Multicompartment Micelles
M_n	Number Average Molecular Weight
$M_{n\ exp}$	Measured Number Average Molecular Weight
$M_{n\ target}$	Targeted Number Average Molecular Weight
M_w	Weight Average Molecular Weight
N	Degree of Polymerisation
NMP	Nitroxide-Mediated Polymerisation
P4VP	Poly(4-Vinylpyridine)
PAA	Poly(Acrylic Acid)
PB	Poly(Butadiene)
PBzMA	Poly(Benzyl Methacrylate)
PCL	Poly(ε-Caprolactone)
PDI	Polydispersity Index
PDMS	Poly(Dimethylsiloxane)
PDMS-MA	Poly(Dimethylsiloxane) Monomethyl Methacrylate
PEO	Poly(Ethylene Oxide)
PFOMA	Poly(1H,1H-Dihydroperfluorooctyl Methacrylate)
PI	Poly(Isoprene)
PMMA	Poly(Methyl Methacrylate)
PPO	Poly(Propylene Oxide)
PS	Poly(styrene)
PVC	Poly(Vinyl Chloride)

P&ID	Piping and Instrumentation Diagram
RAFT	Reversible Addition-Fragmentation Chain Transfer
RESS	Rapid Expansion of Supercritical Solution
ROS	Reactive Oxygen Species
SAXS	Small Angle X-ray Scattering
$ScCO_2$	Supercritical Carbon Dioxide
SEC	Size Exclusion Chromatography
SEM	Scanning Electron Microscopy
SFRP	Stable Free-Radical Polymerisation
SLA	Stereolithography
SLS	Selective Laser Sintering
SORP	Self-Organised Reprecipitation
SPH	Spherical Morphology
TEA	Triethyl Amine
TEM	Transmission Electron Microscopy
T_g	Glass Transition Temperature
TGA	Thermogravimetric Analysis
T_m	Melt Transition Temperature
T_{odt}	Order-Disorder Transition Temperature
ToF-SIMS	Time-of-Flight Secondary Ion Mass Spectrometry
TTIP	Titanium Tetraisopropoxide
XRD	X-ray Diffraction
$w_{polymer}$	Weight Fraction of Polymer
σ	Standard Deviation
χ	Flory-Huggins Interaction Parameter
$Đ$	Dispersity

Contents

Chapter 3 – Microscale and Nanoscale Size Modifications of PMMA-*b*-P4VP Block Copolymers from Supercritical CO$_2$

Chapter 6 – Conclusions and Future Work

Chapter 1 – Introduction

1.1. Overview

This chapter aims to introduce the reader to some of the key topics that will be discussed throughout this thesis. The chapter begins by exploring the important advances in polymer science that have been achieved by diverse polymer architectures, in particular block copolymers. The physical behaviour and some of the synthetic routes to block copolymers are detailed, with a specific focus on the use of controlled radical methods and heterogeneous processes.

The use of supercritical carbon dioxide in green polymer synthesis is outlined, including the unique effects this can have of polymer properties. A general overview of nanomaterial fabrication is also given, as well as the beneficial use of block copolymers in this application. Finally, the current state-of-the-art is summarised and the key aims of this thesis are outlined.

1.2. Polymer Chemistry

1.2.1. Modern Polymer Chemistry

As the world celebrates the recent 100th anniversary of the beginning of polymer science, polymer-based products can now be found ubiquitously in our everyday lives.[1] As of 2015, the majority of polymers produced were used for simple applications such as packaging (42%) and in construction (19%).[2] However, advances in polymer research have also allowed polymeric materials to be used in more advanced bespoke applications such as sensors,[3] biomedical devices[4] and electrochemical storage,[5] to name a few.

Despite these many innovations, polymer science still faces many growing challenges. Most prominent of these are the environmental concerns around polymers, regarding their sourcing, biodegradability and the synthetic procedures employed. With over 90% of polymers being derived from non-renewable sources and most being non-biodegradable, there is now a tremendous push to move the industry towards a more closed-loop economy.[6] Other progressions to make polymer production more 'green' have included performing polymerisations in various new environmentally benign and renewable solvents.[7-9]

As we now move into the second century of polymer science, many new developments continue to emerge around how we can source, synthesise and utilise polymers. The popularity of green polymer research remains ever growing, finding new ways to further a path towards a green polymer economy.[10] Though much of the work presented in this thesis does not directly focus on discovering new green polymer alternatives, the work is conducted with environmental sustainability as a crucial consideration. This is realised primarily by omitting the use of non-renewable solvents, however, polymers derived from oil feedstocks are still required to achieve the thesis aims.

1.2.2. Polymer Architectures

The wide range of applications available to polymers is undoubtedly a result of the ease at which polymer properties can be modified. This is achieved simply by altering the chemistry of the fundamental building blocks, monomers. Polymers with different monomers can have vastly different physical and chemical properties. Furthermore, though a combination of multiple different monomers in a polymer chain, materials with hybrid properties of the corresponding homopolymers can be produced.[11] The properties of these copolymers are

highly dependent on not only the proportion of constituents used but also their respective architectures in the polymer chains.

Major advancements in polymer synthesis now allow for much greater control over the desired architecture of copolymers. Precise chemical functionalities are able to be placed essentially anywhere along a polymer chain.[12] Additionally, architectures beyond the conventional linear chains can be achieved via methods such as branching, grafting and cross-linking. Each case leading to further unique physical properties.[13-15] A few examples of possible architectures are shown below (**Figure 1.1**).

Homopolymer

Random Copolymer

Diblock Copolymer

Triblock Terpolymer

Cross-linked Polymer

Comb Polymer

Brush Polymer

Star Polymer

Ring Block Polymer
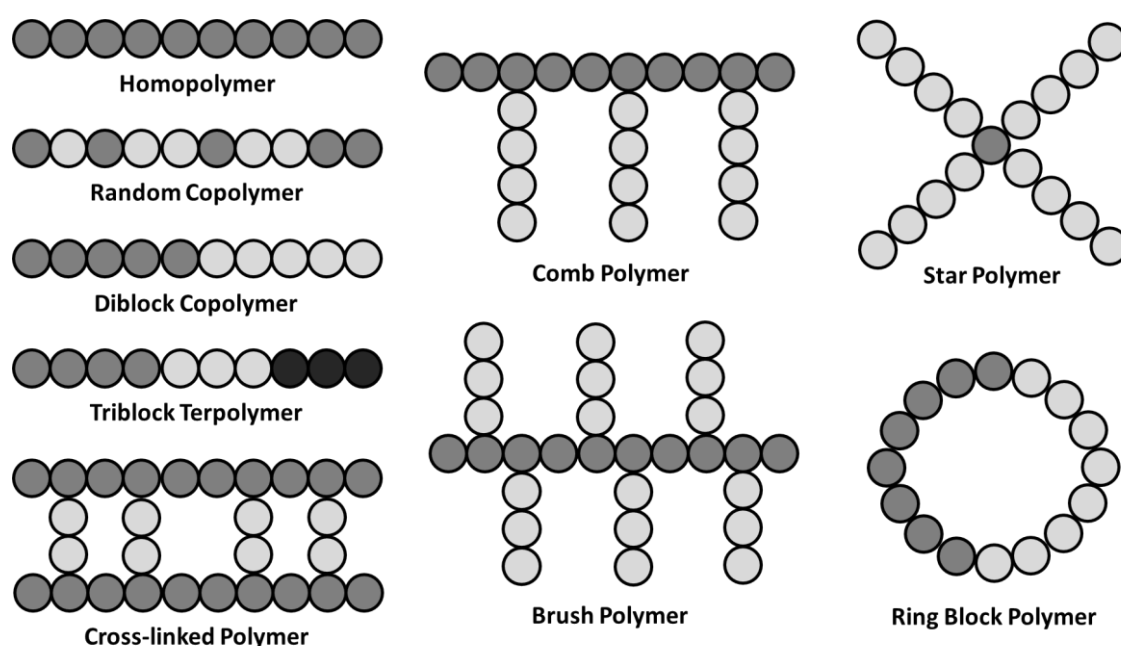
Figure 1.1: *Some examples of basic copolymer architectures.*

Of the possible architectures presented, block copolymers have been some of the most widely studied. This is owed to the ability to place contrasting chemical functionalities at opposing ends of a single macromolecule, creating polymers of an amphiphilic nature. This distinctive physical property gives rise to unique phase behaviour that can be exploited for a range of potential applications.[16]

1.3. Block Copolymers

Block copolymers are a class of copolymer containing distinct regions (or blocks) of individual homopolymer, linked together by covalent bonds. Synthesis of the block copolymer architecture was first demonstrated in the 1950s using anionic polymerisation techniques.[17] Since then they have become a huge topic of academic interest and have seen use in various industrial applications.[18]

Anionic polymerisation provided an initial route to study the fundamental behaviour of these copolymers and is still used when highly pure and monodisperse polymers are required. However, the introduction of controlled radical synthesis techniques has now allowed an extensive range of block copolymer chemistries to be produced.[19] Radical chain growth techniques used to synthesise block copolymers are discussed later in this chapter.

1.3.1. Self-Assembly

The phase behaviour of block copolymers is a unique phenomenon that has driven much of the research in this field. When the individual blocks of a block copolymer become immiscible in one another, the macroscopic phase separation of the blocks remains impossible, due to their covalent linkage. Instead, a self-assembly process known as microphase separation occurs.[20] The process forms various structural morphologies depending on the underlying physical properties of the copolymer and the surrounding environment.[21] The morphologies formed from this are seen at a length scale relative to the length of the copolymer chains (approx. 5-500 nm).[22]

The microphase separation of diblock copolymers is the simplest case and has been the subject of many theoretical and experimental studies over the past few decades. Thus, this process is well understood. Self-assembly of a diblock copolymer is a reversible change of state that transforms the polymer from a homogenous mixture into a regular ordered structure.[23] This can occur in either the bulk copolymer or when the copolymer is in the presence of a solvent, each case leading to different morphologies (**Figure 1.2**). If a solvent is used and is preferential to one polymer block, surfactant-like behaviour is observed and nanoparticulate structures such as micelles and vesicles are produced.[24, 25] Due to its relevance to this thesis, only the bulk self-assembly case will be focussed on in this section.
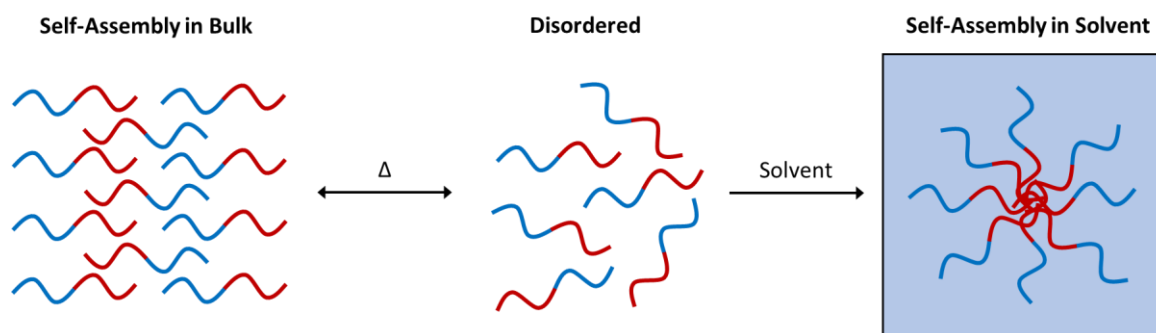
Figure 1.2: *Illustration of the process of self-assembly in bulk block copolymers (left) and in the presence of a selective solvent (right).*

For microphase separation to occur in a bulk diblock copolymer, several criteria must be met. The self-assembly will only be thermodynamically favourable if the enthalpy reduction from separating immiscible blocks outweighs the decrease in entropy when the ordered state is formed. Studies have concluded that in order for this thermodynamic favourability to be met, the copolymer must satisfy the expression given in **Equation 1.1**.[23] The value given is the product of the Flory-Huggins interaction parameter (χ) and the total degree of polymerisation in the copolymer chain (*N*).

$$\chi N > 10.5$$
        (Equation 1.1)

The interaction parameter χ is unique to each pair of polymer blocks based on their relative interactions with one another. The value can be seen as a polymer-polymer incompatibility factor, with larger interactions giving more immiscibility and a higher chance for self-assembly. The parameter is also dependent on temperature. For the vast majority of systems, an increase in temperature lowers the interaction parameter, though some polymer mixtures have also been shown to exhibit a further increase in the parameter at high temperatures. Hence, in most cases self-assembly often occurs upon the cooling of the copolymer from an elevated temperature.[26]

The final criteria for microphase separation to occur is that the copolymer chains must have sufficient mobility to arrange themselves into the new ordered state. This mobility can be provided by solvation, or in the bulk case, by heating the copolymer above the glass transition temperature (T_g). This step is typically referred to as an annealing step.[27]

The exact morphology produced during microphase separation is dictated by what orientation of the copolymer chains gives the minimal interfacial surface area between the two distinct blocks. Limiting this contact area is the thermodynamic driving force to minimise the unfavourable enthalpic interactions.[21] The most favourable equilibrium morphology is determined by the volume fraction (*f*) taken up by each block. In diblock copolymers, when these fractions are similar, flat surfaces are preferable. As one fraction becomes larger and outweighs the other, it becomes more favourable to curve the surface, forming various other shaped morphologies.[28]

The morphologies often seen in diblock copolymers, going from equal to more inequivalent volume fractions, are: lamellar (LAM), bicontinuous cubic gyroid (GYR), hexagonally-packed cylinders (CYL) and spheres (SPH) (**Figure 1.3**).[28] The GYR configuration is only seen over a narrow range of block fractions and has been reported in other metastable configurations, such as a double-diamond structure or hexagonally perforated lamellar. The SPH morphology is often characterised as a body-centred cubic orientation, though some reports of face-centred cubic orientations have also been shown.[29]
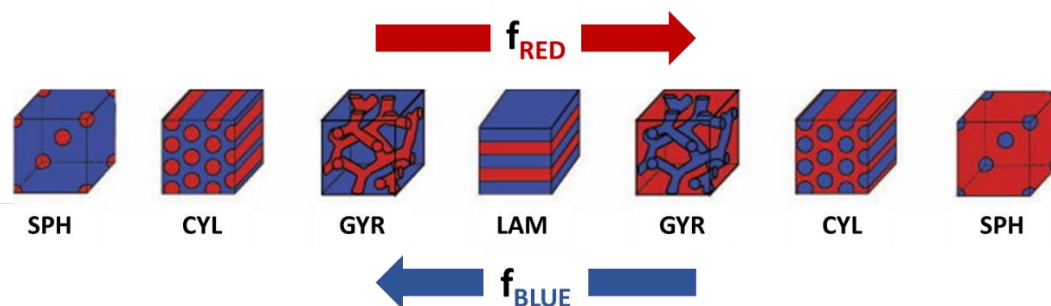
Figure 1.3: The most commonly observed morphologies seen in diblock copolymers, with changing block volume fractions: Spherical (SPH), Cylindrical (CYL), Gyroidal (GYR) and Lamellar (LAM). Figure adapted from literature.[30]

The boundaries between these self-assembled morphologies can be constructed as a phase diagram, with block incompatibility (χN) plotted against a block's volume fraction. This can be plotted experimentally by synthesising and characterising a series of copolymers[31], or theoretically using self-consistent field theory.[32] The self-assembly phase diagram for a linear diblock copolymer system was first derived by Bates and Fredrickson and typically takes the form depicted below (**Figure 1.4**).[23]
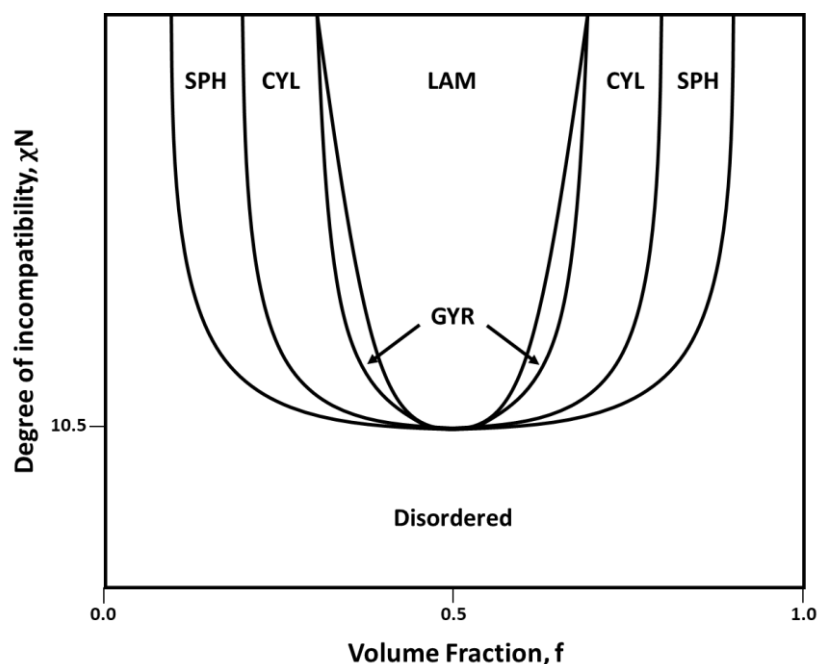
Figure 1.4: *A depiction of the theoretical phase diagram for a diblock copolymer, showing the boundaries between self-assembled morphologies and the disordered states.*

More recently is has been shown that some other phases can also be produced in diblock copolymers. This can be done by controlling the spatial confinement of the copolymer, in a variable number of dimensions.[33] This concept is reviewed further in **Chapter 3**.

Here we have covered the simple case of self-assembly in linear architecture diblock copolymer systems. The self-assembly behaviour of diblocks is also found to be mostly similar to the behaviour seen in triblock copolymers containing only 2 distinct blocks, often referred to as ABA triblock copolymers. With the same morphologies being produced.[34] However, a great number of additional morphologies become accessible whenever additional contrasting blocks are added to the chain, such as in the ABC-type triblock copolymer.[35] Due to the increased number of interaction variables, this greatly increases the complexity of the self-assembly process. This topic is reviewed in depth in **Chapter 4**.

1.3.2. Applications

Due to the unique behaviour of block copolymers in comparison to homopolymers, they have been widely exploited for commercial use. Most prominently, block copolymers are used as thermoplastic elastomers for a variety of applications including adhesives, coatings and sealants.[36] A common example of this type of material is the ABA triblock copolymer of

poly(styrene) (PS) and poly(butadiene) (PB). The PS-*b*-PB-*b*-PS copolymer utilises the hard PS blocks and the soft PB block to give a material with the physical properties of an elastomer, while also behaving as a thermoplastic. When set, the blocks are microphase separated giving the soft rubber-like PB component periodic hard regions of PS that behave like cross-links to give elastomeric behaviour (**Figure 1.5**). However, when heated, the hard PS components also become rubber-like, allowing the material to be easily processed and reused like a typical thermoplastic. In contrast, most other rubbers are thermoset by chemical cross-linking, preventing them from being reshaped.[37, 38]
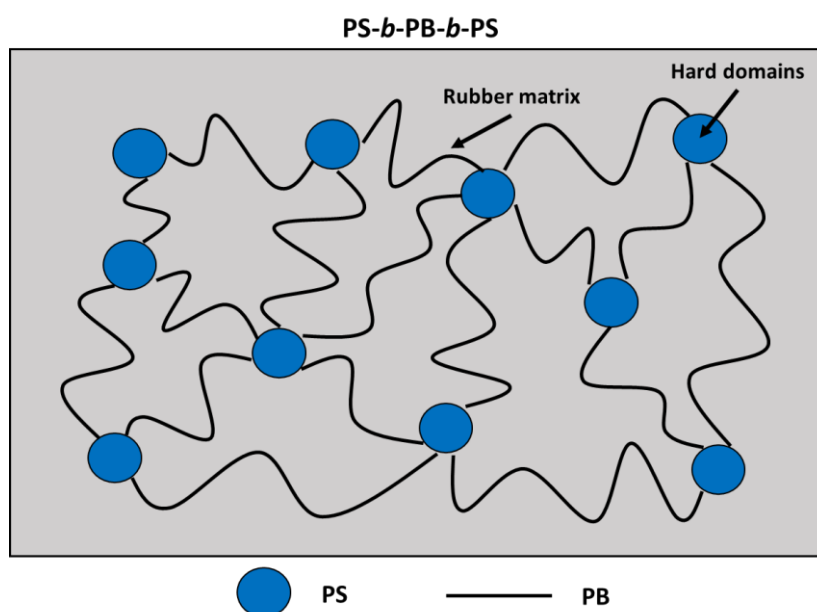
Figure 1.5: *Physical structure of a PS-b-PB-b-PS thermoplastic elastomer. The hard spherical regions of PS act as cross-links to give elastomeric behaviour.*

Another popular type of commercial block copolymer are poloxamers often referred to as 'Pluronics'. Poloxamers are another ABA triblock copolymer consisting of a hydrophilic poly(ethylene oxide) (PEO) blocks with a hydrophobic poly(propylene oxide) (PPO) central block. The amphiphilic nature of poloxamers is highly tuneable based on their block lengths. As such, the controllable non-ionic surfactant behaviour has been utilised in various applications such as in cosmetics, detergents and drug delivery.[39, 40]

Block copolymers have been extensively investigated for use as drug carriers in the body, in most part due to their amphiphilic nature.[41] The polymers can easily assemble around a hydrophobic drug, forming nanoscale vehicles that are small enough to evade the body's

immune response.[42, 43] This interest has grown over time as the synthetic techniques used to make block copolymers have become more sophisticated. Drug delivery polymers can now be synthesised with functional designs to allow them to target specific cells[44], modify the drug release profile[45] or react to particular stimuli, such as pH.[46] These features can be particularly useful when targeting drug delivery to cancer tumours, which have a lower pH than normal tissue.
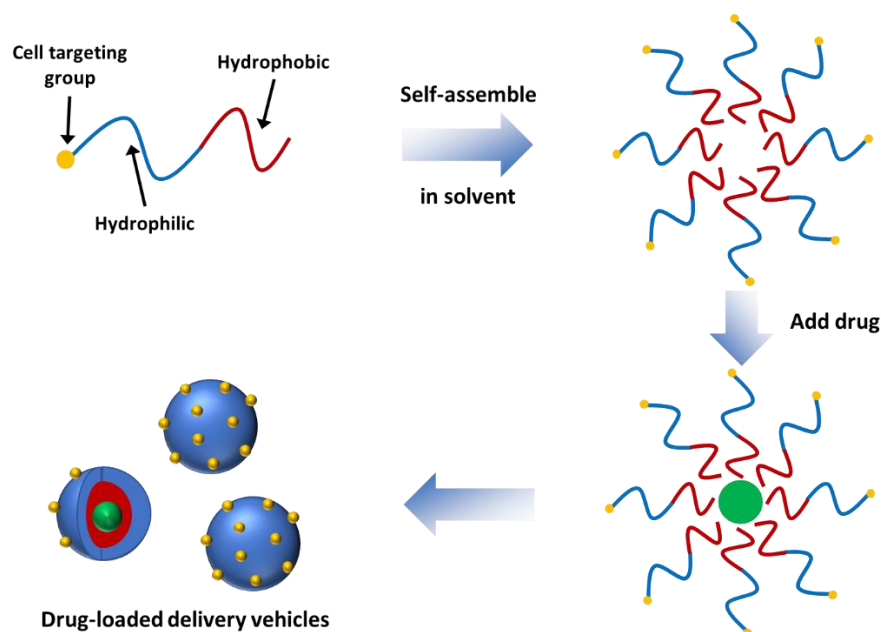
Figure 1.6: Schematic of the assembly of amphiphilic block copolymer micelles used for targeted drug-delivery.

Bulk self-assembled block copolymers are also being explored for use in various non-mechanical applications. For example, application in photonics[47] and optical metamaterials.[48] The regular nanoscale morphologies created by block copolymers are ideal for forming periodic dielectric structures for manipulating visible light. The path length of the periodic structures forms a photonic band gap for photons of the matching wavelength, thus causing them to be reflected constructively. This manipulation of light flow has many desirable uses in high reflective coatings and optical filters.[49] By creating this kind of material from soft block copolymers, there is also an opportunity to alter the size of the photonic band gap by applying stimuli to increase the size of the nanostructures, for example by introducing a solvent to swell the polymer.[50]

Finally, bulk self-assembled block copolymers can be utilised to fabricate an array of functional nanomaterials. The unique nanostructures of block copolymers are highly desirable for many inorganic functional materials.[51] The interesting patterning and high surface areas of these morphologies can lead to enhanced functionality in existing inorganics or can provide entirely new properties. Block copolymers can be used as templates to fabricate these nanomaterials, using both top-down and bottom-up methodologies.[52] These processes are described in detail later in this chapter.

1.4. Polymer Synthesis

Methods of polymerisation are generally classified by the mechanism of the polymer growth, either chain-growth or step-growth.[53] In step-growth methods, bifunctional or multifunctional monomers are reacted together, linking the functional groups to form oligomers first and then eventually longer chain polymers. An example of this is the polycondensation reaction between the amine and carbonyl function groups to produce polyamides, generating water in the process.[54] However, the nature of this type of polymer growth makes it very inaccessible to synthesising block copolymers.

Chain-growth methods involve the sequential addition of monomers to a propagating chain through a reactive functionality, often a vinyl functional group. Each added monomer becomes the reactive centre for the polymer chain and goes on to react with a sequent monomer. When the process is controlled, the monomer feedstock can be easily switched during propagation, to allow the growing polymer to add a new series of monomers to the chain, forming block copolymers. There are several ways to polymerise a vinyl monomer in this way, including anionic, cationic and radical mechanisms to activate the double bond.[55] Due to its relevance in this thesis, only the radical mechanism will be discussed in detail.

1.4.1. Free-Radical Polymerisation

Free-radical polymerisation (FRP) is possibly the most common form of polymerisation, with around 50% of industrially manufactured plastics predicted to be synthesised through this mechanism.[56] This is arguably due to the method's high tolerance towards chemical functionality, making it suitable for a wide range of monomers and solvents. This also allows the reactions to be much more forgiving to chemical impurities, a major advantage over the other ionic methods of chain-growth.[57]

The FRP mechanism occurs in four keys steps (**Figure 1.7**). Firstly, an initiator molecule is broken down to produce active radical species, usually by exposure to heat or light. The radical then goes on to react with the monomer, initiating it into an active propagating molecule. This then reacts sequentially with additional monomers to propagate the chain, rapidly forming a high molecular weight macromolecule. The active radical then eventually terminates by reacting with another active radical species. This can occur either by combination of the two chains into one higher molecular weight chain or by

11

disproportionation where a hydrogen atom is radically abstracted to form one H-terminated chain and one vinyl terminated chain. The preferred method of termination depends on the chemical structure of the monomer being polymerised.[56]

$$I_2 \rightarrow 2I^{\bullet} \qquad \text{(Initiator Decomposition)}$$

$$I^{\bullet} + M \rightarrow IM^{\bullet} \qquad \text{(Initiation)}$$

$$IM^{\bullet} + nM \rightarrow P_{n+1}^{\bullet} \qquad \text{(Propagation)}$$

$$P_n^{\bullet} + P_m^{\bullet} \rightarrow P_{n+m} \qquad \text{(Combination)}$$

$$P_n^{\bullet} + P_m^{\bullet} \rightarrow P_n + P_m \qquad \text{(Disproportionation)}$$
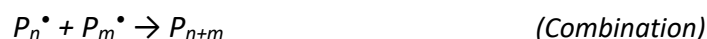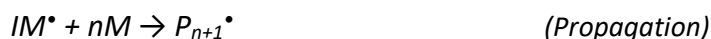
Figure 1.7: The mechanism of FRP showing the four key steps, including both methods of radical termination. I represents the initiator, M is the monomer and P is the polymer.

The propagating step in the FRP mechanism occurs rapidly due to the high reactivity of radical species. During the reaction a quick sharp increase in the average polymer molecular weight is observed as chains propagate. This molecular weight growth then slows as the monomer concentration decreases and termination reactions begin to dominate. The typical plots of molecular weight growth against monomer conversion for the chain and step-growth mechanisms can be seen below (**Figure 1.8**). The plot also shows the 'living' polymerisation trend where no termination reactions occur and molecular weight always proceeds linearly with respect to the reaction conversion. This is seen more in ionic chain-growth mechanisms where propagating chains cannot terminate by reacting with other growing chains.[55]
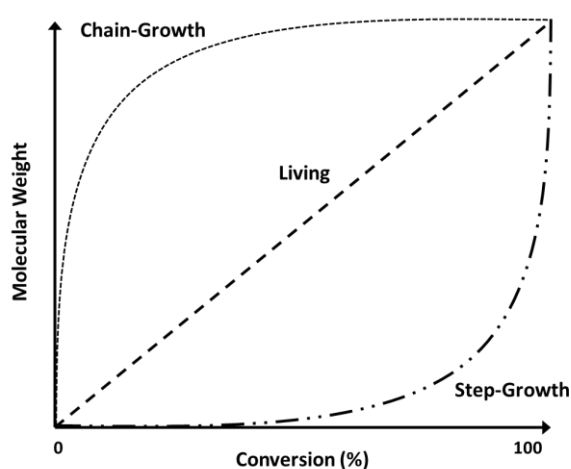
Figure 1.8: A representative plot of the average polymer molecular weight against monomer conversion for the chain growth, step growth and living polymerisation mechanisms.

1.4.2. Controlled Radical Polymerisation

The major disadvantage of the FRP method is the uncontrolled nature of the termination reactions. These reactions can occur at any time during the propagation stage of the reaction and result in the polymer product containing a large distribution of chain lengths. This distribution is quantified using a dispersity value (Đ).[53] Đ is calculated by comparing the weight average molecular weight (M_w) and number average molecular weight (M_n) (**Equation 1.2**). Uncontrolled FRP reactions typically give dispersities of Đ > 2. The termination step also often leaves polymer chains inactive towards any further propagation with a secondary monomer species. These limitations prevent any reasonable control over the desired polymer architecture and potential self-assembly.

$$Đ = \frac{M_w}{M_n}$$

(Equation 1.2)

It is because of these constraints that more sophisticated forms of radical polymerisations have been developed, allowing more complex architectures to be attained. These techniques are referred to as controlled radical polymerisation (CRP) methods.[58] CRP methods utilise an additional step in the free-radical mechanism, radical chain transfer. In this step the active radical of a propagating polymer chain is transferred onto a supplementary reagent. This step can sometimes occur during the usual FRP method by transferring onto another molecule such as a solvent or impurity. This is usually undesirable, leading to even less control in the polymerisation kinetics. However, a carefully designed chain transfer agent can provide an opportunity to capture and control the growing radical chains.[59]

In CRP methods a chain transfer agent is used to limit the concentration of actively propagating radical chains. By reducing this concentration, the termination reactions become much less favourable as their rate depends on $[P_n^\bullet]^2$. The result in a lower but more constant concentration of propagating radicals throughout the reaction; hence the molecular weight of the chains increases more linearly with monomer conversion. This generates a kinetic profile more akin to the living reaction method. Though, termination reactions are not completely eliminated so this is not exactly equivalent. The additional chain transfer agent also forms a functionalised group at the end of the synthesised polymer chains. This group can be removed or re-reacted to allow further polymerisation to take place.[57]

Various CRP mechanisms have now been developed and used to create complex polymer architectures, including block copolymers.[60] The most common forms are stable free-radical polymerisation (SFRP), atom transfer radical polymerisation (ATRP) and reversible addition-fragmentation chain transfer polymerisation (RAFT). In each CRP technique, reagents are added to achieve an equilibrium between active propagating chains and a dormant captured species. The equilibrium is favoured towards the dormant species to ensure the concentration of propagating radicals always remains low.[58]

In SFRP, a stable radical species is utilised as a capping agent to deactivate propagating chains (**Figure 1.9**). This radical species is not capable of initiating its own polymer chains and will degrade back to the original radical species when exposed to high temperatures. The most common capping agents are alkoxyamines. When these are used the method is referred to as nitroxide-mediated polymerisation (NMP).[61]
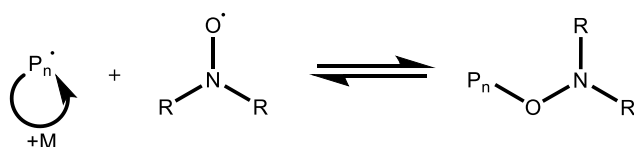
Figure 1.9: The key mechanistic step in the NMP technique, showing reversible termination of the propagating polymer chain.

ATRP uses similar principals to SFRP. Propagating radical chains are deactivated by capping with a halogen atom, which is supplied by a transition metal catalyst (**Figure 1.10**). The metal catalyst originally activates an alkyl halide molecule through a one-electron process, initiating the polymerisation. The oxidised catalyst then reverses the process, capping a radical chain with the halogen atom and then quickly forms an equilibrium between dormant and active radicals.[62]
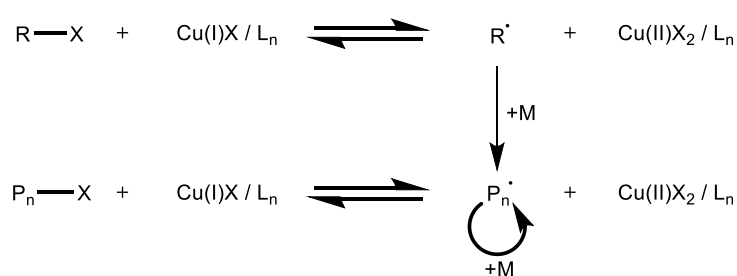
Figure 1.10: The key mechanistic steps for the ATRP technique using a copper catalyst. X is a halide atom and L_n is the ligand(s) for the copper complex.

14

The RAFT technique is the CRP method employed in this thesis and has been reviewed in greater detail than the other methods.

1.4.3. Reversible Addition-Fragmentation Chain Transfer Polymerisation

RAFT polymerisation was first developed in 1998 by Graeme Moad, Ezio Rizzardo and San Thang at the Commonwealth Scientific and Industrial Research Organisation (CSIRO) in Australia.[63] This CRP method uses thiocarbonyl compounds as reversible chain transfer agents in the radical reaction. The process creates a kinetic equilibrium in the chain propagation, causing all chains to grow at a statistical rate. The generic structure of the RAFT agent (**Figure 1.11**) contains two variable R and Z groups that are modified to determine the reagents compatibility with different monomer classes. This variability is one of the key advantages over other CRP techniques, allowing RAFT to be highly versatile and tolerant of a wide range of functionality in monomers and solvents, including in aqueous systems.
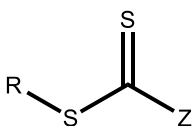
Figure 1.11: *General structure of a RAFT agent.*

The complete mechanism of this CRP technique is detailed below (**Figure 1.12**). The initiator first decomposes and begins chain propagation of the monomer, as in normal FRP. The propagating chain is then captured by the RAFT agent to form the relatively stable thiocarbonyl radical species. The species then fragments to release the R$^\bullet$ group. This then goes on to initiate the propagation of another polymer chain. The new chain can then be recaptured by the RAFT agent and the previous chain released, creating an equilibrium between all growing chains. As with the free-radical mechanism, termination can occur between two propagating chains by either combination or disproportionation to give a dead polymer chain. However, the RAFT equilibrium ensures that the concentration of propagating radicals in the system is always low, reducing the probability of this step occurring.[64]

Decomposition & Initiation:
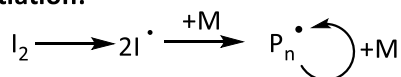
Chain transfer to RAFT agent:
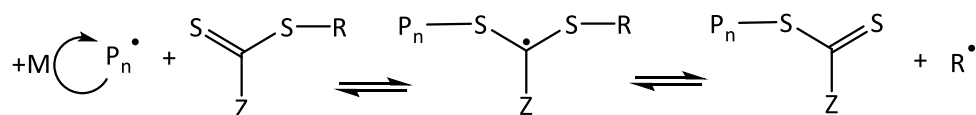
Reinitiation:
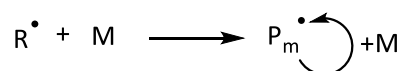
RAFT equilibrium:
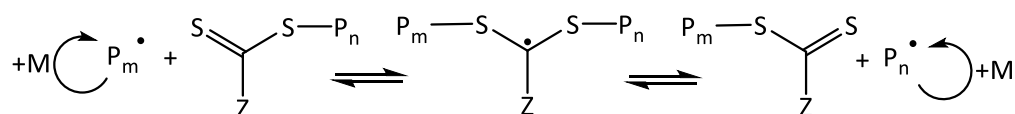
Termination:
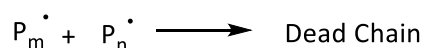
Figure 1.12: *The full mechanism for the RAFT polymerisation technique.*

The specific reactivity of each RAFT agent is tailored by modifying the R and Z groups of the compound. The Z group determines the reactivity of the C=S bond which will influence the stability of the thiocarbonyl radical intermediate in the reaction. The R group must provide a sufficiently weak R-S bond that can be homolytically cleaved to produce a radical leaving species. This radical must then also be capable of reinitiating the chosen monomer.[65]

If it is assumed that all polymer chains undergo the RAFT mechanism, a particular molecular weight for the final polymer can be targeted (**Equation 1.3**). The target molecular weight (M_n $_{Target}$) can be calculated by using the concentration of RAFT agent ([RAFT]), monomer at the start of the reaction ($[M]_0$) and monomer at the end of the reaction ($[M]_t$). The proportion of the converted monomer to the RAFT agent gives the average degree of polymerisation. This is then multiplied by the monomer mass ($M_{r\,monomer}$) and added to the mass of the RAFT end group ($M_{r\,RAFT}$) to give the theoretical average polymer mass. The target calculation assumes the polymerisation is fully living and no termination reactions occur and so is only an approximation.[64]

$$M_{n\,Target} = \frac{[M]_0 - [M]_t}{[RAFT]} \times M_{r\,monomer} + M_{r\,RAFT} \qquad \textbf{(Equation 1.3)}$$

Another consequence of using the RAFT control mechanism over the standard FRP one is that synthesised polymer chains retain a RAFT group moiety at the end of all chains grown via the living mechanism. For some applications this can be troublesome as another synthetic step is required to remove the end groups and obtain the pure polymer product. However, the RAFT end groups also allow the polymer to be re-initiated and grown with an additional monomer, making the technique highly accessible to synthesising block copolymers (**Figure 1.13**).[66] The pre-synthesised polymer essentially acts as the RAFT agent in the mechanism for the next monomer, with the R group now being the first homopolymer block. A polymer used in this way is commonly referred to as a macro-RAFT agent.[67]
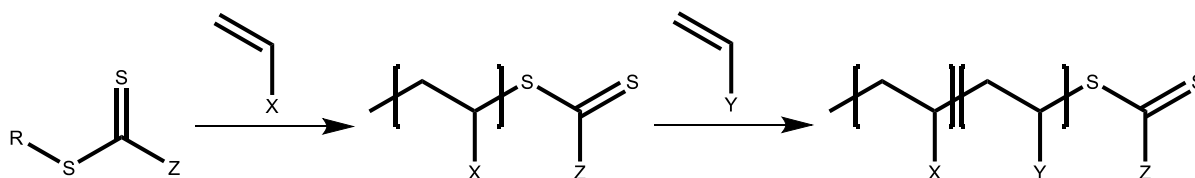
Figure 1.13: *Reaction scheme for polymerising vinyl monomer X with a generic RAFT agent, then using the subsequent macro-RAFT to polymerise vinyl monomer Y, forming a block copolymer.*

The RAFT polymerisation technique has been used to synthesise a diverse range of polymer architectures beyond block copolymers. For example, chain transfer agents with multiple RAFT moieties have been used to synthesise star polymers.[66] Also, RAFT agents with multiple functionalities can be used in combination with other polymerisation techniques, including ATRP and ring opening polymerisation, to produce architectures such as bottle brushes.[68]

It is clear the RAFT technique offers many advantages over other CRP techniques in terms of its versatility towards monomer types and final polymer architectures.[63] The technique also avoids the use of high temperature conditions used for SFRP, generally making it more energy efficient and industrially applicable. Finally, RAFT does not use any metal catalysts unlike in ATRP, a major advantage if the polymer product is to be used in applications involving human contact.[69]

However, RAFT does suffer some undesirable aspects. Primarily, the unwanted discolouration of the final product caused by the RAFT chromophores, which can be difficult to completely

remove. Also, the synthesis of RAFT agents is often complex, expensive and time-consuming, requiring the use of toxic reagents such as carbon disulfide.[70]

1.5. Polymer Processes

Alongside the various reaction techniques used to synthesise polymers, polymerisations can also be categorised into several different processes. These processes are defined as either homogeneous or heterogeneous depending on whether the polymerisation occurs in the same phase as the solvent or not. Homogeneous polymerisations are conducted in either the bulk (monomer only) or a solvent where both monomer and polymer are fully soluble. These processes are relatively straightforward with minimal reaction components and are the easiest to understand in terms of kinetics.[71] The types of heterogeneous processes are more extensive and are the kind used exclusively in this thesis.

1.5.1. Heterogeneous Polymerisation

Any polymerisation process that forms a polymer product which is insoluble in the reaction solvent (the continuous phase) can be considered heterogeneous. The reaction kinetics of these processes are more complex than homogenous ones as most if not all of the polymerisation occurs independently from the continuous phase. However, this does yield several benefits that have made these processes more suitable for use at the industrial scale. These include generally faster reactions kinetics, improved heat dissipation and ability to replace organic solvents with more environmentally friendly alternatives (e.g. water).[56] Heterogeneous processes fall into one of four common categories: precipitation, suspension, emulsion and dispersion.

Precipitation polymerisation begins as a homogeneous system, with both monomer and initiator soluble in the solvent. As polymerisation begins, the propagating polymer chains become insoluble in the continuous phase and precipitate. Polymerisation then continues predominantly around the surface of the flocculated polymer particles as monomer is absorbed into the polymer phase. This typically yields large particles with irregular and inconsistent morphologies.[72]

In suspension polymerisation, the monomer and initiator are both insoluble in the reaction solvent. The immiscible components are mechanically agitated to form droplets that are stabilised using a surfactant. The polymerisation then takes place only within the monomer droplets, to form polymer particles of up to 100s of microns in size. The process is commonly used in industry to synthesise poly(vinyl chloride) (PVC) and PS particles.[73]

Emulsion polymerisation is probably the most widely used heterogeneous process, being used industrially to make various paints, adhesives and rubbers.[74] The continuous phase in this process is usually water. The water solvent contains a water-immiscible monomer and water-soluble initiator, along with a surfactant. The polymerisation then proceeds in three distinct stages (**Figure 1.14**).[75]
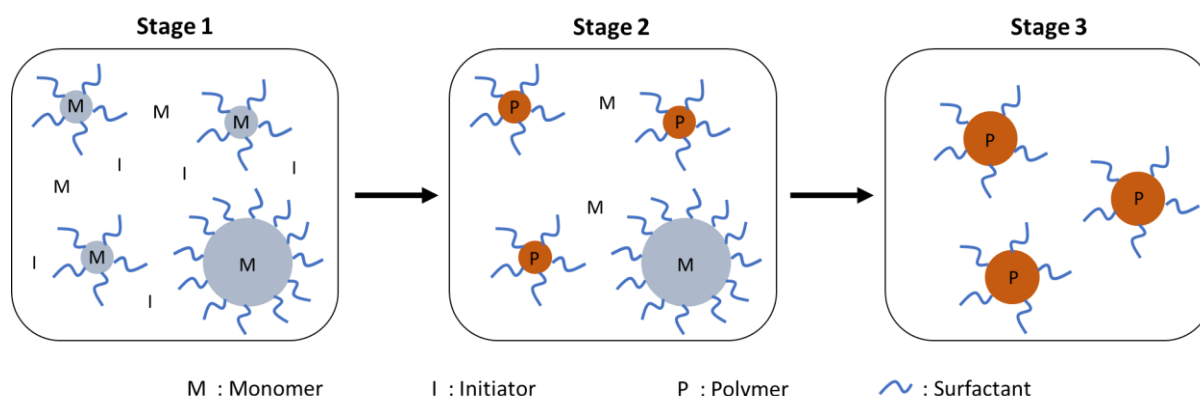
Figure 1.14: *Schematic of the stages involved in a typical emulsion polymerisation process.*

In the first stage, most monomer exists in large, stabilised droplets, with some surfactant micelles swollen with additional monomer. Initiation occurs in the continuous aqueous phase to form short chain insoluble oligomers, which then diffuse into the monomer micelles to continue propagating. This first stage is known as particle nucleation. The next stage then sees additional monomer continually fed into the propagating particles from the large monomer droplets, allowing for a continuous rate of polymerisation. In the final stage, polymerisation rate decreases as the monomer concentration becomes low. This continues until all the monomer is depleted, forming the final latex product.[76]

Emulsion polymerisation can also be divided into sub-categories. The basic form described above is known as *ab initio* and typically produces polymer particles of 100s of nm. Other variants include seeded emulsion, miniemulsion and microemulsion. Seeded emulsion works in the same way as the *ab initio* method, except a previously prepared latex is added to the mixture to omit the nucleation stage.[77] Miniemulsion uses an additional co-surfactant along with high mechanical shear to prevent large monomer droplets forming. This in turn forms smaller polymer particles, up to as small as around 50 nm.[78] Microemulsion also uses a co-

surfactant as well as a very high overall surfactant concentration to achieve particles of <50 nm. In some cases, growing particles can consist of only a single propagating chain.[79]

The final heterogeneous category, dispersion, is utilised in this thesis and is described in the following section.

1.5.2. Dispersion Polymerisation

Dispersion polymerisation is very similar to the precipitation polymerisation process. It has been utilised in industry to create various coatings, toners and packing materials for chromatography columns.[80] The process can be divided into 4 key stages (**Figure 1.15**).
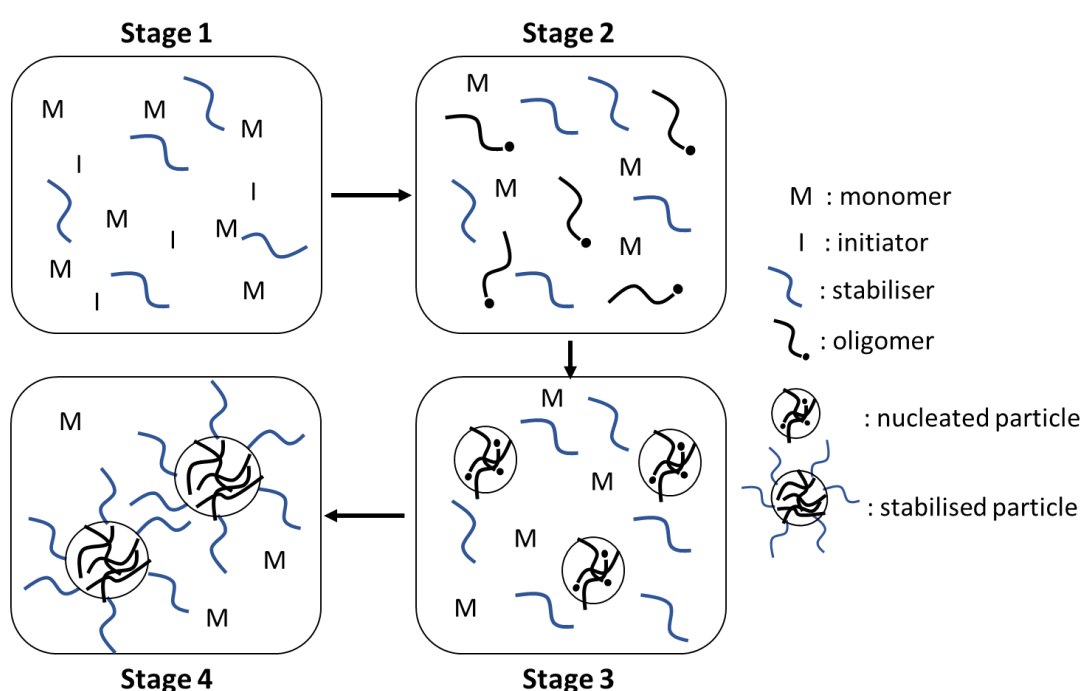
Figure 1.15: Schematic illustrating the key stages of the dispersion polymerisation process.

The first stage is almost identical to the precipitation process, with monomer and initiator soluble in the continuous phase. Dispersion differs by also adding a soluble polymeric stabiliser into the mixture. In the next stage, polymerisation begins in the continuous phase forming short chain propagating oligomers. Then, quickly after this stage, the oligomers reach a critical molecular weight where they become insoluble in the continuous phase. The insoluble oligomers aggregate to form the primary polymer particles for the dispersion. In the final stage, the polymeric stabiliser is adsorbed onto the surface of the nucleated particles, covering them to form a stable heterogeneous mixture. The stabilisers used are typically steric

stabilisers, creating a barrier of repulsive force between particles to overcome the van der Waals attraction between the polymer particles. With further particle aggregation prevented, the polymerisation continues solely by monomer diffusing into the polymer phase, continuing the propagation and growing the size of the polymer particles. The process typically yields highly uniform polymer particles in the size range of 0.1-10 μm.[80, 81]

Aside from filling in the size range of polymer particles left between the emulsion and suspension processes, dispersion offers other unique benefits over emulsion systems. Mechanistically, the process tends to be more facile than typical *ab initio* emulsions. The process also requires less mechanical agitation and a much lower concentration of additional stabiliser than miniemulsion, that can affect the end product.[82]

Despite these advantages, dispersion polymerisation is generally underexplored in comparison to emulsion systems. A key factor in this is the relatively limited number of solvents that are miscible with a monomer but in which the resulting polymer is insoluble. The most common solvents utilised as the continuous phase are alkanes,[83] alcohols[84] and supercritical carbon dioxide.[85]

1.5.3. Heterogeneous RAFT Polymerisation

The CRP techniques introduced in the previous section of this chapter are a versatile and desirable route to produce well-defined polymers for speciality applications. However, for these products to be realised at the industrial scale, CRP techniques must be compatible with the heterogeneous processes utilised by industry. Consequently, over the past 20 years, a significant amount of research has focused on addressing the challenges of integrating CRP methods into heterogeneous systems. Investigations have covered all CRP techniques and has been reviewed in detail.[86, 87] Here though, only the specifics regarding the RAFT polymerisation technique will be addressed.

The main issues with integrating RAFT techniques with heterogeneous processes stems from the additional mechanistic complexity of this technique over traditional FRP. A key challenge is maintaining the same degree of control over the radical propagation when compared to the simpler homogeneous case. For this to be achieved, the RAFT chain transfer agent must remain solely at the polymerisation *loci*, i.e. the phase where polymerisation is occurring. It

has been found that exit of the chain transfer species from the polymer phase can result in a loss of control and a subsequent increase in the product's Đ value.[88]

Another challenge to overcome is the RAFT mechanism's effect on the polymer nucleation stage of heterogeneous processes. The slow initial rate of polymerisation in the RAFT mechanism can delay the particle nucleation stage of the process. This in turn can cause variations in the size of the final polymer particles.[89] A large increase in the particle size distribution can have detrimental effects for the end application.

Several strategies have now been developed to successfully conduct RAFT polymerisation in heterogeneous processes. A simple solution has been to perform these controlled syntheses in miniemulsion type systems.[90] With all monomer converted directly into polymerisation micelles, there is no risk of partitioning the fragmented RAFT species into the large inactive monomer droplets. Other strategies have included using a preformed latex to seed particles for RAFT polymerisation,[91] eliminating the complexities involved with the particle formation. Or using amphiphilic macro-RAFT in place of the usual surfactant used to create the polymerisation micelles, ensuring the chain transfer agent remains at the polymerisation *loci*.[92]. The reader is directed to several review articles that describe these latest developments in more detail.[86, 87, 93, 94]

Concerning the case of RAFT polymerisation in dispersion type heterogeneous systems, one particular approach has proven to be highly popular to produce block copolymers. The process involves using a fully soluble macro-RAFT agent with a solvent-miscible monomer that goes on to form an insoluble polymer. The reaction begins as a simple homogeneous system and then as the solvophobic polymer block grows in molecular weight, unfavourable solvent interactions induce self-assembly of the propagating polymers into nanoscale objects. Polymerisation then continues in the newly formed polymer phase by diffusion of the remaining monomer. The process was coined polymerisation-induced self-assembly (PISA) and has been shown to produce a variety of nanoscale morphologies depending on the reaction parameters, including micelles, vesicles and worms.[95] Such materials are currently being researched for application predominantly in the biomedical field.[96, 97]

RAFT dispersion polymerisation has also been conducted without the use of macro-RAFT stabilisers, instead employing the unique properties of unconventional solvents such as supercritical carbon dioxide.[98]

1.6. Supercritical Carbon Dioxide

1.6.1. Physical Properties

A supercritical fluid is a physical state of matter that can be obtained in many chemical species. A substance is said to be in a supercritical state when it exceeds a particular temperature and pressure, the critical point. At this point, the species changes from having a distinct liquid and vapour phase to having a single supercritical phase, with mixed physical properties of both the liquid and gas states. The fluid has a liquid-like density yet possesses the viscosity and diffusivity of a gas. Tuning the pressure and temperature of the fluid also allows the solvation properties to be changed, something not possible with conventional liquid solvents.[99]

The supercritical state for carbon dioxide (scCO$_2$) is relatively easy to obtain, with a critical point at 31.1 °C and 73.8 bar (**Figure 1.16**), making it desirable for industrial scale use. Other benefits include its abundance from waste streams, chemical inertness and that it is a non-flammable solvent. Characteristic that adhere to several of the principals of green chemistry. These attributes, combined with the tuneable solvent power and ease of separation from other chemical species at ambient pressure, have led to scCO$_2$ being utilised in a variety of chemical processes. Examples include the synthesis many organic, inorganic and polymeric species; chemical extractions, polymer processing and the fabrication of electronics.[100]
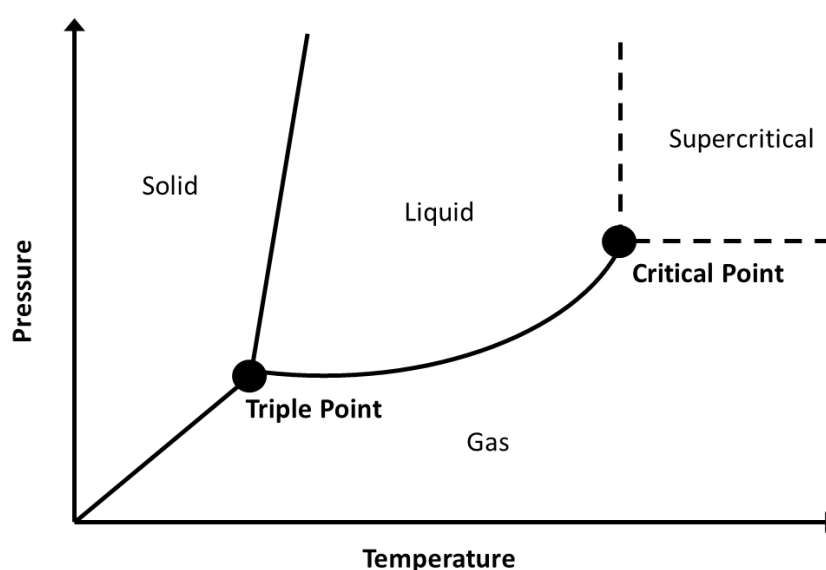
Figure 1.16: *Illustration of the phase diagram of pure CO$_2$. The triple point is indicated at -56.4 °C and 5.2 bar. The critical point is indicated at 31.1 °C and 73.8 bar.*

The main limitation of $scCO_2$ for these applications is the poor solubility of polar molecules and high molecular weight substances. However, this does make $scCO_2$ a good candidate for conducting heterogeneous polymerisations.

1.6.2. Polymers in $scCO_2$

Under moderate conditions, $scCO_2$ is a poor solvent for most polymers. Notable exceptions however include fluorinated and siloxane-based polymers.[101] As such, only a few examples of homogenous solution polymerisations in $scCO_2$ exist. The majority of polymer syntheses in this solvent are performed using precipitation and dispersion type processes, with some limited examples of emulsion and suspension methods.[9] Dispersion polymerisation is reviewed extensively in the literature, due to the environmentally advantages of the solvent and the ease of separating the polymer particles after the synthesis, simply by releasing the pressure and venting the gaseous CO_2. Most examples use fluorinated polymers such as Krytox[TM] or siloxanes such as poly(dimethyl siloxane) (PDMS) as the polymeric stabiliser.[102]

Many reaction techniques have also been demonstrated in $scCO_2$, including cationic, ring opening and condensation polymerisations.[102] FRP is a popular technique used in $scCO_2$ as the CO_2 molecules are highly unreactive towards radical species. This makes unwanted radical chain transfer to the solvent highly unlikely. However, it has been noted that $scCO_2$ can alter radical initiator decomposition and FRP reaction rates.[103] FRP in $scCO_2$ is a versatile technique and has been applied to a range of monomers including several methacrylates,[85, 104] styrene,[105] divinyl benzene,[106] N,N-dimethyl acrylamide (DMA)[107] and N-vinyl pyrrolidone.[108] All cases yielding well-defined microparticles, indicating stable dispersions were formed.

Though CO_2 may have a very poor solvating capacity for most polymers, it is still able to undergo strong interactions with many polymers while in the liquid or supercritical state. The CO_2 can penetrate into polymer matrices, intercalating between polymer chains and causing the material to swell. As the polymer's intermolecular spacing increases, the chains become more mobile, leading to a depression in the polymer T_g and can also influence crystallisation.[109, 110] The phenomenon is often exploited in polymer processing to foam materials by rapid release of pressure[111] or to diffuse CO_2-soluble species into the polymer phase, such as drugs[112] or nanoparticles.[113]

The extent of the sorption of CO_2 into a polymer matrix depends on the physical interactions of CO_2 with the polymer's chemical structure. CO_2 interacts with polymer chains by the standard van der Waals interactions. These interactions are complex and can be difficult to predict, largely owing to the large quadrupole moment of CO_2.[101] Additionally, CO_2 has been shown to act as an electron acceptor for polymers containing functional groups with lone electron pairs, e.g. carbonyl groups.[114] These factors all determine the 'CO$_2$-philicity' of a polymer and subsequently the extent of swelling caused by CO_2.

1.6.3. CRP and Block Copolymers in scCO₂

A wide range of CRP techniques have also been attempted in scCO$_2$ dispersion polymerisation, including ATRP,[115] NMP[116] and RAFT,[98] with varying degrees of success. A more detailed review of CRP techniques in scCO$_2$ can be found elsewhere.[117]

Many reports of CRP in the literature utilise control agents that also act as the stabiliser in the dispersion process, occasionally referred to as inistab molecules. Examples include macroligands in ATRP to solubilise the copper complex and stabilise the nucleated particles,[118] polymeric alkoxyamines in NMP dispersion[119] and fluorinated macro-RAFT agents.[120] The vast majority of these cases report relatively low dispersity values (<1.5) and good agreement between the target and experimental molecular weights, likely owing to control species guaranteed to be at the polymerisation *loci*. However, many also report highly agglomerated particles or large particle size distributions, indicating a possible loss of stabilisation in the dispersion.

RAFT dispersion polymerisation in scCO$_2$ has been explored extensively by the Howdle group. Their first report demonstrates the synthesis of poly(methyl methacrylate) (PMMA) in scCO$_2$ in the presence of a common RAFT agent and a monomethacrylate terminated PDMS (PDMS-MA) stabiliser.[98] The resulting polymers were shown to have the desired molecular weight, low dispersity (≤1.2) and spherical particle morphologies. However, it was noted that particle size distribution was broad due to a large inhibition period in particle nucleation. If particle nucleation is allowed to occur over a long period of time, then stabiliser concentration tends to be distributed unevenly across particles, with the first nucleated particles attracting more stabiliser. This then causes particles to grow asymmetrically, giving a large distribution of particle sizes.

Many subsequent reports by the Howdle group continue to adopt separate stabiliser and RAFT agent molecules to control the polymerisation.[121, 122] A more recent study demonstrates how RAFT agent solubility in $scCO_2$ must be carefully selected to enable full partition of the transfer agent to the polymer phase, ensuring good control is achieved.[123] This study highlighted that for adequate control to be maintained, the RAFT agent must be fully soluble in $scCO_2$ at the early homogeneous stage of the dispersion polymerisation, but then quickly partition into seeded polymer particles once they were formed. It is likely then that for this to be successful, the RAFT agent must be more soluble in the polymer than the $scCO_2$ continuous phase. Thus far, successfully determining if this balance has been achieved has only been possible though empiric investigation of the polymerisation kinetics.[123]

As a natural progression from the investigations of CRP in $scCO_2$, many groups have also used these techniques to synthesise block copolymers.[117] A number of reports use $scCO_2$ soluble polymers as the first block, acting as a macroinitiator or transfer agent. For example a $scCO_2$ soluble poly(1H,1H-dihydroperfluorooctyl methacrylate) (PFOMA) first block was used by Xia et al. for ATRP[115], and Zong et al. for RAFT[120] synthesis of PFOMA-*b*-PMMA block copolymers.

Beyond this, several examples of fully insoluble block copolymers synthesised by $scCO_2$ dispersion have also been reported. Minami et al. synthesised a poly(acrylic acid) (PAA) first block by ATRP in $scCO_2$,[124] while O'Connor et al. synthesised PAA, PS and PDMA first blocks using NMP control.[125] Both cases use a two-step synthesis strategy, obtaining and purifying the first block macroinitiators before synthesis of the resulting block copolymers.

Recently, Howdle et al. have demonstrated the synthesis of several PMMA containing block copolymers using RAFT control via a one-pot synthetic procedure.[126] In this method, the second monomers are fed into the reactor by a high-performance liquid chromatography (HPLC) pump once synthesis of the PMMA macro-RAFT agent is complete. Most block copolymers were found to have relatively low dispersity (<1.7) and spherical microparticle structure. Examination of the internal morphologies of the microparticles also found a variety of self-assembled nanostructures, which could be altered by changing the block fractions of the constituent blocks (**Figure 1.17**).
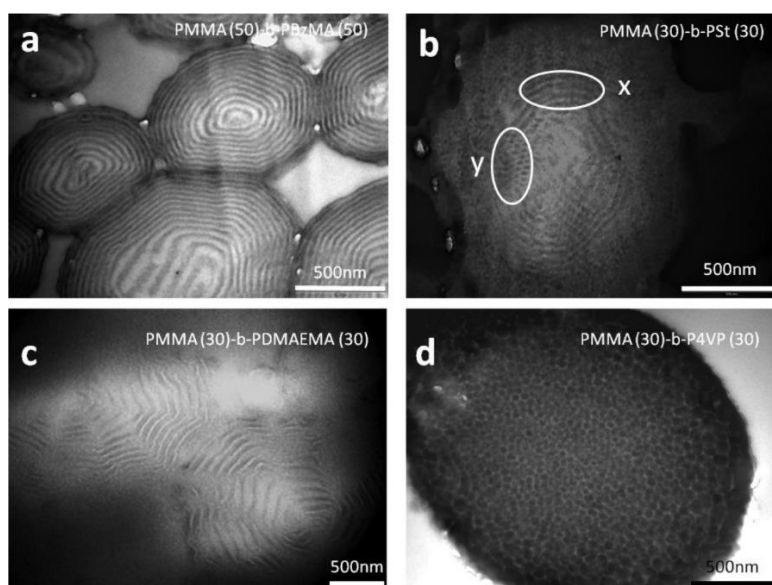
Figure 1.17: *TEM cross-sectional images of several PMMA block copolymers microparticles. Images show internal self-assembled morphologies including LAM (a, c), CYL (b) and SPH (d).*

From this study the Howdle group also concluded that the interaction of scCO$_2$ with the block copolymers profoundly affected the self-assembly behaviour of the resulting materials. Self-assembly was shown to occur *in situ* during the synthesis and gave unexpected morphologies based on the targeted block fractions.[127] The self-assembly behaviour of block copolymers in scCO$_2$ is described further in **Chapter 3**.

This synthetic procedure demonstrates a facile and environmentally benign route to block copolymers with diverse morphologies and a structural hierarchy. The group predicted these materials may find use in various applications including drug delivery, impact modification and as structural templates. In particular, their use as soft nanoscale templates for functional materials has received the most interest and will be the focus of this thesis.

1.7. Nanomaterials

Nanomaterials are defined as a material possessing any external dimensions on the nanoscale. General categories of nanomaterials include nanoparticles, nanowires, ultra-thin films and mesoporous or microporous materials. Such materials are desirable for their extremely high active surface areas and the unusual phenomena exhibited by certain materials at the nanoscale.[128] Nanomaterials occupy an enormous range of academic research and are now gradually being commercialised for use in retail products.[129] Some nanomaterials are even beginning to emerge as commodities in their own right through platforms such as the INSCX™ worldwide exchange marketplace.[130]

Despite the recent progress in nanomaterial utilisation, industrial-scale integration of these materials has been slow and continues to be an issue for some emerging technologies. Common issues that have arisen include supply insecurities, high integration costs and inconsistencies in material quality.[131, 132] Hence, most concerns originate in the bulk fabrication process of nanomaterials.

1.7.1. Fabrication of Nanomaterials

Generally, the fabrication of nanomaterials can be divided into two approaches, top-down and bottom-up methods.[133] Top-down methodologies involve taking a large bulk material and reducing the materials dimensions towards the nanoscale. The most popular of these methods is optical lithography, a physical method of fabrication employed in the microelectronic industry (**Figure 1.18**).[134]
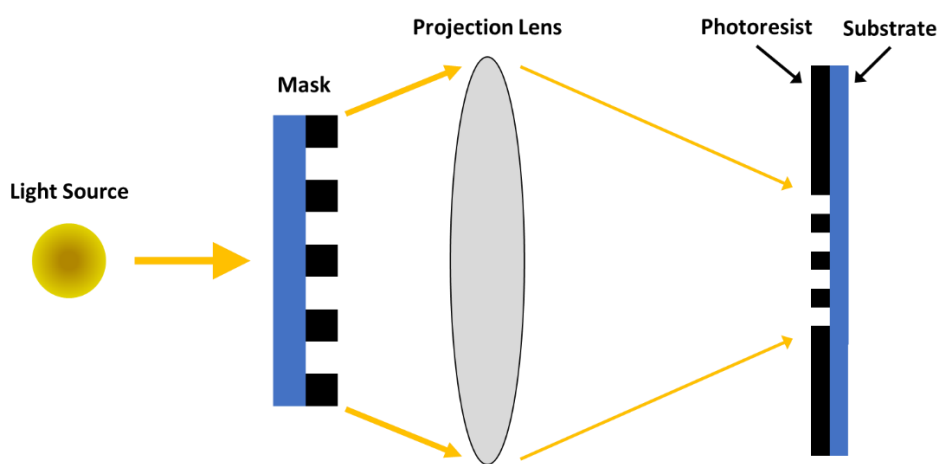
Figure 1.18: *Schematic illustration of the conventional optical lithography process.*

Optical lithography uses a light source, often UV, to transfer a desired pattern from a mask to a light sensitive material called a photoresist. The patterned photoresist is then subsequently transferred to a substrate, usually by etching. The minimum sized pattern of this technique is dependent of the light source used, with resolution limited by the optical wavelength. To produce nanoscale patterns, costly far-UV and X-ray sources must be used.[134, 135] Other physical top-down methods have been developed, including mask-less lithography techniques. These include electron beam and ion beam lithography. Both scan a tightly focussed particle beam across the sample in the desired pattern instead of using the usual projected photons. Though extremely small patterns can be printed in this way, the techniques suffer from high cost and low throughput.[136, 137]

Chemical top-down techniques can also be used to produce nanoscale features, including selective dealloying and anisotropic dissolution, to name a few. Selective dealloying can generate nanoporous metals by using chemicals to remove the most reactive components of a metallic alloy. Anisotropic dissolution can create nanostructures by selectively dissolving certain crystallographic facets in semi-crystalline materials. Though chemical top-down methods tend to be cheaper and more scalable, they can only be applied to a narrow range of materials.[138]

Bottom-up methods of nanofabrication take smaller building blocks, usually individual molecules, and builds them up into a nanostructure. Such processes mimic those used in nature to build biological structures, utilising physical forces to build-up a desired structure hierarchically.[139] The increased manufacturing costs of many top-down methods has driven more interest towards bottom-up approaches, although, they can often be difficult to design and control. Many of the man-made techniques use the concepts of self-assembly to drive the fabrication process.[133]

Examples of bottom-up fabrication techniques include chemical vapour deposition (CVD), DNA-assisted assembly and sol-gel synthesis. CVD deposits gaseous chemical components onto a desired surface in a vacuum chamber. In this way structures can be deposited and built up one monolayer at a time. This is particularly useful for creating nano-thin layers and nanofibers.[140, 141] DNA-assisted assembly utilises nature's own molecular design to self-assemble nanostructures. The basic DNA structure can be modified and programmed to self-

assemble into an array of nanoscale objects referred to as DNA origami. When attached to inorganic components, the DNA building blocks can be used to rapidly fabricate many 3D nanoscale objects.[142]

Sol-gel synthesis is a method of producing solid inorganic materials from molecular components, commonly used for the synthesis of metal oxides such as TiO_2 and SiO_2. A solution or colloidal suspension of inorganic precursor(sol) is created, before gelation occurs to form a continuous inorganic network in the liquid phase (gel). The solvent is then evaporated, and the resulting inorganic is often annealed to yield the final material. The process is particularly desirable for its mild reaction conditions, low cost and easy scalability..[143] By carefully controlling the physical conditions of gelation, or by incorporating additives to act as directing agents, the formation of the inorganic species can be confined to the nanoscale.[144, 145] Sol-gel syntheses have been used to fabricate different inorganic nanoparticles, nanocomposites and highly porous materials.[146]

1.7.2. Block Copolymers in Nanofabrication

Due to their ability to readily self-assemble into periodic nanostructures, block copolymers have been widely exploited in nanofabrication.[147] Examples are found primarily in bottom-up fabrication approaches, though they can also be used to aid top-down methods.

Block copolymers have gained much interest for their potential use in nano-lithography. While one approach is to reduce the wavelength of the optical light source in lithography, another less expensive method can be to reduce the size of the mask (**Figure 1.19**). Block copolymers can be deposited on a substrate and cast as a thin film before annealing to induce microphase separation into the polymer's preferred nanostructure. PS-*b*-PMMA block copolymers have generally been explored for this application as the PMMA block can be selectively removed after the pattern is formed, due to its quick degradation when exposed to UV light.[148] In this way, bottom-up self-assembly is used to aid in a top-down method of nanofabrication.
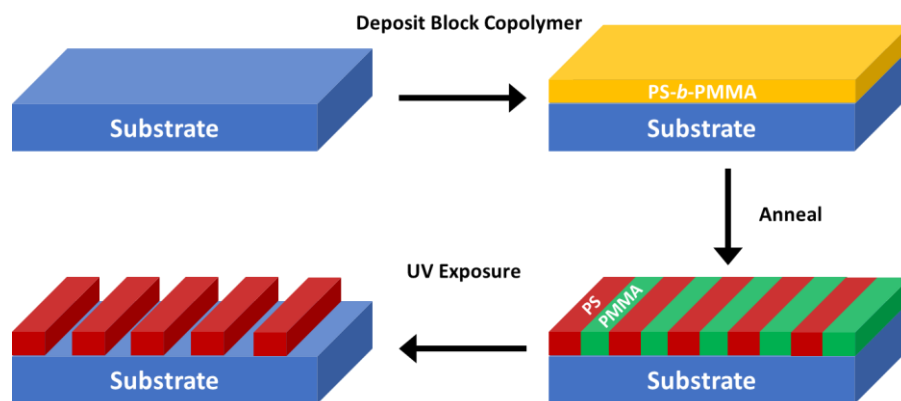
Figure 1.19: *Schematic of a nano-lithography procedure using a LAM block copolymer mask.*

In the literature, block copolymers are often used in bottom-up techniques. This is particularly true when more complex 3D nanoscale architectures are desired, which are inaccessible using normal lithography methods.[149] As stated earlier, block copolymer can readily self-assemble in the bulk phase to give various 3D morphologies. These morphologies must then be transferred to the desired functional material. This can be achieved by incorporating some chemical functionality into one of the polymers blocks to allow for insertion of a functional material post-assembly.[150, 151] However, some methods have attempted to include the desired functionality during self-assembly either by adding the inorganic material into the polymer mixture[152] or by incorporating the functionality directly into the polymer chains.[153] Though, these modifications often drastically alter the self-assembly behaviour of the block copolymer.

A polymer often employed to bind inorganic components into the polymer structure is poly(4-vinylpyridine) (P4VP). The coordinative ability of the pyridinyl nitrogen offers large scope for inorganic complexation and ultimately acts as a means to template a block copolymer's morphology to an inorganic material.[154] For 3D assemblies, this can be accomplished by incorporating the P4VP in a sol-gel synthesis of the inorganic material. In this way the gelation of the inorganic species is confined to the P4VP regions of the block copolymer. The pyridine rings are known to both chelate to inorganic precursors or can be protonated to act as hydrophilic acid catalyst sites for the gelation process.[155-159]

Recently, the Howdle group has utilised a PMMA-*b*-P4VP block copolymer from scCO$_2$ in the sol-gel nanofabrication of TiO$_2$ and LiFePO$_4$ (**Figure 1.20**).[159] The PMMA-*b*-P4VP microparticles with an internal spherical P4VP nanostructure were used to contain the inorganic precursors

of the sol, creating polymer-inorganic composite particles. The polymer template was then removed by calcination to afford the pure nanostructured metal oxides, either with or without a residual carbon layer depending on the calcination conditions. This report not only demonstrated a method of simple bulk scale bottom-up nanofabrication, but also combines the green chemistry aspects of scCO$_2$ for a minimal environmental impact. Nevertheless, only a single block copolymer morphology was demonstrated in this study.
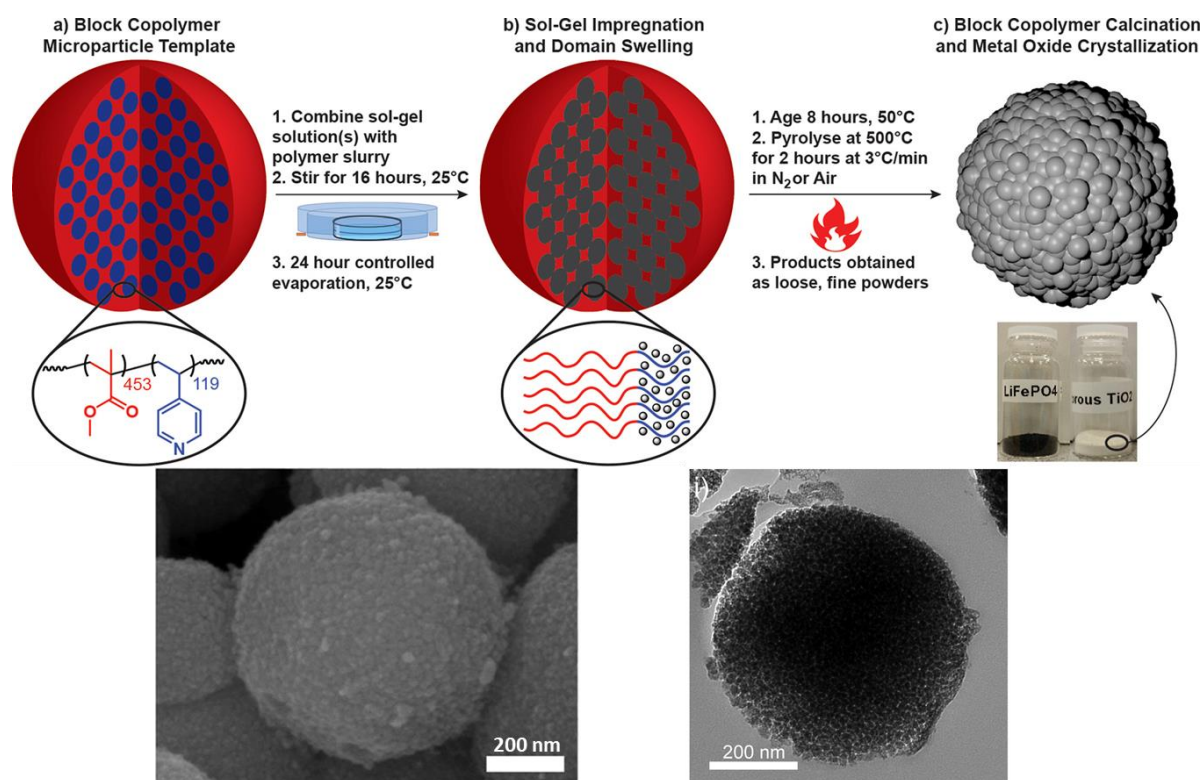
Figure 1.20: *Schematic process for transforming a spherically structured PMMA-b-P4VP block copolymer into nanostructured TiO$_2$/LiFePO$_4$, and the resulting microscopy images.*[159]

1.8. Summary and Research Aims

This chapter has outlined some of the fundamental concepts on which the work of this thesis is based. In particular, the phase behaviour of block copolymers, their green synthesis via RAFT-mediated dispersion in scCO$_2$ and their potential use in nanofabrication of inorganic functional materials.

Initial tests by the Howdle group have shown that PMMA-*b*-P4VP nanostructured microparticles could offer a route towards industrial-scale nanofabrication of a variety of inorganic materials, with minimal environmental impact.[159] However, the scope of this method has yet to be fully realised, both in terms of the range of nanostructures that may be templated and the specific benefits that the template may have to a variety of end applications.

Also, in the initial sol-gel nanofabrication tests, the greatest limitation was found to be the tight restriction on the copolymer's block composition. A composition of approximately 20-30 wt% P4VP was necessary in the copolymer to give high fidelity in the pattern transfer to the final inorganic product, though this was only investigated for a single polymer molecular weight (~67 kg mol^{-1}). Templating outside of this P4VP fraction range was found to produce microparticle aggregation in the final inorganics and loss of the structural hierarchy found in the original polymer. This general rule still lacks a full understanding of the fundamental interactions that influence templating success and has also only been proven for the TiO$_2$ sol-gel system. However, it can be expected that this rule should apply to other inorganic systems that interact with P4VP and polymer templates of similar molecular weight.

In **Chapter 3**, modifications to the synthesis of PMMA-*b*-P4VP in scCO$_2$ are explored in order to alter both the microscale and nanoscale dimension of the structural template. Control over both these length scales in the template can help facilitate size optimisation studies of certain inorganic materials. Specifically, this is explored in lithium-based inorganics for application in rechargeable batteries.

In **Chapter 4**, alternate block copolymer chemistries are researched to add more morphological diversity to the P4VP templates. The restriction of the 20-30 wt% P4VP content prevents other morphologies being achieved in diblock copolymer systems. Therefore, triblock copolymer systems of P4VP are studied to increase the wealth of available template

morphologies. The sol-gel synthesis of TiO_2 is used as a benchmark to test the effectiveness of the new triblock copolymer templates and their application in photocatalysis is explored.

Finally, **Chapter 5** aims to further progress the low environmental impact of this nanofabrication methodology. Instead of sol-gel reactions, synthesis of the inorganic component is attempted in $scCO_2$ alongside the block copolymer self-assembly, reducing the number of synthetic steps required. Silver nanoparticles are used as a basis for this study and the resulting silver-polymer composites are explored for their use in biomedical applications.

Overall, this thesis aims to demonstrate the versatility of P4VP block copolymer templates from $scCO_2$ in nanofabrication. This will be achieved by investigating synthetic strategies to control the size and shape of the templates, as well as utilising them for several end applications in the energy and healthcare sectors.

1.9. References

1.   H. Frey and T. Johann, *Polymer Chemistry*, 2020, **11**, 8-14.
2.   R. Geyer, J. R. Jambeck and K. L. Law, *Science Advances*, 2017, **3**, e1700782.
3.   S. Cichosz, A. Masek and M. Zaborski, *Polymer Testing*, 2018, **67**, 342-348.
4.   D. Banoriya, R. Purohit and R. K. Dwivedi, *Materials Today: Proceedings*, 2017, **4**, 3534-3541.
5.   J. Lopez, D. G. Mackanic, Y. Cui and Z. Bao, *Nature Reviews Materials*, 2019, **4**, 312-330.
6.   M. Peplow, *Nature*, 2016, **536**, 266-268.
7.   T. Erdmenger, C. Guerrero-Sanchez, J. Vitz, R. Hoogenboom and U. S. Schubert, *Chemical Society Reviews*, 2010, **39**, 3317-3333.
8.   D. M. O'Brien, R. L. Atkinson, R. Cavanagh, A. A. C. Pacheco, R. Larder, K. Kortsen, E. Krumins, A. J. Haddleton, C. Alexander, R. A. Stockman, S. M. Howdle and V. Taresco, *European Polymer Journal*, 2020, **125**, 109516.
9.   A. I. Cooper, *Journal of Materials Chemistry*, 2000, **10**, 207-234.
10.   H. N. Cheng, P. B. Smith and R. A. Gross, in *Green Polymer Chemistry: Biocatalysis and Materials II*, American Chemical Society, 2013, ch. 1, pp. 1-12.
11.   J. M. G. Cowie, in *Alternating Copolymers*, ed. J. M. G. Cowie, Springer, Boston, MA, 1985, ch. 1, pp. 1-18.
12.   N. Hadjichristidis, M. Pitsikalis, S. Pispas and H. Iatrou, *Chemical Reviews*, 2001, **101**, 3747-3792.
13.   K. Matyjaszewski, in *Macromolecular Engineering: Precise Synthesis, Materials Properties, Applications*, eds. K. Matyjaszewski, Y. Gnanou and L. Leibler, Wiley-VCH, Weinheim, 2007, ch. 2, pp. 731-1385.
14.   Y. Tezuka and H. Oike, *Progress in Polymer Science*, 2002, **27**, 1069-1122.
15.   G. Polymeropoulos, G. Zapsas, K. Ntetsikas, P. Bilalis, Y. Gnanou and N. Hadjichristidis, *Macromolecules*, 2017, **50**, 1253-1290.
16.   N. Hadjichristidis, S. Pispas and G. Floudas, in *Block Copolymers*, eds. N. Hadjichristidis, S. Pispas and G. Floudas, Wiley, New Jersey, 2002, ch. 21, pp. 383-408.
17.   A. S. Dunn and H. W. Melville, *Nature*, 1952, **169**, 699-700.
18.   C. M. Bates and F. S. Bates, *Macromolecules*, 2017, **50**, 3-22.
19.   J. Krstina, G. Moad, E. Rizzardo, C. L. Winzor, C. T. Berge and M. Fryd, *Macromolecules*, 1995, **28**, 5381-5385.
20.   F. S. Bates, *Science*, 1991, **251**, 898-905.
21.   L. Leibler, *Macromolecules*, 1980, **13**, 1602-1617.
22.   I. W. Hamley, in *Developments in Block Copolymer Science and Technology*, ed. I. W. Hamley, John Wiley & Sons, West Sussex, 2004, ch. 1, pp. 1-31.
23.   F. S. Bates and G. H. Fredrickson, *Annual Review of Physical Chemistry*, 1990, **41**, 525-557.
24.   K. J. Hanley, T. P. Lodge and C.-I. Huang, *Macromolecules*, 2000, **33**, 5918-5931.
25.   Z. Tuzar and P. Kratochvíl, *Advances in Colloid and Interface Science*, 1976, **6**, 201-232.
26.   M. Tambasco, J. E. G. Lipson and J. S. Higgins, *Macromolecules*, 2006, **39**, 4860-4868.
27.   Y. Mai and A. Eisenberg, *Chemical Society Reviews*, 2012, **41**, 5969-5985.
28.   I. W. Hamley, *Physics of Block Copolymers*, Oxford University Press, Oxford, 1998.
29.   M. W. Matsen and F. S. Bates, *Macromolecules*, 1996, **29**, 7641-7644.
30.   M. Li and C. K. Ober, *Materials Today*, 2006, **9**, 30-39.

31.   A. K. Khandpur, S. Foerster, F. S. Bates, I. W. Hamley, A. J. Ryan, W. Bras, K. Almdal and K. Mortensen, *Macromolecules*, 1995, **28**, 8796-8806.

32.   N. Hadjichristidis, S. Pispas and G. Floudas, *Block Copolymers: Synthetic Strategies, Physical Properties, and Applications*, John Wiley & Sons, New Jersey, USA, 2003.

33.   A.-C. Shi and B. Li, *Soft Matter*, 2013, **9**, 1398-1413.

34.   M. W. Matsen, *The Journal of Chemical Physics*, 2000, **113**, 5539-5544.

35.   P. Tang, F. Qiu, H. Zhang and Y. Yang, *The Journal of Physical Chemistry B*, 2004, **108**, 8434-8438.

36.   J. G. Drobny, *Handbook of Thermoplastic Elastomers*, Elsevier, Oxford, 2014.

37.   G. Holden, in *Rubber Technology*, ed. M. Morton, Springer, Dordrecht, Netherlands, 3rd edn., 1999, ch. 16, pp. 465-481.

38.   R. J. Spontak and N. P. Patel, *Current Opinion in Colloid & Interface Science*, 2000, **5**, 333-340.

39.   P. Alexandridis and T. Alan Hatton, *Colloids and Surfaces A: Physicochemical and Engineering Aspects*, 1995, **96**, 1-46.

40.   M. Almeida, M. Magalhães, F. Veiga and A. Figueiras, *Journal of Polymer Research*, 2017, **25**, 31.

41.   H. Cabral, K. Miyata, K. Osada and K. Kataoka, *Chemical Reviews*, 2018, **118**, 6844-6892.

42.   G. Kwon, S. Suwa, M. Yokoyama, T. Okano, Y. Sakurai and K. Kataoka, *Journal of Controlled Release*, 1994, **29**, 17-23.

43.   M. Yokoyama, A. Satoh, Y. Sakurai, T. Okano, Y. Matsumura, T. Kakizoe and K. Kataoka, *Journal of controlled release : official journal of the Controlled Release Society*, 1998, **55**, 219-229.

44.   M. Licciardi, Y. Tang, N. C. Billingham, S. P. Armes and A. L. Lewis, *Biomacromolecules*, 2005, **6**, 1085-1096.

45.   H. S. Yoo and T. G. Park, *Journal of controlled release : official journal of the Controlled Release Society*, 2001, **70**, 63-70.

46.   V. Torchilin, *European Journal of Pharmaceutics and Biopharmaceutics*, 2009, **71**, 431-444.

47.   C. Paquet and E. Kumacheva, *Materials Today*, 2008, **11**, 48-56.

48.   M. Stefik, S. Guldin, S. Vignolini, U. Wiesner and U. Steiner, *Chemical Society Reviews*, 2015, **44**, 5076-5091.

49.   A. L. Liberman-Martin, C. K. Chu and R. H. Grubbs, *Macromolecular Rapid Communications*, 2017, **38**, 1700058.

50.   Y. Kang, J. J. Walish, T. Gorishnyy and E. L. Thomas, *Nature materials*, 2007, **6**, 957-960.

51.   I. Vukovic, G. t. Brinke and K. Loos, *Polymer*, 2013, **54**, 2591-2605.

52.   F. H. Schacher, P. A. Rupar and I. Manners, *Angewandte Chemie International Edition*, 2012, **51**, 7898-7921.

53.   G. Odian, *Principles of Polymerisation*, Wiley-Interscience, New York, NY, 4th edn., 2004.

54.   W.-F. Su, in *Principles of Polymer Design and Synthesis*, ed. W.-F. Su, Springer, Berlin, 2013, ch. 6, pp. 111-135.

55.   D. Walton and P. Lorimer, *Polymers*, Oxford University Press, Oxford, 2001.

56.   K. Matyjaszewski and T. P. Davis, *Handbook of Radical Polymerisations*, Wiley-VCH, New Jersey, USA, 2002.

57. G. Moad and D. H. Solomon, *The Chemistry of Radical Polymerisations*, Elsevier, Oxford, 2006.
58. N. V. Tsarevsky and B. S. Sumerlin, *Fundamentals of Controlled/living Radical Polymerisation*, Royal Society of Chemistry, Dorchester, 2013.
59. H. Fischer, *Chemical Reviews*, 2001, **101**, 3581-3610.
60. K. Matyjaszewski and J. Spanswick, *Materials Today*, 2005, **8**, 26-33.
61. C. J. Hawker, A. W. Bosman and E. Harth, *Chemical Reviews*, 2001, **101**, 3661-3688.
62. J.-S. Wang and K. Matyjaszewski, *Macromolecules*, 1995, **28**, 7901-7910.
63. J. Chiefari, Y. K. Chong, F. Ercole, J. Krstina, J. Jeffery, T. P. T. Le, R. T. A. Mayadunne, G. F. Meijs, C. L. Moad, G. Moad, E. Rizzardo and S. H. Thang, *Macromolecules*, 1998, **31**, 5559-5562.
64. S. Perrier, *Macromolecules*, 2017, **50**, 7433-7447.
65. G. Moad, E. Rizzardo and S. H. Thang, *Aust. J. Chem.*, 2009, **62**, 1402-1472.
66. Y. K. Chong, T. P. T. Le, G. Moad, E. Rizzardo and S. H. Thang, *Macromolecules*, 1999, **32**, 2071-2074.
67. D. J. Keddie, G. Moad, E. Rizzardo and S. H. Thang, *Macromolecules*, 2012, **45**, 5321-5342.
68. J. Bolton and J. Rzayev, *ACS Macro Letters*, 2012, **1**, 15-18.
69. K. Matyjaszewski and S. G. Gaynor, in *Applied Polymer Science: 21st Century*, eds. C. D. Craver and C. E. Carraher, Elsevier, Oxford, 2000, pp. 929-977.
70. J. T. Lai, D. Filla and R. Shea, *Macromolecules*, 2002, **35**, 6754-6756.
71. M. F. Cunningham and R. Hutchinson, in *Handbook of Radical Polymerization*, eds. K. Matyjaszewski and T. P. Davis, Wiley, 2002, ch. 7, pp. 333-360.
72. C. E. Carraher, *Polymer Chemistry*, Marcel Dekker Inc., New York, USA, 2003.
73. E. Vivaldo-Lima, P. E. Wood, A. E. Hamielec and A. Penlidis, *Industrial & Engineering Chemistry Research*, 1997, **36**, 939-965.
74. C. Barner-Kowollik, *Handbook of RAFT polymerisation*, Wiley-VCH, Weinheim, Germany, 2008.
75. W. D. Harkins, *Journal of the American Chemical Society*, 1947, **69**, 1428-1444.
76. C. S. Chern, *Progress in Polymer Science*, 2006, **31**, 443-486.
77. M. Okubo, A. Yamada and T. Matsumoto, *Journal of Polymer Science: Polymer Chemistry Edition*, 1980, **18**, 3219-3228.
78. J. Ugelstad, M. S. El-Aasser and J. W. Vanderhoff, *Journal of Polymer Science: Polymer Letters Edition*, 1973, **11**, 503-513.
79. F. Yan and J. Texter, *Soft Matter*, 2006, **2**, 109-118.
80. A. P. Richez, H. N. Yow, S. Biggs and O. J. Cayre, *Progress in Polymer Science*, 2013, **38**, 897-931.
81. J. M. Asua, *Polymeric Dispersions: Principles and Applications*, Springer Netherlands, 2012.
82. Y. Li and S. P. Armes, *Angewandte Chemie International Edition*, 2010, **49**, 4042-4046.
83. K. E. J. Barrett, *Dispersion Polymerisation in organic Media*, wiley, New York, 1975.
84. S. Shen, E. D. Sudol and M. S. El-Aasser, *Journal of Polymer Science Part A: Polymer Chemistry*, 1993, **31**, 1393-1402.
85. J. M. DeSimone, E. E. Maury, Y. Z. Menceloglu, J. B. McClain, T. J. Romack and J. R. Combes, *Science*, 1994, **265**, 356-359.
86. P. B. Zetterlund, S. C. Thickett, S. Perrier, E. Bourgeat-Lami and M. Lansalot, *Chemical Reviews*, 2015, **115**, 9745-9800.

87. J. K. Oh, *Journal of Polymer Science Part A: Polymer Chemistry*, 2008, **46**, 6983-7001.

88. A. Butté, G. Storti and M. Morbidelli, *Macromolecules*, 2001, **34**, 5885-5896.

89. P. J. Saikia, J. M. Lee, B. H. Lee and S. Choe, *Macromolecular Symposia*, 2007, **248**, 249-258.

90. H. de Brouwer, J. G. Tsavalas and F. J. Schork, *Macromolecules*, 2000, **33**, 9239-9246.

91. S. W. Prescott, M. J. Ballard, E. Rizzardo and R. G. Gilbert, *Macromolecules*, 2002, **35**, 5417-5425.

92. C. J. Ferguson, R. J. Hughes, B. T. T. Pham, B. S. Hawkett, R. G. Gilbert, A. K. Serelis and C. H. Such, *Macromolecules*, 2002, **35**, 9243-9245.

93. J. B. McLeary and B. Klumperman, *Soft Matter*, 2006, **2**, 45-53.

94. P. Gurnani and S. Perrier, *Progress in Polymer Science*, 2020, **102**, 101209.

95. N. J. Warren and S. P. Armes, *Journal of the American Chemical Society*, 2014, **136**, 10174-10185.

96. F. D'Agosto, J. Rieger and M. Lansalot, *Angewandte Chemie International Edition*, 2020, **59**, 8368-8392.

97. N. J. W. Penfold, J. Yeow, C. Boyer and S. P. Armes, *ACS Macro Letters*, 2019, **8**, 1029-1054.

98. A. M. Gregory, K. J. Thurecht and S. M. Howdle, *Macromolecules*, 2008, **41**, 1215-1222.

99. J. A. Darr and M. Poliakoff, *Chemical Reviews*, 1999, **99**, 495-542.

100. E. J. Beckman, *The Journal of Supercritical Fluids*, 2004, **28**, 121-191.

101. F. Rindfleisch, T. P. DiNoia and M. A. McHugh, *The Journal of Physical Chemistry*, 1996, **100**, 15581-15587.

102. J. L. Kendall, D. A. Canelas, J. L. Young and J. M. DeSimone, *Chemical Reviews*, 1999, **99**, 543-564.

103. Z. Guan, J. R. Combes, Y. Z. Menceloglu and J. M. DeSimone, *Macromolecules*, 1993, **26**, 2663-2669.

104. M. R. Giles, R. M. T. Griffiths, D. J. Irvine and S. M. Howdle, *European Polymer Journal*, 2003, **39**, 1785-1790.

105. D. A. Canelas, D. E. Betts and J. M. DeSimone, *Macromolecules*, 1996, **29**, 2818-2821.

106. A. I. Cooper, W. P. Hems and A. B. Holmes, *Macromolecules*, 1999, **32**, 2156-2166.

107. A. Galia, A. Muratore and G. Filardo, *Industrial & Engineering Chemistry Research*, 2003, **42**, 448-455.

108. N. A. Birkin, N. J. Arrowsmith, E. J. Park, A. P. Richez and S. M. Howdle, *Polymer Chemistry*, 2011, **2**, 1293-1299.

109. R. G. Wissinger and M. E. Paulaitis, *Journal of Polymer Science Part B: Polymer Physics*, 1987, **25**, 2497-2510.

110. Y.-T. Shieh, J.-H. Su, G. Manivannan, P. H. C. Lee, S. P. Sawan and W. Dale Spall, *Journal of Applied Polymer Science*, 1996, **59**, 695-705.

111. E. Reverchon and S. Cardea, *The Journal of Supercritical Fluids*, 2007, **40**, 144-152.

112. O. R. Davies, A. L. Lewis, M. J. Whitaker, H. Tai, K. M. Shakesheff and S. M. Howdle, *Advanced Drug Delivery Reviews*, 2008, **60**, 373-387.

113. B. Wong, S. Yoda and S. M. Howdle, *The Journal of Supercritical Fluids*, 2007, **42**, 282-287.

114. S. G. Kazarian, M. F. Vincent, F. V. Bright, C. L. Liotta and C. A. Eckert, *Journal of the American Chemical Society*, 1996, **118**, 1729-1736.

115. J. Xia, T. Johnson, S. G. Gaynor, K. Matyjaszewski and J. DeSimone, *Macromolecules*, 1999, **32**, 4802-4805.

116. R. McHale, F. Aldabbagh, P. B. Zetterlund, H. Minami and M. Okubo, *Macromolecules*, 2006, **39**, 6853-6860.

117. P. B. Zetterlund, F. Aldabbagh and M. Okubo, *Journal of Polymer Science Part A: Polymer Chemistry*, 2009, **47**, 3711-3728.

118. B. Grignard, C. Jérôme, C. Calberg, R. Jérôme, W. Wang, S. M. Howdle and C. Detrembleur, *Macromolecules*, 2008, **41**, 8575-8583.

119. J. Ryan, F. Aldabbagh, P. B. Zetterlund and M. Okubo, *Polymer*, 2005, **46**, 9769-9777.

120. M. Zong, K. J. Thurecht and S. M. Howdle, *Chem. Commun.*, 2008, DOI: 10.1039/B812827H, 5942-5944.

121. K. J. Thurecht, A. M. Gregory, W. Wang and S. M. Howdle, *Macromolecules*, 2007, **40**, 2965-2967.

122. J. Jennings, M. Beija, J. T. Kennon, H. Willcock, R. K. O'Reilly, S. Rimmer and S. M. Howdle, *Macromolecules*, 2013, **46**, 6843-6851.

123. A. Alves Costa Pacheco, A. Fernandes Da Silva Filho, K. Kortsen, M. Hanson-Heine, V. Taresco, J. Hirst, M. Lansalot, F. D'Agosto and S. M. Howdle, *Chemical Science*, 2021, DOI: 10.1039/D0SC05281G.

124. H. Minami, A. Tanaka, Y. Kagawa and M. Okubo, *Journal of Polymer Science Part A: Polymer Chemistry*, 2012, **50**, 2578-2584.

125. P. O'Connor, R. Yang, W. M. Carroll, Y. Rochev and F. Aldabbagh, *European Polymer Journal*, 2012, **48**, 1279-1288.

126. J. Jennings, M. Beija, A. P. Richez, S. D. Cooper, P. E. Mignot, K. J. Thurecht, K. S. Jack and S. M. Howdle, *Journal of the American Chemical Society*, 2012, **134**, 4772-4781.

127. J. Jennings, S. P. Bassett, D. Hermida-Merino, G. Portale, W. Bras, L. Knight, J. J. Titman, T. Higuchi, H. Jinnai and S. M. Howdle, *Polymer Chemistry*, 2016, **7**, 905-916.

128. G. Cao and Y. Wang, *Nanostructures and Nanomaterials: Synthesis, Properties, and Applications*, World Scientific, 2011.

129. J. J. Ramsden, *Nanotechnology Perceptions*, 2013, **3**, 102-118.

130. C. McGovern, *Nanotechnology Perceptions*, 2010, **6**, 155-178.

131. K. Cooper, *Micromachines*, 2017, **8**, 20.

132. S. Lubik and E. Garnsey, *Nanotechnology Perceptions*, 2008, **4**, 225-238.

133. A. Biswas, I. S. Bayer, A. S. Biris, T. Wang, E. Dervishi and F. Faupel, *Advances in Colloid and Interface Science*, 2012, **170**, 2-27.

134. T. Ito and S. Okazaki, *Nature*, 2000, **406**, 1027-1031.

135. R. Petr, A. Bykanov, J. Freshman, D. Reilly, J. Mangano, M. Roche, J. Dickenson, M. Burte and J. Heaton, *Rev. Sci. Instrum.*, 2004, **75**, 2551-2559.

136. Y. Chen, *Microelectron. Eng.*, 2015, **135**, 57-72.

137. J. E. E. Baglin, *Appl. Surf. Sci.*, 2012, **258**, 4103-4111.

138. H.-D. Yu, M. D. Regulacio, E. Ye and M.-Y. Han, *Chemical Society Reviews*, 2013, **42**, 6006-6018.

139. V. K. Khanna, in *Integrated Nanoelectronics*, Springer India, New Delhi, 2016, pp. 397-417.

140. Y. Zhang, L. Zhang and C. Zhou, *Acc. Chem. Res.*, 2013, **46**, 2329-2339.

141. Z. Cai, B. Liu, X. Zou and H.-M. Cheng, *Chemical Reviews*, 2018, **118**, 6091-6133.

142. Z. Peng and H. Liu, *Chemistry of Materials*, 2016, **28**, 1012-1021.

143. C. J. Brinker and G. W. Scherer, *Sol-Gel Science: The Physics and Chemistry of Sol-Gel Processing*, Elsevier Science, San Diego, CA, 2013.

144. J. D. Mackenzie and E. P. Bescher, *Acc. Chem. Res.*, 2007, **40**, 810-818.

145. B. B. Lakshmi, P. K. Dorhout and C. R. Martin, *Chemistry of Materials*, 1997, **9**, 857-862.
146. A. E. Danks, S. R. Hall and Z. Schnepp, *Materials Horizons*, 2016, **3**, 91-112.
147. C. Cummins, R. Lundy, J. J. Walsh, V. Ponsinet, G. Fleury and M. A. Morris, *Nano Today*, 2020, **35**, 100936.
148. J. Bang, U. Jeong, D. Y. Ryu, T. P. Russell and C. J. Hawker, *Advanced Materials*, 2009, **21**, 4769-4792.
149. C. A. Ross, K. K. Berggren, J. Y. Cheng, Y. S. Jung and J.-B. Chang, *Advanced Materials*, 2014, **26**, 4386-4396.
150. J. Kao, K. Thorkelsson, P. Bai, B. J. Rancatore and T. Xu, *Chemical Society Reviews*, 2013, **42**, 2654-2678.
151. M. C. Orilall and U. Wiesner, *Chemical Society Reviews*, 2011, **40**, 520-535.
152. B. C. Garcia, M. Kamperman, R. Ulrich, A. Jain, S. M. Gruner and U. Wiesner, *Chemistry of Materials*, 2009, **21**, 5397-5405.
153. P. R. L. Malenfant, J. Wan, S. T. Taylor and M. Manoharan, *Nature Nanotechnology*, 2007, **2**, 43-46.
154. J. G. Kennemur, *Macromolecules*, 2019, **52**, 1354-1370.
155. A. Khanal, Y. Inoue, M. Yada and K. Nakashima, *Journal of the American Chemical Society*, 2007, **129**, 1534-1535.
156. J. Chai and J. M. Buriak, *ACS Nano*, 2008, **2**, 489-501.
157. Y. H. Jang, M. A. Cha and D. H. Kim, *Polym.-Korea*, 2008, **32**, 465-469.
158. D. Chen, S. Park, J.-T. Chen, E. Redston and T. P. Russell, *ACS Nano*, 2009, **3**, 2827-2833.
159. T. M. Bennett, G. He, R. R. Larder, M. G. Fischer, G. A. Rance, M. W. Fay, A. K. Pearce, C. D. J. Parmenter, U. Steiner and S. M. Howdle, *Nano Letters*, 2018, **18**, 7560-7569.

Chapter 2 – Equipment and Characterisation Techniques

2.1. Overview

This chapter details the key experimental apparatus and characterisation techniques employed throughout this thesis. The first section describes the high-pressure equipment set-up used for the polymer synthesis in $scCO_2$. This also includes a general standard operating procedure for undertaking a high-pressure reaction. The second section describes the main analytical techniques utilised in subsequent thesis chapters to evaluate the various materials synthesised throughout this thesis.

2.2. High-Pressure Equipment

2.2.1. General Set-Up

Polymer synthesis in $scCO_2$ requires specialist equipment to generate and withstand the high-pressures required. The general set-up for all the high-pressure experiments in this thesis consists of a CO_2 source, connecting pipework, control electronics and a reaction vessel (discussed later in this chapter). This set-up is summarised in a simplified piping and instrumentation diagram(P&ID) (**Figure 2.1**).

Pressure was generated using a PM-101 high-pressure pump (New Ways of Analytics, Germany) attached directly to a liquid CO_2 cylinder with a dip tube. The CO_2 pump was powered by an external air compressor providing roughly 3-5 bar of pressure. This compressed the CO_2 in the pump to the pressure required for the reactions; a significantly higher pressure than supplied by the original CO_2 cylinder.

The CO_2 pressurised by the pump was supplied to individual fume hoods through $1/16^{th}$ inch stainless steel pipework (Swagelok, SS316). The flow of CO_2 was controlled using a series of HIP (High-Pressure Equipment Co.) needle valves. The supply lines were also fitted with non-return valves (NRV) to prevent the back flow of reagents from the reaction vessels to the CO_2 cylinder.

The pressure supplied to the reaction vessel was monitored by a quartz piezoelectric transducer (RDP Electronics) placed on the inlet pipe. Placement of the transducer on the inlet pipe rather than inside the reaction vessel avoids contact with reagents and prevents the build-up of obstructing polymer coatings on the sensor. The transducer was connected to an in-house built digital display, indicating the measured pressure in pounds per square inch (psi).

The temperature of the reaction vessel was both monitored and controlled by an in-house built temperature control box connected to a band heater (Watlow) and thermocouple (K type, RS Components). The power for this temperature control box was supplied through a trip-fuse device, coupled to the pressure monitor. If the pressure recorded by the monitor exceeded the 300 bar (4350 psi) working limit of the reactor, power is disconnected from the temperature control box to help relieve the excess pressure.
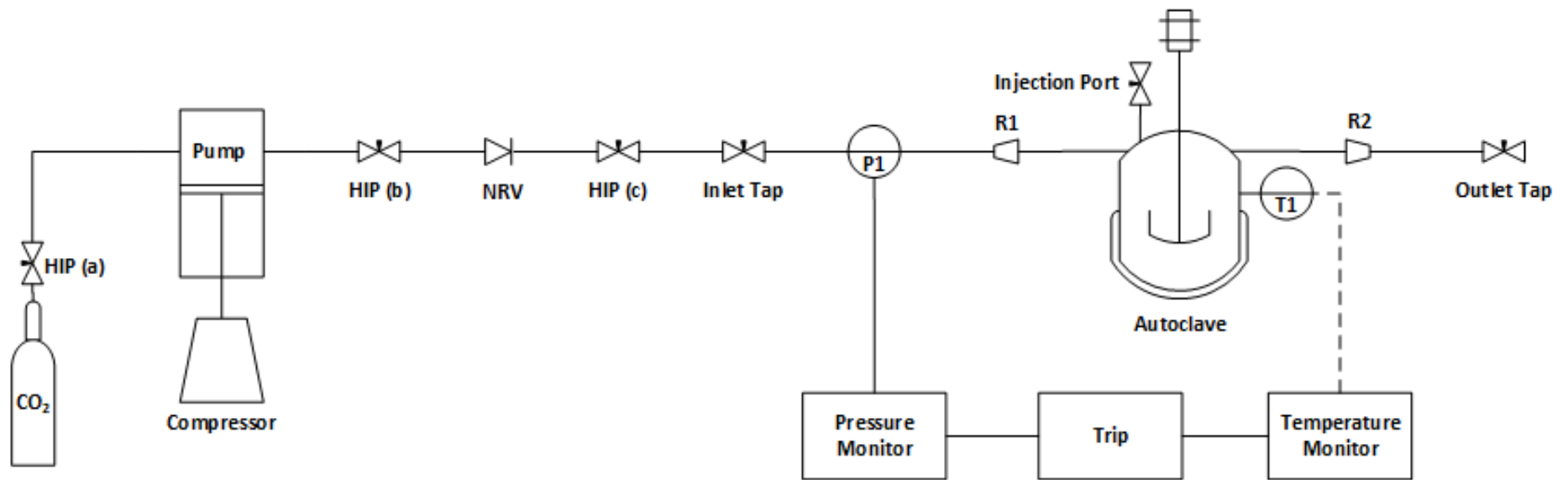
Figure 2.1: *Schematic diagram of the high-pressure equipment used in this thesis.*

2.2.2. MKIII Autoclave

The high-pressure reaction vessel for this set-up was an in-house built MKIII clamp sealed autoclave (**Figure 2.2**). The autoclave was a 60 mL vessel made from 316 stainless steel with maximum working conditions of 300 bar and 300 °C. The autoclave was comprised of a head unit and removable base, sealed together with an ethylene propylene diene monomer (EPDM) O-ring seal and clamp. The use of the EPDM type O-ring in this set-up restricts the safe working temperatures to between -50 and 120 °C.

The autoclave head was equipped with a magnetically coupled stirrer shaft (**Figure 2.2, A**) for use with a mechanical overhead stirrer, as well as six apertures. Two of the apertures were used to fit inlet and outlet Swagelok piping (**Figure 2.2, F/G**), connected to the CO_2 supply line and HIP vent tap respectively. Another aperture was also modified to include a second inlet pipe, sealed with a HIP tap (**Figure 2.2, B**), for the addition of liquid reagents while the system was under pressure (discussed later in this chapter). The remaining three apertures were used to attach a thermocouple (**Figure 2.2, D**) to monitor the internal system temperature, as well as two mechanical safety features.

The first mechanical safety feature included on the autoclave is a spring-loaded relief valve (Swagelok SS4R3A) (**Figure 2.2, C**) designed to open when above a maximum allowed pressure of 345 bar, then re-seal again once below this level. The emergency vent pressure was set above the pressure limit of the electronic trip-fuse as a 'final' safety measure, as this method of pressure relief would also result in ejection of the toxic reagents. The final safety feature was a small opening on the autoclave head that must be sealed using a safety needle (**Figure 2.2, E**) to hold pressure. The head of this safety needle also serves as a uniquely shaped key to unscrew the clamp seal (**Figure 2.2, J**) between the autoclave head and base. Hence the clamp seal for the autoclave cannot be undone without first safely venting the excess pressure through the small needle opening on the autoclave head.
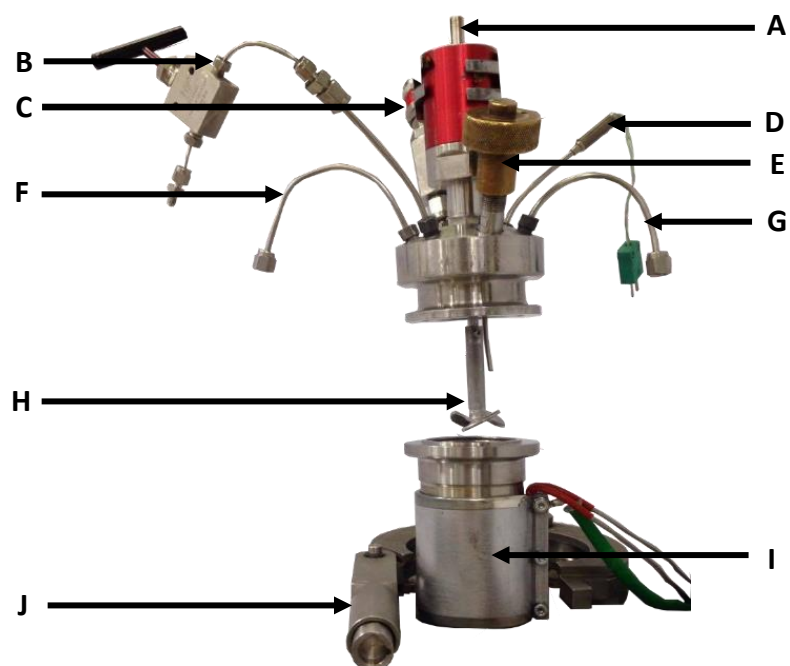
Figure 2.2: *Image of the high-pressure MKIII autoclave showing: (A) Magnetic coupled stirrer, (B) Reagent addition port, (C) Spring-loaded pressure relief valve, (D) Thermocouple, (E) Clamp key/Safety needle, (F, G) Inlet/outlet pipes, (H) Stirrer blades, (I) Heating jacket, (J) Clamp seal.*

2.2.3. In-Situ Monomer Addition

Many of the syntheses described throughout this thesis require the addition of subsequent reagents once a particular time point in the reaction is reached. Notably the addition of the second monomer in the synthesis of block copolymers. This was achieved by using a high-performance liquid chromatography (HPLC) pump (Jasco PU-980) to supply liquid reagents to the autoclave through the reagent addition port. The set-up for the HPLC pump and connecting pipework is summarised in the P&ID diagram below (**Figure 2.3**).
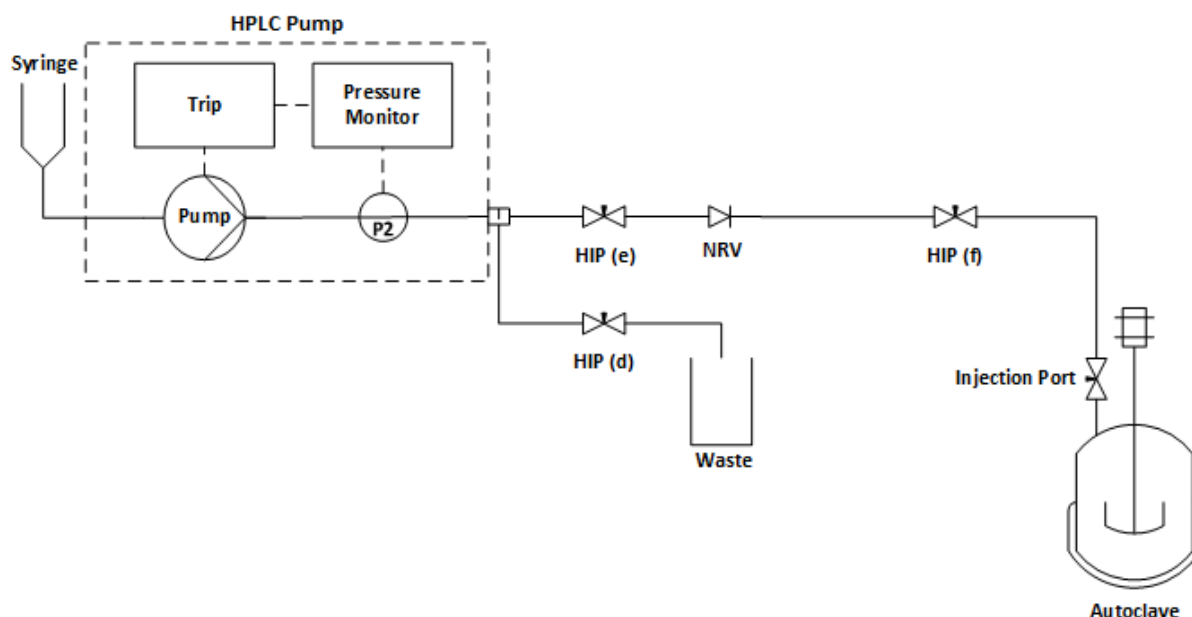
Figure 2.3: *Schematic diagram of the equipment used for in-situ addition of monomer into the autoclave.*

The HPLC pump incorporates the pump component, an internal pressure monitoring device and an electronic trip set to cut power to the pump if an excessively high pressure is reached. Liquid reagents are fed into the pump via a syringe and then pumped through 1/16th inch stainless steel pipework (Swagelok, SS316). Reagents can be pumped directly into a waste container by opening a purge valve, intended for solvent rinses and the removal of any air bubbles from the line. When the purge valve is closed, a separate HIP valve can be opened to pump the reagents through further pipework connected to the reagent addition port of the autoclave. This section of pipework is also fitted with a NRV to prevent the contents of the autoclave reaching the HLPC pump.

2.2.4. Standard Operating Procedure

To ensure safe operation when using the high-pressure equipment, a standard operating procedure was followed carefully for all reactions. Only minor adjustments were made to the method depending on the type of reaction being performed. The procedure for a standard block copolymer synthesis is as follows:

(1)   An EPDM O-ring was placed in the recess in the autoclave base, then the base and head units were clamped together and tightened using the safety key. The safety key was then screwed into the autoclave head to create a pressure seal. The band heater

was then securely fastened around the autoclave base but remained unplugged from the control box.

(2) The outlet HIP tap was closed, then the inlet HIP tap was opened slowly to add CO_2 to the autoclave. The inlet was closed when a pressure of approximately 50 bar was recorded on the pressure monitor. The system was then checked for leaks using Snoop® liquid leak detector.

(3) If required, the system was vented by opening the outlet tap and any leaking fittings were adjusted, before again repeating step 2. Leaking fittings were never tightened under pressure.

(4) Once the system was determined to be leak free, the autoclave was vented, the safety key removed and the outlet tap was then closed. Residual oxygen in the system was removed by slightly opening the inlet tap to produce a CO_2 flow of around 2-3 bar through the autoclave for at least 30 minutes.

(5) A degassed monomer solution (usually containing initiator, RAFT agent and polymeric stabiliser) was added via syringe through the open keyhole against the positive pressure of CO_2, preventing the ingress of air. The system was then sealed by screwing in the safety key.

(6) The autoclave containing the reaction solution was then pressurised to around 50 bar. The overhead stirrer was then turned on and set to 300 rpm. The heating jacket was then plugged into the control box and the target temperature was set to 65 °C. The system was allowed to heat, with the pressure monitored throughout.

(7) Once the target temperature was achieved, the system was further pressurised to the reaction pressure of 241 bar. The addition of CO_2 often caused the autoclave to cool slightly. When this occurred, pressurisation was stopped until the temperature stabilised again, then the process was continued.

(8) After the desired reaction time for the first polymer block was reached, a small polymer sample was collected from the system by quickly opening then closing the outlet tap. This procedure also lowered the autoclave pressure, providing space for the second monomer to be added.

(9) The second monomer was then added to the system using the HPLC pump set-up:

   i. The pump's syringe reservoir was primed with the degassed second monomer solution.

ii.   The purge valve was opened and the solution was pumped through to the waste container to remove any air bubbles from the line.

iii.   The purge valve was closed and 1/16th inch piping of the pump set-up was connected to the autoclave addition port.

iv.   The tap on the pump line was opened, keeping the isolating tap on the reagent addition port closed. The monomer solution was pumped through the line to build up pressure, to the point at which pressure was equal to that inside the autoclave.

v.   The isolating tap on the reagent addition port was opened and the monomer was pumped into the autoclave at a flow rate of 0.5 mL/min. The pressure inside the autoclave began to rise and pumping was discontinued if the safety limit was reached.

vi.   After the desired amount of monomer solution was added, the isolating tap was closed and pumping was stopped. The pump line was disconnected from the autoclave and the entire system was flushed with acetone to remove residual monomer.

(10)   After the desired reaction time for the second monomer block was reached, the temperature control box was set to 0 °C and the heating jacket was disconnected.

(11)   Once the autoclave was cooled to room temperature, stirring was stopped and the outlet tap was slowly opened to vent the CO_2.

(12)   Once at atmospheric pressure, the safety key was removed and the clamp seal loosened to open the autoclave and collect the reaction product.

2.3. Characterisation Techniques

Described here are the details and procedures of some of the key analytical techniques employed throughout this thesis. However, this list of techniques is not exhaustive and additional specialist techniques are also detailed in the experimental section of the chapters to which they pertain.

2.3.1. Gel Permeation Chromatography

A fundamental technique for the analysis of polymers is gel permeation chromatography (GPC), also referred to as size exclusion chromatography (SEC). This technique is used to determine the molecular weight (M_n) and molecular weight dispersity ($Đ$) of polymer samples. Both parameters are of interest due to their ability to influence the end properties of the polymer. This is especially relevant in controlled radical polymerisations where molecular weight values can be targeted and controlled.

The technique works by first dissolving the sample in a suitable solvent to be used as the mobile phase. The sample is then passed through a series of columns containing a bed of porous beads, the stationary phase. The beads then separate the polymer chains based on their hydrodynamic volume in the selected solvent; longer polymer chains will have a larger hydrodynamic radius. The longer chains elute first as they are too large to pass through the bead pores, thus taking a shorter more direct route to the end of the column. Shorter chains pass through more of the pores, taking a longer time to filter through and elute.

Eluting polymer chains can be detected through various different means. The most common and the one used in this thesis is detection through changes in the refractive index (RI) of the eluted solvent. A higher concentration of polymer in the solvent will cause a greater change in the RI value, enabling a signal to be produced and plotted. The detected elution times can then be compared to calibration values produced by reference samples. These are near-monodisperse samples of common polymers such as PMMA and PS. The comparison to these reference elution times is used to calculate both the number average and weight average molecular weights for the sample. Values from samples with different chemical structures to these standards can only be taken as approximations, and the error in these approximations is propagated through both the number and weight average values.

In this thesis two GPC systems were used. The most commonly used system, and the one for analysing all P4VP-based polymers, was an Agilent 1260 infinity SEC system equipped with a Wyatt Optilab dRI detector. The mobile phase was a solvent mixture of chloroform and ethanol (9:1) with a triethyl amine (TEA) stabiliser (1% v/v). Samples were prepared as 3-5 mg mL^{-1} solutions and filtered through 0.2 μm PTFE syringe filters (Agilent) to remove any particulates. Samples were injected at a flow rate of 0.5 mL min^{-1} and passed through a guard column followed by two separation columns (2 x Agilent PLgel 5 μm mixed D). The system was calibrated using PMMA narrow standards (M_n range: 0.5-2,000 kg mol^{-1}). Detector responses were analysed using ASTRA 6.1 software (Wyatt Technology).

Additionally, a separate Polymer Labs PL-120 SEC system equipped with an Agilent differential refractometer was used to analyse PMMA-*b*-PBzMA and PMMA-*b*-PS block copolymers. THF was used as the mobile phase. Samples were prepared as 2-3 mg mL^{-1} solutions and filtered through 0.2 μm PTFE syringe filters (Agilent) to remove any particulates. Samples were injected at a flow rate of 1.0 mL min^{-1} and passed through a guard column followed by two separation columns (2 x Agilent PLgel 5 μm mixed D). The system was calibrated using PMMA narrow standards (M_n range: 0.5-2,000 kg mol^{-1}). Detector responses were analysed using ASTRA 6.1 software (Wyatt Technology).

2.3.2. Nuclear Magnetic Resonance Spectroscopy

Nuclear magnetic resonance (NMR) spectroscopy is a common analytical technique used to confirm the chemical structure of a compound. The technique identifies any nuclei with a nuclear spin that can interact with an applied magnetic field. The different chemical environments of these nuclei give slightly different responses in the NMR, which are plotted as chemical shift values (δ) relative to a standard. The δ values can be related to the electron density surrounding the particular nuclei, thus, functional groups can be identified and the chemical structure deduced. Intensities of the generated peaks are also relative to the number of active nuclei in the sample. This means integration values of the peaks can be compared to assess the abundance of each particular functional group.

In this thesis proton (^{1}H) NMR is utilised, being the most applicable NMR active nuclei in the synthesised polymers. ^{1}H NMR was used to determine the presence and abundance of particular polymer species in a product based on its unique functional groups. Spectra were

obtained on a Bruker AV-III 400 MHz spectrometer on samples dissolved in $CDCl_3$. Data was analysed using MestReNova software. Some of the unique discernible signals for the polymers studied in this thesis are given in **Table 2.1**.

Table 2.1: *List of ^1H NMR unique chemical shift regions for polymers used in this thesis.*

Polymer	Functional group	Number of protons (nH)	Chemical shift in $CDCl_3$ (ppm)
PMMA	Methyl group	3	3.6
P4VP	Pyridine ring	2	8.2-8.6
PS	Benzene ring	3	6.8-7.2
PBzMA	CH_2 adjacent to benzene ring	2	4.8-5.0

Primarily, this technique was used to assess the composition of the synthesised block copolymers. Often this is presented as a weight fraction of the P4VP block to the other polymer block(s) (w_{P4VP}). This was calculated by first integrating the polymer peaks for each block to give peak intensity values (I_{block}). The peak intensities were all normalised by dividing by the number of protons (nH) that the integral represents. The normalised intensity for the P4VP block is then divided by the sum of the normalised intensities for all blocks in the copolymer to give a molar fraction of P4VP (nf_{P4VP}) (**Equation 2.1**).

$$nf_{P4VP} = \frac{\dfrac{I_{P4VP}}{nH_{P4VP}}}{\sum_i \dfrac{I_{block\,i}}{nH_{block\,i}}}$$

(Equation 2.1)

This molar fraction value can then be converted to a weight fraction value (w_{P4VP}) by taking into account the molar masses of each of the block's constituent monomer (**Equation 2.2**).

$$w_{P4VP} = \frac{nf_{P4VP} \cdot M_{r\,4VP}}{\sum_i nf_{block\,i} \cdot M_{r\,monomer\,i}}$$

(Equation 2.2)

2.3.3. Scanning Electron Microscopy

The micro-scale morphology of samples was assessed by scanning electron microscopy (SEM). Images of the sample can be produced by exposing the sample to a focussed electron beam. The electrons interact with the surface atoms of the sample producing a variety of measurable signals. The most commonly used SEM mode and the one used in this work measures the

secondary electrons emitted by the sample when excited by the electron beam. Secondary electrons hit a detector to produce an electrical signal which is amplified and displayed as an image pixel based on the signal intensity. The electron beam is then moved across the sample surface in a raster scan pattern. The combination of the beam position and the signal intensity produces a topographical image of the sample.

Samples were prepared by mounting on aluminium stubs with sticky carbon tabs (Agar Scientific) and sputter-coated with a thin layer (~6 nm) of platinum (Polaron SC7640). This conductive layer helps to prevent charge build-up and degradation of the sample, a common problem for polymeric materials. Samples were imaged using a JEOL 6490LV SEM at an accelerating voltage of 10 kV over a range of magnifications.

The images produced with this technique were also used to derive the number average particle diameter (d_n) of samples. Values reported are mean averages taken from at least 100 measured particles (ImageJ processing software). Particle size distributions were reported by calculating the coefficient of variation (CV) for the particles measured (**Equation 2.3**). CV is given as a percentage of the population's standard deviation (σ) in proportion to the mean average particle diameter. Hence, particle size distributions can be compared between samples, regardless of the relative size of the particles in the sample.

$$CV = \frac{\sigma}{d_n}$$
(Equation 2.3)

2.3.4. Transmission Electron Microscopy

The nano-scale morphology of samples was evaluated using transmission electron microscopy (TEM). TEM works using the same basic principles as an ordinary light microscope, instead using electrons for superior resolution due to their smaller wavelength. A focussed beam of electrons is shone through a very thin sample, where interactions between the electrons and sample atoms occur.

Some electrons will be scattered or absorbed by the sample based on the sample's thickness and chemical composition. A thicker sample or sample with higher atomic density will scatter more of the incident electrons. Remaining electrons transmit through the sample and are collected on a detector, usually a charge-coupled device (CCD) camera. Areas of the sample

that scatter more electrons will have a lower intensity and therefore appear darker in the final image.

All materials in this thesis were too thick to be imaged in their neat form. To prepare thin sections of the materials, samples were first embedded in an epoxy resin (Agar 100) and cured at 50 °C for at least 24 hours. Embedded samples were ultra-microtomed (RMC PowerTome PTXL) at room temperature to ~100 nm thick slices using a diamond knife (Leica Diatome Ultra 45°). Sections were collected on copper TEM grids (Agar Scientific).

For polymer materials, samples also needed to be stained before imaging. The contrast between different types of polymer in the TEM is often very low due to their similar elemental compositions. For this reason, polymers are selectively stained with heavier elements to enhance electron scattering in one of the polymers. A variety of different chemical stains can be used depending on the functional groups of the polymer.[1] Sample sections containing PS or PBzMA polymer blocks were stained using RuO_4 vapour for 2 hours, while P4VP blocks were stained with I_2 vapour for 2 hours. Polymer samples containing inorganic components were not stained.

Sections were imaged using a JEOL 2100+ TEM equipped with a Gatan US1000 camera, at an accelerating voltage of 80 kV. Samples were imaged over a range of magnifications. In this thesis some of the images produced were also used to measure the average P4VP domain size in phase separated block copolymers (D_{P4VP}). Values reported are mean averages taken from at least 100 measured nanoscale features (ImageJ processing software).

2.3.5. Small-Angle X-ray Scattering

Small-angle X-ray scattering (SAXS) was utilised during several studies in this thesis to gain insight into the nanoscale morphologies of some block copolymer materials. Nanoscale density differences in a material can cause a coherent beam of X-rays to be scattered elastically at small angles (0.1 - 10°). The pattern of this scattering can give information about both the size and shape of the nanoscale structure. This has become a particularly valuable tool for analysing self-assembled block copolymers and is useful for complementing observations made through TEM analysis.

Typically, SAXS analysis is performed using a synchrotron source of monochromatic X-rays. The high intensity beam is fired through the sample with the majority of X-ray passing straight through the material. However, the small fraction of X-rays that do interact with the sample can become scattered, at angles of 2θ, and recorded as a scattering pattern. In a 1D pattern, the scattering intensity is plotted as a function of the scattering vector (q) (**Equation 2.4**). The position of peaks (q_{max}) in the scattering intensity can be used to discern possible morphology shape and the size of the periodic features (D) (**Equation 2.5**).

$$q = \frac{4\pi}{\lambda} sin\theta \qquad \textbf{(Equation 2.4)}$$

$$D = \frac{2\pi}{q_{max}} \qquad \textbf{(Equation 2.5)}$$

SAXS patterns in this thesis were recorded at a synchrotron source (Diamond Light Source, station I22, Didcot, UK) using monochromatic X-ray radiation (wavelength λ = 0.999 Å), with scattering vector q ranging from 0.003 to 0.25 Å^{-1} (calibrated using silver behenate) and a 2D Pilatus 2M pixel detector (Dectris, Switzerland; pixel size = 172 µm). Scattering data were reduced and corrected (masking, estimation of Poisson uncertainties, time, flux & transmission normalisation, subtraction of empty cell scattering, thickness correction) before being normalised with glassy carbon being used for the absolute intensity calibration utilising standard routines available at the beamline.[2] All measurements were taken on powdered samples.

This procedure was carried out by Dr Matthew Derry and Prof. Paul Topham (Aston Institute of Materials Research, Aston University, UK).

2.3.6. Differential Scanning Calorimetry

Differential scanning calorimetry (DSC) was used to determine the glass transition temperatures (T_g) of polymer materials. The T_g of a polymer is the temperature at which the polymer chains transition from a rigid glass-like state to a more flexible rubber-like state. A polymer with more readily mobile chains will have a lower T_g.

The T_g of a polymer blend is dependant of the compatibility of the of the blend components. A homogenous blend of multiple types of polymer will have a single T_g somewhere between

the T_g values of the constituent polymers, depending on the exact composition. Whereas a phase separated material containing heterogeneous phases will undergo the multiple glass transitions of the individual components.[3] Measurement of a sample's T_g was therefore used to indicate whether a synthesised block copolymer had formed a phase separated morphology.

DSC functions by measuring the amount of energy required to heat a sample relative to an empty reference pan. Changes to this measured heat flow are indicative of phase transitions in the material, including glass transition points.

Samples were analysed using a TA instruments Q2000 DSC, equipped with an auto-sampler. A ~10 mg sample was placed in a Tzero aluminium pan (TA instruments) and press sealed prior to use. Samples were heated to 200 °C, then cooled to -90 °C before a final heating cycle back to 200 °C (10 °C min^{-1} ramp) under a N_2 atmosphere. Data was collected during the second heating run. Data was analysed using TA Universal Analysis software.

2.3.7. Thermogravimetric Analysis

Thermogravimetric analysis (TGA) was used to probe changes occurring to samples during calcination processes. TGA is a method of thermal analysis in which a sample is heated at a constant rate while recording the sample's mass. The profile of the sample's mass change against temperature gives useful information about physical phenomena taking place, such as phase transitions, desorptions and decompositions.

In this thesis, the technique was primarily used to analyse polymer-inorganic composite materials. Data obtained from TGA measurements were used to determine polymer decomposition temperatures, quantity of solvent residue and quantity of uncombusted material. Since the inorganic components of the composites were stable up to high temperatures, the remaining sample mass could be taken to be a measure of the inorganic fraction in the material.

Measurements were performed using a TA instruments Q500 TGA using platinum crucibles. Samples were heated at a rate of 10 °C min^{-1} to the desired isothermal temperature. The heating was performed under the appropriate gaseous atmosphere for the material being analysed. Data was analysed using TA Universal Analysis software.

2.3.8. Infrared Spectroscopy

Fourier transform infrared (FTIR) spectroscopy is a commonly used analytical technique in the chemical sciences to probe the bonding of molecules. Substances can absorb IR radiation at characteristic wavelengths in order to excite the vibrational modes of the molecules. This absorbance is specific to the type of bonding present within the molecules and can be used as a method to determine chemical structure. In this thesis FTIR spectroscopy is used to analyse some of the polymer-inorganic composites produced. The resulting spectra are used to identify any changes to the bonding of the polymers upon addition of inorganic materials.

IR spectra were obtained using a Bruker ALPHA II FTIR spectrometer equipped with an attenuated total reflection (ATR) attachment. Samples were analysed in their solid state directly on the ATR crystal.

2.3.9. Powder X-ray Diffraction

Powder x-ray diffraction (XRD) was used to determine the crystal structures of synthesised inorganic materials. In powder XRD, a small amount of sample is exposed to a coherent beam of x-rays which interact with the atoms of the sample. X-rays have wavelengths of a similar scale to that of inter-atomic distances. This means they are small enough to enter the crystal lattice of a sample and be diffracted by its atoms. Due to the highly symmetric arrangement of atoms in crystalline materials, diffracted x-rays can interfere constructively to give increased signal intensity at specific angles, according to Bragg's law. X-ray signal counts can therefore be plotted against diffraction angle to give characteristic peaks.

In this work, the diffractogram peaks measured from a sample were compared to known standards to confirm the existence of a particular crystal phase in the synthesised metal oxide. The measurement is also useful to confirm a sample is mostly crystalline in nature. Thus, confirming a sample had been adequately annealed and amorphous polymer material removed.

XRD measurements were obtained on a PANalytical X'pert pro MPD diffractometer using a Cu-Kα radiation source (λ = 1.5406 Å). Samples were placed on a silicon zero background holder and analysed over a 2θ range from 10° to 80°.

2.3.10. Surface Area Analysis

The surface area of some of the polymer and inorganic materials synthesised in this thesis were measured quantitatively. This provided a metric to compare the physical structures of materials and postulate their effectiveness in end applications. The surface areas and average pore sizes of materials were calculated by measuring nitrogen sorption onto the material surfaces.

Nitrogen sorption measurement are performed by first degassing a sample of known mass, to remove all surface molecules from the material. The adsorbate gas is then administered to the sample in controlled doses and the relative pressure in the sample container is measured. The pressure in the sealed sample container can then be related to the quantity of gas adsorbed on the sample surface, indicating the available surface area. Nitrogen gas continues to be added in this way to form an isotherm plot which is used to quantify the surface area. Several different theoretical models can be employed to calculate the surface area from the isotherm data, based on various assumptions about the material.

Sorption measurements usually conclude by also recording the nitrogen desorption; a vacuum is applied to obtain the reverse isotherm. The complete data can often form a hysteresis loop between the adsorption and desorption plots. The size and shape of this loop can be telling of the type of porosity present in the material and is also used to calculate an average pore diameter for the material. Again, several different theoretical models can be applied to calculate the pore size distribution.

All nitrogen sorption measurements were performed on a Micrometric 3FLEX sorptometer at -196 °C. Polymer samples were degassed at 50 °C for 16 hours while inorganic samples were degassed at 200 °C for 12 hours prior to measurement. The Brunauer–Emmett–Teller (BET) method was used to calculate the surface area from the isotherm plots, while the Barrett-Joyner-Halenda (BJH) method was used to calculate pore size distributions.

2.4. References

1.   G. H. Michler, *Electron Microscopy of Polymers*, Springer, Berlin, 2008.
2.   B. R. Pauw, A. J. Smith, T. Snow, N. J. Terrill and A. F. Thünemann, *J. Appl. Cryst.*, 2017, **50**, 1800-1811
3.   H. Diamon, H. Okitsu and J. Kumanotani, *Polym. J.*, 1975, **7**, 460-466.

Chapter 3 – Microscale and Nanoscale Size Modifications of PMMA-*b*-P4VP Block Copolymers from Supercritical CO$_2$

3.1. Overview

This chapter explores how the micro and nanoscale dimensions of hierarchically structured PMMA-*b*-P4VP block copolymers from scCO$_2$ can be altered through changes to the synthetic parameters. The aim being to demonstrate a high level of versatility in the design of these block copolymers for use in structure direction of inorganic functional materials.

Microparticle size control was investigated by altering the quantity of polymeric stabiliser used in the scCO$_2$ dispersion polymerisation. This simple but effective method has proven successful in previous studies on free-radical homopolymer synthesis but has yet to be applied to controlled radical synthesis of block copolymers in dispersion. Nanoscale size control was investigated by varying the overall molecular weight of the block copolymers. This was achieved by altering the quantity of RAFT agent in the controlled polymerisation.

Further to this, the various size block copolymer particles were applied to the sol-gel synthesis of LiFePO$_4$, a lithium-ion battery cathode material that is expected to show a marked increase in electrochemical performance when a hierarchical morphology is applied. The polymer templates were removed by anaerobic calcination to give highly pure and crystalline LiFePO$_4$ with a residual carbon coating to aid in electrical conductivity. The resulting morphology and surface area of the battery materials is shown to be heavily dependent on the microparticle size of the polymer template used to create them. The electrochemical performance of the final materials is also explored by fabricating them into electrodes and assembling coin cell lithium-ion batteries.

3.2. introduction

This introduction develops on the general concepts presented in **Chapter 1**. Specifically, block copolymer self-assembly behaviour is explored in greater detail. This includes the interaction of $scCO_2$ with block copolymers, the effect of spatial confinement on self-assembly and routes to form hierarchically structured arrangements of block copolymers. These topics are discussed to provide the reader with a more detailed insight into the principles governing the formation of phase separated block copolymer microparticles in $scCO_2$.

In addition, a brief overview is provided regarding the inorganic materials used in rechargeable battery applications, as this will be the targeted function of materials fabricated in this chapter. Particular focus is placed upon the limitations suffered by the bulk cathode materials and the potential benefits of applying nanoarchitectures to enhance the capabilities of these materials.

3.2.1. Block Copolymer Self-Assembly in scCO₂

In **Chapter 1** the theory regarding diblock copolymer phase separation in the bulk state was discussed. It was explained that the resulting thermodynamically stable morphology was determined by the volume fraction of the two constituent blocks.[1] The volume fraction of each block is generally altered by changing the polymer composition, adjusting the molecular weight of each block. However, block volume fractions, and therefore the bulk phase behaviour of block copolymers, can also be heavily influenced by the introduction of additives.[2-5]

For an additive to cause a change in the expected morphology for a particular block composition, its interaction with the copolymer components must be asymmetric.[6] This means the additive must have a higher preference to one particular polymer block, causing its volume to increase disproportionately over the other block and lead to a shift in the preferred morphology. Examples of additives that are capable of achieving this effect are solvent vapours,[7, 8] low molecular weight homopolymers,[9] dilute acids/bases[10] and small amounts of liquid solvent.[6, 11] Here, CO_2 is discussed as such an additive.

The use of CO_2 as an additive to modify block copolymer phase behaviour has been the focus of several studies.[12-14] As mentioned previously, due to the gas-like diffusivity of $scCO_2$, the solvent has a particular affinity to intercalate into polymer matrices causing the materials to

swell.[15] The extent of this swelling is determined by the solvent parameters (pressure and temperature) as well as the degree of solubility CO_2 has in the polymer structure.[16] Though CO_2 solvent interactions can be difficult to model and predict, it is generally accepted that quadrupole-polar interactions play a substantial role.[17] A recent report modelling CO_2 interactions with various compounds shows that $scCO_2$ tends to have strong interactions with unsaturated polar bonds, such as $C=O$ and $C\equiv N$ groups.[18] The high 'CO₂-philicity' of these particular functional groups causes certain classes of polymers, such as methacrylates, to undergo a large degree of swelling in $scCO_2$ due to the high solubility of CO_2 in the polymer matrices.[19]

A study by Zhang *et al.* quantified the CO_2 sorption and swelling of several homopolymers when exposed to $scCO_2$ at various pressures. They also studied the swelling of a number of block copolymers made up of the individually studied homopolymers, with a range of block volume fractions.[20] Interestingly, they found a linear dependence of the degree of swelling with the block fractions of the copolymer. This suggested that sorption of CO_2 by the copolymers was quantitatively comparable and unchanged when compared to the constituent homopolymers.

Jennings *et al.* studied the influence of $scCO_2$ on the phase behaviour of a number of block copolymer compositions.[12] The block copolymer microparticles were synthesised via RAFT-mediated dispersion polymerisation in $scCO_2$, targeting various weight fractions for each material. After the polymerisations, reactions were cooled before releasing the CO_2 from the block copolymers. As such, the morphology of the block copolymers would be a representation of the thermodynamically equilibrated structure formed in the presence of $scCO_2$. This morphology is first fixed by cooling below the T_g of the polymer blocks and then contracted slightly by subsequently removing the liquified CO_2 from the polymer matrix. This left the materials assembled in their kinetically trapped scCO₂-state morphologies, with only the domain size features expected to change slightly when analysed in the ambient state.[21] The self-assembled morphologies were studied by cross-sectional TEM of the particles and used to construct experimental phase diagrams for the observed morphologies (**Figure 3.1**).[12]

In the case of block copolymers comprised of all-methacrylate polymer blocks, poly(methyl methacrylate-*b*-benzyl methacrylate) (PMMA-*b*-PBzMA), the phase diagram showed good

agreement with the theoretical phase diagram for bulk phase self-assembly. However, in the case of the methacrylate-styrene composition, PMMA-*b*-PS, the phase diagram showed a large divergence to the expected morphologies for the standard bulk material, with non-spherical geometries only produced at very low weight fractions of PMMA. This was attributed to the asymmetric swelling of the two blocks, due to the higher solubility of CO_2 in the PMMA block.[12] This study demonstrates the challenge in producing a non-spherical morphology in a PMMA-*b*-P4VP block copolymer synthesised in $scCO_2$ (comparable to the PMMA-*b*-PS phase diagram, as PMMA is known to swell more than P4VP in $scCO_2$).[20]
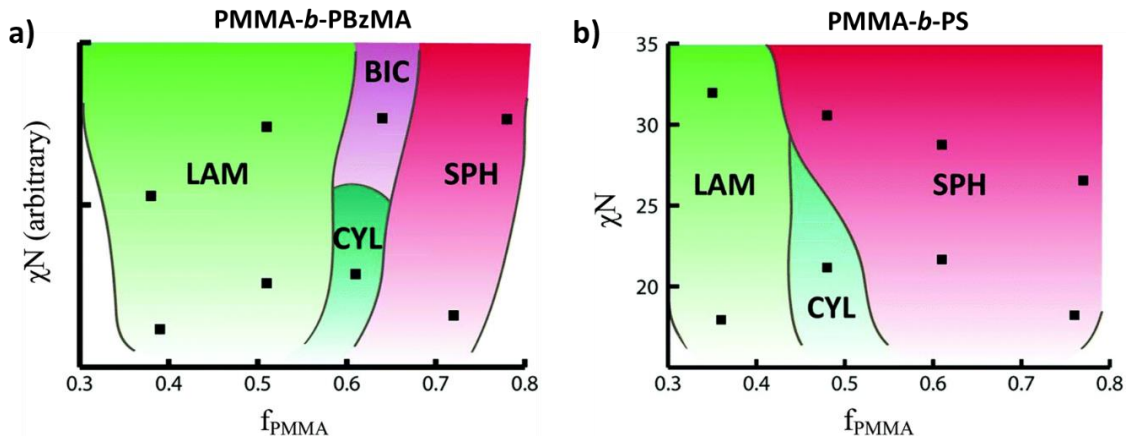
Figure 3.1: *Experimental phase diagrams for (a) PMMA-b-PBzMA and (b) PMMA-b-PS synthesised in scCO₂.[12]*

Along with the possibility to manipulate the preferred morphology of block copolymers, $scCO_2$ has also been shown to influence the necessary conditions required to induce phase separation.[12, 22-25] Typically, thermal annealing is used to increase the mobility of chains to a disordered state, above the polymer T_g and generally to a point where χN < 10.5, as χ is known to decrease as temperature increases. The block copolymer is then cooled, inducing phase separation when χN again becomes greater than 10.5. The temperature at which this transition occurs is referred to as the order-disorder transition temperature (T_{ODT}).[26]

ScCO₂ has a great influence on the thermal annealing process as sorption of CO_2 into the block copolymer structure has the ability to reduce both the polymer T_g, making it more mobile, and the T_{ODT}. For example, the group of Watkins has studied the effect of $scCO_2$ on the T_{ODT} for several block copolymers including PS-*b*-poly(n-alkyl methacrylates)[23], PS-*b*-poly(isoprene)[24] and high molecular weight PS-*b*-PMMA.[25] They found that in the majority of materials, the T_{ODT} was significantly depressed with the addition of $scCO_2$ and the degree of

depression could be tuned by increasing the solvent pressure.[24] This was shown to successfully induce phase separation, whereas when identical materials were heated to the same temperature in vacuum this was not the case.[25] The depression in T_{ODT} was attributed to screening of the unfavourable enthalpic interactions between the polymer blocks by the added CO_2 molecules, allowing them to reach the disordered state at lower temperatures.[23]

This demonstrates that $scCO_2$ can be applied to anneal block copolymers at much lower temperatures, much in the same way as solvent vapour annealing techniques are used to induce phase separation in block copolymer thin films.[26, 27] The comparison between these two systems is logical, due to the gas-like nature of $scCO_2$. In the same way as in solvent vapour annealing, annealing in the presence of $scCO_2$ is particularly useful for enabling self-assembly of block copolymers with low degradation temperatures or when the T_g is close to the degradation point.

When $scCO_2$ is used as the reaction solvent during synthesis of block copolymers, this effect is applied during the polymerisation. As such, the necessity for a post-synthesis annealing step can be circumvented as phase separation occurs simultaneously with chain growth.[12] This is not only an efficient method but can also be used as a facile route to create internally self-assembled microparticles, when a heterogeneous synthetic approach is adopted.[21, 28-30]

3.2.2. Spatial Confinement of Block Copolymers

It has been established that the self-assembly of diblock copolymers in the bulk state usually results in one of four distinct repeating morphologies: spheres, cylinders, gyroid or lamellar.[1] Conventional self-assembly in solution also only leads to a limited number of geometries such as micelles, worms and vesicles.[31] However, an extensive range of studies over the past few decades have identified various methodologies to expand upon these possible assemblies of diblock copolymers. Such methods can lead to the formation of unusual geometries and produce structural hierarchies in block copolymers.

A particular approach that has gained a great deal of attention in experimental and theoretical studies is the confinement of block copolymers during phase separation.[32] Spatial confinement in any number of dimensions has the potential to break the symmetry of the bulk morphologies and frustrate the self-assembly to give unusual morphological arrangements.[33] In such studies, block copolymers are often studied under 2D and 3D

confinement. Practically, this relates to confinement of block copolymers in cylindrical pores and spherical cavities respectively. 1D confinement is also extensively studied as this relates to the self-assembly of block copolymers cast as thin films.[34-36]

Literature on this topic is extensive and is not reviewed in full here. The reader is directed to several review articles on this topic.[32, 33, 37] Morphologies produced under confinement can be affected by preferential surface interactions with a particular polymer block[38], geometry of the confining surface[39] and the overall size of the confinement.[40] All these are in addition to the usual volume fraction considerations that determine optimal morphology. Arguably, the confinement size is the most studied variable to influence self-assembly. Examples of these include Monte Carlo simulations performed by Yu *et al.* of block copolymers under confinement in both cylindrical and spherical nanopores of various dimensions (**Figure 3.2**).[40-42] Confinement size is denoted as D/L_0, a measure of the ratio of confinement diameter to the bulk period dimension of the block copolymer.
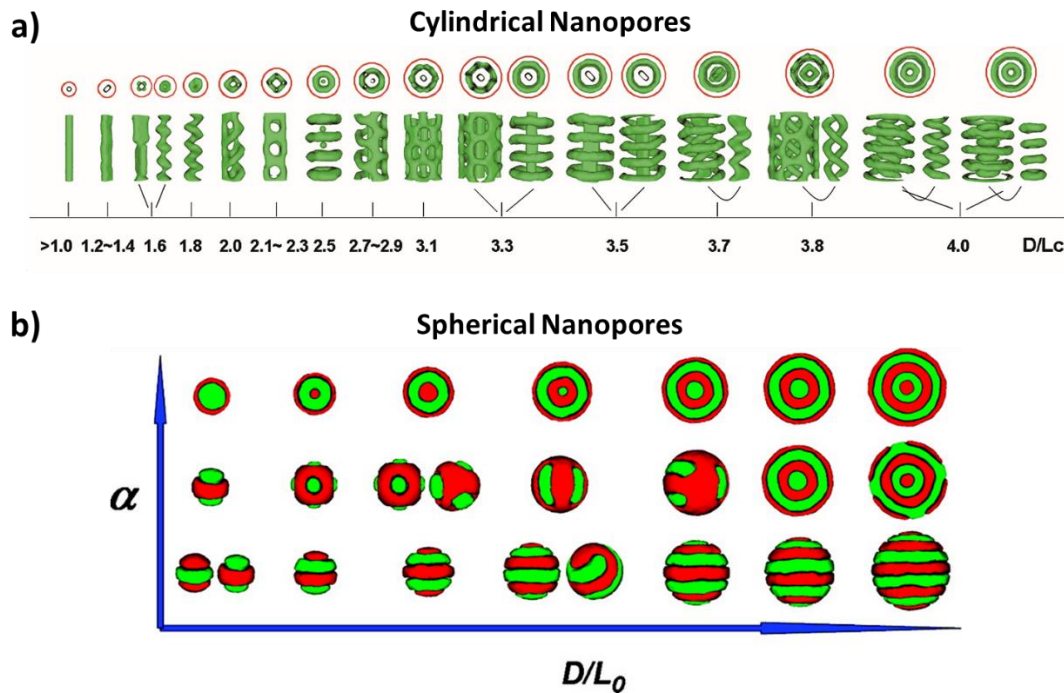
Figure 3.2: *Monte Carlo simulations demonstrating the effect of (a) 2D[40] and (b) 3D confinement[42] on the expected phase separated morphology. α denotes an increase in preferential surface interactions.*

From these simulations it was clear that a vast range of morphologies could be obtained from a single block copolymer composition under different confinement dimensions. In cylindrical nanopores, various helical and stacked toroid geometries were often predicted up to D/L_0 =

4.[40] In spherical nanopores, a number of nanoparticles with patterned surfaces and onion-type morphologies were predicted.[42] In both cases the predicted morphologies were found to be highly dependent on the surface interactions of each block with the pore walls.[40, 42] It is also apparent from these and similar studies that for confinement to have a meaningful effect on self-assembly, D must be of a similar order of magnitude to L_0 ($D/L_0 < 5$).[33, 40, 43-45]

Experimentally, block copolymer self-assembly under confinement has been studied by preparing copolymers in microporous solids, such as alumina[45] or silica[46], or by preparing block copolymer particles.[47] Different methods for obtaining block copolymers confined in particles are outlined in the following section. Dispersion polymerisation can be used to achieve this[21], though particle sizes obtained are commonly too large (> 500 nm) to achieve low enough D/L_o values to induce confinement effects on the observed morphologies.[48, 49] However, particle size control of block copolymers via dispersion polymerisation in scCO₂ has yet to be studied. If significantly low particles sizes can be achieved using this method, this could be coupled with the synthesis of block copolymers with large domain size features to potentially induce some of these interesting confinement effects.

3.2.3. Hierarchically Structured Block Copolymers

Structural hierarchies are employed extensively in natural materials.[50] Through control of a material's morphology over multiple length scales, Nature has been able to produce materials with extraordinary properties not attainable using conventional synthetic alternatives. Common examples of this are found in cellulose and collagen-based materials, bone, animal shells and gecko feet.[50, 51] The exceptional physical properties of these and other natural resources have inspired a great deal of research into producing bio-mimetic systems that harness the benefits of hierarchical material structures. Utilising some of these principles has led to the creation of metamaterial[52, 53], auxetic structures[54] and hierarchically porous networks.[55]

While block copolymers generally offer a route to form intricate morphologies only at the nanoscale, methodologies have been developed to also produce structural hierarchies in these polymeric materials.[56] To achieve this, block copolymer phase separation is commonly combined with at least one other self-assembly pathway, either simultaneously or stepwise. This can be accomplished by combining block copolymers with other polymeric components

such as small oligomeric amphiphiles, colloidal particles or rigid rod-like polymers.[56-60] These additional components can induce secondary polymer interactions that cause nanostructures to aggregate into larger building blocks, leading to formation of a structural hierarchy (**Figure 3.3**).
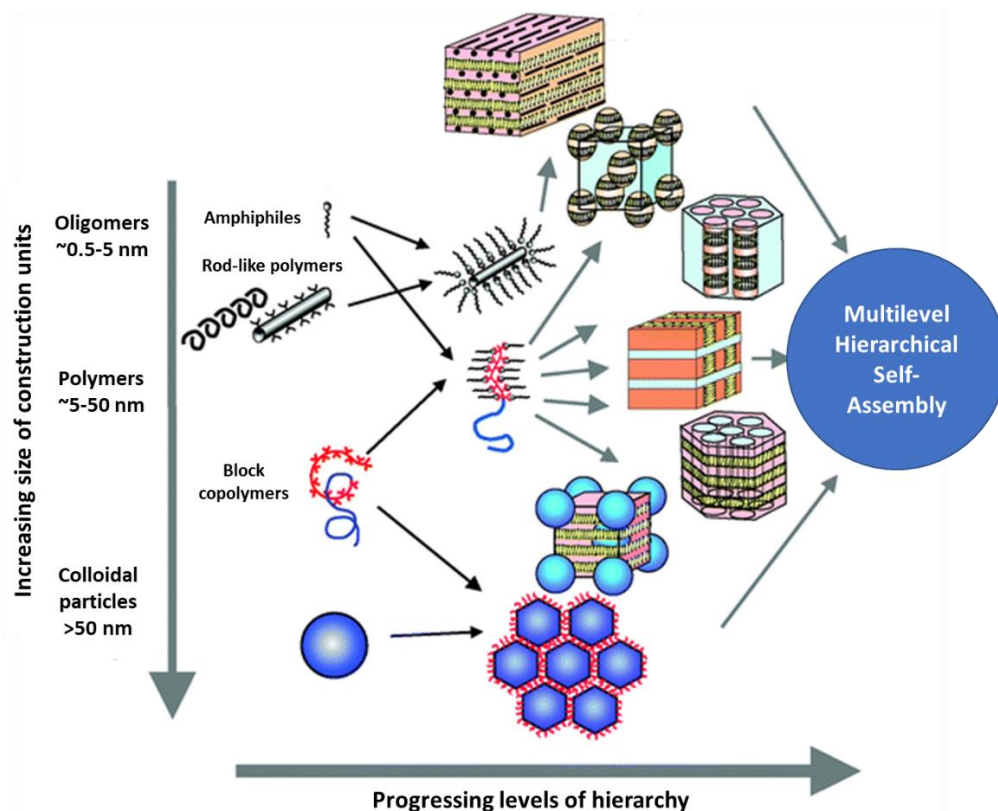
Figure 3.3: General schematic demonstrating how the combination of different sized polymer components can cause assembly on multiple length scales, producing hierarchical structures. Figure adapted from the literature.[56]

Literature on the topic of hierarchical assembly using different polymeric components is extensive and is not reviewed here in full.[56, 61-64] Some significant examples include the use of copolymer building blocks with anisotropic compositions to induce intermicellar interactions to build arrays of larger assemblies.[65, 66] Ruokolainen *et al.* demonstrated that by combining PS-*b*-P4VP copolymers with small oligomeric amphiphiles capable of hydrogen bonding to the pyridine groups, small lamellar structures could be introduced within the block copolymer morphologies (**Figure 3.4 a**).[57] Also, Ianiro *et al.* used block copolymers of poly(ethylene oxide) (PEO) and poly(ε-caprolactone) (PCL) to create leaf-like structures by carefully controlling the interplay of the phase separation between the two blocks with their inherent ability to crystallise (**Figure 3.4 b**).[67]
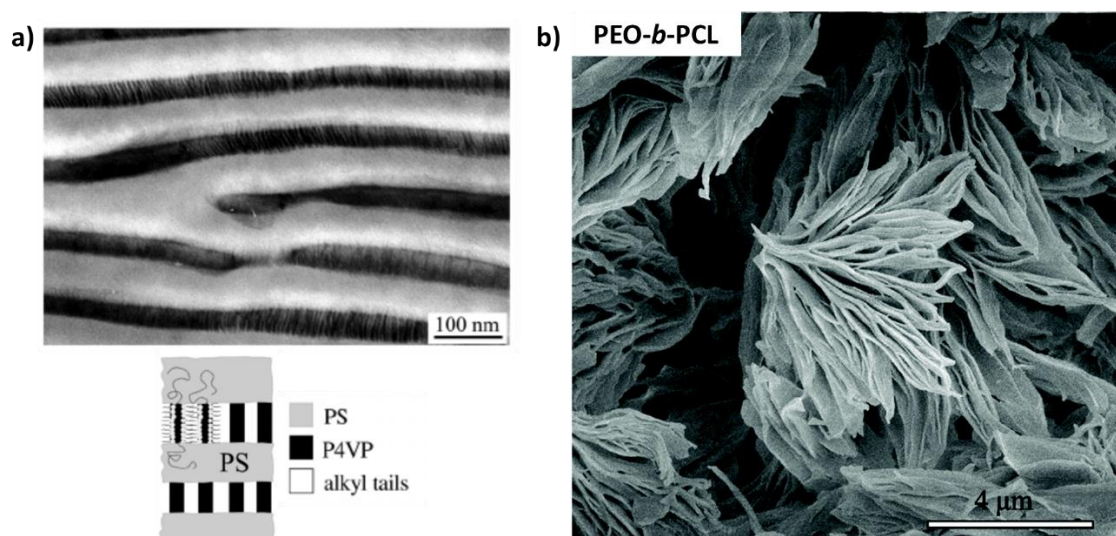
Figure 3.4: *Examples of hierarchical assemblies produced using block copolymers with (a) the addition of small amphiphiles[57] and (b) control over the crystallisable polymer blocks.[67]*

However, a particular hierarchical assembly that appears frequently in the literature is the formation of particulate self-assembled block copolymers.[68-71] This structural arrangement can be reasonably easy to obtain when compared to other hierarchical structures and as stated previously, can also lead to unique self-assembly behaviour when particle confinement is small enough. The confining particle sizes usually range from 100s of nm to a few microns. These kinds of hierarchical arrangements have received considerable attention recently, particularly for their use in storing active materials, such as drugs, for controlled and prolonged release.[72-74] They are also of interest for use in various other applications including impact modifiers[75], photonics[68] and protein separation[76] to name a few.

Popular methods of producing self-assembled block copolymer microparticles involve the removal of solvent from a block copolymer solution to gradually increase the quantity of anti-solvent or surfactant to drive the microscale assembly.[12, 29, 77] Common methods using this principle include evaporation induced self-assembly (EISA)[78], solvent organised reprecipitation (SORP)[77] and routes involving the removal of solvent by dialysis, like those employed by Holder *et al.*[79, 80] However, all these approaches suffer significant drawbacks. The use of large quantities of volatile organic solvents and low polymer loading in the final solutions (typically < 1wt%) are the main limitations for producing these hierarchical materials on a large scale.

Another alternative to producing these materials is to synthesise them directly using controlled radical polymerisation techniques in heterogeneous systems.[71] The group of Okubo presents examples of simultaneous synthesis and self-assembly of block copolymers particles in miniemulsion systems.[81, 82] As mentioned previously, the Howdle group has also demonstrated efficient synthesis of these hierarchal block copolymer structures in scCO₂ dispersion through a single pot reaction.[21, 29] However, the group has yet to demonstrate control of the size of these structures at either the micro or nano length scales; a feature that should prove useful for tailoring the materials for a specific application.

3.2.4. Nanostructured Materials for Rechargeable Batteries

Lithium-ion rechargeable batteries have become commonplace in our everyday lives. Their use is wide-ranging in the electronics industry, powering all manner of portable devices from mobile phones to laptops. Their use is also likely to become even more prevalent in the coming decades as society moves away from fossil-fuel power and requires solutions to store renewably generated alternatives. The possible high demand for these materials in the near future is diving current research towards decreasing the cost and increasing the performance of lithium-ion technology.[83, 84]

Lithium-ion batteries function by transferring Li^+ ions from one electrode to another to store energy and then release it as needed. During the charging cycle, lithium atoms in the cathode material are ionised by an electrical charge and transported through an electrolyte to the anode material where they recombine with their electrons (**Figure 3.5**). The process is then reversed when current is drawn from the battery and the stored energy is released.[85] Graphite powder is the most commonly used anode material to intercalate Li^+ in commercial batteries, while a selection of lithium-containing transition metal oxides can be used to construct the cathode.[86] Generally, it is believed that the performance of a lithium-ion battery is mainly determined by the cathode material used in the cell construction.[87]

A number of cathode materials are currently used in lithium-ion batteries, such as layered $LiCoO_2$, spinel structured $LiMn_2O_4$ and olivine structured $LiFePO_4$. Mixed metal oxides such as $LiNi_{1-x-y}Mn_xCo_yO_2$ and a variety of other emerging oxide materials are also available.[88] Each type of material carries with it specific advantages and disadvantages based on their intrinsic chemistries that limit their performance.[84] For example, $LiCoO_2$ offers a high energy density

and good electrical conductivity but suffers from high cost and relatively short lifespan. In contrast, LiFePO$_4$ offers high thermal stability, low cost and high discharge rate but suffers from low energy density and low electrical conductivity.[88]
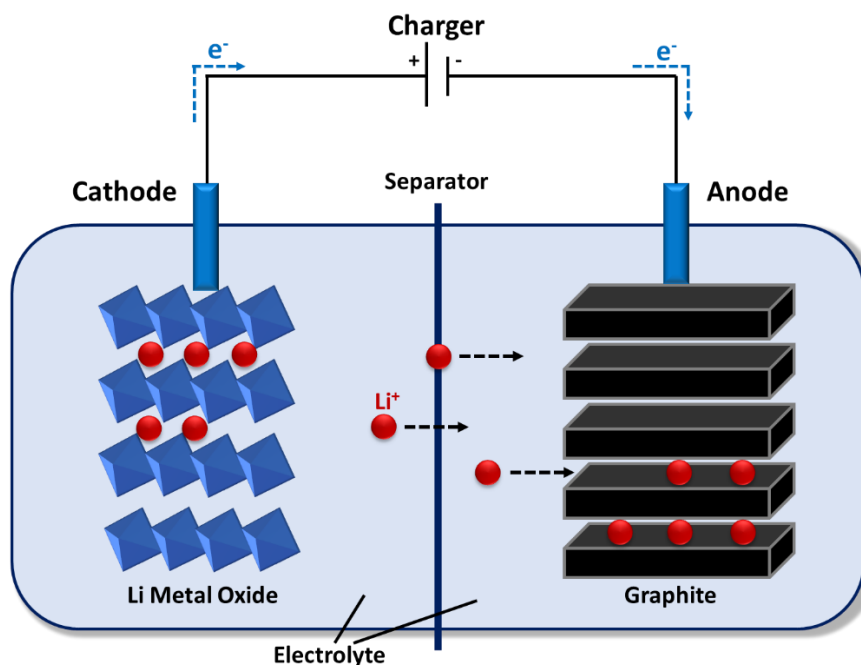
Figure 3.5: *Schematic illustration of a lithium-ion battery showing the movement of Li⁺ through the components during a charging cycle.*

Any method to improve the performance of the battery cathode material involves either changing the chemical formulation of the metal oxide or altering the structural morphology of the material.[89] Incorporating various high surface area nanoarchitectures into cathode materials, such as nanoparticles, nanorods and nanoplates, has proven to be a popular approach to enhance the performance of commonly used metal oxides.[90] This is because a nanostructured cathode material offers much shorter Li⁺ diffusion pathways, allowing the ions to be inserted and extracted with much greater efficiency. Many reports in the literature show that this can lead to a higher total charge/discharge capacity, closer to the theoretical limit, along with faster charging rates.[91-94]

Currently, solid-state calcination processes are widely employed by industry to synthesise cathode materials, leading to bulk morphologies with low surface areas and a high degree of impurities.[95] Many new approaches have been explored to fabricate nanostructured lithium metal oxide materials to replace this current approach, including freeze drying[96],

solvothermal[97], hydrothermal[98] and templating methods.[99] Naturally, for templating approaches, block copolymers are a frequent occurrence in the literature as a soft template to scaffold cathode materials before removal by calcination or chemical etching.[90]

Despite the benefits offered by introducing nanostructure to cathode materials, it has been noted that this can also lead to serious performance issues, particularly when using nanoparticulate metal oxides. The high surface area of nanoparticles gives them greater reactivity and therefore a higher tendency to undergo side reactions during the charge/discharge cycles of the battery. Unwanted processes such as particle aggregation and formation of solid electrolyte interfaces leads to greatly reduced performance over the lifetime of the battery.[99, 100] Dispersions of nanoparticles can also reduce the packing of active cathode material in the battery, leading to low volumetric energy densities.[101]

A promising solution to this limitation is to instead incorporate hierarchical morphologies into lithium-ion cathode materials, taking advantage of the short Li$^+$ diffusion pathways while limiting the material's ability to aggregate and degrade.[102] Examples include hierarchically porous materials[99, 103, 104], pomegranate-inspired clusters[105], yolk-shell microspheres[106, 107] and porous particles.[108-110] All result in exceptional electrochemical performances and sample stability. A variety of synthesis approaches are employed to obtain these different hierarchical arrangements, though only a limited number utilise block copolymers in their construction.

3.2.5. Summary and Research Objectives

This introduction has reviewed the topic of bulk-phase block copolymer self-assembly in greater detail than the simple overview provided in **Chapter 1**. Specifically, studies from the literature have shown that the expected thermodynamically stable morphology of a block copolymer can be altered by the influence of scCO$_2$ as an additive or by confining the space in which a polymer can self-assemble. Block copolymer self-assembly can also be combined with other assembly pathways to yield hierarchical structures with morphological features on multiple length scales. All these topics are brought together when considering the nature of block copolymer self-assembly within microparticles synthesised in scCO$_2$ dispersion polymerisation.

From this review of the literature, it is clear that the synthesis and self-assembly of block copolymers in scCO$_2$ has proven to be an attractive route to produce hierarchically structured

block copolymer particles. The main advantage being the facile production of internally nanostructured microparticles in a one-pot synthetic method with low environmental impact and on the gram scale. This is due to the ability of $scCO_2$ to enable *in-situ* self-assembly of the block copolymer and the addition of polymeric stabiliser to form the microparticle structure simultaneously. However, aside from changes to the block composition, manipulation of these hierarchical structures has yet to be fully explored in $scCO_2$. In particular, controlling the dimensions of both the internal nanoscale morphologies and the microparticle size is key to demonstrate the versatility in this synthetic approach, especially when pursuing structure directing applications.

In this chapter, control of the microscale and nanoscale dimensions of PMMA-*b*-P4VP block copolymer particles is investigated. Microscale size control is studied by varying the quantity of stabiliser used in the $scCO_2$ dispersion, a method already proven to be successful for homopolymer particles.[48] Nanoscale size modification is studied by altering the overall molecular weight of the PMMA-*b*-P4VP block copolymer to control the domain size of the internal spherical morphology.

This introduction has also highlighted the growing need for new synthetic approaches to produce lithium-ion cathode materials with enhanced electrochemical performance. Imparting complex hierarchical morphology onto the cathode material has proven to be an effective method to achieve this. Here, the hierarchically structured PMMA-*b*-P4VP block copolymers are attempted to be used as sacrificial templates to direct the structure of $LiFePO_4$ during its sol-gel synthesis. The various sized block copolymer templates are investigated for their effectiveness in producing $LiFePO_4$ with different dimensions. It is hoped that providing a method to tune the dimensions of the polymer template will offer a route to optimise the end properties of the desired battery material.

3.3. Experimental

3.3.1. Materials

Methyl methacrylate (MMA, ProSciTech, 99%) and 4-vinylpyridine (4VP, Acros Organics, 95%) were purified by eluting through a basic alumina column to remove inhibitor. 2,2'-azobis(2-methylpropionitrile) (AIBN, Sigma Aldrich, 98%) was purified by recrystallisation from methanol. Dry CO_2 (BOC, SFC grade, 99.99%), 2-(Dodecylthiocarbonothioylthio)-2-methylpropionic acid (DDMAT, Sigma Aldrich, 98%) and poly(dimethylsiloxane) monomethyl methacrylate (PDMS-MA, Fluorochem, M_n ~10 kg mol⁻¹) were all used as received.

FeCl₃ (Sigma Aldrich, 97%) was made up as a 1 M standard solution in ethanol, whereas LiCl (Sigma Aldrich, 99%), and L-ascorbic acid (Sigma Aldrich, ≥99%) were made up as 1 M standard solutions in water. H_3PO_4 (Sigma Aldrich, 85 wt% in water) was diluted to a 50 wt% in water solution.

3.3.2. One-Pot Synthesis of PMMA-*b*-P4VP

All PMMA-*b*-P4VP diblock copolymers in this chapter were synthesised using a one-pot dispersion method in scCO₂. All these reactions were performed using the high-pressure equipment detailed in **Chapter 2** and operated following the standard operating procedure described in **Section 2.2.4**.

The following procedure describes the synthesis of a PMMA-*b*-P4VP block copolymer with target molecular weight of 67 kg mol⁻¹, a composition of 25 wt% P4VP and a stabiliser loading of 5 wt% with respect to the total mass of monomer. A solution of MMA (7.5 g, 74.9 mmol), AIBN (12.3 mg, 0.07 mmol), DDMAT (54.6 mg, 0.15 mmol) and PDMS-MA polymeric stabiliser (0.5 g) was mixed in a sealed vial at 0 °C and degassed by purging with argon for 30 minutes. The monomer solution was then added to the degassed 60 mL high-pressure autoclave via syringe against a positive pressure of CO₂ to prevent the ingress of air. The autoclave was then sealed, heated to 65 °C and pressurised to 241 bar, following the standard operating procedure. After stirring at 300 rpm for 24 hours, a small sample of the PMMA macro-RAFT agent was taken from the outlet tap for analysis. The second monomer solution, 4VP (2.5 g, 23.8 mmol) with AIBN (6.25 mg, 0.04 mmol), was degassed before adding directly into the pressurised autoclave via a HPLC pump at a rate of 0.5 mL min⁻¹. After a further 24 hours, the

reaction was cooled to room temperature, slowly vented to atmospheric pressure and the dry, off-white diblock copolymer powder was collected (typical yield ~85-90%).

Parameters for these syntheses were chosen based on previous experiments performed by the Howdle group.[12, 21, 29] This included target molecular weights based on previous quantities of RAFT agent used in $scCO_2$. Also, a reaction temperature of 65 °C was chosen to ensure adequate thermal degradation of the AIBN, and a reaction pressure of 241 bar was applied to ensure good solubility of the PDMS-MA stabiliser was achieved. A monomer addition rate of 0.5 mL min^{-1} was applied to prevent a sudden high concentration of 4VP disrupting the PMMA dispersion. The rate of monomer addition was still far quicker than the RAFT kinetics. It is noted that alterations to these high-pressure reaction parameters could be a beneficial line of investigation for block copolymer synthesis but goes beyond the scope of this thesis.

3.3.3. Sol-Gel Synthesis of LiFePO₄

Before use in LiFePO₄ synthesis, PMMA-b-P4VP block copolymer samples (1 g) were rinsed with ethanol (2 x 40 mL) and hexane (30 mL) then dried at room temperature under vacuum, to remove any impurities or P4VP homopolymer. Polymers were rinsed by dispersing in the solvent, centrifuging for 10 mins and then decanting the solvent.

The LiFePO₄ sol was prepared by adding FeCl₃ (0.106 mL, 1 M), ascorbic acid (0.158 mL, 1 M), LiCl (0.109 mL, 1 M) and H₃PO₄ (0.016 mL, 50 wt% in water) were added in turn to ethanol (7 mL) then stirred for 1 hour. Ascorbic acid was employed as a reducing agent to form the desired Fe^{2+} ions in the solution. Simultaneously, the PMMA-b-P4VP block copolymer (50 mg) was suspended in ethanol (2 mL) by rapid mixing at 1200 rpm for 1 hour. The block copolymer slurry was then transferred dropwise into the LiFePO₄ sol and stirred for a further 24 hours. The contents were then poured into a petri dish and left at room temperature for 72 hours to evaporate the solvent. Once dried, a thin film of polymer-inorganic composite was collected as a fine yellow powder (78 mg). The composite was then annealed at 700 °C for 2 hours in an argon atmosphere to yield a fine black powder of carbon coated LiFePO₄ (34 mg).

For characterisation requiring a larger quantity of material, the sol-gel synthesis was performed in batches of multiple reactions in unison. Dried polymer-inorganic composites were then collected and combined before annealing.

3.3.4. Characterisation

The Majority of the characterisation techniques used in this chapter are described in **Section 2.3** of this thesis.

Electrochemical performance of the $LiFePO_4$/C cathode materials was achieved by fabricating the material into an electrode and assembling the electrode in a battery cell. Electrode films were fabricated by mixing $LiFePO_4$/C samples with conductive carbon black (Timcal Super C65) and a polyvinylidene fluoride binder (Kynar) in a 75:15:10 weight ratio. N-methyl-2-pyrrolidone (NMP) was added to the mixtures to form a paste that was cast onto aluminium foil. Circular electrodes (1/2 inch) were cut and dried at 80 °C under vacuum overnight. The $LiFePO_4$/C electrodes were then assembled into Swagelok cell inside an argon filled glovebox, with lithium metal (0.75 mm) used as the counter electrode. $LiPF_6$ (1.0 M) in 1:1 v/v ethylene carbonate/ethyl methyl carbonate (Sigma Aldrich, battery grade) was used as the electrolyte and a glass fibre disk (Whatman, grade GF/B) was used as the separator. Galvanostatic cycling tests were then conducted at room temperature using an Arbin BT 2043 to investigate the rate performance (voltage range 2 to 4.5 V vs. Li/Li^+). This procedure was carried out by Andrea Palumbo and Prof. Ullrich Steiner (Adolphe Merkle Institute, University of Fribourg, Switzerland).

3.4. Results and Discussion

3.4.1. Microparticle Size Changes

The first study of this chapter concerns the change in microparticle size of the PMMA-*b*-P4VP block copolymer templates. The microscale dimensions of the block copolymers were altered by varying the quantity of polymeric stabiliser (PDMS-MA) in the scCO₂ dispersion. This follows the same procedure as a previous study on particle size control for a PMMA homopolymer synthesised via free-radical dispersion polymerisation in scCO₂.[48] Additional polymeric stabiliser allows for a greater number of polymer particles to be nucleated in the early stage of the dispersion polymerisation. This results in a smaller overall size in the microparticles. Though, when extremely high or low loadings of stabiliser are used, the dispersion tends to falter and produce aggregated particles or particles with a large size distribution.[111]

Only the quantity of stabiliser was changed during the one-pot synthesis of PMMA-*b*-P4VP, described in **Section 3.3.2**. All PMMA-*b*-P4VP block copolymers were synthesised with the same target molecular weight ($M_{n\,target}$) of 67 kg mol^{-1}. The target weight fraction of the P4VP block (w_{P4VP}) was also kept constant at 25 wt% (50 kg mol^{-1} PMMA, 17 kg mol^{-1} P4VP). This has proven to be the optimal weight fraction to give high fidelity in the pattern transfer of the spherical polymer morphology to an inorganic material, via sol-gel synthesis.[112]

To confirm all the synthesised polymers were chemically comparable, the molecular weight of all products ($M_{n\,exp}$) was measured through GPC analysis (**Figure 3.6 a**). Samples of the PMMA macro-RAFT intermediate were collected partway through the reaction; their molecular weights were also evaluated. The weight fraction of P4VP was calculated from ^{1}H NMR analysis of the block copolymers (**Figure 3.6 b**), using the method described in **Section 2.3.2**. Values are summarised below (**Table 3.1**).
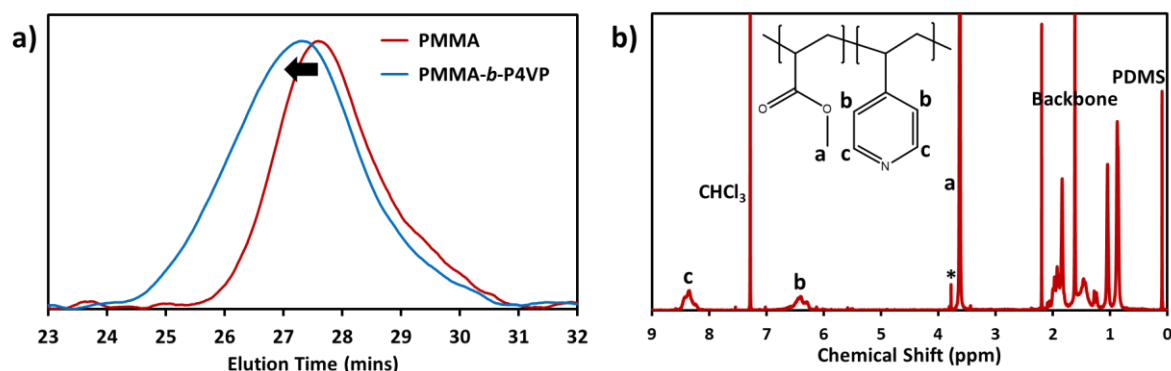
Figure 3.6: *Chemical characterisation data for the PMMA-b-P4VP block copolymer synthesised with 2.5 wt% stabiliser. Data is representative of the complete sample set. (a) GPC chromatograms at each stage of the polymerisation. (b) ^1H NMR Spectrum and assignments for the block copolymer product. * assignment relates to small MMA monomer impurity (< 1%).*

Table 3.1: *Summary of characterisation data for the PMMA-b-P4VP block copolymer samples synthesised with various quantities of PDMS-MA stabiliser.* [a]

Stabiliser loading (wt%)	PMMA $M_{n\,exp}$ [b] (kg mol^{-1})	Đ [b]	PMMA-*b*-P4VP $M_{n\,exp}$ [b] (kg mol^{-1})	Đ [b]	w_{P4VP} [c]	f_{P4VP} (vol%)	d_n (µm) [d]
2.5	53.8	1.28	71.3	1.38	26	27	2.45
5	52.5	1.39	74.2	1.45	25	26	1.52
10	52.9	1.18	73.6	1.37	22	23	1.12
20	51.2	1.22	70.8	1.38	23	24	0.52

[a] *Conditions: 7.5 g of MMA polymerised at 65 °C and 241 bar for 24 hrs, initiator:RAFT ratio 0.5:1, then 2.5 g of 4VP added for a further 24 hrs.* [b] *Obtained from GPC, eluting in a chloroform/ethanol/TEA mixture, measured with dRI detector calibrated against PMMA narrow standards.* [c] *Obtained from ^1H NMR integrations.* [d] *Measured from SEM images.*

GPC analysis showed a narrow molecular weight distribution for all PMMA and block copolymer samples (Đ < 1.5), demonstrating good control of the radical polymerisation. Chain extension of the PMMA macro-RAFT agents with the 4VP was evidenced by the shift in peak positions to lower retention time, indicating the successful growth of the polymer chains. The calculated $M_{n\,exp}$ values were in relatively good agreement with the target values and were consistent over all samples, regardless of stabiliser loading. $M_{n\,exp}$ values for the final PMMA-*b*-P4VP block copolymers were slightly higher than the target value of 67 kg mol^{-1}. This is attributed to an error in the GPC analysis, whereby block copolymer retention times are

directly compared to pure PMMA standards. The hydrodynamic volume, and hence retention time, is likely to be slightly larger than pure PMMA, due to swelling of the P4VP by the ethanol co-solvent. Thus, a minor error in the measurement it expected.

^{1}H NMR analysis was used to calculate the w_{P4VP} values for all block copolymers, using integrations of the distinct polymer peaks. By using this method instead of directly comparing the $M_{n\,exp}$ values, any error in the GPC calculations can be circumvented. Though, this method also carries errors as it assumes all P4VP is in the form of a block copolymer, with no formation of homopolymer. Though blocking efficiency is known to be high when utilising RAFT synthesis in scCO₂, it is never 100% efficient.[113] The w_{P4VP} values were found to be in the range of 22-26 wt%, in good agreement with the target composition of 25 wt% and predicted to self-assemble into the spherical-type morphology.[12] NMR spectra also showed each polymerisation ran to almost full conversion of monomer to polymer, with only minor monomer impurities seen (< 1%).

From the data, all the block copolymers were confirmed to be almost completely chemically identical. This proved that the concentration of stabiliser, and consequently the number of nucleated particles, could be altered without any effect on the RAFT polymerisation process or subsequent chain extension with the 4VP monomer.

The thermal properties of the block copolymer samples were assessed by DSC analysis (**Figure 3.7**). All samples produced two visible step transitions in the heat flow plot, relating to the T_g values of each constituent block. These observed T_g values were in good agreement with the literature values for the homopolymers (PMMA ~125 °C, P4VP ~150 °C).[114] Not only does this further confirm the correct chemical composition, but also suggests each sample has undergone self-assembly, phase separating into a nanoscale morphology. Homogeneous polymer blends have only one distinct thermal transition, at a value between the component polymer's transition temperatures.[115] The presence of individual T_g values signifies the polymer blocks remain physically separated within the sample, a good indication of self-assembly.
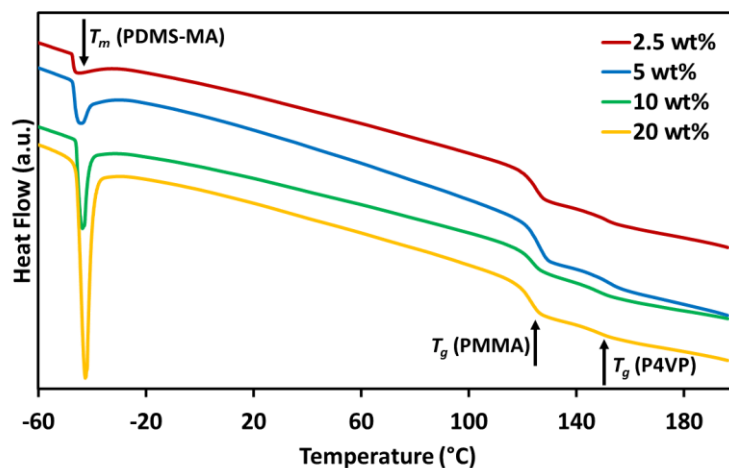
Figure 3.7: DSC heat flow plots for the PMMA-b-P4VP block copolymers synthesised with various quantities of PDMS-MA stabiliser.

The DSC analysis also revealed an endothermic peak at around -45 °C, relating to a melting point (T_m) in each sample. This was attributed to the T_m of the PDMS-MA stabiliser on the surface of the block copolymer particles.[116] The size of the PDMS-MA peak was also shown to increase in samples with higher loading of stabiliser, directly relating to the higher concentration of PDMS-MA in each sample.

The microscale morphology of the block copolymers was assessed by SEM analysis (**Figure 3.8**). Average particle sizes (d_n) were measured from SEM images using the method described in **Section 2.3.3** and the particle dispersity was reported as the coefficient of variation (CV) in the size measurements. All block copolymers were found to consist of well-defined microparticles, with the average size decreasing with increasing stabiliser concentration (**Table 3.1**).
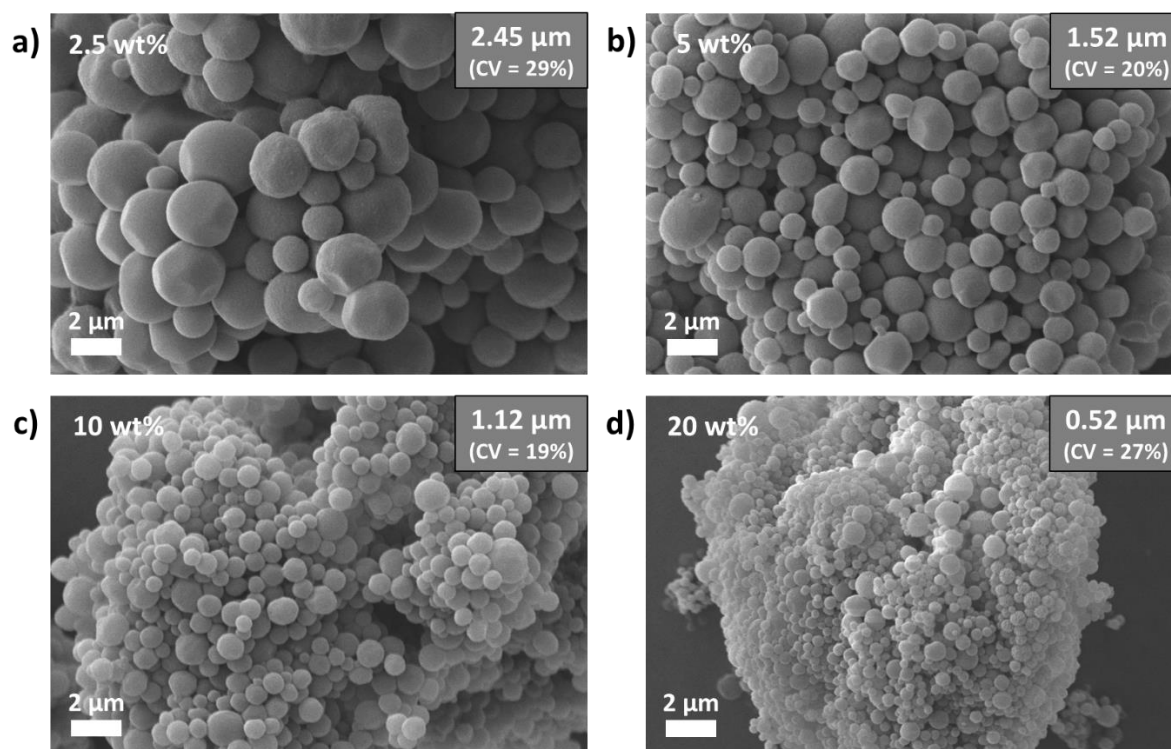
Figure 3.8: *SEM micrographs of the PMMA-b-P4VP block copolymers synthesised with (a) 2.5 wt%, (b) 5 wt%, (c) 10 wt% and (d) 20 wt% of PDMS-MA stabiliser.*

From this study it was clear that by altering the PDMS-MA concentration in the scCO₂ dispersion, the microparticle size could be controlled without any adverse effect on the controlled polymerisation reaction. A slight increase in particle size dispersity was seen towards the higher and lower end of the PDMS-MA concentrations used. This was not unexpected, as the particle nucleation process will become less uniform with too many or too few particles being formed. Hence, these stabiliser loadings represent a good range where particle formation is relatively well-controlled; beyond this range it is expected particle homogeneity will decrease dramatically.

Microparticle size was well-controlled between the approximate sizes of 0.5-2.5 μm. These values were directly compared to the previous study on free-radical polymerisation of PMMA (**Figure 3.9**).[48] This study focusing on block copolymer synthesis gave comparable sizes to the previous study. Overall, a slightly larger particle size dispersity was observed for the block copolymer particles. This is not surprising as the kinetics of the RAFT polymerisation likely delays and slightly disrupts the particle nucleation phase of the dispersion polymerisation.
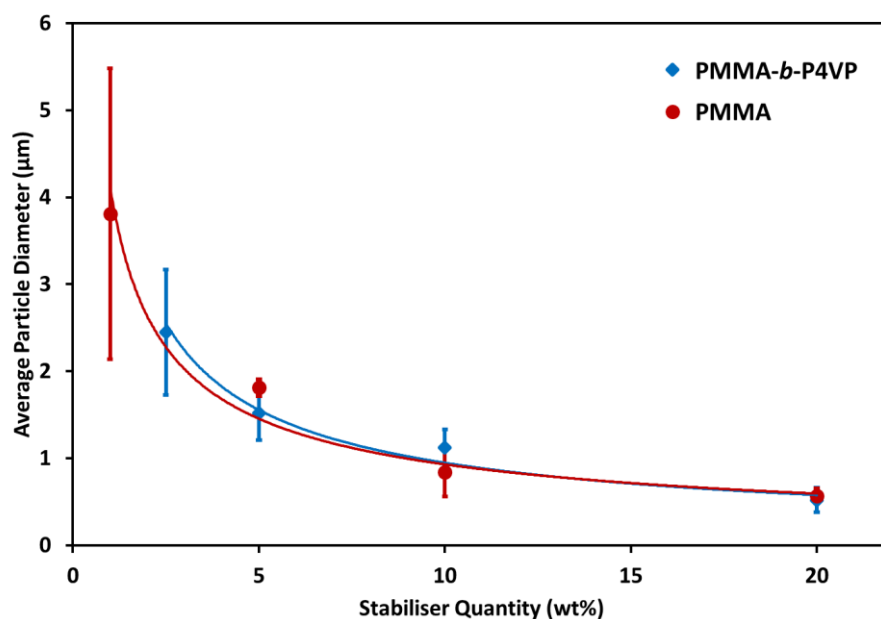
Figure 3.9: *Plot of the change in average particle size diameter with increased loading of PDMS-MA stabilisers for the PMMA-b-P4VP polymerisation (Blue) and the previous study of PMMA homopolymer synthesised by free-radical polymerisation (Red).[48] Trendlines are added to highlight the similarity in microparticle size change.*

Finally, the internal nanoscale morphology of the block copolymer particles was assessed by cross-sectional TEM (**Figure 3.10**). All block copolymer sections were stained with I_2 vapour prior to imaging. Staining was required to enhance the contrast in the images, as each unstained polymer block is fairly similar in terms of their electron contrast. I_2 vapour stains only the P4VP regions of the polymer through selective binding to the pyridinyl nitrogen group, increasing the elemental mass of these regions and making them appear darker in the TEM images.

The TEM images clearly show the presence of distinct dark circular regions within the microparticles, for all samples. This shows that all the synthesised block copolymers self-assembled into the spherical-type morphology, with P4VP spheres phase separated within a PMMA matrix. Analysis of the images also revealed that the size of the P4VP spherical domains remained roughly unchanged between samples (~22-26 nm). This confirms that the microscale dimensions of the block copolymer could be altered independently of the internal nanoscale features. In addition, the TEM analysis indicated that even at the smallest microparticle size (0.52 μm), no change in the self-assembled morphology was observed due to spatial confinements effects. This was to be expected due to the ~20-fold difference

between the microparticle confinement size and morphology feature size. Confinement effects are not likely to be observed until $D/L_0 < 5$.[42]
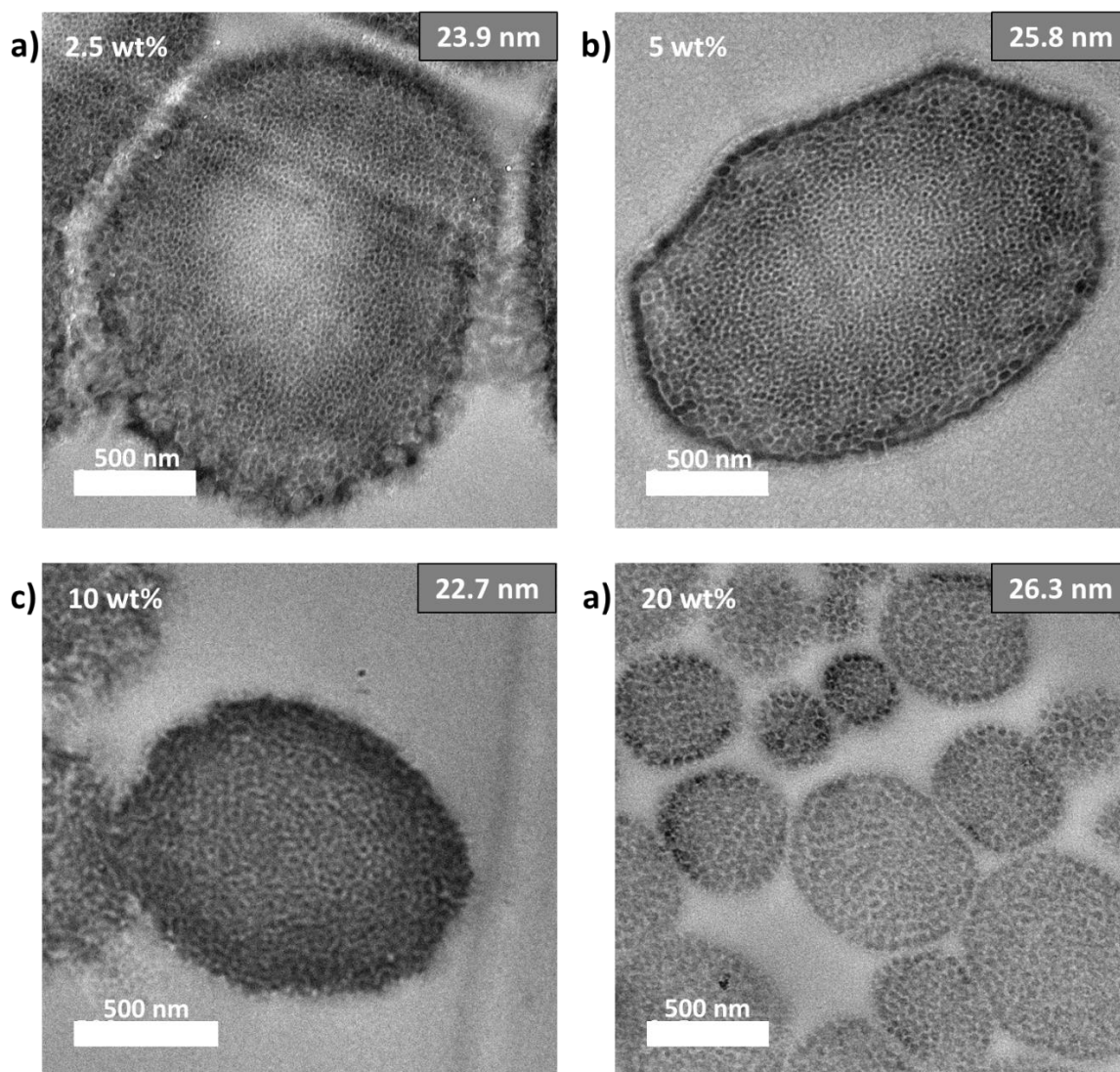
Figure 3.10: *TEM cross-sectional micrographs of the PMMA-b-P4VP block copolymers synthesised with (a) 2.5 wt%, (b) 5 wt%, (c) 10 wt% and (d) 20 wt% of PDMS-MA stabiliser. Samples were stained with I_2 vapour to improve contrast by darkening the P4VP domains. Average P4VP domain sizes are displayed on each micrograph.*

3.4.2. Nanoscale Size Changes

The next study attempted to alter the internal nanoscale dimensions of the block copolymer templates. The size of the spherical P4VP domains is dictated by the overall length of the polymer chains, and therefore the block copolymer molecular weight. The domain size of the self-assembled structures can be related to the molecular weight by the equation proposed by Helfand and Wasserman (**Equation 3.1**).[117] Where D is the average domain size, α is the

statistical monomer segment length, N is the total degree of polymerisation and χ is the Flory-Huggins interaction parameter between the two blocks.

$$D = \alpha N^{\frac{2}{3}} \chi^{\frac{1}{6}}$$ **Equation (3.1)**

The equation has several limitations and is treated in this study only as an approximation. The above relationship is derived by computational theory of monodisperse and symmetrical block copolymers, of which the block copolymers studied here are neither.[118] It is also noted in the literature that the calculated exponent value of N in the equation (i.e. 2/3) can vary between both theoretical and experimental studies.[1, 118-121] The calculation also does not hold true at low values of N, where χN < 10.5, or at extremely high values of N where kinetics limit the ability to self-assemble. Nevertheless, the relationship is a good guide to demonstrate how the domain sizes may be expected to change, even if the calculated values are not precise.

As the PMMA-*b*-P4VP block copolymers are synthesised through controlled radical polymerisation, their molecular weight can readily be altered. The polymer chains grow in a pseudo-living fashion, with all chains growing at roughly the same rate, the molecular weight can be changed by adjusting the number of propagating chains. In RAFT polymerisation this is achieved by simply adjusting the ratio of RAFT agent to monomer in the reaction (**Equation 3.2**).

$$N = \frac{[Monomer]}{[RAFT\ agent]}$$ **Equation (3.2)**

Here, the degree of polymerisation applies only to the first monomer polymerised, the MMA. The quantity of injected 4VP to grow on the end of the PMMA chains in the next step is kept constant. As the number of propagated PMMA chains is altered in the first step, the effective concentration of PMMA macro-RAFT agent is also changed for the subsequent polymerisation step. In this way, the molecular weight of the P4VP block is scaled to that of the PMMA block, with the w_{P4VP} value remaining constant throughout.

The quantity of the RAFT agent, DDMAT, was altered in the one-pot scCO₂ dispersion polymerisation, described in **Section 3.3.2**. All other reagent quantities were kept constant, aside from the initiator, which was always kept at a ratio of 0.5:1 initiator to RAFT agent. RAFT

agent quantity was altered to aim for $M_{n\,target}$ values for the PMMA block between 25 and 400 kg mol^{-1} (**Table 3.2**). The expected P4VP domain sizes were calculated using **Equation 3.1**, applying values of α = 0.7 nm and $\chi_{PMMA/P4VP}$ = 0.08 acquired from the literature.[122, 123] The value of α was kept constant for both MMA and 4VP monomers due to their comparable molecular weights.

Table 3.2: *Summary of target PMMA-b-P4VP molecular weights and the resulting domain sizes of the P4VP.*

RAFT agent quantity (mg) [a]	PMMA $M_{n\,target}$ (kg mol^{-1})	P4VP $M_{n\,target}$ (kg mol^{-1})	N_{total}	D_{P4VP} (nm) [b]
109.4	25	8.4	330	**21.9**
54.7	50	16.7	658	**34.8**
27.3	100	33.4	1316	**55.2**
13.7	200	66.8	2633	**87.6**
6.8	400	133.6	5266	**139.1**

[a] RAFT agent quantities relate to polymerisation of 7.5 g of MMA and 2.5 g of 4VP. [b] Calculated from Equation 3.1 using α = 0.7 nm and $\chi_{PMMA/P4VP}$ = 0.08.

The actual molecular weight, $M_{n\,exp}$, of the block copolymer products and their PMMA macro-RAFT counterparts was assessed by GPC analysis (**Figure 3.11**). A high monomer conversion (> 98%) was confirmed in all case by ^{1}H NMR. Recorded spectra in all cases were near identical to that shown in (**Figure 3.6**). NMR peak integrations were also used to calculate the values of w_{P4VP}, using the method described in **Section 2.3.2** of this thesis. All calculated composition values are summarised below (**Table 3.3**).

The GPC traces for the PMMA-*b*-P4VP block copolymers showed a clear shift towards lower retention time, and hence higher molecular weight, when a lower RAFT agent quantity was used. This was reflected in the calculated $M_{n\,exp}$ values, though many of the results deviate heavily from the expected $M_{n\,target}$ values. The divergence between measured and expected molecular weights became more prominent as higher degrees of polymerisation were targeted. This was a foreseen consequence, as the total concentration of RAFT agent in the reaction becomes low, so too does the total number of living chains to adequately control the radical polymerisation process. As a result, some monomer undoubtedly polymerised by the

uncontrolled free-radical mechanism, forming some undesirable low molecular weight impurities and reducing the overall $M_{n\ exp}$ of the product. This loss of control is also reflected by the increase in $Đ$ as RAFT agent quantity decreases. This is not too surprising, as the controlled synthesis of ultrahigh molecular weight polymers using RAFT is rarely reported and only under very specific reaction conditions, based on the kinetic parameters of the monomers involved.[124]

Table 3.3: *Summary of characterisation data for the PMMA-b-P4VP block copolymer samples synthesised with various quantities of RAFT agent.* [a]

RAFT agent quantity (mg)	$M_{n\ target}$ per block (kg mol⁻¹)	PMMA		PMMA-*b*-P4VP		w_{P4VP} [c]	d_n (µm) [d]
		$M_{n\ exp}$ [b] (kg mol⁻¹)	$Đ$ [b]	$M_{n\ exp}$ [b] (kg mol⁻¹)	$Đ$ [b]		
109.4	25 - 8	29.8	1.26	40.9	1.55	23	1.53
54.7	50 - 17	52.5	1.39	74.2	1.45	25	1.52
27.3	100 - 33	76.4	1.33	94.7	1.56	25	1.66
13.7	200 - 67	140.6	1.52	185.4	1.77	26	1.89
6.8	400 - 134	220.2	1.52	269.9	1.98	23	2.04

[a] *Conditions: 7.5 g of MMA polymerised at 65 °C and 241 bar for 24 hrs, initiator:RAFT ratio 0.5:1, then 2.5 g of 4VP added for a further 24 hrs.* [b] *Obtained from GPC, eluting in a chloroform/ethanol/TEA mixture, measured with dRI detector calibrated against PMMA narrow standards.* [c] *Obtained from ¹H NMR integrations.* [d] *Measured from SEM images.*

The $M_{n\ exp}$ value of the block copolymer synthesised using the largest quantity of RAFT agent was slightly higher than the $M_{n\ target}$. Upon collecting this powdered product, a small quantity of bright yellow material was found towards the bottom of the autoclave. This impurity was found to contain a high quantity of unreacted RAFT agent. This explained the unexpectedly high molecular weight of the product, as not all the DDMAT RAFT agent formed living polymer chains in the reaction. From previous studies it is known that DDMAT only has a limited solubility in the scCO₂ solvent, giving it good control in the heterogeneous process because of its preference to reside only in the polymer phase of the dispersion.[18] It is clear that by increasing the DDMAT concentration in the scCO₂ to such a large value, the solubility limit was exceeded. To target lower molecular weight block copolymers, a more soluble RAFT agent must be selected or the monomer concentration in the solvent must be decreased.
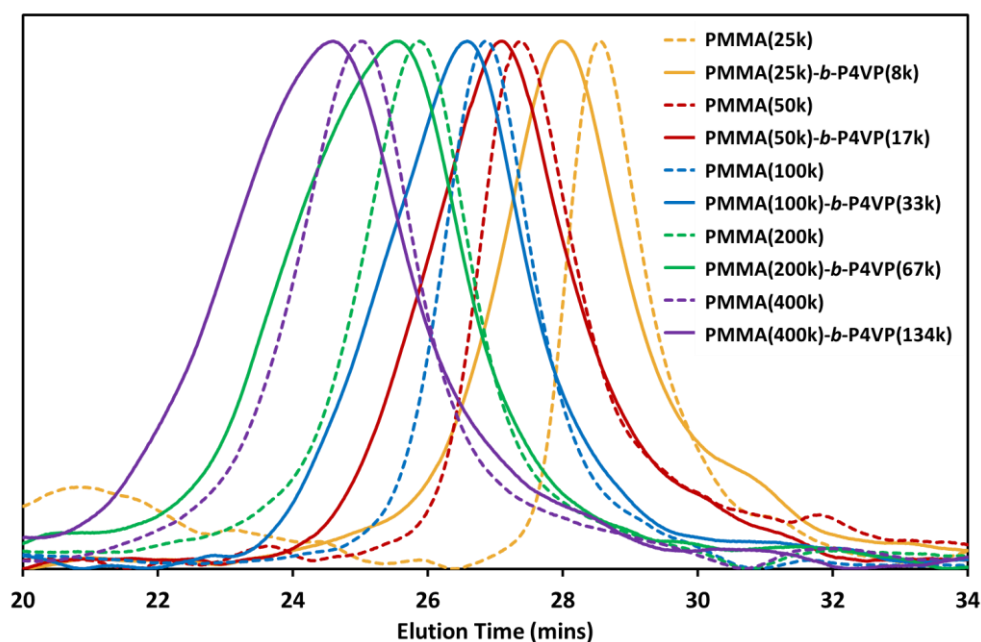
Figure 3.11: *GPC chromatograms for the PMMA macro-RAFT agents synthesised with various quantities of RAFT agent (dotted lines) and their resulting block copolymers (solid lines).*

Despite the loss of control in the desired molecular weights, the GPC analysis clearly showed the formation of block copolymers in all cases. This was evident by the visible peak shift of the PMMA macro-RAFT agents to lower elution times upon addition of the 4VP monomer, indicating successful extension of the polymer chains. Albeit, with a large degree of dispersity in the case of the higher molecular weight products. Overall, by altering the concentration of RAFT agent in the dispersion polymerisation, several block copolymers of various chain lengths were successfully synthesised. For greater clarity, the number average molecular weight distributions for the PMMA-*b*-P4VP products are also plotted separately (**Figure 3.12**).
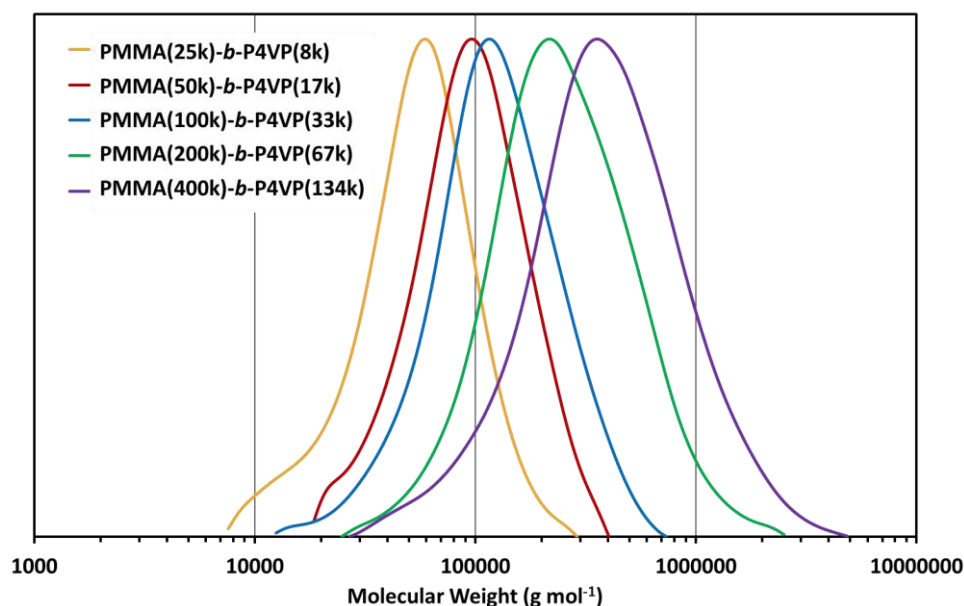
Figure 3.12: *Molecular weight distributions for the PMMA-b-P4VP products, calculated via GPC.*

The microscale morphology of the block copolymer products was evaluated through SEM analysis (**Figure 3.13**). SEM images were used to measure the particle d_n values and their relative size dispersities, using the method described in **Section 2.3.3**. All values are reported as insets on the relevant images and are also tabulated above (**Table 3.1**).

SEM images confirmed the formation of reasonable well-defined microparticles in all cases. However, the two highest molecular weight block copolymers did present a number of microparticles with unusual surface textures. These particles appeared to be agglomerations of smaller nano-sized spheres, rather than displaying the usual smooth surface topography of the other microparticles. This may be caused by larger P4VP domains protruding through the particles' surfaces. The fact that this was only observed in a fraction of the imaged particles could imply that only small portion of high molecular weight PMMA-*b*-P4VP was formed during these polymerisations.
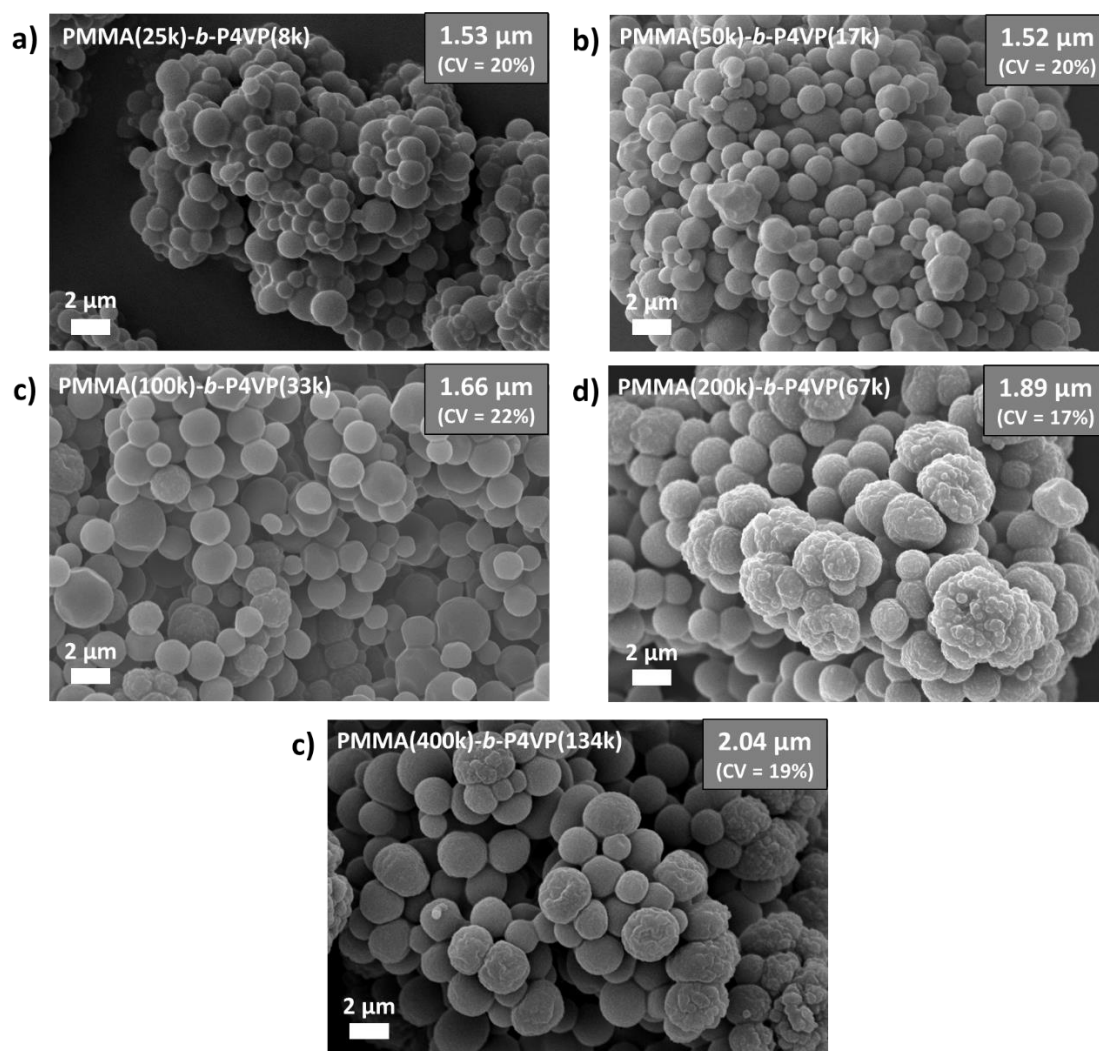
Figure 3.13: *SEM micrographs of the various molecular weight PMMA-b-P4VP block copolymers.*
Target molecular weights are shown on the relevant micrographs.

Average microparticle size was also shown to increase slightly with increasing targeted molecular weight. This may be due to a slower rate of polymerisation as lower quantities of RAFT agent, and more importantly initiator, were used. The slower reaction kinetics may lead to the nucleation of fewer particles during the early stages of the reaction, hence causing them to grow disproportionally in size in the later propagation stage of the polymerisation.

The internal nanoscale morphology of the block copolymers was assessed by TEM imaging of particle cross-sections (**Figure 3.14**). As in the previous study, sections were stained with I_2 vapour prior to imaging to increase the electron contrast in the P4VP domains. The P4VP domains were measured, with the average domain length (D_{P4VP}) reported as inserts on the TEM images. Measured D_{P4VP} values are also tabulated below (**Table 3.4**) along with expected values calculated using **Equation 3.1**. Expected D_{P4VP} values were obtained using the

measured block copolymer molecular weights, calculated using the PMMA $M_{n\,exp}$ values from GPC and the w_{P4VP} fractions measured from ^{1}H NMR.

TEM images showed all molecular weight PMMA-*b*-P4VP samples has successfully self-assembled into the spherical-type block copolymer morphology, as expected due to the comparable w_{P4VP} values. Size analysis of these spherical P4VP domains shows an increase in measured D_{P4VP} size. However, this increase in size is very small between each sample, with reported sizes diverging greatly from the expected values that were calculated (**Table 3.4**). It was determined that the recorded increase in D_{P4VP} was too minor to be statistically significant, with most differences in size barely larger than the margin for error in the measurements.

The TEM images also revealed minor inconsistences in the P4VP morphology in the largest two molecular weight samples. This is reflected in the larger CV values for these size measurements. In these samples, some microparticles were found to consist of larger P4VP domains only at the outer edges of the particles, similar to the effect seen in the matching SEM images. This was likely a reflection of the more uncontrolled nature of these two polymerisations (Đ > 1.7). Polymer chains towards to outside of the particles may have grown to larger molecular weights than the polymer chains at the centre of the particles. This would lead to the large distribution in domain sizes depending on their position in the microparticles. The relatively small D_{P4VP} values recorded for these samples is a direct result of this large size distribution. Only a small fraction of the larger P4VP domains were seen around the edges of the microparticles, so their significance is diminished when taking the mean average of all the measured domains.
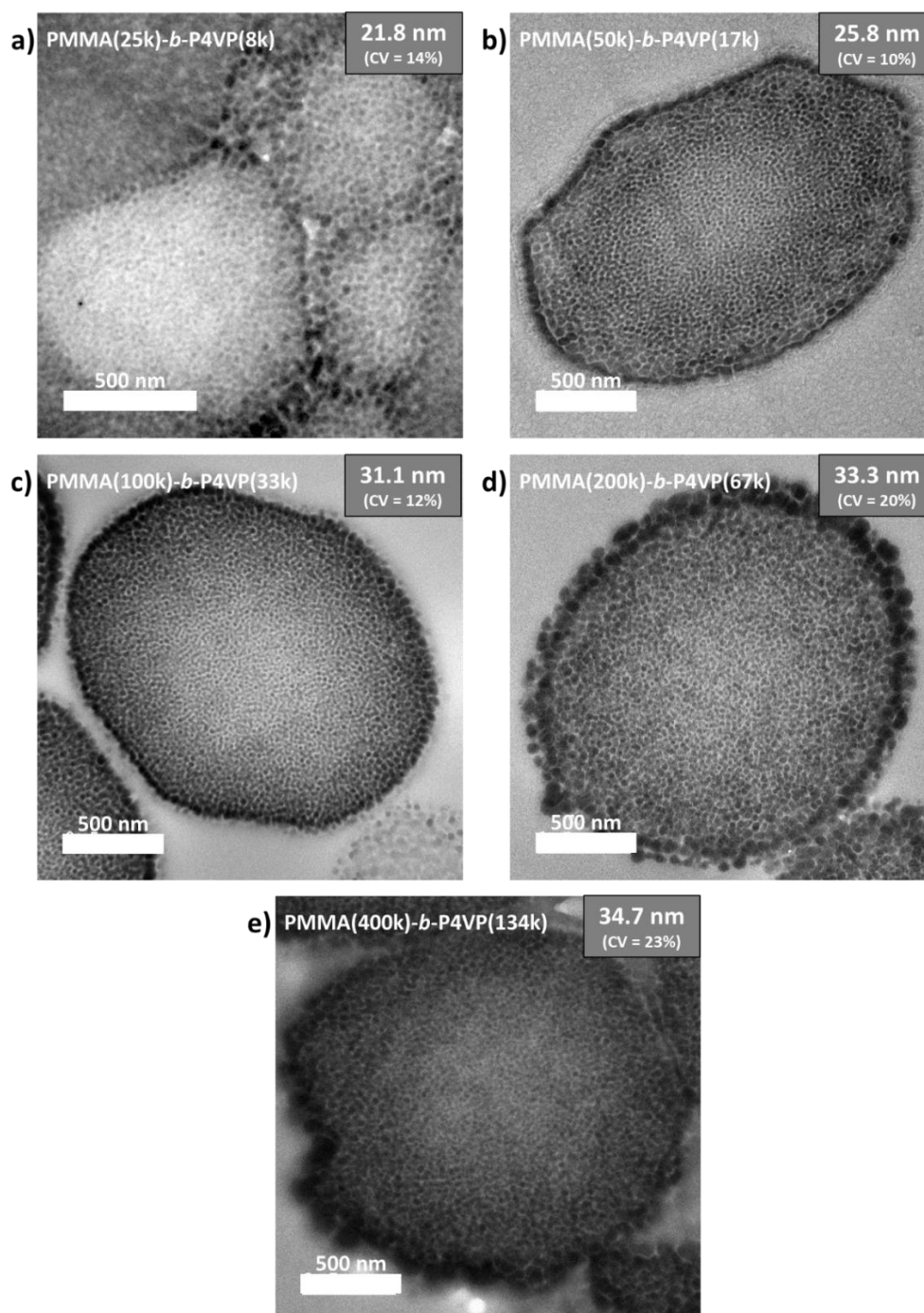
Figure 3.14: *Cross-sectional TEM micrographs of various molecular weight PMMA-b-P4VP microparticles. Target molecular weights, average P4VP domain sizes and size dispersities (CV values) are displayed on each micrograph. Samples were stained with I₂ vapour to improve contrast.*

From these images it can be reasoned that increasing the molecular weight can indeed increase D_{P4VP}. However, the main issue here is inconsistency in the polymerisations, particularly when high molecular weights are targeted. The highest molecular weight block copolymers were not adequately controlled by the heterogeneous RAFT method, leading to

an uneven distribution of P4VP domains sizes. A reasonable degree of uniformity will be required in the nanoscale structure of the PMMA-*b*-P4VP polymers for them to be suitable for use as structure-directing agents in nanofabrication.

Table 3.4: *Summary of the expected and measured dimensions for the internal nanoscale P4VP domains with the block copolymers of varying molecular weight.*

$M_{n\ target}$ (kg mol^{-1})	$M_{n\ exp}$ (kg mol^{-1}) [a]	N_{total}	Calculated D_{P4VP} (nm) [b]	Measured D_{P4VP} (nm) [c]
33.4	38.7	382	**24.2**	**21.8**
66.7	69.7	688	**35.8**	**25.8**
133.4	101.7	1004	**46.1**	**31.1**
266.8	189.3	1867	**69.7**	**33.3**
533.6	286.1	2826	**91.8**	**34.7**

[a] *Extrapolated from PMMA $M_{n\ exp}$ values from GPC, applying the w_{P4VP} values from ${}^1H$ NMR.* [b] *Calculated from Equation 3.1 using $\alpha = 0.7$ nm and $\chi_{PMMA/P4VP} = 0.08$.* [c] *Measured from TEM images.*

Accurate measurement of D_{P4VP} via TEM analysis proved problematic. This was mainly due to the very small sample size being analysed and the large distribution of domain sizes in some of the materials. Inaccuracies in taking the measurements from the images was also a major concern. It was noted that small deviations in the sample height on the TEM stage will have caused the recorded scale bars in the images to be slightly incorrect. Small changes in sample height could not be ruled out and was an entirely foreseeable consequence if ultramicrotome cut sections were not cut with complete precision for every sample.

To provide a more exact and reliable quantitative analysis of the D_{P4VP} values in the PMMA-*b*-P4VP block copolymers, SAXS analysis was performed (**Figure 3.15**). SAXS patterns were obtained from the powdered samples following the procedure described in **Section 2.3.5**.
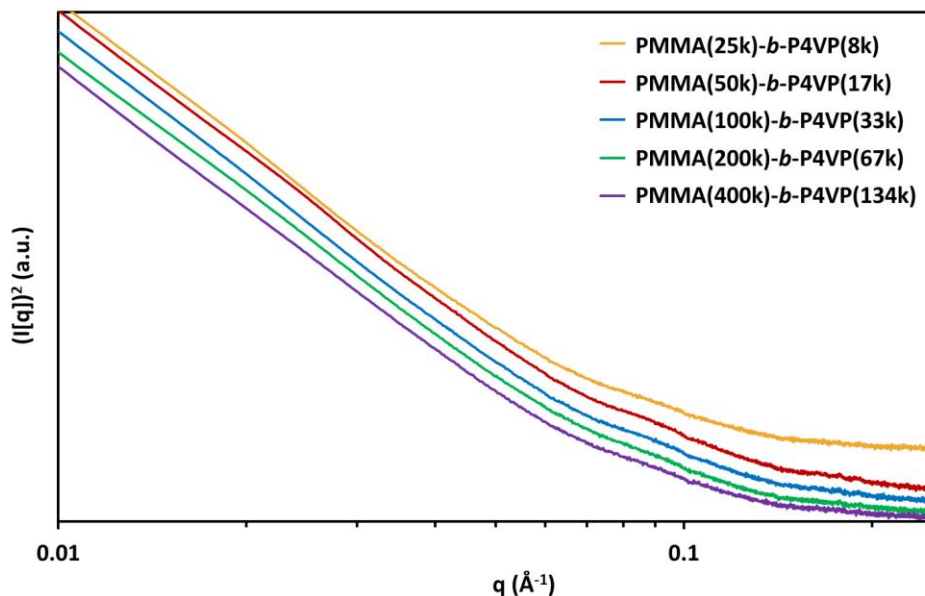
Figure 3.15: *1D SAXS data for the PMMA-b-P4VP block copolymers with various targeted molecular weights. Data is plotted against the square of the scattering intensity, I(q), to enhance features at low q. The y-axis is plotted on a logarithmic scale and sample data are staggered on the y-axis for greater clarity.*

Unfortunately, the SAXS patterns for all PMMA-*b*-P4VP polymers showed no significant scattering peaks. The data appear to exhibit the structure factor of polydisperse spheres at the length scale of block copolymer nanostructures, but still requires more rigorous fitting. This could usually indicate that self-assembly had not occurred to a significant extent through the bulk quantity of all samples. However, this was unlikely given that no microparticles without internal structure was found in any of the TEM images. Instead, the lack of distinct scattering features may have been a result of poor resolution, caused by weak scattering contrast between the PMMA and P4VP blocks.[125]

Due to the lack of discernible features in the SAXS analysis, D_{P4VP} values were measure solely from the TEM images of the PMMA-*b*-P4VP. Though this does provide evidence that the size of the nanoscale features can be altered to a small degree, inaccuracies in the measurements undermine the possible extent of the size changes. Also, the loss of control exhibited in some of the polymerisations means precise control over the desired size of D_{P4VP} could not be achieved. To summarise this study, the expected and measured values of D_{P4VP} are plotted below (**Figure 3.16**), illustrating the limited control of the nanoscale size features in these hierarchical materials.
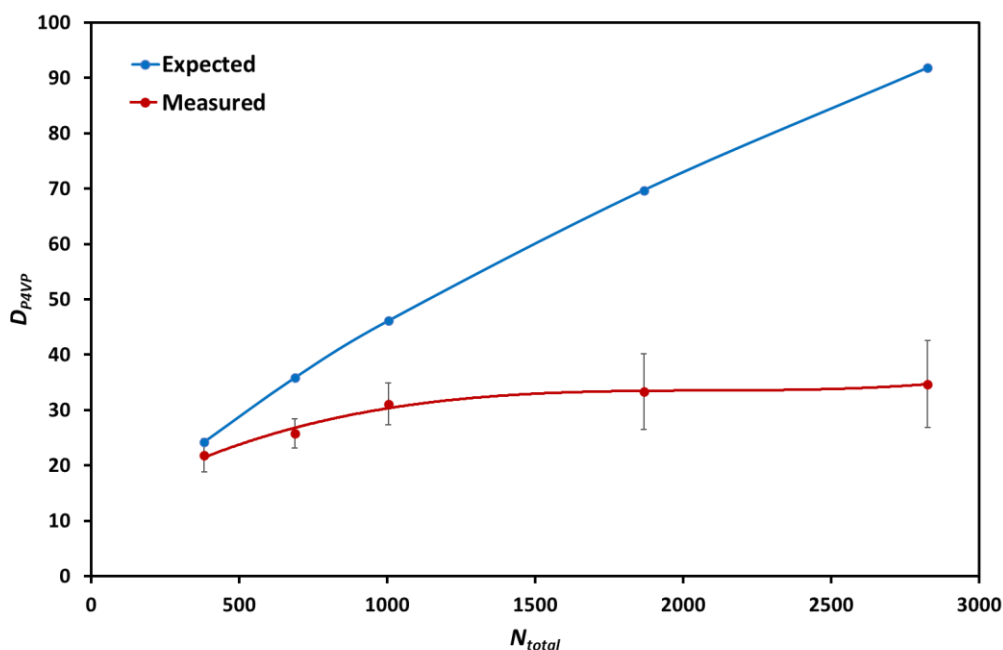
Figure 3.16: *Plot of the expected (Blue) and measured (Red) internal nanoscale sizes of the spherical P4VP morphology with increasing molecular weight of the overall block copolymer.*

3.4.3. Synthesis of LiFePO₄-Polymer Composites

In the next stage of this work, the PMMA-*b*-P4VP block copolymers were used as directing agents in the sol-gel synthesis of LiFePO₄. Only the series of block copolymers with varying microparticle dimension were used in this study, as the synthesis of these polymers appeared more successful, covering a wide range of particle sizes to investigate.

The LiFePO₄-polymer composites were synthesised using the method described in **Section 3.3.3**. An ethanol sol containing Li^+, Fe^{2+} and PO_4^{3+} was prepared before adding a slurry of the desired PMMA-*b*-P4VP microparticles. A target inorganic mass fraction of 25 wt% was targeted for the final composite materials. This matched previously successful studies sol-gel templating TiO_2 with a block copolymer of identical composition.[112] Though not the same, this has informed the conditions of these LiFePO₄ sol-gel reactions. For a 10 mL sol-gel reaction, 50 mg of PMMA-*b*-P4VP template was used, equating to a total volume of 11.3 µL P4VP, assuming an ideal weight fraction of 25% in the copolymer. Inorganic precursors were added to synthesise a volume of 4.7 µL LiFePO₄ (density = 3.6 g cm⁻³). Though this is considerably less than the total P4VP volume, the material is likely to be of lower density than bulk LiFePO₄. Another factor to consider is the increase in volume of the P4VP component upon addition of the compatible ethanol solvent. However, this is difficult to accurately predict given that the

P4VP is integrated into insoluble PMMA microparticles which will restrict the movement of ethanol to the soluble P4VP. Therefore, only a moderate increase in the P4VP volume is expected. This small increase may be significant enough to shift the preferred morphology from spheres to a more interconnected morphology such as cylinders or gyroidal. Further investigation would be needed to fully confirm this transition.

The mixture was stirred to allow the inorganic components to infuse into the P4VP domains of the microparticles before removing the ethanol solvent by evaporation. Ethanol was chosen as the solvent to preferentially swell the P4VP regions of the block copolymers, allowing infiltration of the inorganic components into the polymer without complete solvation of the hierarchically structured scaffold. The resulting yellow composite powders were first analysed using SEM (**Figure 3.17**) to confirm the microparticle structure of the original polymers was maintained during the sol-gel synthesis.
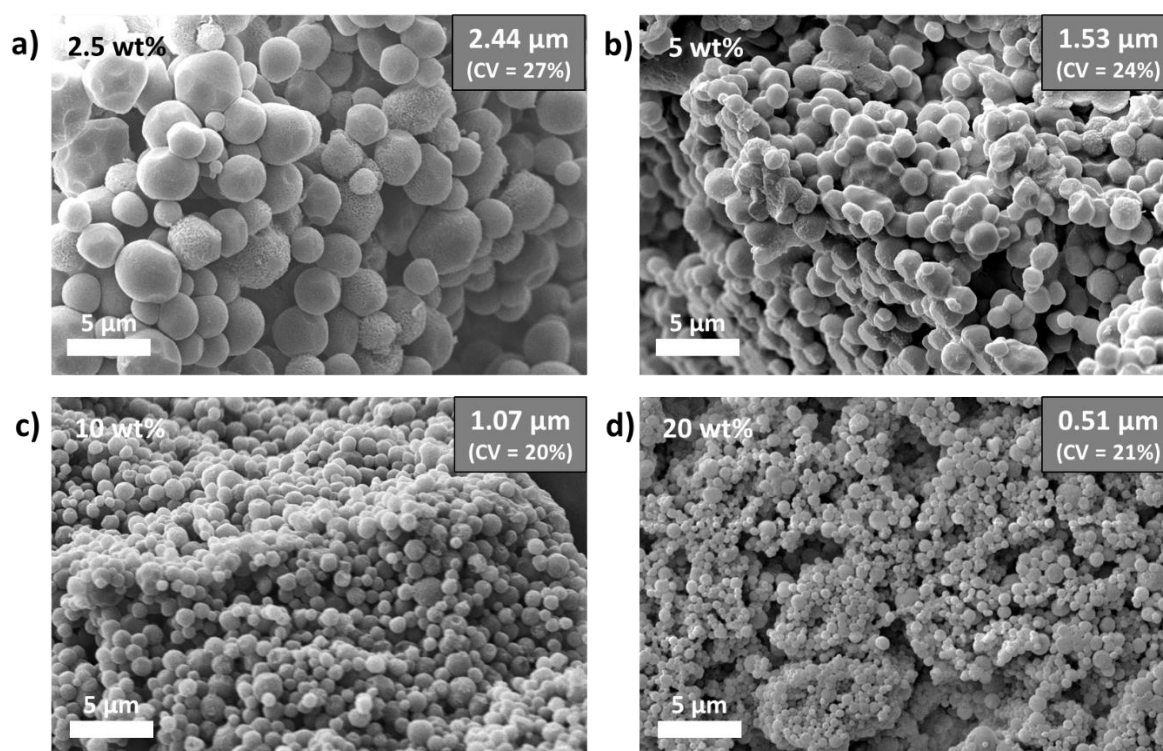
Figure 3.17: *SEM micrographs of LiFePO$_4$-polymer composites, templated using PMMA-b-P4VP block copolymers synthesised with (a) 2.5 wt%, (b) 5 wt%, (c) 10 wt% and 20 wt% PDMS-MA stabiliser.*

The microscale structure of the LiFePO$_4$-polymer composites was relatively comparable to the original microstructure of their respective polymer templates (**Figure 3.8**). All samples consisted of well-defined microparticles with d_n values almost identical to those of the original

block copolymers. This indicates that the inorganic material was fully incorporated into the polymer microparticles during the sol-gel process, with no obvious formation of untemplated aggregates.

To confirm that the inorganic component of the composites was distributed solely in the P4VP domains of the block copolymers, the particles were examined using cross-sectional TEM (**Figure 3.18**). Composite samples were prepared in the same manner as the previous polymer samples, by embedding particles in resin and cutting ultra-thin sections (<100 nm). However, the key difference in the preparation of these samples was the omission of the I_2 staining agent. Instead, contrast in the images was formed primarily by the higher atomic weighted inorganic material.

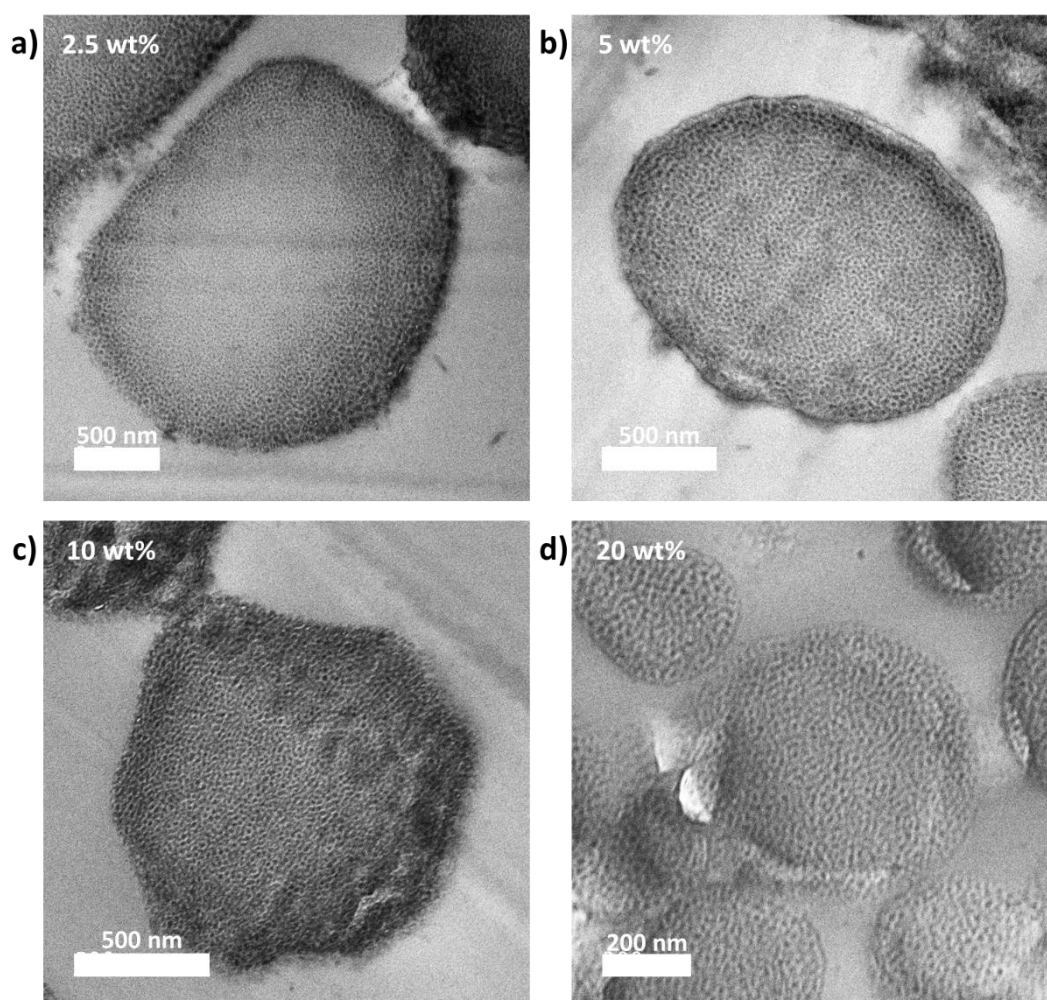***Figure 3.18:*** *Cross-sectional TEM micrographs of the LiFePO₄-polymer composites, templated using PMMA-b-P4VP block copolymers synthesised with (a) 2.5 wt%, (b) 5 wt%, (c) 10 wt% and 20 wt% PDMS-MA stabiliser. No staining agents were applied.*

The internal morphologies of the LiFePO$_4$-polymer composites were shown to consist of small dark spherical regions within the lighter matrix of the microparticles. This was analogous to the spherical-type block copolymer morphology seen for all the original PMMA-*b*-P4VP materials. As no staining agents were used to enhance the contrast between the polymer blocks in these images, it could be assumed that the inorganic component of the composites resided only within the spherical P4VP regions of the polymer templates. This confirms that the mechanism of structure direction is indeed preferential association of the inorganic sol to the P4VP domains of the block copolymer.

To corroborate the mechanism of structure direction in the sol-gel process, FTIR spectroscopy was performed on both the original block copolymer and the LiFePO$_4$-polymer composite (**Figure 3.19**). Absorption of radiation in the infrared region can be used to infer information about the functional groups and bonding in the polymer structure. Comparing this before and after the sol-gel synthesis yields information about any changes in bonding when the inorganic components are added.
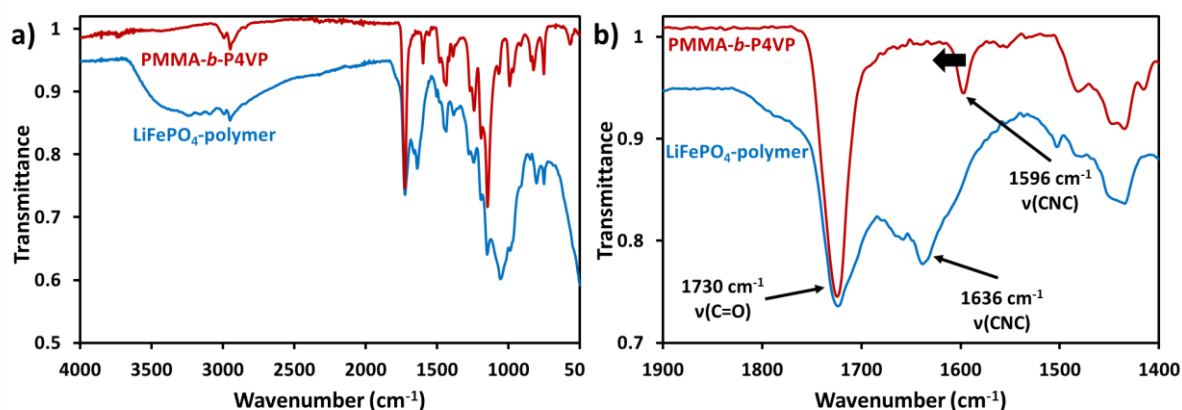
Figure 3.19: *FTIR spectra for the PMMA-b-P4VP block copolymer (red) and the resulting LiFePO₄-polymer composite (blue), with relevant absorption peaks labelled.*

The FTIR spectrum for the original PMMA-*b*-P4VP block copolymer shows two key peaks to identify each polymer block. An absorbance at 1730 cm^{-1} for the v(C=O) carbonyl stretch of the PMMA and a lower intensity absorbance at 1596 cm^{-1} for the v(CNC) stretch of the aromatic pyridine ring of the P4VP.[126, 127] In the FTIR spectrum for the LiFePO$_4$ composite material, a broad band appeared in the region of ~2500-3500 cm^{-1}. This was attributed to the v(OH) stretch of residual ethanol in the composite. While the majority of the remaining peaks

aligned with those for the PMMA-*b*-P4VP, the v(CNC) stretching band was shown to shift to slightly higher wavenumber (1636 cm^{-1}).

The observed shift of the pyridine band to higher wavenumber is indicative of bonding interaction of the nitrogen lone pair to a Lewis acid site. Studies have shown interaction of pyridine rings to these sites causes a shift in electron density, leading to strengthening of the CNC bonds and therefore a higher energy v(CNC) absorbance.[128] This is likely due to association of the P4VP with the Fe^{2+} ions in the sol, leading to accumulation of inorganic components in only the P4VP regions of the polymer structure. However, it cannot be ruled out that the v(CNC) band shift may also be caused by protonation of the pyridine rings during the sol-gel reaction.[129]

3.4.4. Formation of LiFePO₄/C

To obtaine pure crystalline materials capable of being utilised as rechargeable battery cathodes, the polymeric portion of the LiFePO₄-polymer composites had to be removed. The inorganic portion of the composite also required thermal annealing to fully crystalise the desired olivine-type LiFePO₄ structure. Both these steps were achieved simultaneously by calcining the composite materials under an argon atmosphere to prevent both unwanted oxidation and the formation of lithium nitride. Anaerobic degradation of the polymer template also leaves carbon residues within the battery cathode material, which is particularly advantageous for low electrically conducting materials such as LiFePO₄. The samples were calcined at 700 °C for two hours, matching previous reported syntheses of LiFePO₄.[130, 131] Though, it is known that the polymer can be fully degraded at temperatures as low as 500 °C.[112] The effect of calcination on the LiFePO₄-polymer composites was studied using TGA analysis (**Figure 3.20**).
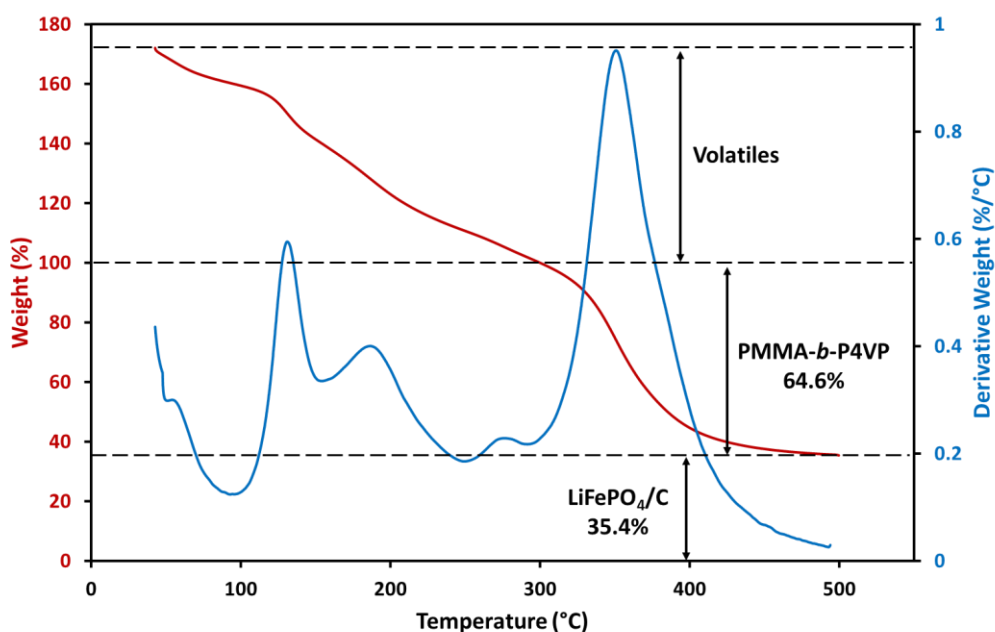
Figure 3.20: *TGA profile for the calcination of LiFePO₄-polymer composite under an argon atmosphere. Weight is scaled to account for the loss of volatiles before degradation of the polymer. Only data for the composite with d_n = 1.53 μm is shown.*

In the TGA analysis, the derivative of weight loss was also plotted in blue alongside the weight loss curve, to clearly indicate the points at which weight losses occurred. Some weight loss in the sample occurred at low temperature, which was attributed to the removal of volatile and residual compounds from the sol-gel synthesis, as these temperatures were too low to degrade the block copolymer. The sample weight was then scaled to equal 100% at ~300 °C, before the onset of the polymer degradation peak. Weight loss of the polymer was shown to plateau close to 500 °C, leaving the remaining components equating to around 35 wt% of the original LiFePO₄-polymer composite sample.

The LiFePO₄ portion of the composite was expected to represent ~25 wt% of the composite. However, due to calcination in an argon atmosphere, the block copolymer was not fully combusted or completely removed from the composite. Instead, the polymer degraded to form a carbon residue distributed throughout the LiFePO₄ material, confirmed by the uniform deep black colour of the calcined LiFePO₄/C. Carbon coating is often applied post-synthesis to LiFePO₄ to increase electrical conductivity of the battery material, so formation of this carbon layer *in-situ* is considered to be advantageous for this particular application.[132] Providing the

target value of 25 wt% inorganic content in the composite was achieved, the TGA analysis indicates that the final LiFePO$_4$/C materials consisted of approximately 29 wt% carbon.

To confirm that LiFePO$_4$ was successfully formed during the calcination process, powder XRD analysis was performed on the resulting black powders (**Figure 3.21**). The diffraction patterns of the LiFePO$_4$-polymer composite and the final calcined LiFePO$_4$/C materials were compared to the known diffraction pattern of the LiFePO$_4$ mineral, triphylite. This olivine-type crystal structure is the typical polymorph for crystalline LiFePO$_4$ formed under ambient pressure.[133]

The original LiFePO$_4$-polymer composite was shown to be highly amorphous with very broad X-ray scattering seen and no discernible diffraction peaks. This is to be expected as the composite consists mostly of amorphous polymeric material, with the remainder being pre-annealed inorganic components. After heating at 700 °C for two hours, the broad scattering was replaced by definitive diffraction peaks that coincide with those expected for LiFePO$_4$, with no other visible peaks. Therefore, the XRD analysis demonstrates that calcination under these conditions yields both a highly crystalline and highly pure LiFePO$_4$ material. Purity of all the final LiFePO$_4$/C materials was investigated with further XRD analysis (**Figure 3.22**).
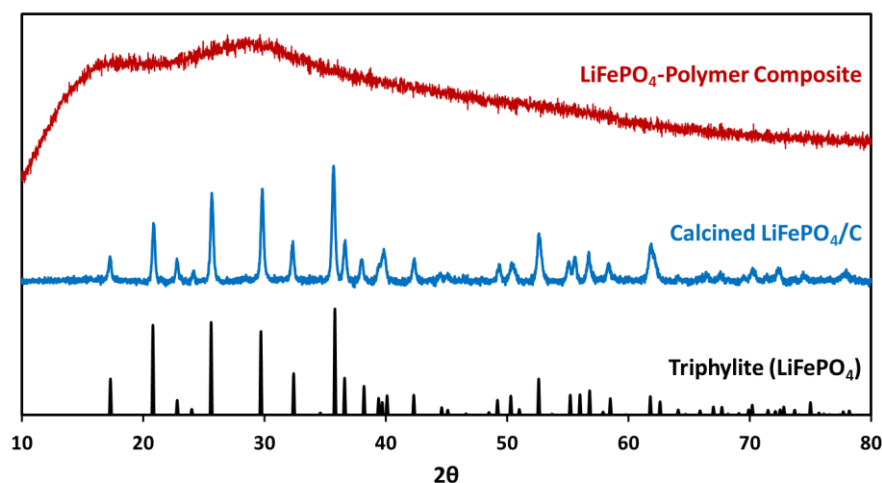
Figure 3.21: Powder XRD diffractograms of the LiFePO$_4$-polymer composite (red) with d_n = 1.53 μm and resulting calcined LiFePO$_4$/C material. Triphylite reference pattern is also shown at the bottom of the plot.[112]
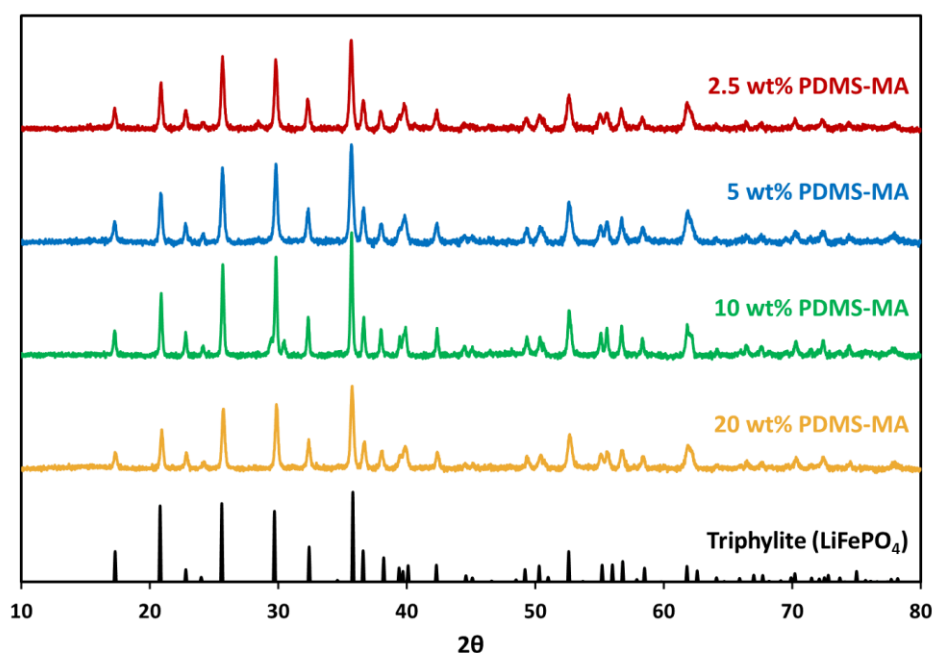
Figure 3.22: *Powder XRD diffractograms of all calcined LiFePO₄/C materials, templated using PMMA-b-P4VP block copolymers synthesised with various quantities of PDMS-MA stabiliser. Triphylite reference pattern is also shown at the bottom of the plot.*

All calcined LiFePO₄/C materials were shown to consist of crystalline LiFePO₄, with matching diffraction peaks seen throughout all the materials. No additional diffraction peaks were noticeable, except in the case of the 10 wt% material (composite d_n = 1.07 µm), where small impurity peaks were noticed at 2θ ≈ 30°. These peaks likely correspond to trace amounts of iron oxide impurity, possibly in the form of magnetite (Fe_3O_4).[134] It is unclear why this impurity formed for only this particular sized LiFePO₄/C material. Due to the low intensity of the diffraction peaks, the impurity was only expected to contribute a small fraction of the cathode material.

With the purity of the LiFePO₄/C materials confirmed, the next step was to assess the morphology of the cathode materials. The microstructure of the metal oxides was assessed by SEM analysis (**Figure 3.23**).
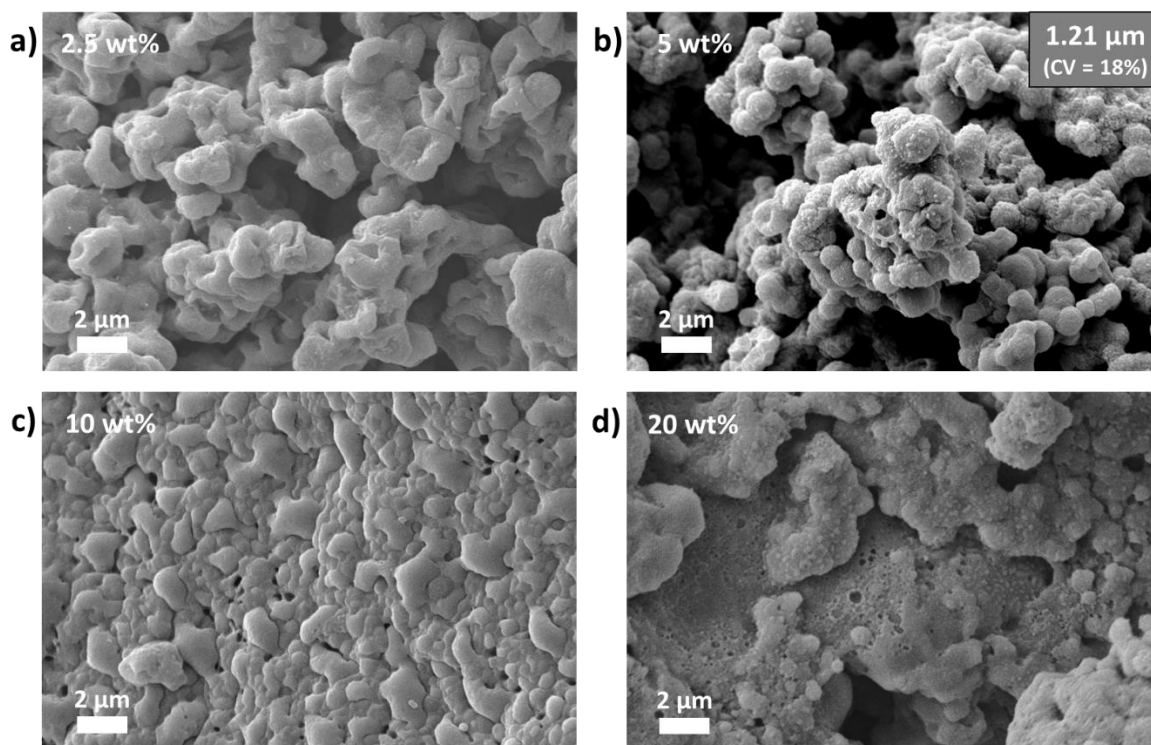
Figure 3.23: *SEM micrographs of the calcined LiFePO₄/C materials, templated using PMMA-b-P4VP block copolymers synthesised with (a) 2.5 wt%, (b) 5 wt%, (c) 10 wt% and 20 wt% PDMS-MA stabiliser.*

From the SEM images it was clear that the morphology of the LiFePO₄-polymer composites changed considerably during the calcination process. The final LiFePO₄/C materials possessed various microstructures depending on the size of the original PMMA-*b*-P4VP microparticle templates. The LiFePO₄/C synthesised using the block copolymer with 5 wt% PDMS-MA was the only sample shown to retain reasonably well-defined microparticle structure, with d_n = 1.21 µm, and a limited amount of aggregated material. The decrease in d_n in the final metal oxide was expected due to contraction of the particles as the polymer template was removed during calcination. It should also be noted that this retention of microstructure proved to be reproduceable for this polymer when additional syntheses were performed to obtain enough sample to analyse using the other techniques presented here.

LiFePO₄/C samples synthesised with the smaller polymer microparticles (10 and 20 wt% PDMS-MA) were shown to contain significant aggregation. Though some of the original microstructure was still visible, it was clear that the particles had fused considerably to form large masses of LiFePO₄/C. This may have been due to a tighter packing of the smaller LiFePO₄-polymer composite particles. As the composites are heated, the block copolymer will briefly

pass through the T_g and begin to flow, deforming the microscale structure. A closer packing arrangement will have led to greater surface contact between particles and may have encouraged greater aggregation of particles during this heating process, before a high enough temperature was achieved to combust the polymer. It is possible a slightly faster heating rate during the calcination step could reduce this aggregation.

The LiFePO$_4$/C templated with the largest polymer microparticles (2.5 wt% PDMS-MA) also showed ill-defined microparticle structure. However, this sample still contained a great deal of surface texture and did not appear to be as agglomerated as the other smaller samples, indicating a different mechanism for loss of the microparticle structure. Some images appeared to show slight crumpling of the microparticles, which may imply that instead of inter-particle fusion being the main cause for loss of morphology, internal particle collapse was perhaps the more prominent cause. This suggests that the large size of the original block copolymer microparticles may have led to an uneven distribution of inorganic material within the composite. This would lead to irregular morphology in the LiFePO$_4$ once the surrounding polymer was removed.

Though the SEM revealed agglomerated microstructure in some of the LiFePO$_4$/C materials, it was not clear if this was also reflected in the nanoscale structure. Cross-sectional TEM was performed on all the LiFePO$_4$/C samples to gain insight into their resulting nanoscale morphology after calcination (**Figure 3.24**).

Figure 3.24: *Cross-sectional TEM micrographs of the calcined LiFePO₄/C materials, templated using PMMA-b-P4VP block copolymers synthesised with (a) 2.5 wt%, (b) 5 wt%, (c) 10 wt% and 20 wt% PDMS-MA stabiliser.*
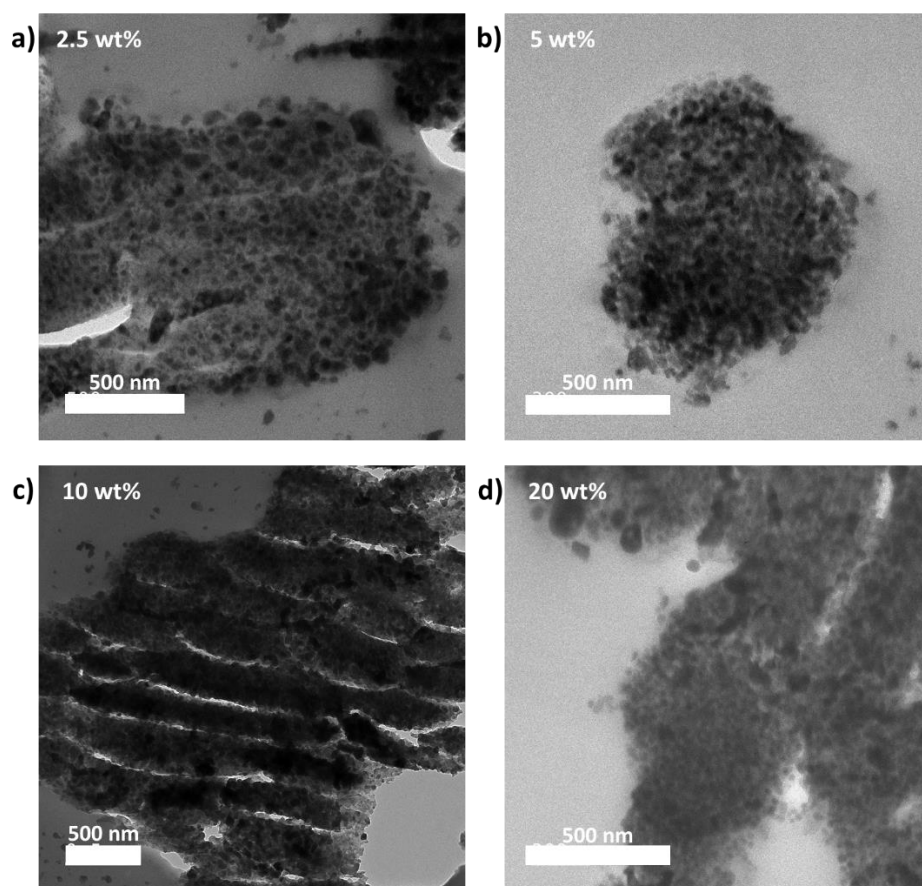
Apart from the LiFePO₄/C synthesised with the 5 wt% PDMS-MA block copolymer, TEM images revealed little evidence of defined microparticle structure, as expected from the SEM analysis. However, it was clear from the TEM images that all LiFePO₄/C samples contained some degree of nanoscale particulates. These nanoscale structures appeared to be of a similar size to the original P4VP spherical domains (~20-30 nm). This indicated that LiFePO₄ was successfully confined within the P4VP regions of the block copolymers and did not appear to undergo significant aggregation during calcination, regardless of any loss in the microparticle structure.

The TEM analysis provided evidence that all LiFePO₄/C cathode materials contained a significant degree of nanostructure, provided by the PMMA-*b*-P4VP block copolymers. Though the microscale morphology of the polymers was not translated successfully in most cases, this nanostructure indicated that the cathode materials may all still possess large accessible surface areas to enhance their ability to transport Li⁺ ions. To confirm this, the

surface areas of the LiFePO$_4$/C materials was assessed by nitrogen sorption measurements (**Figure 3.25**). The calculated surface area values for each material are displayed next to the relevant sorption isotherms.
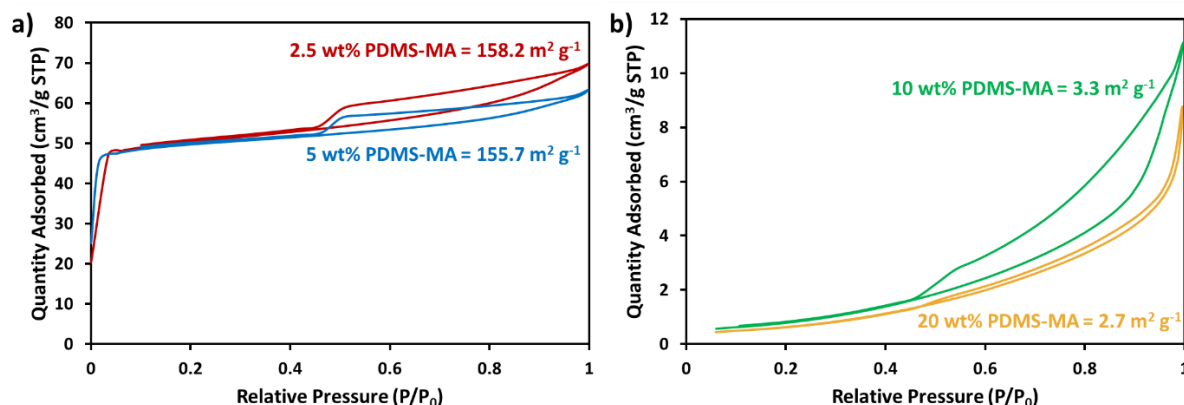
Figure 3.25: *N$_2$ sorption isotherms for the LiFePO$_4$/C materials, templated using PMMA-b-P4VP block copolymers synthesised with various loadings of PDMS-MA. Data are plotted on separate graphs due to their large difference in magnitudes.*

The LiFePO$_4$/C materials synthesised using the largest microparticles (2.5 and 5 wt% PDMS-MA) proved capable of adsorbing large quantities of N$_2$. This demonstrated that the materials have very high available surface areas, with values of >150 m^2 g^{-1} calculated using the Brunauer-Emmett-Teller (BET) method. In contrast, the LiFePO$_4$/C synthesised using the smallest microparticles (10 and 20 wt% PDMS-MA) adsorbed very small quantities of N$_2$, giving extremely low surface areas consistent with bulk materials (<5 m^2 g^{-1}).

The shapes of the isotherms also revealed valuable information about the sample morphology. All sample sorption measurements roughly resemble type IV BET isotherms, with hysteresis loops formed between the adsorption-desorption measurements at high relative N$_2$ pressure. This effect occurs due to capillary condensation within mesopores of the samples. Mesopores are typically around 2-50 nm in diameter, so it is likely this porosity is a direct result of the P4VP nanoscale morphology being applied to the LiFePO$_4$/C samples. Also, for the high surface area LiFePO$_4$/C samples, the large initial adsorption of N$_2$ at low relative pressure is indicative of microporosity in the samples. This refers to pores that are <2 nm in diameter and are likely formed in the carbon layers of the cathode materials, as this size is much smaller than the D_{P4VP} sizes of the block copolymers.[135]

Overall, the surface area analysis pairs well with the morphological features observed in the TEM images. Battery materials synthesised with the larger PMMA-*b*-P4VP microparticles retain the microstructural features to a greater extent, granting them greater accessible surface area. Much of this surface area likely come from the carbon coating formed during the calcination process, due to the large degree of microporosity. Whereas, for the materials synthesised with the smaller microparticles, inter-particle aggregation appears to be favoured, resulting in large monolith structures with very low surface area. This aggregation also prevents any formation of any microporous carbon structures.

Preliminary electrochemical performance tests of the two high surface area LiFePO₄/C materials were performed. The materials were fabricated into electrodes and assembled into lithium-ion battery cells, following the method described in **Section 3.3.4**. Galvanostatic charge/discharge cycles were performed on the battery cells over a range of different charge rates (**Figure 3.26**). The charge rate applied is displayed in units of C below each cycle period, with C equal to the reciprocal of the charge/discharge time in hours. Charge rate was increased every 10 cycles up to 20 C then reduced to 0.1 C for a final 40 cycles.
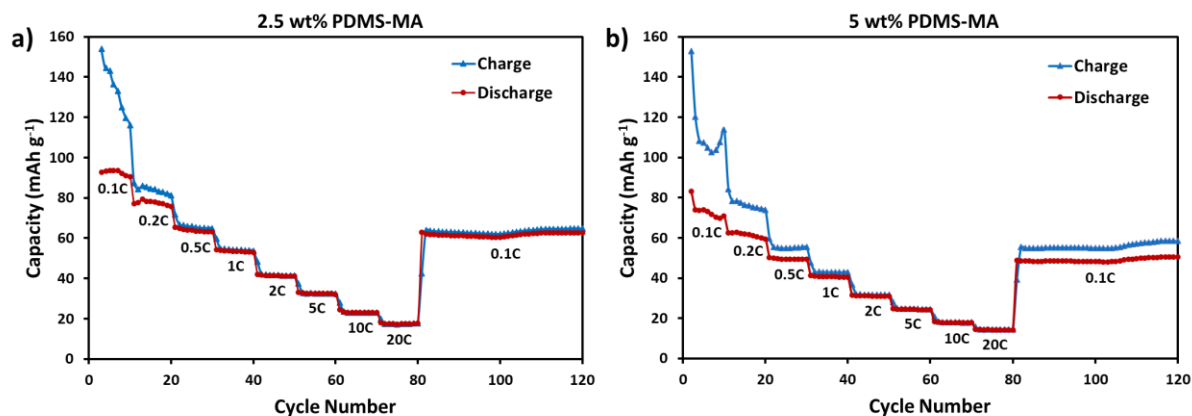
Figure 3.26: *Electrochemical performance of the LiFePO₄/C materials templated with PMMA-b-P4VP synthesised with (a) 2.5 wt% and (b) 5 wt% PDMS-MA. Charge (Blue) and discharge (Red) capacities were measured from galvanostatic cycling at different rates over a total of 120 cycles.*

Galvanostatic cycling of the assembled lithium-ion battery cells showed that the initially high charge capacities (close to the theoretical limit of 170 mAh g^{-1})[136] quickly reduced despite a constant charge rate of 0.1 C being applied. The charge and discharge capacities are then gradually reduced as higher charge rates are applied, as is to be expected due to the higher stress on the electrode materials.[137] A relatively consistent discharge rate is then achieved as

charge rate was again reduced to 0.1 C. Values of around 60 mAh g^{-1} and 50 mAh g^{-1} were obtained for the 2.5 wt% and 5 wt% PDMS-MA samples respectively.

The discharge capacities presented here in this initial test are rather low when compared to other nanostructured LiFePO$_4$/C materials reported in the literature, regardless of the charge rates applied.[138-141] Measured discharge capacities at high charge rates were also very low, which is contradictory to what should be expected for a high surface area electrode.[99] The large initial drop in charge capacity may indicate that other competing processes are occurring during the charge/discharge cycles, leading to degradation or formation of defects in the cathode materials.[142, 143] Although, degradation processes may instead have occurred in other cell components such as the lithium metal anode or in the electrolyte.[144] Furthermore, it has been shown that an excessively thick carbon layer can lead to inefficient Li$^+$ insertion/extraction, which could also be the case with these materials.[145]

Due to the time constraints imposed on this work, a more thorough electrochemical analysis was not possible. Further study will be needed to accurately determine the cause of the low performance in these preliminary constructed battery cells and make any necessary modifications. It may also be beneficial in the future to synthesise a control LiFePO$_4$ without using any block copolymer template to use as a direct comparison for electrochemical data. This will allow for accurate quantitative evaluation of the benefits gained by employing the block copolymer templates.

3.5. Conclusions

In this chapter, the microscale and nanoscale dimensions of self-assembled PMMA-*b*-P4VP microparticles from scCO₂ were successfully modified. Microparticle size was altered in the range of 0.5-2.5 µm by simply adjusting the loading of PDMS-MA stabiliser in the dispersion polymerisation. Particle size dispersity was kept reasonably low throughout with no adverse effects seen on the RAFT polymerisation mechanism of the block copolymer either. A spherical internal nanoscale morphology was observed in all cases, with even the smallest microparticle size shown to give no spatial confinement effects on the block copolymer self-assembly. Size modification beyond this range was predicted to dramatically increase the particle size dispersity of the product.[48]

The internal nanoscale dimensions of the block copolymer were altered to a small extent, between the range of 22-35 nm for the P4VP domain size. PMMA-*b*-P4VP was synthesised with total molecular weight ranging from ~40-290 kg mol^{-1} by changing the quantity of RAFT agent used in the polymerisation. Analysis showed that molecular weight dispersity increased dramatically when higher molecular weights were targeted, likely due to an insufficient number of living polymer chains in the reaction. As a result, P4VP domain sizes were also found to vary greatly in size, leading to reduced control of the overall structural dimensions. From this study it was clear that changes to molecular weight could be used to alter the nanoscale dimensions to a small degree. However, alternate synthesis approaches are likely needed in the dispersion polymerisation to produce high molecular weight block copolymers with enough control to give uniformly distributed products.

After their synthesis, the various sized PMMA-*b*-P4VP microparticles were utilised as structure directing agents in the sol-gel synthesis of LiFePO₄. All the polymer templates successfully confined the formation of LiFePO₄ to the P4VP regions of the block copolymer particles, providing all the composite materials with good hierarchical structure. However, it was discovered that upon calcination of the composites to remove the polymer templates, the morphology of each of the final LiFePO₄/C product varied greatly depending on the size of the microparticle structures. The larger microparticles appeared to retain the structural hierarchy in the final material, while the smaller microparticles gave aggregated products, possibly due to the tighter packing of the composite particles. This observation was similarly reflected in the surface area measurements, with the aggregated products demonstrating

extremely low N$_2$ sorption. Meanwhile, the hierarchically structured LiFePO$_4$ materials were shown to possess both micro and meso porosity, with very high surface areas of >150 m^2 g^{-1} reported. Overall, this study highlights the requirement of large microscale dimensions when attempting to fabricate hierarchically structured LiFePO$_4$ particles using block copolymer templates in this manner.

All LiFePO$_4$/C samples showed good chemical purity and crystallinity in the powder XRD analysis, despite their differences in morphology. The higher surface area LiFePO$_4$/C materials were fabricated into electrodes and assembled in coin cells to test their electrochemical performance. An initial study showed their charge/discharge capacities reduced rapidly over a few cycles and stabilised at low values (<60 mAh g^{-1}). Capacities were found to be significantly lower than those reported in the literature, particularly when high charge rates were applied.[138-141] Though a high surface area hierarchical morphology was successfully achieved for these LiFePO$_4$/C samples, it appeared further optimisation would be required when constructing the electrochemical cells. Further study is needed to determine the exact cause of their low performance and determine a strategy for their redesign.

3.6. References

1.   I. W. Hamley, *The Physics of Block Copolymers*, Oxford University Press, New York, 1998.
2.   Y. Mai and A. Eisenberg, *Chemical Society Reviews*, 2012, **41**, 5969-5985.
3.   M. W. Matsen, *Macromolecules*, 1995, **28**, 5765-5773.
4.   T. P. Lodge, K. J. Hanley, B. Pudil and V. Alahapperuma, *Macromolecules*, 2003, **36**, 816-822.
5.   V. Abetz and P. F. W. Simon, in *Block Copolymers I*, ed. V. Abetz, Springer, Berlin, Heidelberg, 2005, ch. 2, pp. 125-212.
6.   C. Lai, W. B. Russel and R. A. Register, *Macromolecules*, 2002, **35**, 841-849.
7.   K. W. Gotrik, A. F. Hannon, J. G. Son, B. Keller, A. Alexander-Katz and C. A. Ross, *ACS Nano*, 2012, **6**, 8052-8059.
8.   J. Peng, D. H. Kim, W. Knoll, Y. Xuan, B. Li and Y. Han, *The Journal of Chemical Physics*, 2006, **125**, 064702.
9.   H. Tanaka, H. Hasegawa and T. Hashimoto, *Macromolecules*, 1991, **24**, 240-251.
10.   L. Zhang, K. Yu and A. Eisenberg, *Science*, 1996, **272**, 1777-1779.
11.   K. J. Hanley and T. P. Lodge, *Journal of Polymer Science Part B: Polymer Physics*, 1998, **36**, 3101-3113.
12.   J. Jennings, S. P. Bassett, D. Hermida-Merino, G. Portale, W. Bras, L. Knight, J. J. Titman, T. Higuchi, H. Jinnai and S. M. Howdle, *Polymer Chemistry*, 2016, **7**, 905-916.
13.   M. M. M. Ito, K. Ito, M. Shibayama, K. Sugiyama and H. Yokoyama, *Macromolecules*, 2015, **48**, 3590-3597.
14.   T. Shinkai, M. Ito, K. Sugiyama, K. Ito and H. Yokoyama, *Soft Matter*, 2012, **8**, 5811-5817.
15.   R. G. Wissinger and M. E. Paulaitis, *Journal of Polymer Science Part B: Polymer Physics*, 1987, **25**, 2497-2510.
16.   K. Gong, S. R. Panuganti and W. G. Chapman, *Journal of Applied Polymer Science*, 2017, **134**.
17.   F. Ingrosso and M. F. Ruiz-López, *ChemPhysChem*, 2017, **18**, 2560-2572.
18.   A. A. C. Pacheco, A. F. da Silva Filho, K. Kortsen, M. W. D. Hanson-Heine, V. Taresco, J. D. Hirst, M. Lansalot, F. D'Agosto and S. M. Howdle, *Chemical Science*, 2021, **12**, 1016-1030.
19.   T. Shinkai, K. Ito and H. Yokoyama, *The Journal of Supercritical Fluids*, 2014, **95**, 553-559.
20.   Y. Zhang, K. K. Gangwani and R. M. Lemert, *The Journal of Supercritical Fluids*, 1997, **11**, 115-134.
21.   J. Jennings, M. Beija, A. P. Richez, S. D. Cooper, P. E. Mignot, K. J. Thurecht, K. S. Jack and S. M. Howdle, *Journal of the American Chemical Society*, 2012, **134**, 4772-4781.
22.   T. Shinkai, M. Ito, K. Sugiyama, K. Ito and H. Yokoyama, *Soft Matter*, 2013, **9**, 10689-10693.
23.   B. D. Vogt, V. S. RamachandraRao, R. R. Gupta, K. A. Lavery, T. J. Francis, T. P. Russell and J. J. Watkins, *Macromolecules*, 2003, **36**, 4029-4036.
24.   B. D. Vogt, G. D. Brown, V. S. RamachandraRao and J. J. Watkins, *Macromolecules*, 1999, **32**, 7907-7912.
25.   V. S. RamachandraRao, R. R. Gupta, T. P. Russell and J. J. Watkins, *Macromolecules*, 2001, **34**, 7923-7925.

26. X. Yu and Y. Han, in *Directed Self-assembly of Block Co-polymers for Nano-manufacturing*, eds. R. Gronheid and P. Nealey, Elsevier, Cambridge, 2015, ch. 3, pp. 47-66.

27. C. Sinturel, M. Vayer, M. Morris and M. A. Hillmyer, *Macromolecules*, 2013, **46**, 5399-5415.

28. G. He, T. M. Bennett, M. Alauhdin, M. W. Fay, X. Liu, S. T. Schwab, C.-g. Sun and S. M. Howdle, *Polymer Chemistry*, 2018, **9**, 3808-3819.

29. M. Alauhdin, T. M. Bennett, G. He, S. P. Bassett, G. Portale, W. Bras, D. Hermida-Merino and S. M. Howdle, *Polymer Chemistry*, 2019, **10**, 860-871.

30. G. He, T. M. Bennett, K. Alias, L. Jiang, S. T. Schwab, M. Alauhdin and S. M. Howdle, *Polymer Chemistry*, 2019, **10**, 3960-3972.

31. A. Blanazs, S. P. Armes and A. J. Ryan, *Macromolecular Rapid Communications*, 2009, **30**, 267-277.

32. A.-C. Shi and B. Li, *Soft Matter*, 2013, **9**, 1398-1413.

33. C. R. Stewart-Sloan and E. L. Thomas, *European Polymer Journal*, 2011, **47**, 630-646.

34. J. Y. Cheng, C. A. Ross, H. I. Smith and E. L. Thomas, *Advanced Materials*, 2006, **18**, 2505-2521.

35. M. J. Fasolka and A. M. Mayes, *Annual Review of Materials Research*, 2001, **31**, 323-355.

36. J. N. L. Albert and T. H. Epps, *Materials Today*, 2010, **13**, 24-33.

37. Z. Jin and H. Fan, *Soft Matter*, 2014, **10**, 9212-9219.

38. M. Ma, E. L. Thomas, G. C. Rutledge, B. Yu, B. Li, Q. Jin, D. Ding and A.-C. Shi, *Macromolecules*, 2010, **43**, 3061-3071.

39. B. Yu, P. Sun, T. Chen, Q. Jin, D. Ding, B. Li and A.-C. Shi, *The Journal of Chemical Physics*, 2007, **126**, 204903.

40. B. Yu, P. Sun, T. Chen, Q. Jin, D. Ding, B. Li and A.-C. Shi, *The Journal of Chemical Physics*, 2007, **127**, 114906.

41. B. Yu, Q. Jin, D. Ding, B. Li and A.-C. Shi, *Macromolecules*, 2008, **41**, 4042-4054.

42. B. Yu, B. Li, Q. Jin, D. Ding and A.-C. Shi, *Macromolecules*, 2007, **40**, 9133-9142.

43. K. Shin, H. Xiang, S. I. Moon, T. Kim, T. J. McCarthy and T. P. Russell, *Science*, 2004, **306**, 76-76.

44. H. Xiang, K. Shin, T. Kim, S. Moon, T. J. Mccarthy and T. P. Russell, *Journal of Polymer Science Part B: Polymer Physics*, 2005, **43**, 3377-3383.

45. P. Dobriyal, H. Xiang, M. Kazuyuki, J.-T. Chen, H. Jinnai and T. P. Russell, *Macromolecules*, 2009, **42**, 9082-9088.

46. D. A. Rider, J. I. L. Chen, J.-C. Eloi, A. C. Arsenault, T. P. Russell, G. A. Ozin and I. Manners, *Macromolecules*, 2008, **41**, 2250-2259.

47. T. Higuchi, A. Tajima, K. Motoyoshi, H. Yabu and M. Shimomura, *Angewandte Chemie International Edition*, 2008, **47**, 8044-8046.

48. T. D. McAllister, L. D. Farrand and S. M. Howdle, *Macromolecular Chemistry and Physics*, 2016, **217**, 2294-2301.

49. T.-M. Yong, W. P. Hems, J. L. M. van Nunen, A. B. Holmes, J. H. G. Steinke, P. L. Taylor, J. A. Segal and D. A. Griffin, *Chem. Commun.*, 1997, 1811-1812.

50. P. Fratzl and R. Weinkamer, *Prog. Mater Sci.*, 2007, **52**, 1263-1334.

51. *Hierarchical Structures in Biology as a Guide for New Materials Technology*, The National Academies Press, Washington, DC, 1994.

52. M. Miniaci, A. Krushynska, A. S. Gliozzi, N. Kherraz, F. Bosia and N. M. Pugno, *Physical Review Applied*, 2018, **10**, 024012.
53. I. Levchenko, K. Bazaka, M. Keidar, S. Xu and J. Fang, *Advanced Materials*, 2018, **30**, 1702226.
54. H. Seifi, A. R. Javan, A. Ghaedizadeh, J. Shen, S. Xu and Y. M. Xie, *Scientific Reports*, 2017, **7**, 41183.
55. M.-H. Sun, S.-Z. Huang, L.-H. Chen, Y. Li, X.-Y. Yang, Z.-Y. Yuan and B.-L. Su, *Chemical Society Reviews*, 2016, **45**, 3479-3563.
56. O. Ikkala and G. ten Brinke, *Chem. Commun.*, 2004, 2131-2137.
57. J. Ruokolainen, G. t. Brinke and O. Ikkala, *Advanced Materials*, 1999, **11**, 777-780.
58. R. Mezzenga, J. Ruokolainen, G. H. Fredrickson, E. J. Kramer, D. Moses, A. J. Heeger and O. Ikkala, *Science*, 2003, **299**, 1872-1874.
59. J. Ruokolainen, R. Mäkinen, M. Torkkeli, T. Mäkelä, R. Serimaa, G. t. Brinke and O. Ikkala, *Science*, 1998, **280**, 557-560.
60. M. Knaapila, O. Ikkala, M. Torkkeli, K. Jokela, R. Serimaa, I. P. Dolbnya, W. Bras, G. t. Brinke, L. E. Horsburgh, L.-O. Pålsson and A. P. Monkman, *Appl. Phys. Lett.*, 2002, **81**, 1489-1491.
61. R. M. Dorin, H. Sai and U. Wiesner, *Chemistry of Materials*, 2014, **26**, 339-347.
62. H. Jung, W. H. Shin, T. W. Park, Y. J. Choi, Y. J. Yoon, S. H. Park, J.-H. Lim, J.-D. Kwon, J. W. Lee, S.-H. Kwon, G. H. Seong, K. H. Kim and W. I. Park, *Nanoscale*, 2019, **11**, 8433-8441.
63. S.-H. Tung, N. C. Kalarickal, J. W. Mays and T. Xu, *Macromolecules*, 2008, **41**, 6453-6462.
64. K. Brassat and J. K. N. Lindner, *Advanced Materials Interfaces*, 2020, **7**, 1901565.
65. Y. Lu, J. Lin, L. Wang, L. Zhang and C. Cai, *Chemical Reviews*, 2020, **120**, 4111-4140.
66. S. C. Glotzer and M. J. Solomon, *Nature materials*, 2007, **6**, 557-562.
67. A. Ianiro, M. Chi, M. M. R. M. Hendrix, A. V. Koç, E. D. Eren, M. Sztucki, A. V. Petukhov, G. de With, A. C. C. Esteves and R. Tuinier, *Polymer Chemistry*, 2020, **11**, 2305-2311.
68. S.-M. Yang, S.-H. Kim, J.-M. Lim and G.-R. Yi, *Journal of Materials Chemistry*, 2008, **18**, 2177-2190.
69. A. Nykänen, A. Rahikkala, S.-P. Hirvonen, V. Aseyev, H. Tenhu, R. Mezzenga, J. Raula, E. Kauppinen and J. Ruokolainen, *Macromolecules*, 2012, **45**, 8401-8411.
70. Z. Hou, M. Ren, K. Wang, Y. Yang, J. Xu and J. Zhu, *Macromolecules*, 2020, **53**, 473-481.
71. J. Jennings, G. He, S. M. Howdle and P. B. Zetterlund, *Chemical Society Reviews*, 2016, **45**, 5055-5084.
72. M. J. Robb, L. A. Connal, B. F. Lee, N. A. Lynd and C. J. Hawker, *Polymer Chemistry*, 2012, **3**, 1618-1628.
73. M.-K. Park, S. Jun, I. Kim, S.-M. Jin, J.-G. Kim, T. J. Shin and E. Lee, *Adv. Funct. Mater.*, 2015, **25**, 4570-4579.
74. A. Rahikkala, V. Aseyev, H. Tenhu, E. I. Kauppinen and J. Raula, *Biomacromolecules*, 2015, **16**, 2750-2756.
75. Y. Zhu, X. Gao and Y. Luo, *Journal of Applied Polymer Science*, 2016, **133**.
76. H. Yu, X. Qiu, S. P. Nunes and K. V. Peinemann, *Nature communications*, 2014, **5**, 4110.
77. H. Yabu, *Polym. J.*, 2013, **45**, 261-268.
78. C. J. Brinker, Y. Lu, A. Sellinger and H. Fan, *Advanced Materials*, 1999, **11**, 579-585.
79. B. E. McKenzie, F. Nudelman, P. H. H. Bomans, S. J. Holder and N. A. J. M. Sommerdijk, *Journal of the American Chemical Society*, 2010, **132**, 10256-10259.

80.   B. E. McKenzie, J. F. de Visser, G. Portale, D. Hermida-Merino, H. Friedrich, P. H. H. Bomans, W. Bras, O. R. Monaghan, S. J. Holder and N. A. J. M. Sommerdijk, *Soft Matter*, 2016, **12**, 4113-4122.

81.   Y. Kagawa, H. Minami, M. Okubo and J. Zhou, *Polymer*, 2005, **46**, 1045-1049.

82.   Y. Kitayama, Y. Kagawa, H. Minami and M. Okubo, *Langmuir*, 2010, **26**, 7029-7034.

83.   M. Armand and J. M. Tarascon, *Nature*, 2008, **451**, 652-657.

84.   A. Manthiram, *ACS Central Science*, 2017, **3**, 1063-1069.

85.   J. B. Goodenough and K.-S. Park, *Journal of the American Chemical Society*, 2013, **135**, 1167-1176.

86.   J. Asenbauer, T. Eisenmann, M. Kuenzel, A. Kazzazi, Z. Chen and D. Bresser, *Sustainable Energy & Fuels*, 2020, **4**, 5387-5416.

87.   Z. Zou, S. Zhang and S. Li, *Materials Technology*, 2020, **35**, 300-315.

88.   A. Manthiram, *Nature communications*, 2020, **11**, 1550.

89.   N. Nitta, F. Wu, J. T. Lee and G. Yushin, *Materials Today*, 2015, **18**, 252-264.

90.   M.-J. Uddin, P. K. Alaboina and S.-J. Cho, *Materials Today Energy*, 2017, **5**, 138-157.

91.   E. Hosono, T. Kudo, I. Honma, H. Matsuda and H. Zhou, *Nano Letters*, 2009, **9**, 1045-1051.

92.   Y. Sun, Y. Yang, H. Zhan, H. Shao and Y. Zhou, *J. Power Sources*, 2010, **195**, 4322-4326.

93.   C. Delacourt, P. Poizot, S. Levasseur and C. Masquelier, *Electrochemical Solid State Letters*, 2006, **9**, A352.

94.   B. Kang and G. Ceder, *Nature*, 2009, **458**, 190-193.

95.   T. V. S. L. Satyavani, A. Srinivas Kumar and P. S. V. Subba Rao, *Engineering Science and Technology, an International Journal*, 2016, **19**, 178-188.

96.   V. Palomares, A. Goñi, I. G. d. Muro, I. de Meatza, M. Bengoechea, O. Miguel and T. Rojo, *J. Power Sources*, 2007, **171**, 879-885.

97.   J. Zhu, J. Fiore, D. Li, N. M. Kinsinger, Q. Wang, E. DiMasi, J. Guo and D. Kisailus, *Crystal Growth & Design*, 2013, **13**, 4659-4666.

98.   Y. Park, K. C. Roh, W. Shin and J.-w. Lee, *RSC Advances*, 2013, **3**, 14263-14266.

99.   A. Vu and A. Stein, *Chemistry of Materials*, 2011, **23**, 3237-3245.

100.   N. Liu, H. Li, Z. X. Wang, X. J. Huang and L. Q. Chen, *Electrochem. Solid State Lett.*, 2006, **9**, A328-A331.

101.   M. Wang, Y. Yang and Y. Zhang, *Nanoscale*, 2011, **3**, 4434-4439.

102.   O. Birkholz and M. Kamlah, *Energy Technology*, 2021, 2000910.

103.   L. Wu, Y. Li, Z. Fu and B.-L. Su, *National Science Review*, 2020, **7**, 1667-1701.

104.   W. Tong, Y. Huang, Y. Cai, Y. Guo, X. Wang, D. Jia, Z. Sun, W. Pang, Z. Guo and J. Zong, *Appl. Surf. Sci.*, 2018, **428**, 1036-1045.

105.   N. Liu, Z. Lu, J. Zhao, M. T. McDowell, H.-W. Lee, W. Zhao and Y. Cui, *Nature Nanotechnology*, 2014, **9**, 187-192.

106.   Y. Ma, A. Huang, H. Zhou, S. Ji, S. Zhang, R. Li, H. Yao, X. Cao and P. Jin, *Journal of Materials Chemistry A*, 2017, **5**, 6522-6531.

107.   Z. Chen, D. Chao, M. Chen and Z. Shen, *RSC Advances*, 2020, **10**, 18776-18783.

108.   A. C. Wagner, N. Bohn, H. Geßwein, M. Neumann, M. Osenberg, A. Hilger, I. Manke, V. Schmidt and J. R. Binder, *ACS Applied Energy Materials*, 2020, **3**, 12565-12574.

109.   A. Magasinski, P. Dixon, B. Hertzberg, A. Kvit, J. Ayala and G. Yushin, *Nature materials*, 2010, **9**, 353-358.

110.   Y. Li, W. Jiang, G. Ding, F. Yan, X. Jing, Z. Zhu, Y. Gao, L. Wu, G. Xu and F. Sun, *J. Alloys Compd.*, 2021, **859**, 157825.

111.   S. T. Ha, O. O. Park and S. H. Im, *Macromolecular Research*, 2010, **18**, 935-943.

112.   T. M. Bennett, G. He, R. R. Larder, M. G. Fischer, G. A. Rance, M. W. Fay, A. K. Pearce, C. D. J. Parmenter, U. Steiner and S. M. Howdle, *Nano Letters*, 2018, **18**, 7560-7569.

113.   J. Jennings, M. Beija, J. T. Kennon, H. Willcock, R. K. O'Reilly, S. Rimmer and S. M. Howdle, *Macromolecules*, 2013, **46**, 6843-6851.

114.   M. Shoji, M. Eguchi, J. M. Layman, M. P. Cashion, T. E. Long and H. Nishide, *Macromolecular Chemistry and Physics*, 2009, **210**, 579-584.

115.   I. M. Kalogeras and W. Brostow, *Journal of Polymer Science Part B: Polymer Physics*, 2009, **47**, 80-95.

116.   N. Bosq, N. Guigo, J. Persello and N. Sbirrazzuoli, *Physical Chemistry Chemical Physics*, 2014, **16**, 7830-7840.

117.   E. Helfand and Z. R. Wasserman, in *Developments in Block Copolymers-I*, ed. I. Goodman, Applied Science, New York, 1982, ch. 3, pp. 99-126.

118.   F. S. Bates and G. H. Fredrickson, *Annual Review of Physical Chemistry*, 1990, **41**, 525-557.

119.   K. W. Guarini, C. T. Black and S. H. I. Yeung, *Advanced Materials*, 2002, **14**, 1290-1294.

120.   T. Xu, H.-C. Kim, J. DeRouchey, C. Seney, C. Levesque, P. Martin, C. M. Stafford and T. P. Russell, *Polymer*, 2001, **42**, 9091-9095.

121.   C. T. Black, R. Ruiz, G. Breyta, J. Y. Cheng, M. E. Colburn, K. W. Guarini, H. Kim and Y. Zhang, *IBM Journal of Research and Development*, 2007, **51**, 605-633.

122.   J. D. Ferry, *Viscoelastic Properties of Polymers*, Wiley, New York, 3rd edn., 1980.

123.   J. G. Kennemur, *Macromolecules*, 2019, **52**, 1354-1370.

124.   S. Perrier, *Macromolecules*, 2017, **50**, 7433-7447.

125.   L. Boldon, F. Laliberte and L. Liu, *Nano Reviews*, 2015, **6**, 25661.

126.   G. Duan, C. Zhang, A. Li, X. Yang, L. Lu and X. Wang, *Nanoscale research letters*, 2008, **3**, 118-122.

127.   Y. Xue and H. Xiao, *Polymers*, 2015, **7**, 2290-2303.

128.   R. Ferwerda, J. H. van der Maas and F. B. van Duijneveldt, *J. Mol. Catal. A: Chem.*, 1996, **104**, 319-328.

129.   M. I. Zaki, M. A. Hasan, F. A. Al-Sagheer and L. Pasupulety, *Colloids and Surfaces A: Physicochemical and Engineering Aspects*, 2001, **190**, 261-274.

130.   M. G. Fischer, X. Hua, B. D. Wilts, E. Castillo-Martínez and U. Steiner, *ACS applied materials & interfaces*, 2018, **10**, 1646-1653.

131.   S. Beninati, L. Damen and M. Mastragostino, *J. Power Sources*, 2009, **194**, 1094-1098.

132.   M. Doeff, Y. Hu, F. McLarnon and R. Kostecki, *Electrochem. Solid-State Lett.*, 2003, **6**, A207-A209.

133.   G. Zeng, R. Caputo, D. Carriazo, L. Luo and M. Niederberger, *Chemistry of Materials*, 2013, **25**, 3399-3407.

134.   A. Ruíz-Baltazar, R. Esparza, G. Rosas and R. Pérez, *Journal of Nanomaterials*, 2015, **2015**, 240948.

135.   M. Thommes, K. Kaneko, A. V. Neimark, J. P. Olivier, F. Rodriguez-Reinoso, J. Rouquerol and K. S. W. Sing, *Pure Appl. Chem.*, 2015, **87**, 1051-1069.

136.   D. Saikia, J. R. Deka, C.-J. Chou, C.-H. Lin, Y.-C. Yang and H.-M. Kao, *ACS Applied Energy Materials*, 2019, **2**, 1121-1133.

137.   T. S. Bryden, A. Holland, G. Hilton, B. Dimitrov, C. P. de León Albarrán and A. Cruden, *Energy Procedia*, 2018, **151**, 194-198.

138. M. G. Fischer, X. Hua, B. D. Wilts, I. Gunkel, T. M. Bennett and U. Steiner, *ACS applied materials & interfaces*, 2017, **9**, 22388-22397.

139. C. M. Doherty, R. A. Caruso, B. M. Smarsly and C. J. Drummond, *Chemistry of Materials*, 2009, **21**, 2895-2903.

140. Y. Hou, X. Wang, Y. Zhu, C. Hu, Z. Chang, Y. Wu and R. Holze, *Journal of Materials Chemistry A*, 2013, **1**, 14713-14718.

141. C. M. Doherty, R. A. Caruso, B. M. Smarsly, P. Adelhelm and C. J. Drummond, *Chemistry of Materials*, 2009, **21**, 5300-5306.

142. K. Striebel, A. Guerfi, J. Shim, M. Armand, M. Gauthier and K. Zaghib, *J. Power Sources*, 2003, **119-121**, 951-954.

143. M. Dubarry and B. Y. Liaw, *J. Power Sources*, 2009, **194**, 541-549.

144. J. Henschel, C. Peschel, S. Klein, F. Horsthemke, M. Winter and S. Nowak, *Angewandte Chemie International Edition*, 2020, **59**, 6128-6137.

145. Z. Jiang and Z.-j. Jiang, *J. Alloys Compd.*, 2012, **537**, 308-317.

Chapter 4 – ABC Triblock Copolymer Synthesis in Supercritical CO$_2$

4.1. Overview

This chapter explores the synthesis of ABC-type triblock copolymer microparticles and their possible use in nanofabrication. The aim being to access a range of more complex nanoscale polymer morphologies without the need to change the volume fraction of the active template block, the P4VP.

PMMA-*b*-PS-*b*-P4VP copolymers were synthesised via RAFT-mediated scCO$_2$ dispersion using a simple one-pot method, whereby monomers were injected into the autoclave sequentially under high-pressure. In addition, the copolymers were also synthesised using a more recently developed two-pot seeded dispersion method. The self-assembly of the copolymer microparticles was investigated using a range of analytical techniques, including TEM and X-ray scattering, in order to assign the internal morphologies. Several new morphologies were observed, unseen before in previous studies of block copolymer self-assembly in scCO$_2$.

The resulting P4VP triblock copolymers were then utilised in the sol-gel synthesis of TiO$_2$, a simple inorganic material that has potential application in photocatalysis. After removal of the polymer templates, the resulting nanostructured TiO$_2$ was fully characterised and compared to the equivalent TiO$_2$ material synthesised using a PMMA-*b*-P4VP diblock copolymer template. One particular triblock copolymer was found to produce porous hollow-cored TiO$_2$ microparticles, with an active surface area more than six times that of the diblock counterpart. Finally, the photocatalytic activity of the resulting materials was directly compared through H$_2$ evolution measurements, giving evidence of enhanced functional activity when utilising the new triblock copolymer template.

4.2. Introduction

This introduction develops on the general concepts presented in **Chapter 1**. In particular, the subjects of block copolymer self-assembly and nanofabrication. The theoretical phase behaviour of the more complex ABC-type triblock copolymer system is discussed and how this can result in a wider range of possible morphologies, when compared to the more common diblock systems. Experimental studies into these materials are discussed, as well as the current state-of-the-art of their use in nanofabrication.

In addition, the nanofabrication of TiO$_2$ is described, as this was the desired functional material to study the structure directing capability of the new polymer morphologies. An overview of the material's potential use in photocatalysis is provided, as well as some of the current limitations that may be mitigated by applying nanofabrication strategies.

4.2.1. Triblock Copolymer Self-Assembly

As stated previously, the basic AB-type diblock copolymer typically self-assembles into four distinct morphologies in the bulk phase, spherical (SPH), cylindrical (CYL), bicontinuous gyroidal (GYR) and lamellar (LAM).[1] The self-assembly principles also remain almost identical when considering an ABA-type triblock system.[2] However, when a third unique block is introduced into the chain, the potential to form a wealth of additional nanostructures arises.

When transitioning to an ABC-type system, the available parameter space used to determine the optimal geometry for minimal enthalpic interactions is greatly expanded. Self-assembly is now dictated by three independent Flory-Huggins interaction parameters rather than one (χ_{AB}, χ_{BC}, χ_{AC}), as well as an additional block volume fraction parameter (f_A, f_B, f_C).[3] Furthermore, the sequence of each constituent block in the chain must also be considered, i.e. ABC, BAC or CAB. For example, a change in the block sequence of a poly(isoprene-*b*-styrene-*b*-2-vinylpyridine) triblock copolymer was found to give significantly different morphologies, even when the volume fractions of each block remained unchanged.[4, 5]

The expansion in parameter space represents a significant problem for both experimental and theoretical investigations of ABC triblock copolymers. Theoretical studies become much more computationally demanding to fully map the possible phase diagrams. Modelling techniques may also struggle to predict some of the complex 3D microphases that can be observed, especially regarding any long-lived metastable configurations.[6] Experimentally, synthesis of a

vast series of block copolymers becomes necessary, covering many possible compositions. Characterisation of each composition quickly becomes an insurmountable task. Hence, the precise nature of ABC self-assembly is not as well-defined as the diblock case.[7]

Though a complete understanding of ABC systems remains a challenge, many studies have begun to reveal some of the possible morphologies that can be obtained in the bulk and solution states of these materials (**Figure 4.1**). Studies in the bulk phase have shown that the relative magnitudes of each χ parameter can frustrate the self-assembly and favour particular morphologies. An ABC triblock copolymer with three equal block fractions and $\chi_{AB} \approx \chi_{BC} \approx \chi_{AC}$ will form a three-phase lamellar morphology (**Figure 4.1 a**). However, when $\chi_{AB} << \chi_{BC,}$ curvature of the AB and BC surfaces becomes thermodynamically favoured and core-shell spherical or hexagonal morphologies are formed (**Figure 4.1 b, k**).[3] In another case, where $\chi_{AC} << \chi_{AB} \approx \chi_{BC}$, the middle block in strongly disfavoured by the adjoining blocks and tends to intercalate AC interfaces as spheres, cylinders or rings, maximising the low energy AC contact (**Figure 4.1 c, d, e**).[8, 9] Finally, in the opposing case ($\chi_{AC} >> \chi_{AB} \approx \chi_{BC}$), morphologies with staggered lattices of A and C in a B matrix become favourable, such as the ordered tricontinuous double gyroid morphology (**Figure 4.1 l**).[10, 11]
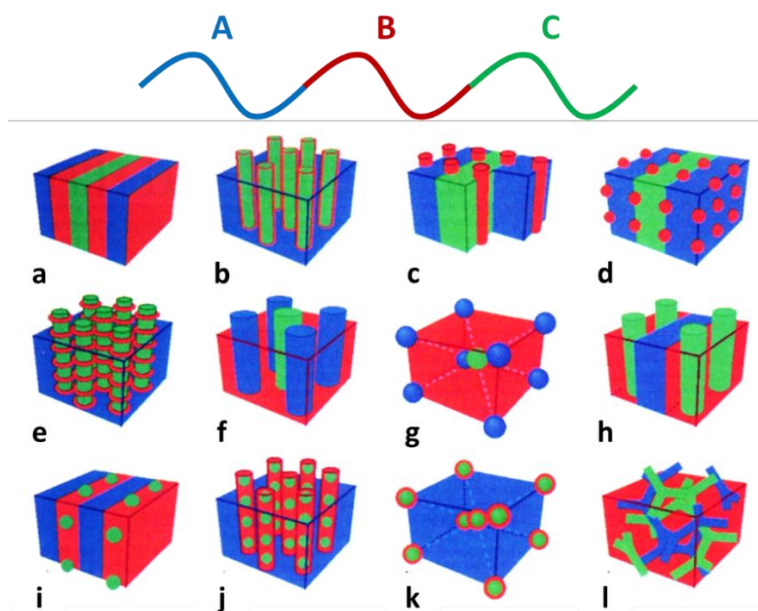
Figure 4.1: *Some possible morphologies for ABC triblock copolymers in the bulk phase. (a) Lamellar, (b) coaxial cylinder, (c) lamella-cylinder, (d) lamella-sphere, (e) cylinder-ring, (f) cylinders in square lattice, (g) spheres in a bcc type structure, (h) lamella-cylinder II, (i) lamella-sphere II, (j) cylinder-sphere, (k) concentric spherical, (l) tricontinuous double gyroid. Figure adapted from literature.[7]*

Several reports in the literature now show evidence of a number of triblock copolymers forming some of the bulk morphologies illustrated in **Figure 4.1**.[12-15] Some studies also demonstrate the formation of additional morphologies including knitting patterns,[16] tetragonally perforated lamellae[17] and helical morphologies.[18] Theoretical studies have proposed ternary phase diagrams for some triblock copolymers, indicating the morphology presented at different block fractions, like those available for diblock copolymers (**Figure 4.2 a**).[3, 19-21] Experimentally derived phase diagrams have also been proposed. Notably in the case of the extensively studied triblock copolymers of PS, PMMA and polybutadiene (PB) (**Figure 4.2 b**).[22-25] However, these phase diagrams are only applicable to a single triblock copolymer chemistry, including the block ordering.
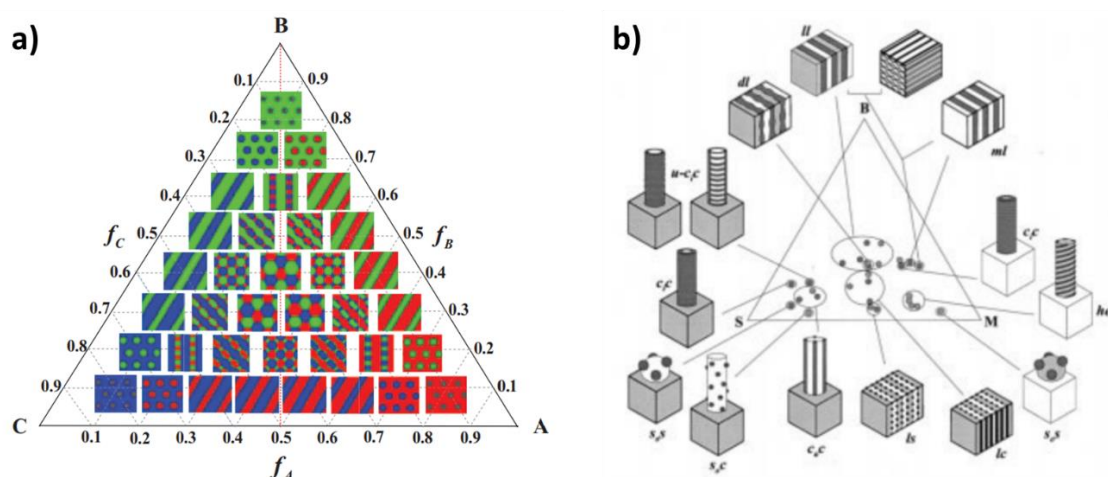
Figure 4.2: *Ternary phase diagrams for ABC triblock copolymer morphologies, constructed (a) using self-consistent field theory modelling[19] and (b) experimentally.[25]*

Self-assembly of ABC triblock copolymers has also been studied in the solution phase, though this is less applicable to this thesis. Again, this process in well understood for the AB system, but additional interactions of the third block cause this process to become very complex for the triblock case. The interaction of each block with the solvent must now be considered (χ_{AS}, χ_{BS}, χ_{CS}) alongside the three polymer-polymer interactions.[26] Research is ongoing, but so far ABC triblock copolymers have been found to give core-shell-corona micelles[27], different surface patterned micelle or worm structures[28, 29] and multicompartment micelles (MCMs).[30] Müller et al. reported that by carefully controlling the introduction of solvents, even hierarchically structured MCM assemblies can be produced using triblock copolymers.[31]

Triblock copolymer structures produced in solution are of particular interest for use in the biomedical field, specifically drug delivery. The morphologies produced can be utilised to encapsulate multiple active agents[32, 33], or the additional block chemistry can be used to respond to multiple different physiological stimuli.[34] Also, triblock copolymers have been studied for their use in creating Janus type particles in solution.[26] Janus particles are nano or microscale particles with two distinct hemispherical faces, each with different physical properties. Their surface anisotropy makes them highly desirable for a wealth of applications in electronics, optics and catalysis.[35, 36]

Other factors influencing phase separation in triblock copolymers have also been considered in recent studies. For example, several reports consider the self-assembly of miktoarm star shaped triblock copolymers, with each block connected to a single common junction point.[37-39] In solution, this was found to considerably disfavour the formation of concentric shelled micelles and instead favour MCM geometries (**Figure 4.3 a**).[39]
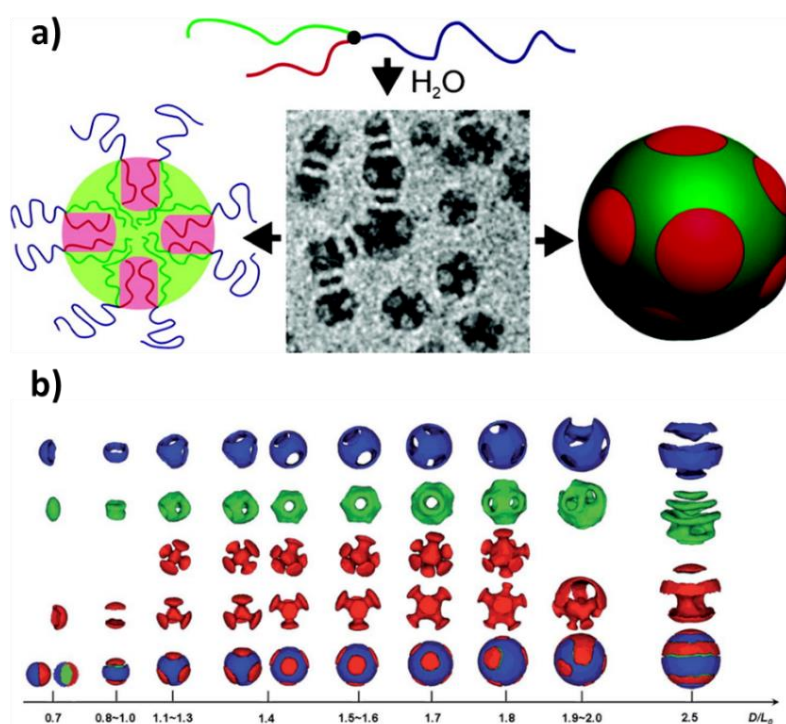
Figure 4.3: *Studies into the effects of ABC triblock copolymer self-assembly when (a) a star shaped architecture is applied[39] and (b) under 3D spherical confinement.[40]*

Additionally, in a recent computational simulation study by Yu et al., the effect of 3D spatial confinement was considered on triblock copolymers self-assembly. The study modelled the

self-assembly of a linear ABC triblock copolymer with three identical volume fractions, confined in spherical nanopores with increasing diameter. The model found that the size of the nanopores could be used to control the morphology of the triblock copolymer spheres, with increasingly patchy surfaces formed within larger nanopores (**Figure 4.3 b**).[40] Such confinement studies can be useful for predicting potential morphologies when synthesising triblock copolymers in heterogeneous processes.

4.2.2. Triblock Copolymers in Nanofabrication

In **Chapter 1**, the use of block copolymers in nanofabrication was discussed, covering the broad use of all block copolymers for this application. Highlighted here are several examples of the use of ABC triblock copolymers in nanofabrication and their specific advantage over equivalent methods employing AB diblock copolymers.

As mentioned previously, block copolymers show potential to be used as pattern masks in nanolithography.[41] Thin films of block copolymers can be cast, then annealed on the surface of a substrate, self-assembling into a periodic nanostructured mask that can be transferred to the substrate, usually via etching. However, in the case of diblock copolymers, the pattern templates available are limited by the geometry of the few morphologies that can be achieved during the self-assembly. Typically, these are either close packed dots or parallel lines, though the morphology can be manipulated slightly further by carefully controlling the annealing conditions of the thin film, for example via selective solvent vapour annealing.[42] The richness of attainable triblock copolymer morphologies offers a route to many additional 2D patterns that may be applied to the substrate.

Particularly desirable lithography patterns for microelectronic components include square packed spherical arrays[43] and ring-shaped structures,[44] both achievable using ABC triblock copolymer chemistries. Such patterns can potentially be used to fabricate high-density magnetic storage media,[45, 46] sensors[47] and quantum devices.[48] Ross et al. demonstrated that a linear poly(isoprene-*b*-styrene-*b*-ferrocenylsilane) (PI-*b*-PS-*b*-PFS) copolymer could be used to create a square-symmetry array, via chloroform solvent-annealing.[49] The self-assembled pattern was then transferred to a silicon substrate using etching techniques (**Figure 4.4 a**). The same group also used a self-assembled PB-*b*-PS-*b*-PMMA copolymer film to pattern transfer ring structures onto silicon substrates (**Figure 4.4 b**).[44] Both studies highlight the

potential advantages to be gained when adopting triblock copolymers over diblock equivalents.
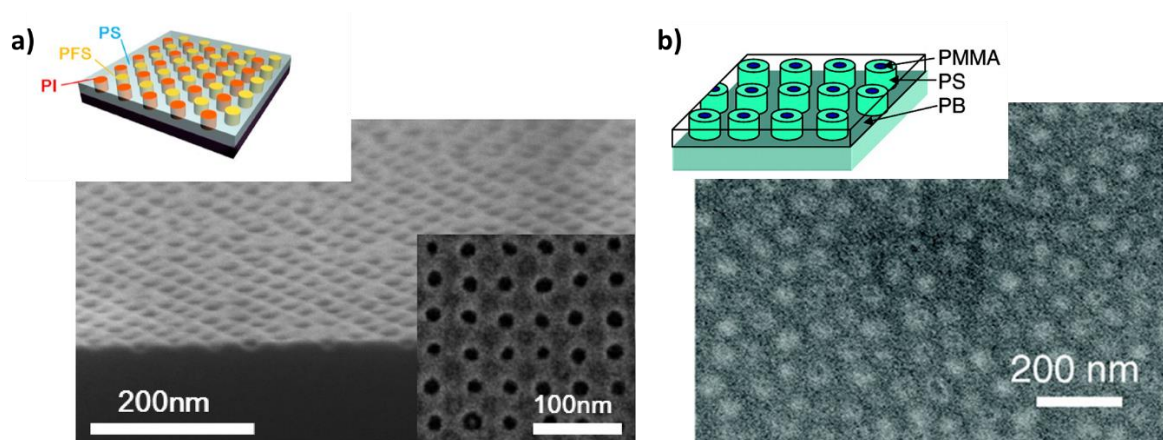
Figure 4.4: *ABC Triblock copolymer thin-films used in nanolithography to pattern transfer (a) a square-dotted array[49] and (b) ring shaped structures[44] on to silicon substrates.*

Looking beyond lithography techniques, ABC triblock copolymers have also been used to template inorganic nanostructures by chemical association of polymer blocks directly to inorganic species.[50] In particular, this method is useful for fabricating complex 3D nanoscale network architectures, desirable for application in some microelectronics and energy storage devices, where efficient charge transport is required.[51-53] ABC triblock copolymers are particularly suited to creating these specific inorganic nanostructures, as it has been shown triblock network structures can form over a much larger composition window (4-14 vol%)[20, 54] than the gyroid structure of the AB diblock copolymer (2-6 vol%).[55, 56] Despite this, there are still relatively few examples of nanofabrication of 3D or hierarchical architectures using triblock copolymers in the literature. Hence, this particular type of structure directing remains an area of untapped potential.

Work in this field was recently pioneered by the group of Ullrich Wiesner. The group has utilised poly(isoprene-*b*-styrene-*b*-ethylene oxide) (PI-*b*-PS-*b*-PEO, or ISO) copolymers to direct the formation of mesoporous titania,[57] niobia[58] and aluminosilicate[59] network structures. Fabrication of the nanostructures was achieved by co-assembly of the triblock copolymers with either the metal oxide sol-gel precursors, or metal oxide nanoparticles. The inorganic components were selectively associated with the hydrophilic PEO block and co-assembled with the polymer upon annealing. The ISO templates were then removed via a

reactive oxygen plasma etch, to leave free-standing mesoporous networks (**Figure 4.5**). In addition, the quantity of inorganic material was varied to alter the effective volume fraction of the PEO block, resulting in formation of a variety of 3D network structures from a single copolymer.[58]
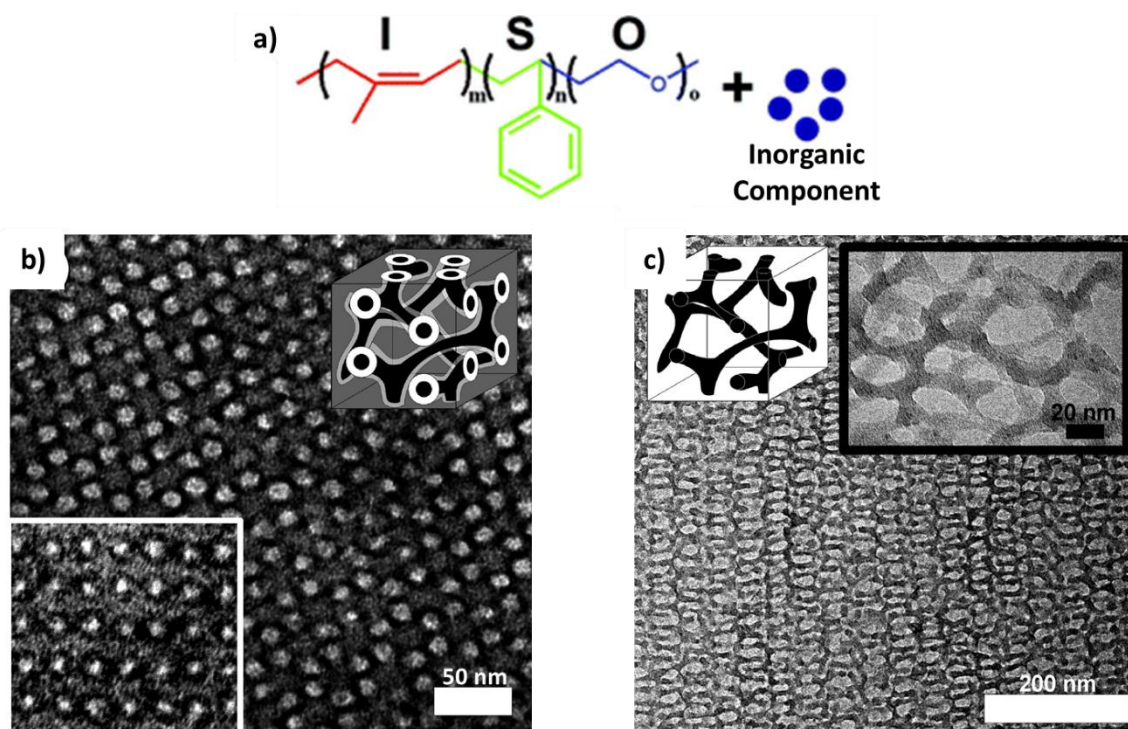
Figure 4.5: *(a) Chemical composition of the ISO triblock copolymer structural template, co-assembled with inorganic species.[58] TEM micrographs of (b) a core-shell double gyroid network morphology formed during co-assembly with aluminosilicate and (c) the resulting free-standing aluminosilicate structure after removal of the polymer template.[59]*

The advantages of using triblock copolymers for inorganic structure directing over diblock copolymers extends beyond the added richness in possible morphologies. Addition of another chemically distinct polymer block gives the possibility to direct multiple inorganic species simultaneously, forming multicomponent inorganic nanomaterials.[60] This can be achieved by judicious control of the block chemistries. As demonstrated by Li et al., Pt and Au nanoparticles were functionalised with different surface ligands to give them each preferential association to the different regions of a poly(isoprene-*b*-styrene-*b*-(*N,N*-dimethylamino)ethyl methacrylate) copolymer.[61] The result being control of the final superstructure of the binary nanoparticle mixture.

Multicomponent inorganics can also be fabricated by orthogonal degradation of a triblock copolymer morphology. Wiesner et al. synthesised various poly(isoprene-*b*-styrene-*b*-propylene carbonate) (PI-*b*-PS-*b*-PPC) copolymers capable of self-assembling into several three-phase network morphologies. The PI and PPC blocks could then be removed independently by either a UV or NaOH etch (**Figure 4.6 a**). Stepwise etching of the morphology allows the resulting porous copolymer to be backfilled with two different inorganic precursors, between each etching step. As a proof of concept, this was achieved by backfilling the copolymer with Au after the UV etch to remove the PI block, followed by etching of the PPC block and a final backfilling of Cu. Analysis revealed the final material consisted of independent Au and Cu networks, once the final PS matrix was also removed (**Figure 4.6 b**).[60]
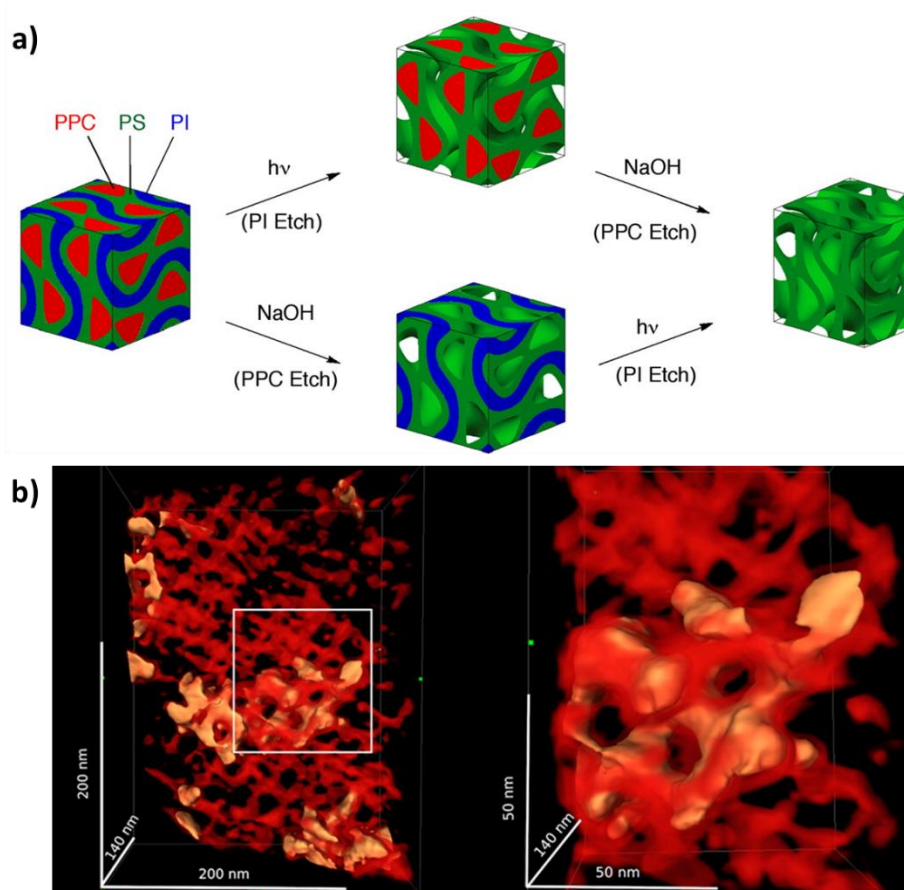
Figure 4.6: *(a) schematic demonstrating the orthogonal degradation of PI and PPC block in the triblock copolymer. (b) 3D rendering from TEM tomography analysis of Cu (red) and Au (yellow) interpenetrating networks, formed by sequential backfilling of the triblock copolymer template.[60]*

4.2.3. Nanostructured TiO_2

Block copolymers can be useful for directing the structure of many inorganic materials for a wide range of possible applications.[62-64] However, TiO_2 is a particularly common choice of inorganic material selected for use in block copolymer templating, used to create several nanostructures including nanoparticles,[65] nanorods[66, 67] and mesoporous TiO_2.[57, 68] Recently, the Howdle group has published the use of a PMMA-*b*-P4VP diblock copolymer, synthesised via scCO₂ dispersion, to control the nanostructure of sol-gel synthesised TiO_2, producing mesoporous microparticles. [69]

Titania's popularity in this field is undoubtedly a consequence of the material's simple fabrication, low cost and high abundance.[70] In addition, its semiconductor properties also make it highly promising for use in a wide range of applications, such as photovoltaics,[71] sensors,[72] self-cleaning devices,[73] water-treatment[74] and hydrogen production.[75] The material's properties become particularly desirable for these applications when nanoscale dimensions are utilised.

The attractiveness of TiO_2 for many of these applications stem from the metal oxide's photocatalytic activity and hydrophilicity.[76] When TiO_2 is irradiated, photons of sufficient energy can excite electrons from the valence band to the conduction band of the semiconductor. The resulting free electrons, as well as the associated positive electron holes, can participate in redox reactions, leading to the splitting of water molecules and breakdown of chemical pollutants (**Figure 4.7**).[77] High surface area to volume ratio of the photocatalyst is crucial to maximise the quantity of adsorbed reagents undergoing the redox reactions.
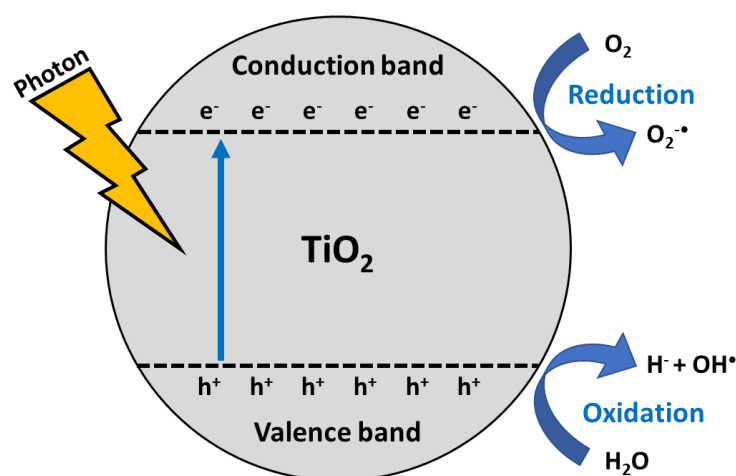
Figure 4.7: *Illustration of the mechanism for TiO_2 photocatalysis.*

However, there are several obstacles that limit the practical application of TiO_2 for photocatalytic purposes. TiO_2 has a relatively large band gap (~ 3.2 eV), requiring high energy photons to induce photoactivation.[78] This means only a relatively small fraction of solar light, the UV portion, can be used to activate TiO_2, giving low catalytic efficiency. TiO_2 also suffers from a high rate of electron-hole recombination, deactivating the photocatalyst before redox chemistry can occur.[79] Finally, the use of nanoparticulate TiO_2 can sometimes become an issue depending on the application, when recovery of the photocatalyst is required for example in water-treatment.[80]

As a result, numerous publications have outlined various strategies to overcome these limitations.[78, 81-83] Many reports focus on modifications to the chemistry of TiO_2, often through doping with rare earth metals to lower the band gap energy or recombination rate.[82, 84, 85] Other studies highlight the strong dependence of overall photocatalytic activity of the type of nanostructure given to the TiO_2.[86-89] Hence, these studies are often intertwined with the use of block copolymer directing agents, as a reliable and efficient method to provide these intricate nanostructures to TiO_2.[57, 66, 67, 90, 91]

4.2.4. Summary and Research Objectives

A review of the literature has shown that the addition of a third unique polymer unit to a block copolymer can lead to the formation of many intricate nanoscale morphologies, not achievable using simpler AB diblock copolymers. The added richness in available morphologies, and the extra chemical functionality possible through the additional block, have already proven to be valuable in inorganic nanofabrication, especially when compared to their diblock counterparts. However, despite these successes, many of the reports suffer from the same drawback. The triblock copolymer templates are synthesised using non-sustainable and demanding living techniques, like anionic polymerisation, that may prove difficult to implement at a large scale.

In this chapter, the synthesis of ABC-type triblock copolymers is explored, using the RAFT-mediated scCO₂ dispersion method already employed to successfully synthesise diblock copolymers. Resulting copolymers contain the P4VP functional block to allow them to be used in nanofabrication. The aim being to produce a greater wealth of P4VP morphologies to template inorganic materials, without the need to change the block volume fraction of the

active P4VP. The hope is that these triblock templates may offer similar benefits to nanofabrication as those already expressed in the literature, while also expanding the field to produce new types of hierarchically structured nanomaterials. This is by way of the additional microstructure provided by the dispersion polymerisation method. Moreover, the new synthetic methodology in $scCO_2$ also provides a solution to current limitations in the synthesis of polymer templates, by being a more environmentally benign and scalable process.

It should be noted that the synthesis of ABA-type block copolymers has also yet to be explored in $scCO_2$. Though this may offer a route to further explore and modify the nanoscale self-assembly behaviour of block copolymers, the morphology change is not likely to be significant when compared to the three-phase systems offered by ABC-type block copolymers. Therefore, only ABC-type block copolymers are selected for study here to maximise impact.

The synthesised ABC triblock copolymers are tested as structure directing agents in the synthesis of TiO_2, a well-studied photocatalytic functional material. This simple material is used as a benchmark to test the effectiveness of the new triblock copolymer morphologies. The functionality of the fabricated TiO_2 is directly compared to the mesoporous TiO_2 synthesised previously using the equivalent PMMA-*b*-P4VP diblock copolymer.[69] Specifically, the rate of hydrogen production is measured to assess the resulting photoactivities.

4.3. Experimental

4.3.1. Materials

Methyl methacrylate (MMA, ProSciTech, 99%), styrene (Sigma Aldrich, >99%), benzyl methacrylate (BzMA, Sigma Aldrich, 96%) and 4-vinylpyridine (4VP, Acros Organics, 95%) were purified by eluting through a basic alumina column to remove inhibitor. 2,2'-azobis(2-methylpropionitrile) (AIBN, Sigma Aldrich, 98%) was purified by recrystallisation from methanol. Dry CO_2 (BOC, SFC grade, 99.99%), 2-(Dodecylthiocarbonothioylthio)-2-methylpropionic acid (DDMAT, Sigma Aldrich, 98%), Poly(dimethylsiloxane) monomethyl methacrylate (PDMS-MA, Fluorochem, M_n ~10 kg mol^{-1}) titanium tetraisopropoxide (TTIP, Sigma Aldrich, 97%) and hydrochloric acid (Sigma Aldrich, 12 M) were all used as received.

4.3.2. One-pot Polymerisation

Several diblock and triblock copolymers in this chapter were synthesised using a one-pot method in scCO$_2$. All these reactions were performed using the high-pressure equipment detailed in **Chapter 2**. All equipment was operated following the standard operating procedure described in **Section 2.2.4**.

Diblock copolymers were synthesised by first preparing a solution of MMA (6 g, 59.9 mmol), AIBN (9.8 mg, 0.06 mmol), DDMAT (43.7 mg, 0.12 mmol) and PDMS-MA polymeric stabiliser (0.6 g). The solution was mixed in a sealed vial at 0 °C and degassed by purging with argon for 30 minutes. The monomer solution was then added to the degassed 60 mL high-pressure autoclave via syringe against a positive pressure of CO_2 to prevent the ingress of air. The autoclave was then sealed, heated to 65 °C and pressurised to 241 bar, following the standard operating procedure. After stirring at 300 rpm for 24 hours, a small sample of the PMMA macro-RAFT agent was taken from the outlet tap for analysis. The second monomer solution, either BzMA (6 g, 34.1 mmol) or styrene (6 g, 57.6 mmol), with AIBN (4.9 mg, 0.03 mmol) was degassed before adding directly into the pressurised autoclave via a HPLC pump at a rate of 0.5 mL min^{-1}. After either 48 or 72 hours, the reaction was cooled to room temperature, slowly vented to atmospheric pressure and the dry, white diblock copolymer powder was collected (typical yield ~85-90%).

Triblock copolymers syntheses using one-pot were performed using the same procedure as above, with the inclusion of an extra sampling and monomer addition step for the third P4VP

block. Monomer quantities were adjusted depending on the target weight fractions in the final copolymer.

4.3.3. Two-pot Polymerisation

Triblock copolymers in this chapter were also synthesised using a two-pot reaction method in scCO$_2$. Again, all high-pressure equipment was operated following the standard operating procedure described in **Section 2.2.4**.

The following method describes the two-pot synthesis of a PMMA-*b*-PS-*b*-P4VP triblock copolymer, with target total molecular weight of 100 kg mol^{-1} and weight fractions of 25% PMMA, 50% PS and 25% P4VP. MMA (10 g, 99.9 mmol), AIBN (32.8 mg, 0.20 mmol), DDMAT (145.7 mg, 0.40 mmol) and PDMS-MA polymeric stabiliser (0.5 g) were mixed in a sealed vial at 0 °C and degassed by purging with argon for 30 minutes. The monomer solution was then added to the degassed 60 mL high-pressure autoclave via syringe against a positive pressure of CO$_2$ to prevent the ingress of air. The autoclave was sealed, heated to 65 °C and pressurised to 241 bar, following the standard operating procedure. After stirring at 300 rpm for 24 hours, the reaction was cooled to room temperature, slowly vented and the PMMA macro-RAFT agent product collected as a fine free-flowing powder (9.50 g, 89%).

For the second reaction stage, the PMMA macro-RAFT agent (3 g, M$_n$ ~25 kg mol^{-1}) and additional PDMS-MA (0.45 g) were loaded into the 60 mL autoclave and degassed by flushing with CO$_2$ at 1-2 bar for 30 minutes. The autoclave was then sealed, heated to 65 °C and pressurised to 241 bar, following the standard operating procedure. After stirring at 300 rpm for ~1 hour to re-disperse the polymer particles, a degassed solution of styrene (6 g, 57.6 mmol) and AIBN (9.8 mg, 0.06 mmol) was added to the autoclave via a HPLC pump at a rate of 0.5 mL min^{-1}. After 72 hours a small sample of the diblock copolymer was collected through the outlet tap for analysis. After, a degassed solution of 4VP (3 g, 28.5 mmol) and AIBN (7.5 mg, 0.05 mmol) was added to the autoclave in the same manner as the styrene. Total monomer loading was always 12 g, irrespective of target molecular weights. After a further 24 hours, the reaction was cooled to room temperature, slowly vented and the triblock copolymer product collected as an off-white, dry free-flowing powder (9.21 g, 74%).

Other triblock copolymers with different weight fractions were prepared by synthesising PMMA macro-RAFT agents of the desired molecular weight then re-dispersing with the

appropriate quantity of subsequent monomers. The total monomer loading always equating to 12 g.

4.3.4. Sol-gel Synthesis of TiO$_2$

TiO$_2$ was synthesised by a typical hydrolytic sol-gel procedure, with addition of the triblock copolymers as structure directing agents in the gelation process. TiO$_2$-polymer composites were synthesised targeting a mass of 25 wt% TiO$_2$ in the final composites.

The sol–gel solution was created by adding TTIP (0.062 mL, 0.21 mmol) to a solution of concentrated hydrochloric acid (0.031 mL, 37 wt % HCl in water) in ethanol (7.92 mL) for a total volume of 8 mL. The solution was stirred for 1 hour before addition of a slurry of the triblock copolymer microparticles in ethanol (2 mL, 25 mg mL^{-1}). The sol-gel mixture was then stirred for a further 24 hours before being evaporated in a petri dish for approximately 48 hours at room temperature. The polymer-TiO$_2$ composite materials were obtained as fine white powders (77 mg) that were loosely settled on the dish surface.

The pure TiO$_2$ materials were obtained by calcining the composite material in a tube furnace under an air atmosphere (500 °C, 2 hours, 10 °C min^{-1} ramp). The products were obtained as fine white powders (19 mg). For analytical techniques requiring a larger quantity of material, the sol-gel reactions were conducted in parallel, and the final products combined.

4.3.5. Characterisation

The Majority of the characterisation techniques used in this chapter are described in **Section 2.3** of this thesis.

Photocatalytic activity of the TiO$_2$ samples was assessed by measuring hydrogen evolution when exposed to simulated solar radiation. Samples were prepared by suspending of 25 mg of the TiO$_2$ photocatalyst in 50 ml of an aqueous solution with 20 Vol% of Methanol. The suspension was sonicated for 15 mins and placed in a 90 mL quartz reactor. The reactor was purged with vacuum and argon to remove the residual atmosphere gases. The H$_2$ produced was extracted by a continuous flux of Ar, to a Gas Chromatograph Agilent 7890B equipped with a Thermal Conductivity Detector (TCD). A Cermax Xe lamp (300 W) was used as the irradiation source, equipped with AM 1.5G filter and a water column to attenuate the thermal effect induced by the IR radiation. The irradiation power was adjusted to 300 mW cm^{-2},

calibrated using a photometer (Gentec XLP 12-3S-H2-D0). This procedure was carried out by Higor Andrade Centurion and Prof. Renato Vitalino Gonçalves (São Carlos Intitule of Physics, University of São Paulo, Brazil).

4.4. Results and Discussion

4.4.1. Investigation of Suitable Polymer Blocks

The first step in producing a triblock copolymer for structure directing applications was to determine a suitable chemical composition to investigate. Since the previous nanofabrication studies used PMMA-b-P4VP block copolymers, the new triblock material was chosen to be as chemically similar to this as possible, for easy comparison. PMMA would be kept as the first block and P4VP as the final block. Also, the overall weight fraction of the P4VP block in the copolymer would be kept the same as the diblock equivalent (~25 wt%). This was due to the known impact of this block fraction on the success of the sol-gel nanofabrication process.

Previous studies by the Howdle group regarding diblock copolymer synthesis meant there were already a selection of known polymers that could be successfully grown from a PMMA macro-RAFT agent in scCO$_2$.[92] PMMA macro-RAFT agents were used to synthesise block copolymers with PS, P4VP, PBzMA, poly(N,N-dimethylacrylamide) (PDMA) and poly(2-dimethylaminoethyl methacrylate) (PDMAEMA) in scCO$_2$ dispersion. For this study, the PBzMA and PS polymer blocks were selected as potential candidates for the central block of the triblock copolymer. This was due to their chemical dissimilarity to the P4VP block, with no nitrogen bearing functional groups.

Both PBzMA and PS were trialled to ensure they would be suitable to form the centre block of a triblock copolymer adjoined by a PMMA and P4VP block. Each polymer was required to chain extend from a PMMA macro-RAFT agent to form a diblock copolymer with reasonably low molecular weight dispersity (Đ). This ensures the resulting triblock copolymers would also have sufficiently low Đ, causing self-assembly to be relatively uniform throughout the material. The diblock copolymers must also readily phase separate in scCO$_2$ when synthesised. Separation of the PMMA and second polymer block was key for forming three-phase morphologies in the final triblock materials.

These criteria were already satisfied for PMMA-*b*-PBzMA and PMMA-*b*-PS block copolymers synthesised in scCO$_2$ dispersion, from a previous study.[92] However, key syntheses of these materials were repeated to ensure reproducibility in this project. The preliminary test involved repeating the synthesis of a 100 kg mol^{-1} block copolymers with a 50 kg mol^{-1} PMMA macro-RAFT agent (**Figure 4.8**), identical to the previous publication.[92]
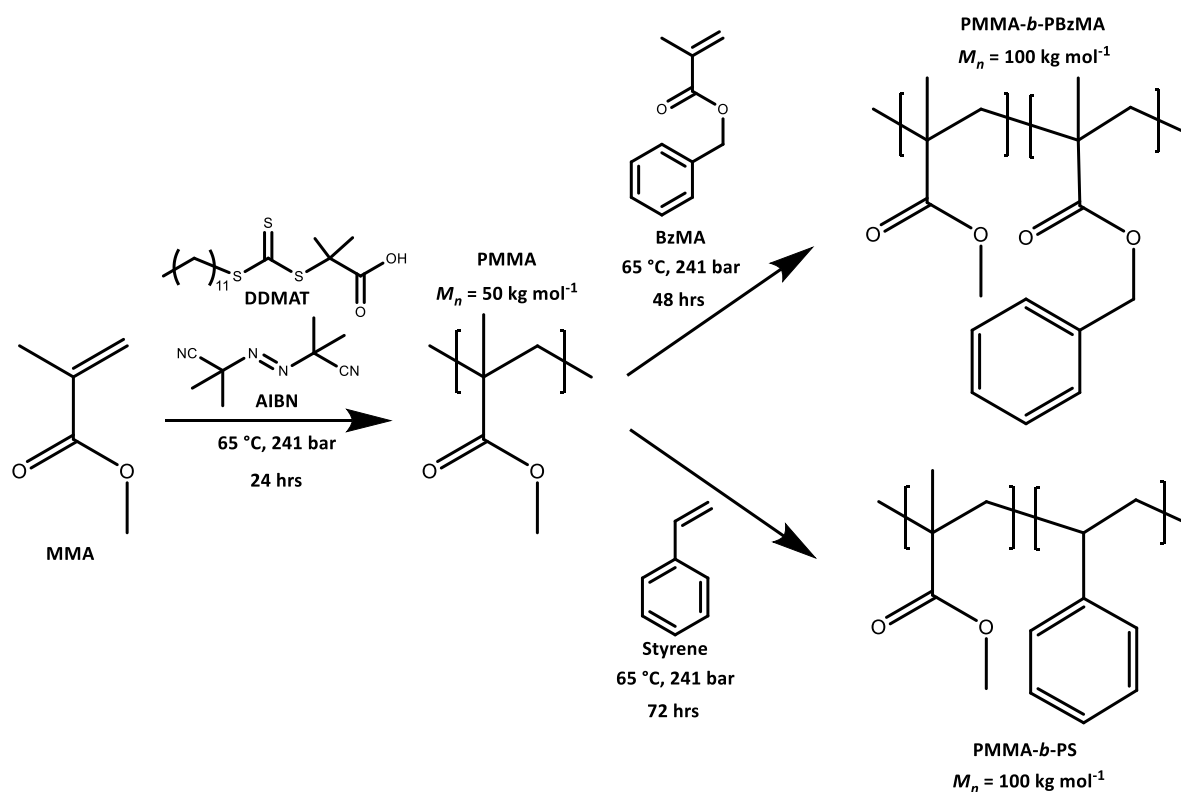
Figure 4.8: *Reaction scheme for the one-pot synthesis of PMMA-b-PBzMA and PMMA-b-PS in scCO₂. The first reaction step, forming the PMMA macro-RAFT agent, is the same in both syntheses. Polymer structures are simplified and do not include the RAFT or initiator end groups.*

Both block copolymers were synthesised using a one-pot dispersion method, described in **Section 4.3.2**. MMA was polymerised for 24 hours with a 0.5:1 molar ratio of AIBN to DDMAT RAFT agent. Afterwards, an equivalent mass of BzMA or styrene was injected into the autoclave with additional AIBN and polymerised for a further 48-72 hours. A small sample of the PMMA macro-RAFT agent was taken from the outlet tap prior to injecting in the second monomer to analyse the growth of the block copolymers. GPC chromatograms of the polymer products are shown below (**Figure 4.9**), and the experimental molecular weights ($M_{n\ exp}$) are summarised (**Table 4.1**).

Measured molecular weight values showed a good agreement with those from the previous study.[92] Reasonably low Đ values (<1.5) were seen for the PMMA macro-RAFT agents and the PMMA-*b*-PBzMA block copolymer. However, a slightly higher dispersity (Đ = 1.60) was seen for the PMMA-*b*-PS block copolymer, which was also evident by the broader peak in the GPC chromatogram. This is almost certainly a result of the varying chemical reactivities between the MMA and styrene monomers. While MMA and BzMA are both methacrylate monomers,

134

propagating through tertiary radical centres, styrene propagates through a secondary radical centre. The difference in reactivities means the PMMA macro-RAFT was less capable of controlling the polymerisation kinetics, resulting in a slightly wider distributions of polymer chain lengths. Nevertheless, this degree of control was still adequate for producing the desired triblock copolymer materials.

Table 4.1: *Summary of molecular weight, dispersity and block fraction data for the PMMA-b-PBzMA and PMMA-b-PS diblock copolymers.[a]*

Second Polymer Block	$M_{n\ Target}$ per block respectively (kg mol^{-1})	PMMA		Block Copolymer		Polymer block ratio (wt%) [c]
		$M_{n\ exp}$ [b] (kg mol^{-1})	$Đ$ [b]	$M_{n\ exp}$ [b] (kg mol^{-1})	$Đ$ [b]	
PBzMA	50 : 50	49.1	1.35	82.4	1.45	49 : 51
PS	50 : 50	55.6	1.34	97.9	1.60	52 : 48

[a] *Conditions: 6 g of MMA polymerised at 65 °C and 241 bar for 24 hrs, then 6 g of BzMA or styrene added for another 48-72 hrs.* [b] *Obtained from GPC, eluting in THF, measured with dRI detector calibrated against PMMA narrow standards.* [c] *Obtained from ^{1}H NMR integrations.*
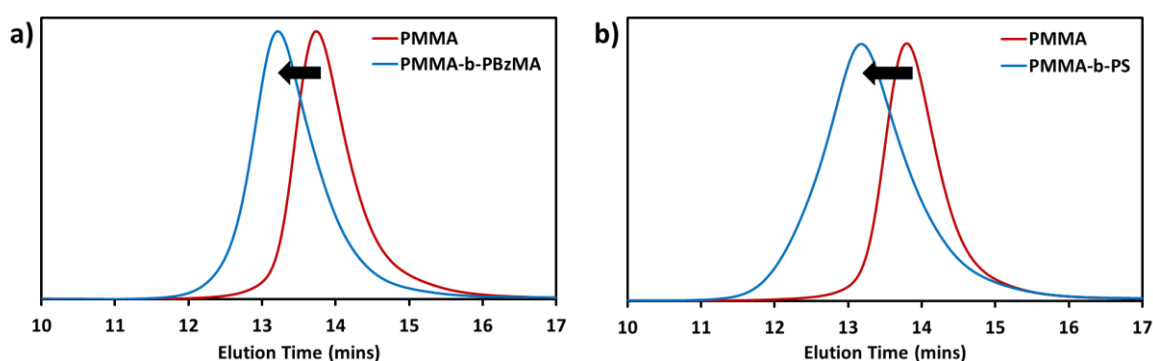
Figure 4.9: *GPC chromatograms at each stage of the polymer growth for (a) PMMA-b-PBzMA and (b) PMMA-b-PS block copolymers.*

The experimental molecular weight for the PMMA-*b*-PBzMA copolymer (82.4 kg mol^{-1}) was slightly below the target value of 100 kg mol^{-1}. This was likely a result of an inaccurate measurement through the GPC, caused by comparing the block copolymer to pure PMMA standards. The difference in the hydrodynamic volume of PBzMA is expected to cause a change in retention time when compared to a PMMA homopolymer.

^{1}H NMR spectra (**Figure 4.10**) were used to confirm the correct block composition of the copolymers. Peak integrals for PMMA were compared to the integrals for the second polymer

block peaks to calculate the block weight ratios, using the method described in **Section 2.3.2**. These were confirmed as approximately 50 wt% in both copolymers, hence, it can be assumed that approximately the correct molecular weights were achieved in both final block copolymers.
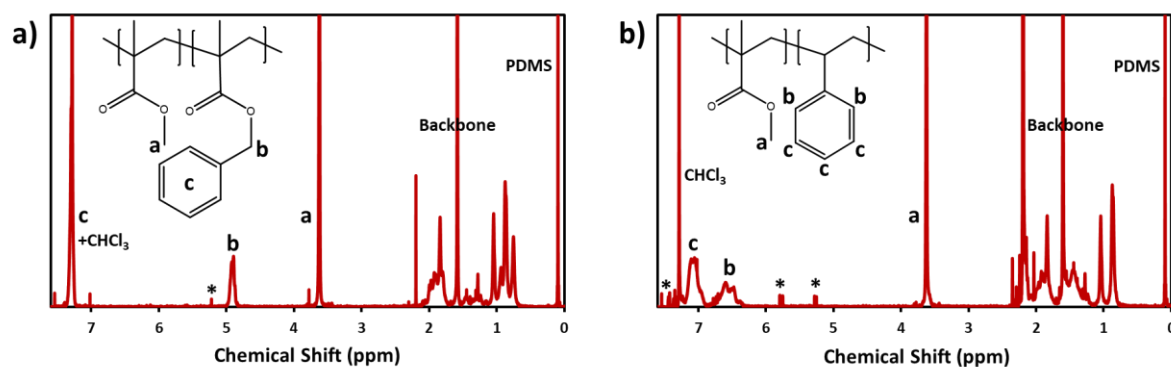
Figure 4.10: *¹H NMR spectra and assignments for the (a) PMMA-b-PBzMA and (b) PMMA-b-PS block copolymers. * Assignments relate to small residual amounts of monomer (< 2%).*

The block copolymer morphologies were investigated by SEM to assess the microstructural features (**Figure 4.11**). Average microparticle diameters (d_n) and coefficient of variation (CV) values were calculated using the method described in **Section 2.3.3** and are displayed on the micrographs. Analysis revealed both block copolymers consisted of well-defined microparticles with a moderate size distribution, shown by the relatively high CV values. Both samples had approximately the same d_n, showing consistent particle growth in both polymerisations. Overall, this indicates a stable polymer dispersion was achieved in both syntheses, even after addition of the second monomers.
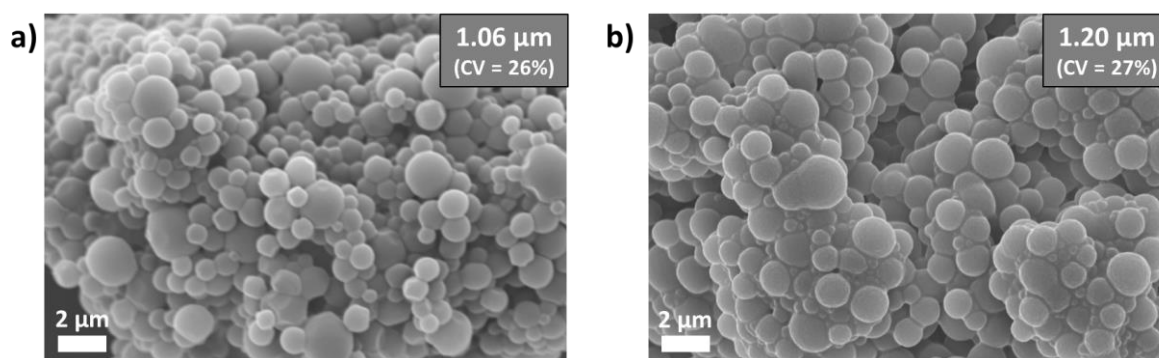
Figure 4.11: *SEM micrographs of the (a) PMMA-b-PBzMA and (b) PMMA-b-PS block copolymers.*

The internal nanoscale morphologies of the block copolymer microparticles were assessed by TEM analysis of RuO$_4$ stained microparticle cross-sections (**Figure 4.12**). From previous investigations, a lamellar and spherical self-assembled morphology were expected for the PMMA-*b*-PBzMA and PMMA-*b*-PS samples respectively, based on their molecular weight and block fractions.[92, 93] Though the spherical block copolymer morphology was clearly evident in all particle cross-sections for the PMMA-*b*-PS, no morphology was seen for the PMMA-*b*-PBzMA. Instead, all imaged microparticles showed a continuous uniform dark contrast.
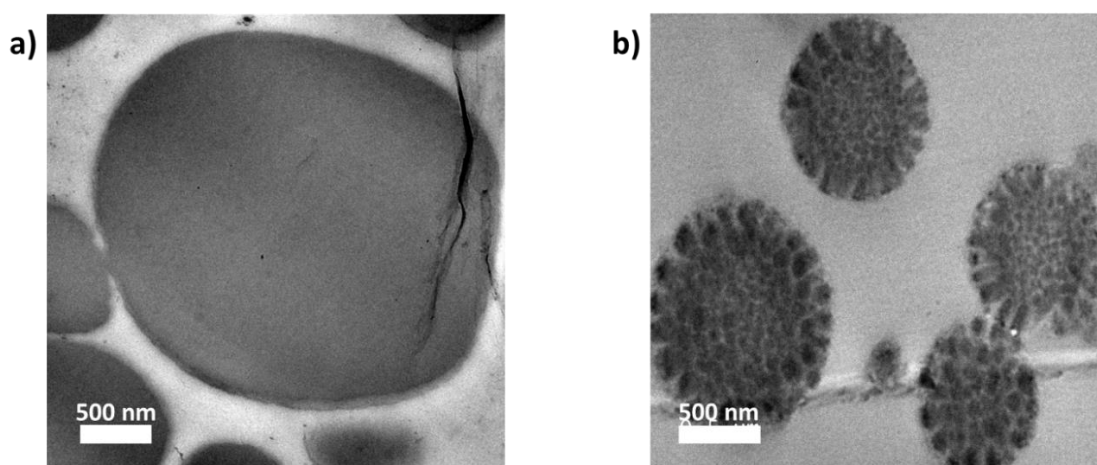
Figure 4.12: *TEM cross-sectional micrographs of the (a) PMMA-b-PbzMA and (b) PMMA-b-PS block copolymers. TEM sections were stained with RuO$_4$ vapour to improve contrast by darkening the PBzMA and PS blocks.*

Though several repeats of the PMMA-*b*-PBzMA synthesis were attempted, the same results were obtained each time. GPC data indicated successful polymerisation and chain extension of the PMMA with PBzMA, but no self-assembled nanoscale morphology could be seen via TEM. It was proposed that the lamellar morphology was either not present at all or only in a small quantity of microparticles, not visible in the small sample size used for TEM analysis. It was noted that in the previous study, when lower molecular weight PMMA-*b*-PBzMA copolymers were synthesised (total M_n < 60 kg mol^{-1}), nanoscale morphology became scarce or non-existent.[93] Much like that observed in this investigation.

Though no exact quantification is available, it can be surmised from this and previous work that the interaction parameter (χ) between PMMA and PBzMA is reasonably low.[93] This is likely due to the chemical similarity between the two methacrylate polymers, making them relatively miscible. The likely magnitude and estimates from the literature of χ parameters

are summarised below for all the polymer block pairs (**Table 4.2**). Given the overall molecular weights targeted here, a value approximately of $\chi > 0.02$ should be significant enough to satisfy the thermodynamic prerequisite for self-assembly (χN > 10.5). It is likely that the value of $\chi_{PMMA/PBzMA}$ is very close to this lower limit. Furthermore, even when this criterion is satisfied, the thermodynamic driving force for self-assembly will be minimal in this block copolymer. This greatly reduces the chance of successfully forming consistent three-phase morphologies in any resulting triblock materials.

Table 4.2: *Summary of the Flory-Huggins interaction parameters (χ) between the different polymer blocks.^{a}*

	Interaction Parameter Pairings (χ)			
	PMMA	*PBzMA*	*PS*	*P4VP*
PMMA		Likely low	0.04	0.08
PBzMA	Likely low		-	Likely high
PS	0.04	-		0.40
P4VP	0.08	Likely high	0.40	

^{a} χ values are close estimates found in the literature ($\chi_{PMMA/PS} = 0.04$,[94] $\chi_{PMMA/P4VP} = 0.08$,[95] $\chi_{PS/P4VP} = 0.4$)[95]. A $\chi_{PBzMA/PS}$ value is not given as no proposed triblock copolymer composition contains both these polymer blocks.

From this, it was hypothesised that any PMMA-*b*-PBzMA-*b*-P4VP triblock copolymers may not reliably phase separate into the desired complex morphologies unless extremely high molecular weights were targeted. Therefore, only the PS block was used to investigate triblock copolymer self-assembly. The three χ parameters for this triblock system are known making self-assembly much more reliable.

4.4.2. One-Pot Synthesis of PMMA-*b*-PS-*b*-P4VP

With the chemical composition of the triblock copolymer decided, the next step was to synthesise a series of copolymers to investigate their self-assembly behaviour. Triblock copolymers were synthesised with varying block fractions to influence the self-assembly behaviour and produce a range of morphologies. As stated previously, the block fraction of P4VP would be kept constant (~25 wt%) due to its importance in the nanofabrication of metal oxides. This also made direct comparison to the previous PMMA-*b*-P4VP diblock copolymer possible. Details of the targeted block compositions are given in **Table 4.3**.

Table 4.3: *Summary of target block compositions for the PMMA-b-PS-b-P4VP triblock copolymers.*

Triblock Copolymer	Total $M_{n\ Target}$ (kg mol⁻¹)	Copolymer Target Composition		
		PMMA (kg mol⁻¹)	PS (kg mol⁻¹)	P4VP (kg mol⁻¹)
TC1	100	25	50	25
TC2	100	37.5	37.5	25
TC3	100	50	25	25

PMMA-*b*-PS-*b*-P4VP copolymers were first synthesised using a one-pot dispersion method (**Figure 4.13**), described in **Section 4.3.2**. This was an extension of the previous method used for diblock copolymer synthesis, with an additional sample collection (for the diblock intermediate) and monomer injection step. It was already established that after a reaction time of 72 hours, high conversion of the styrene monomer could be achieved (> 98%). Hence, it could be assumed that 4VP would be added to the end of the diblock copolymer chains with minimal block tapering by copolymerisation with residual unreacted styrene monomer.
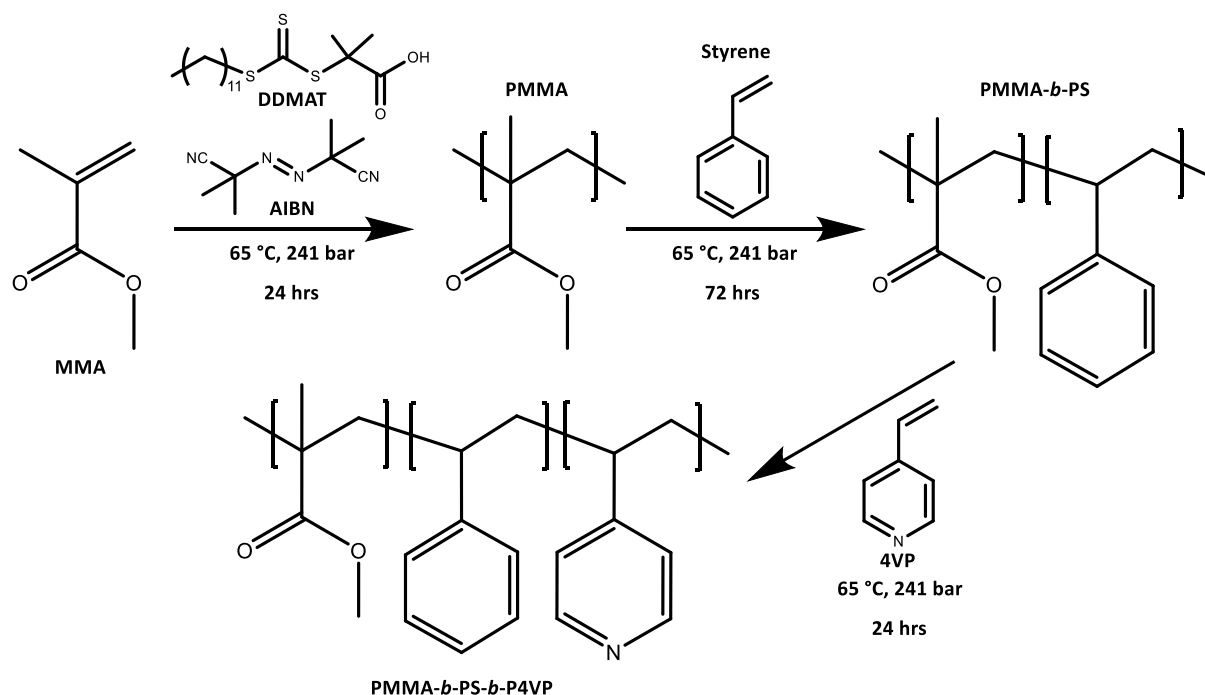
Figure 4.13: *Reaction scheme for the one-pot synthesis of PMMA-b-PS-b-P4VP in scCO₂. Polymer structures are simplified and do not include the RAFT or initiator end groups.*

The one-pot procedure was applied successfully to synthesise the TC2 and TC3 triblock copolymer compositions, however, this proved unfeasible for TC1. This was caused by

limitations in using a fixed volume autoclave to conduct the polymerisations in scCO$_2$. Firstly, a minimum volume of monomer is required to successfully polymerise a monomer (~5 g in the 60 mL autoclave). A low monomer loading results in a low monomer concentration in the scCO$_2$ dispersion, leading to a lower reaction rate and therefore incomplete polymerisation. Secondly, the reaction is limited to a maximum volume of monomer due to the fixed capacity of the autoclave. Injecting large volumes of monomer into a scCO$_2$ dispersion can dramatically increase the pressure in the vessel to levels that are unsafe.

Due to the low target molecular weight of the PMMA in TC1 and subsequent large molecular weight of the PS and P4VP blocks, there was no way to avoid one of the two limits described above. Either too large an amount of styrene would need to be added to the 25 kg mol^{-1} PMMA macro-RAFT agent, or too small a quantity of MMA would be needed in the first stage to reduce the amount of styrene added. This was later solved by employing a staggered two-pot synthesis, described later in this chapter.

One-pot syntheses of the triblock copolymers were performed using the procedure described in **Section 4.3.2**. MMA was polymerised for 24 hours with a 0.5:1 molar ratio of AIBN to DDMAT RAFT agent, before injecting the desired amount of styrene for 72 hours. Finally, 4VP was injected and polymerised for a further 24 hours. Intermediate polymer samples were collected from the outlet tap prior to each monomer injection to assess their molecular weight. GPC chromatograms of the polymer products are shown below (**Figure 4.14**), and the experimental molecular weight data are summarised (**Table 4.4**).

Table 4.4: Summary of molecular weight, dispersity and block fraction data for the PMMA-b-PS-b-P4VP triblock copolymers synthesised using the one-pot procedure.[a]

Triblock Copolymer	PMMA		PMMA-*b*-PS		PMMA-*b*-PS-*b*-P4VP		Polymer block ratios (wt%) [c]
	$M_{n\,exp}$ [b] (kg mol^{-1})	$Đ$ [b]	$M_{n\,exp}$ [b] (kg mol^{-1})	$Đ$ [b]	$M_{n\,exp}$ [b] (kg mol^{-1})	$Đ$ [b]	
TC1			N/A				
TC2	37.9	1.33	62.0	1.61	76.4	1.50	39 : 38 : 23
TC3	56.1	1.22	62.9	1.79	77.2	1.71	60 : 19 : 21

[a] *Conditions: 6 g of MMA polymerised at 65 °C and 241 bar for 24 hrs, then 3-6 g of styrene added for another 72 hrs, then 3-4 g of 4VP added for a final 24 hrs.* [b] *Obtained from GPC, eluting in chloroform/ethanol/TEA solvent mixture, measured with dRI detector calibrated against PMMA narrow standards.* [c] *Obtained from ¹H NMR integrations.*
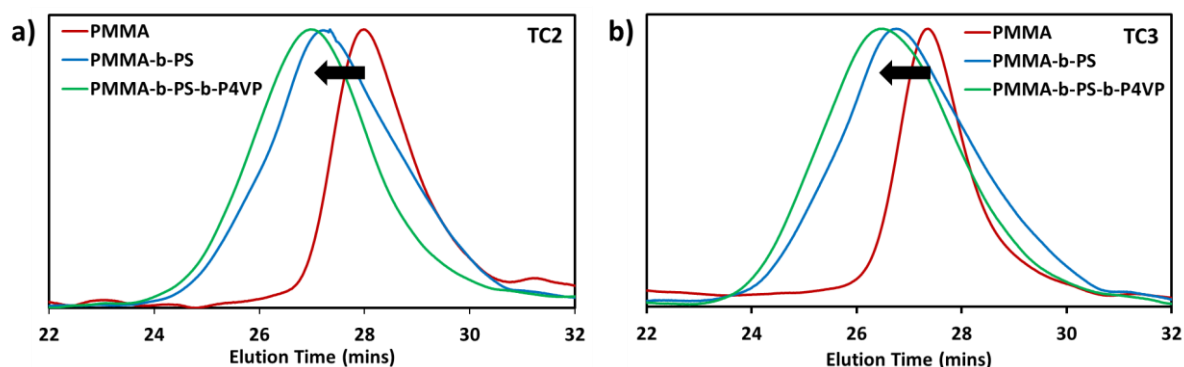
Figure 4.14: *GPC chromatograms at each stage of the polymer growth for PMMA-b-PS-b-P4VP triblock copolymer, with the (a) TC2 composition and (b) TC3 composition.*

Experimentally observed molecular weights deviated from the target composition values, likely due to several factors. The first clear error in experimental values was found by comparing the Đ values of the PMMA-*b*-PS diblock intermediates to their resulting triblock copolymers. A decrease in molecular weight dispersity was observed when adding the final block, a physical impossibility. It was theorised that this was a caused by contamination during the first sample collection through the high-pressure outlet tap. After using this tap to obtain small samples of the PMMA macro-RAFTs, the tap and adjoining pipework were likely contaminated with these PMMA samples when the second PMMA-*b*-PS samples were taken. Therefore, the resulting diblock copolymer samples were expected to be a mixture of PMMA and PMMA-*b*-PS, hence the large Đ and lower than expected $M_{n\,exp}$ values. Though low $M_{n\,exp}$ was also expected as GPC measurements were compared to pure PMMA standards.

PMMA contamination was further verified by calculating the weight percentage of PS in the PMMA-*b*-PS samples using integrals of the assigned ^{1}H NMR peaks (**Figure 4.15**). A reduction in relative PS weight percent was noted between the diblock samples and the final triblock products (2 wt% reduction in TC2, 6 wt% reduction in TC3). This indicated the PMMA-*b*-PS samples were diluted with excess PMMA during the sampling process, assuming no further PS polymerisation occurred after the sample was taken.
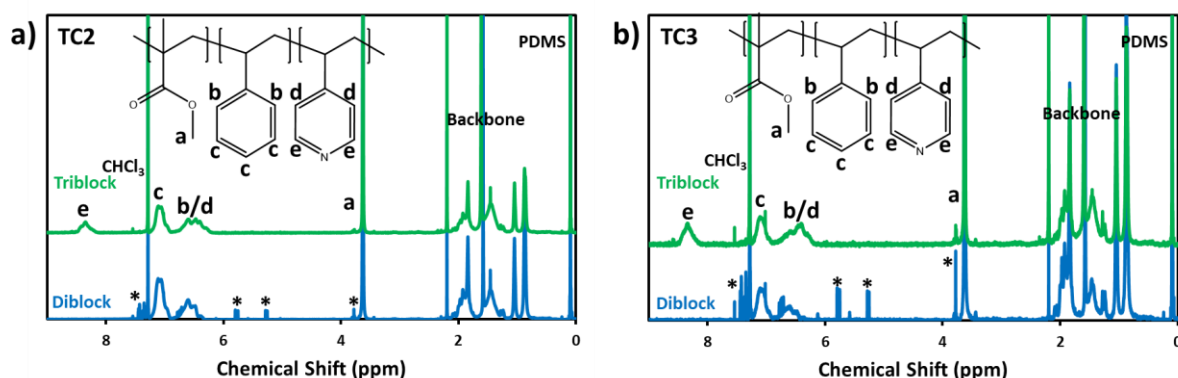
Figure 4.15: *¹H NMR spectra and assignments for the PMMA-b-PS (blue) and PMMA-b-PS-b-P4VP (green) for the (a) TC2 composition and (b) TC3 composition. * Assignments relate to small residual amounts of monomer, expected as part of the sampling process.*

For the TC3 sample, a low overall PS weight percentage was observed as well as a higher Đ (Đ = 1.71). Overlap of the diblock and triblock GPC peaks with the PMMA peak were also visible, indicating the sample contains a higher quantity of unwanted homopolymer. It was predicted that the lower quantity of styrene injected (3 g) to form the target 25 kg mol⁻¹ block could have led to a low polymerisation rate, and subsequently low PS fraction in the final triblock copolymer. Homopolymerisation of the styrene may also have been favoured. Nevertheless, a shift in the GPC peak maximum position at each stage of the polymerisation did indicate a sizable portion of block copolymer was formed during the reaction.

Microstructural features of the triblock copolymers were assessed by SEM analysis (**Figure 4.16**). SEM images showed both triblock samples consisted of well-defined particles with d_n values approximately equal to the previously synthesised diblock copolymers. A slightly larger particle size distribution in seen for TC2 (CV = 33%). This could be caused by some disparity in particle growth during the reaction or the seeding of small homopolymer particles. It is difficult to draw a definitive conclusion from the small sample size used for SEM analysis. However, the images do indicate a reasonable stable dispersion is maintained even when including an extra monomer injection step.
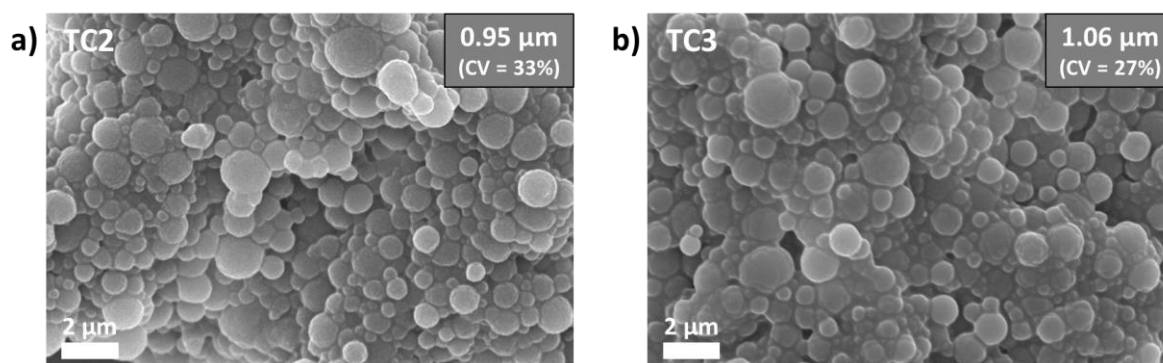
Figure 4.16: *SEM micrographs of the PMMA-b-PS-b-P4VP triblock copolymers with the (a) TC2 composition and (b) TC3 composition.*

4.4.3. Two-pot Synthesis of PMMA-*b*-PS-*b*-P4VP

For synthesis of triblock copolymers with low weight fractions of the starting PMMA block, a two-pot synthetic method was proposed. The method was a seeded dispersion-type heterogeneous process, by which a pre-synthesised microparticulate PMMA macro-RAFT agent is re-dispersed in scCO₂ with the aid of additional PDMS-MA stabiliser. After a stable dispersion is formed, the living nature of the PMMA chains can then be utilised to form block copolymers upon high-pressure injection of the subsequent monomers and initiator.

This two-pot seeded dispersion method has been utilised by the Howdle group previously to synthesise diblock copolymers.[96] The method was first developed as a way to grow multiple block copolymers from a single PMMA macro-RAFT, thus increasing sample reproducibility. Here, the procedure was applied as a solution to the limitations of the fixed volume autoclave, described in the previous section. Using this method, a small quantity of pre-synthesised PMMA macro-RAFT can be re-dispersed, allowing higher quantities of additional monomers to be added without overfilling the high-pressure autoclave. As a result, low weight fraction PMMA block copolymers, such as the TC1 composition, could be synthesised.

The two-pot method, described in **Section 4.3.3**, was applied to synthesise all three triblock copolymer compositions. TC2 and TC3 composition triblock copolymers were re-synthesised to directly compare the two synthetic methods. Polymers synthesised using the two-pot method are identified by addition of a 2P superscript at the end of the composition code. The different molecular weight PMMA macro-RAFT agents were redispersed for a minimum of one hour with a quantity of PDMS-MA stabiliser equal to 5 wt% with respect to the mass of

subsequent styrene and 4VP monomers to be added, to allow for adequate particle growth. PMMA-*b*-PS intermediate samples were taken from the outlet tap prior to the 4VP addition. GPC chromatograms of the polymer products are shown below (**Figure 4.17**), and the experimental molecular weight data are summarised (**Table 4.5**).

Table 4.5: *Summary of molecular weight, dispersity and block fraction data for the PMMA-b-PS-b-P4VP triblock copolymers synthesised using the two-pot procedure.*[a]

Triblock Copolymer	PMMA		PMMA-*b*-PS		PMMA-*b*-PS-*b*-P4VP		Polymer block ratios (wt%) [c]
	$M_{n\,exp}$ [b] (kg mol⁻¹)	$Đ$ [b]	$M_{n\,exp}$ [b] (kg mol⁻¹)	$Đ$ [b]	$M_{n\,exp}$ [b] (kg mol⁻¹)	$Đ$ [b]	
TC1²ᴾ	25.3	1.26	49.7	1.49	74.8	1.59	27 : 52 : 21*
TC2²ᴾ	42.1	1.23	48.5	1.45	92.1	2.85	38 : 33 : 29*
TC3²ᴾ	53.1	1.20	60.9	1.44	73.1	2.29	52 : 22 : 26

[a] *Conditions: 3-6 g of PMMA macro-RAFT seed dispersed with PDMS-MA in scCO₂ at 65 °C and 241 bar, then 3-6 g of styrene added for 72 hrs, then 3 g of 4VP added for a final 24 hrs.* [b] *Obtained from GPC, eluting in chloroform/ethanol/TEA solvent mixture, measured with dRI detector calibrated against PMMA narrow standards.* [c] *Obtained from ¹H NMR integrations.*

*The values here correspond to the relative quantity of each polymer only, as these products cannot be consider to be triblock copolymers.
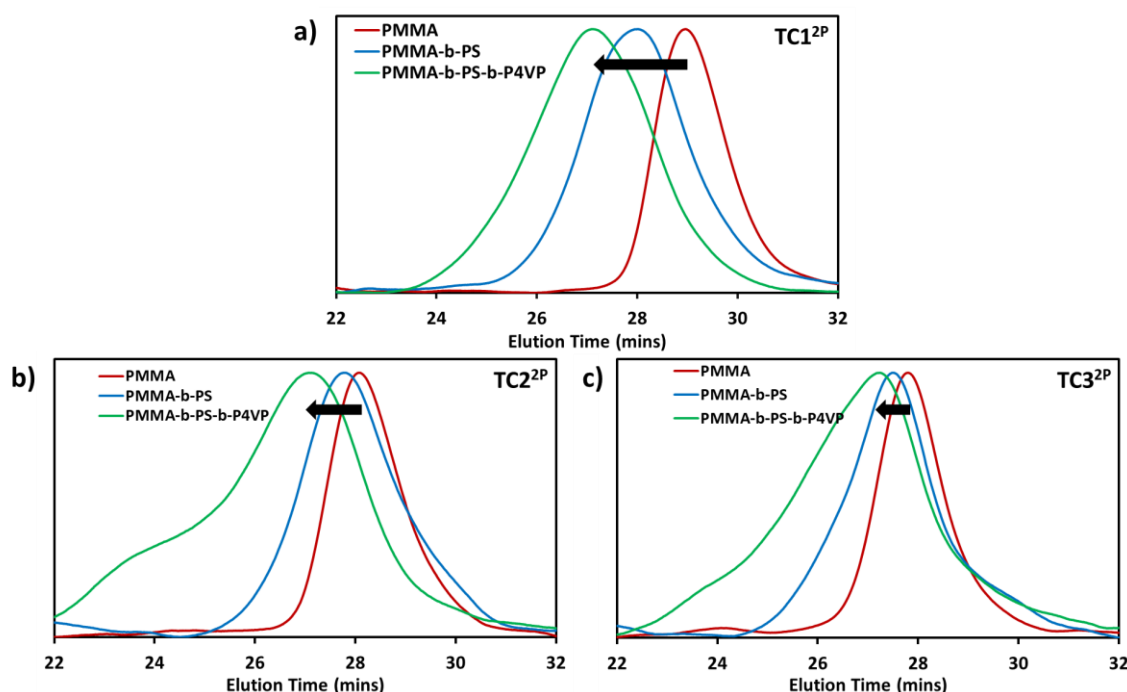
Figure 4.17: *GPC chromatograms at each stage of the polymer growth for PMMA-b-PS-b-P4VP triblock copolymer, via the two-pot method, with the (a) TC1²ᴾ, (b) TC2²ᴾ and (c) TC3²ᴾ composition.*

The TC1^{2P} composition showed excellent chain extension of the PMMA macro-RAFT with the styrene and 4VP monomers, evident by clear shifts in each sample GPC peak. The molecular weight increased in each step with a relatively low increase in Đ. $M_{n\ exp}$ values were slightly below the target values for the diblock and triblock copolymer samples, as in the one-pot syntheses. As before, this can be attributed to inaccuracies by comparing the sample elution times to pure PMMA standards. Again, sample composition was confirmed by integrating ^{1}H NMR peaks to show approximate target weight fractions were achieved. ^{1}H NMR spectra for all samples were identical to those presented for the one-pot triblock copolymers in the previous section.

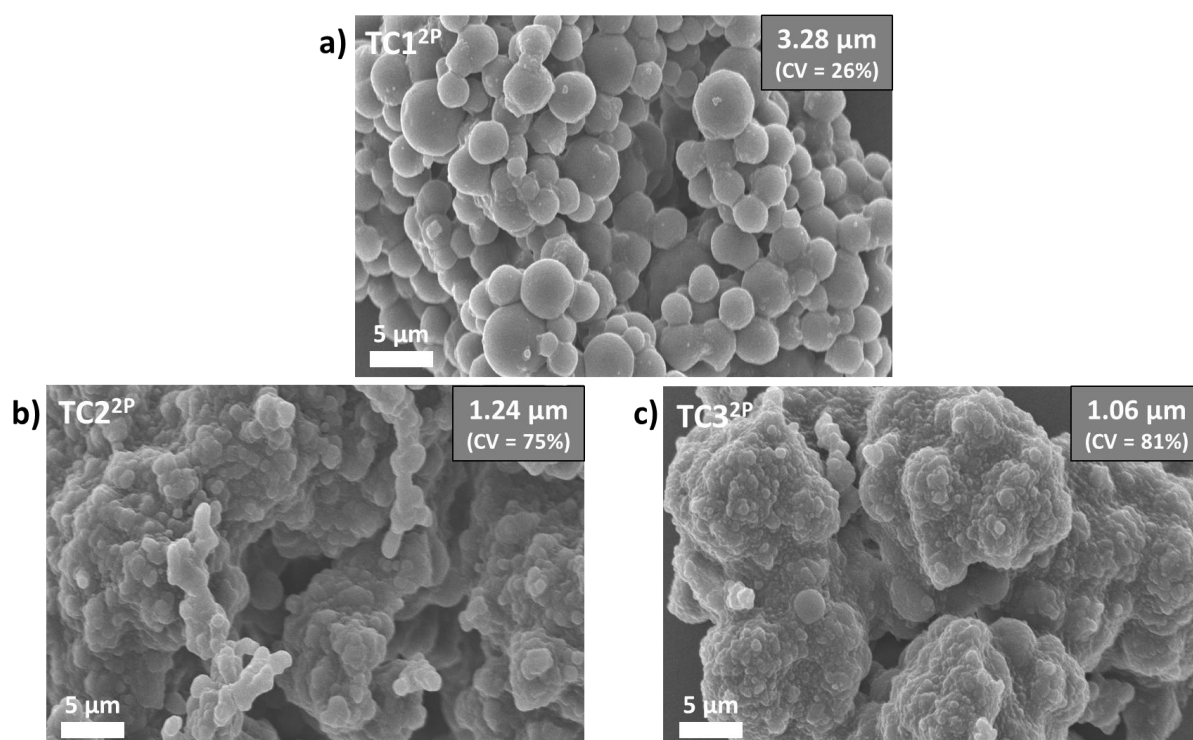Analysis of both the TC2^{2P} and TC3^{2P} composition samples revealed the polymerisations proceeded predominantly by uncontrolled free-radical mechanisms. The diblock samples show a minimal increase in molecular weight when compared to their respective PMMA macro-RAFT agents. Though overall Đ remains low, this is an indication that a sizable portion of the styrene monomer formed low molecular weight homopolymer instead of polymerising onto the PMMA chain ends. In the final samples, uncontrolled homopolymerisation was more evident. High molecular weight shoulders can be seen in the GPC traces as well as a considerable increase in Đ (Đ > 2). Regardless of a shift in the GPC peak maximum being visible, this was a clear indication that a large quantity of P4VP homopolymer was formed and triblock copolymers were not successfully synthesised.

SEM analysis was performed to assess the microscale morphology of the synthesised triblock copolymers (**Figure 4.18**). While TC1^{2P} was found to consist of well-defined particles with a reasonably low size dispersity, the TC2^{2P} and TC3^{2P} samples were far less uniform. Though mostly well-defined particles were visible throughout, two distinct particle size distributions were visible, leading to the considerably higher CV values. A collection of large particles was observed, covered in a sizable number a smaller particle (< 1 μm). The larger particles are expected to be the PMMA seed particles, possibly grown with some additional monomer, while the smaller particles are likely styrene/4VP homopolymer particles formed in a secondary nucleation step. This may indicate that the seed particles for these reactions were not efficiently re-dispersed before addition of the styrene, encouraging the formation of homopolymer and subsequent nucleation of small homopolymer particles.

Figure 4.18: *SEM micrographs of the PMMA-b-PS-b-P4VP triblock copolymers synthesised via the two-pot method with the (a) TC1²P, (b) TC2²P and (c) TC3²P compositions.*

Additionally, of note from the SEM analysis was the increase in average particle size between the TC1²P sample and those synthesised using the one-pot procedure. This is due to a greater number of seeded PMMA particles formed in the first step of the one-pot syntheses. While, in contrast, a low number of PMMA particle seeds are available in the two-pot synthesis as only 3 g of pre-made PMMA particles are re-dispersed. Thus, the subsequent monomers are forced to polymerise in fewer particles and lead to a greater particle size increase.

4.4.4. Morphological Analysis

The self-assembly behaviour of the synthesised triblock copolymers was investigated in detail to look for and assign any three-phase morphologies. Only the TC1²P, TC2 and TC3 samples were selected for analysis, due to the lack of block copolymer formed in the TC2²P and TC3²P samples.

Firstly, the compositions of the triblock copolymers were used to quantify important parameters underpinning the nature of the polymer self-assembly. Weight fraction data were converted to volume fractions ($f_{Polymer}$) for each polymer block. These are fundamental parameters for determining the preferred morphology.[3] Volume fractions were estimated

using the known polymer densities (ρ) at ambient conditions and then applying reported swelling factors for each polymer in scCO$_2$ (**Table 4.6**). Swelling data for polymers in scCO$_2$ is limited and varies between studies, with some data for polymers only available at lower temperatures and pressures than those applied in these syntheses.[97-99] Hence, the volume fractions calculated here are only rough approximations.

Table 4.6: Summary of estimated block volume fractions for the PMMA-b-PS-b-P4VP triblock copolymers, based on scCO$_2$ swelling.[a]

Triblock Copolymer	Polymer block ratios (wt%)	Estimated Copolymer Composition		
		f_{PMMA} (vol%)	f_{PS} (vol%)	f_{P4VP} (vol%)
TC1^{2P}	27 : 52 : 21	28	51	21
TC2	39 : 38 : 23	40	37	23
TC3	60 : 19 : 21	61	18	21

[a] Volume fraction estimates calculated by converting weight fraction data to volume based on known polymer densities (ρ_{PMMA}: 1.16 g cm^{-3}, ρ_{PS}: 1.05 g cm^{-3}, ρ_{P4VP}: 1.11 g cm^{-3}), factoring in approximate volume swelling caused by scCO$_2$ (PMMA: 24.8 $\Delta V/V\%$,[97] PS: 9.4 $\Delta V/V\%$,[98] P4VP: 15 $\Delta V/V\%$[99]).

The calculated volume fractions are almost identical to the measured weight fractions. This is mostly a result of to the offsetting of the PS block's low density with its minimal swelling with addition of scCO$_2$. Based on previous phase behaviour studies of diblock copolymers in scCO$_2$,[93] it is predicted that the f_{PMMA} values are underestimates. This is because a large discrepancy is seen between experimentally observed morphologies for methacrylate-styrenic block copolymers in scCO$_2$, and their thermodynamically favoured morphologies. This is due to the higher degree of swelling in methacrylate polymers in comparison to styrenics, which may be underestimated in these calculations due to lack of reliable data at the conditions used.

The other key parameters for determining favoured polymer morphologies are the χN factors (**Table 4.7**). In diblock copolymers, this is only useful to confirm whether self-assembly is thermodynamically favourable ($\chi N > 10.5$). However, in ABC triblock systems, comparing the relative magnitudes of each block pair's χN value can give insight into the more favourable morphology. χN values were calculated using χ values from the literature.[94, 95] Values for $\chi_{PMMA/P4VP}$ and $\chi_{PS/P4VP}$ are approximations, as no temperature independent χ values could be found for these pairings.

The degree of polymerisation (*N*) for each polymer block was calculated using a volumetric method described in self-consistent field theory studies of block copolymers.[100] This allows for a closer comparison between other triblock copolymer systems studied in the literature. Block molecular weight is calculated by multiplying the total M_n from GPC by the measured weight fraction ($w_{polymer}$) from NMR. The absolute degree of polymerisation is then calculated from the polymer density (ρ), a common monomer reference volume (v_0) of 118 Å^3 and Avogadro's number (N_A) (**Equation 4.1**). The relevant χ value is then multiplied by the sum of the two corresponding $N_{polymer}$ values, to give the final χ*N* factors (**Equation 4.2**).

$$N_{Polymer} = \frac{M_n \cdot w_{polymer}}{\rho v_0 N_A}$$

Equation (4.1)

$$\chi_{ab} N = \chi(N_a + N_b)$$

Equation (4.2)

Table 4.7: Summary of estimated block interaction parameters for the PMMA-b-PS-b-P4VP triblock copolymers.[a]

Triblock Copolymer	$M_{n\ exp}$ (kg mol^{-1})	Polymer block ratios (wt%)	Estimated Interaction Parameters (χ*N*)		
			$\chi_{PMMA/PS}N$	$\chi_{PMMA/P4VP}N$	$\chi_{PS/P4VP}N$
TC1^{2P}	74.8	27 : 52 : 21	30	35	290
TC2	76.4	39 : 38 : 23	30	50	245
TC3	77.2	60 : 19 : 21	30	60	160

[a] χ*N* values calculated using χ values from the literature ($\chi_{PMMA/PS}$ = 0.04,[94] $\chi_{PMMA/P4VP}$ = 0.08,[95] $\chi_{PS/P4VP}$ = 0.4)[95] and a common monomer reference volume of 118 Å^3. Values do not account for scCO$_2$ swelling and are rounded to the nearest multiple of 5.

Calculated $\chi_{PMMA/PS}N$ values remained approximately the same through all samples and therefore should have no bearing on any frustrations in the three-phase morphologies. This is to be expected as the target M_n for all PMMA-*b*-PS diblock copolymers was constant. The $\chi_{PMMA/P4VP}N$ and $\chi_{PS/P4VP}N$ values change as the composition of the triblock copolymers gradually shifts from a lower PMMA composition to a higher one, reflecting the relative changes in block chain lengths. The $\chi_{PS/P4VP}N$ values were found to be the largest by far in all sample compositions, owing to the considerably higher incompatibility between the PS and P4VP blocks. This means any resulting three-phase morphologies should disfavour any contact between PS and P4VP interfaces. Information that will help assign any morphologies with greater certainty.

Visual inspection of the triblock copolymer nanostructures was achieved by TEM analysis of thin particle cross-sections stained with I$_2$ vapour (**Figure 4.19**). I$_2$ vapour selectively binds to the pyridinyl nitrogen, causing the P4VP sections of the morphology to appear darker, leaving the PMMA and PS sections lighter and indistinguishable from one another. Though the I$_2$ stained TEM images do not give a complete view of any three-phase morphologies, they do give necessary insight into changes in the P4VP phase in comparison to the PMMA-*b*-P4VP diblock system. These morphological changes will ultimately affect the morphology of any fabricated inorganic material.
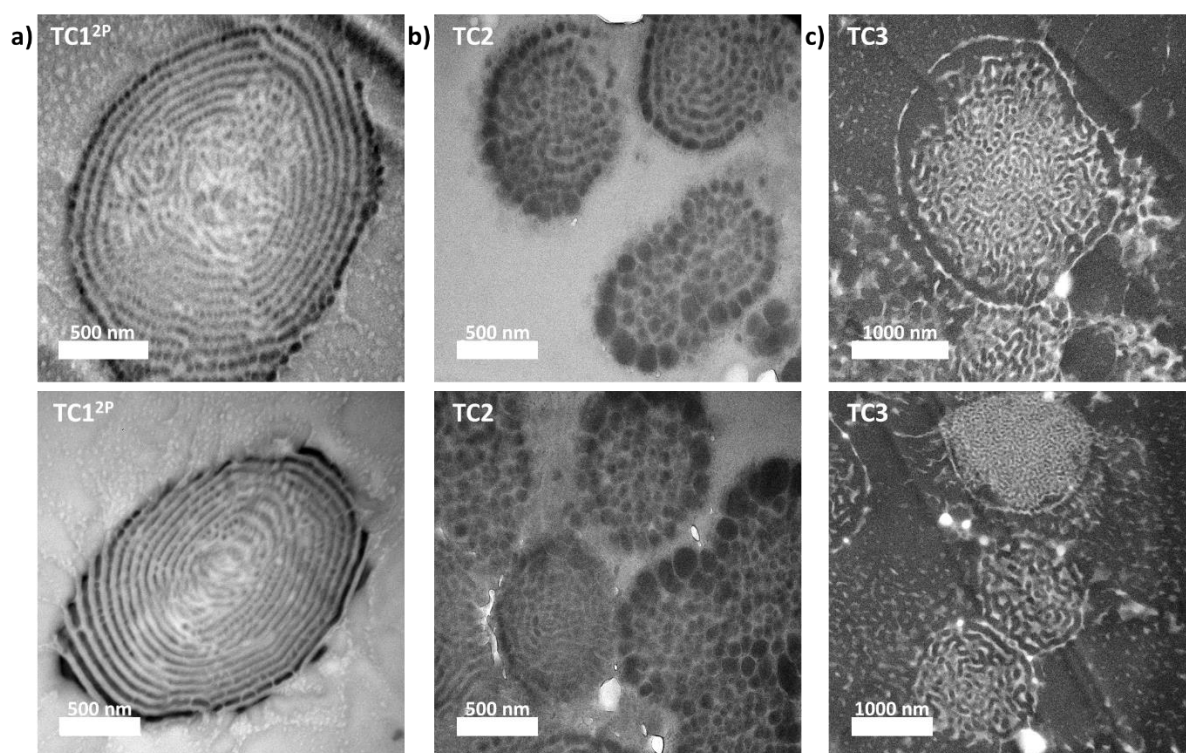
Figure 4.19: *TEM cross-sectional micrographs of the PMMA-b-PS-b-P4VP triblock copolymers with (a) TC1^{2P}, (b) TC2 and (b) TC3 composition. All TEM sections were stained with I$_2$ vapour to improve contrast by darkening the P4VP blocks. PMMA and PS block remain lighter and indistinguishable.*

The TC1^{2P} sample composition presented a complex morphology not seen before in diblock copolymer samples. The P4VP block was seen to be arranged in lamellar rings running through the microparticles, similar to the "onion-like" morphology seen for lamellar-forming diblock copolymers. However, the morphology presented an added degree of complexity as the P4VP forms distinct spherical domains in the lamellae, rather than forming continuous unbroken rings. The combination of spherical and lamellar features suggests formation of a three-phase

morphology as this blend of structural features would not be possible in a diblock copolymer. The morphology also appeared to break down slightly towards the particle centre, leading to a more randomly disordered distribution of P4VP domains. This is likely caused by the increased spatial constraint imposed towards the centre of the microparticles.

The TC2 sample presented a morphology very similar to the spherical morphology seen in PMMA-*b*-P4VP diblock copolymers. Dark nanoscale spheres could be seen within the microparticles, with a lighter PMMA/PS matrix. However, the spherical domains did demonstrate some inconsistency between particles, with some more oval shaped domains visible and noticeably irregular packing in some cases. The available observations suggest a morphology similar to the diblock spherical morphology is formed, with some added irregularity potentially caused by lack of uniformity in the polymer chains. Alternately, this may be caused by the composition's close proximity to a phase boundary between favoured morphologies.

The TC3 sample revealed a very different morphology. The P4VP regions in this sample appeared to be longer and more entangled with the PMMA/PS matrix, a morphology more closely related to the bicontinuous gyroid seen previously in PMMA-*b*-PBzMA diblock copolymers.[93] However, it is challenging to deduce how the PMMA and PS domains may be arranged in the particles, based on these TEM images. As in the TC2 sample, the particles appeared to suffer from some morphological inconsistencies between particles, likely due to the polymer's high Đ (1.71). Hence, considering the lack of regular discernible structure and the rather high molecular weight dispersity, it is not possible to characterise this sample as having a regular ordered self-assembled morphology.

An artefact was noticed in all TEM images for the TC3 sample; the surrounding resin of the particles appeared dark and gave a similar contrast to that expected of the I_2 stained regions. This may have been caused by over-focusing the section in the TEM, an effect known to invert the image contrast. Therefore, for these images, the lighter regions of the image should be taken to be the P4VP domains. This does not influence assessment of the internal morphology observed in the polymer.

In the future, further morphological information may be gained by applying alternate staining procedures to the cut sections. Samples could instead be exposed to a RuO_4 vapour to stain

both the P4VP and PS domains. Performing this analysis in parallel with the I_2 staining could allow each unique polymer phase to be visualised. However, due to time constraints on this study, this analysis was not performed.

To confirm the existence of three distinct polymer phases in each triblock copolymer morphology, thermal characterisation was performed to identify T_g values for each sample. Phase separated polymer materials undergo distinct glass transitions for each polymer phase, whereas blended polymers only exhibit a single transition at an intermediate temperature somewhere between the two component T_g values.[101] Sample T_g values were determined by DSC characterisation and data analysis using the instrument software (**Figure 4.20**).
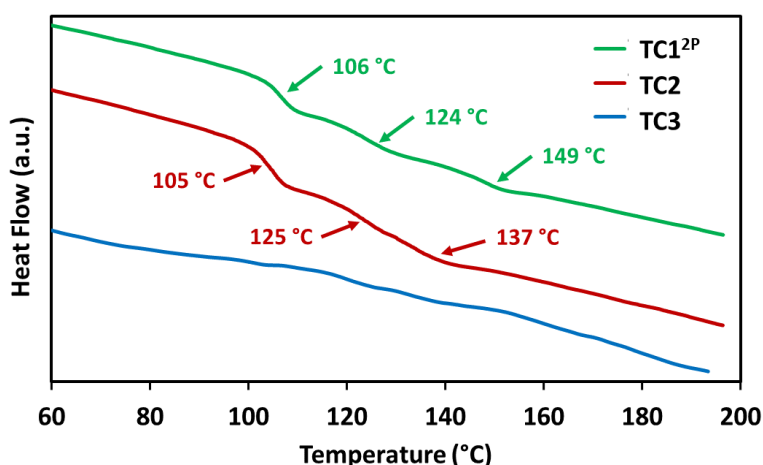
Figure 4.20: *DSC heat flow plots for the PMMA-b-PS-b-P4VP triblock copolymers. Step transitions indicating T_g points are labelled. Sample data are staggered on the y-axis for greater clarity.*

For the triblock compositions TC1^{2P} and TC2, three distinct T_g values were recorded, indicating three separate polymer phases were present in the samples. T_g values for TC1^{2P} showed good agreement with literature values for the PS (106 °C), PMMA (124 °C) and P4VP (149 °C) blocks.[102] However, the observed P4VP T_g for the TC2 sample was slightly lower (137 °C), indicating this block may be partially blended with one of the other lower T_g blocks. No discernible step transitions were observed for the TC3 composition due to excess noise in the data.

Finally, SAXS analysis was performed on the powdered samples (**Section 2.3.5**) in an attempt to gain further insight into the nature of the triblock morphologies (**Figure 4.21**). SAXS analysis is a highly complementary technique to TEM analysis. While TEM provides useful visual

representations of nanostructures for a very small quantity of sample, SAXS is an average measurement of a much larger quantity of sample, helping to confirm persistence of morphology throughout the whole sample.
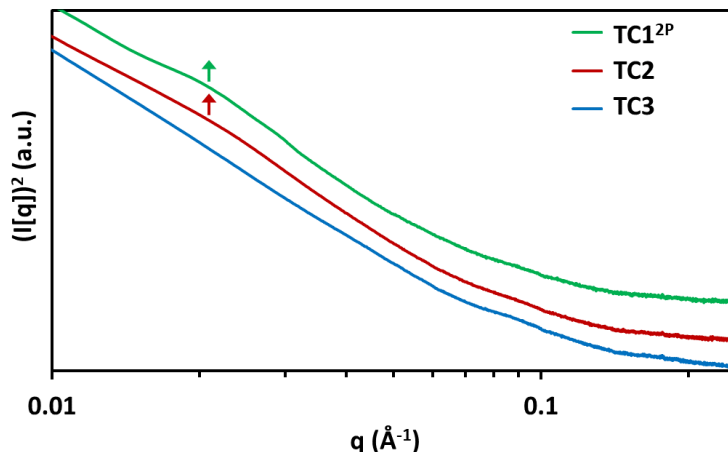
Figure 4.21: *1D SAXS data for the PMMA-b-PS-b-P4VP triblock copolymers, with broad peaks indicated by arrows at q ≈ 0.02 Å^{-1}. Data is plotted against the square of the scattering intensity, I(q), to enhance features at low q. The y-axis is plotted on a logarithmic scale and sample data are staggered on the y-axis for greater clarity.*

SAXS data revealed very subtle, broad features for the TC1^{2P} and TC2 samples, while no scattering was visible for the TC3 sample. Visible peaks at approximately 0.02 Å^{-1} relate to morphology length scale of roughly 30 nm, which is in good agreement with observations from the TEM analysis. Unfortunately, a greater scattering resolution is required to give an idea of the shapes of the morphologies. The poor scattering resolution can be attributed to the presence of the large microparticles, which dominate the scattering profile, since I(q) α V_p^2 (where V_p is the microparticle volume).[103] Low contrast between the three polymer blocks may also have led to poor X-ray scattering.

Nevertheless, internal nanoscale assembly is evident in all TEM images and most SAXS analyses, suggesting the formation of complex polymer morphologies in all cases. However, TEM images and broad SAXS features may suggest there is a low uniformity of the morphologies throughout the individual samples.

More data is needed to attempt to assign an exact morphology for the TC2 and TC3 compositions. The clearer TEM structures observed for the TC1^{2P} composition, along with the

calculated f_{block} and χN values, meant a reasonable conclusion could be made as to the shape of the three-phase morphology, albeit only tentatively. Based on previous studies of ABC-type triblock materials, this morphology is predicted to be a "lamellar with spheres inside a domain" [L+S(II)] type morphology.[21]

For the TC1[2P] composition, the intermediate PMMA-b-PS diblock copolymer is already known to microphase separate to form the simple lamellar morphology, based on previously constructed phase diagrams by the Howdle group.[93] From this, it was postulated that addition of the third block to this structure caused P4VP spherical domains to form in the PMMA lamellar sheets. The P4VP spheres were predicted to form interspersed columns running throughout the PMMA lamellae, connecting the adjacent PS sheets (**Figure 4.22**). The position of the P4VP domains in the PMMA lamellae was based on the lower volume fractions of the two blocks and the high χN value between the PS and P4VP blocks.

a) PMMA-*b*-PS

Addition of
P4VP block

b) PMMA-*b*-PS-*b*-P4VP

■ PMMA	■ PS	■ P4VP

PMMA	28 vol%
PS	52 vol%
P4VP	20 vol%

$\chi_{PMMA/PS}N \approx 30$
$\chi_{PMMA/P4VP}N \approx 35$
$\chi_{PS/P4VP}N \approx 290$
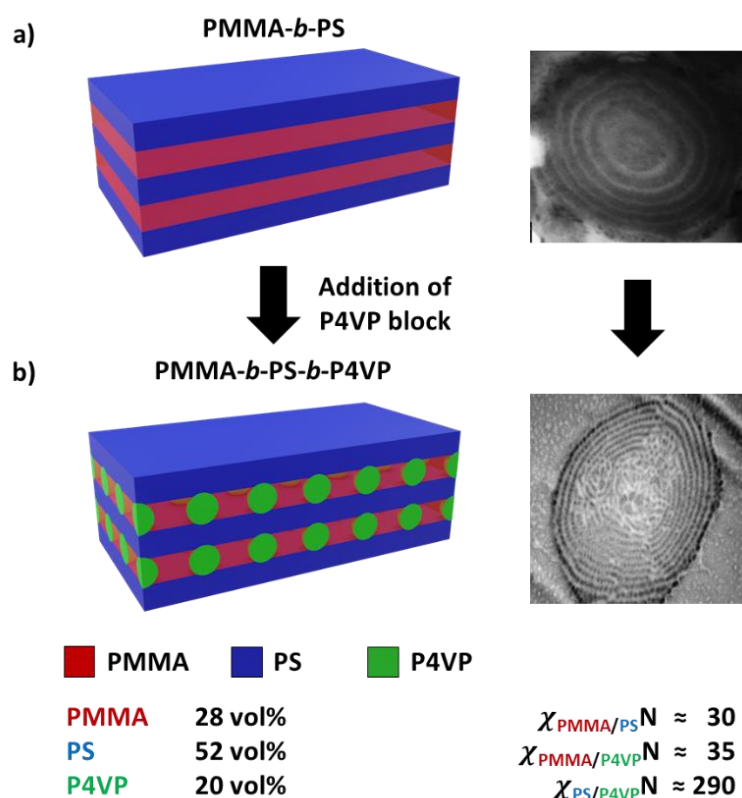
Figure 4.22: Schematic representations and TEM cross-sectional images of (a) lamellar morphology of the PMMA-b-PS diblock copolymer, from previous studies[92, 93] and (b) the proposed lamellar with spheres [L+S(II)] morphology of the TC1[2P] composition PMMA-b-PS-b-P4VP triblock copolymer.

Though this L+S(II) morphology has been reported in the literature, these examples usually form the spherical regions within the central "B" block of the copolymer, rather than the first block as shown above.[3, 21] However, this morphology has only been described for triblock copolymer systems with $\chi_{AC}N \ll \chi_{AB}N \approx \chi_{BC}N$. Alternatively, this PMMA-*b*-PS-*b*-P4VP system follows a $\chi_{BC}N \gg \chi_{AB}N \approx \chi_{AC}N$ regime, making the previous study not directly comparable. Therefore, it is conceivable that the proposed arrangement of the blocks here is accurate, particularly considering the accompanying TEM observations and the calculated self-assembly parameters.

4.4.5. Sol-Gel Synthesis of TiO$_2$

The three characterised PMMA-*b*-PS-*b*-P4VP triblock copolymers were used as structural templates in the sol-gel synthesis of TiO$_2$. It was hoped the three unique morphologies presented for each composition could be translated into the TiO$_2$ functional material. Each polymer was added to hydrolytic sol-gel reactions of titanium tetraisopropoxide (TTIP) in an ethanol solution; an identical synthesis to that reported previously by the Howdle group using a PMMA-*b*-P4VP diblock copolymer template.[69] TTIP precursor is attracted to the ethanol soluble P4VP regions of the polymer and hence TiO$_2$ gelation is confined to the P4VP phase. The target composition of the resulting polymer-TiO$_2$ composite was 25 wt% TiO$_2$, identical to the previous diblock copolymer study.

Sol-gel syntheses were performed following the method described in **Section 4.3.4**. The resulting dried polymer-TiO$_2$ composite materials were taken for microscale structural analysis before calcining at 500 °C to yield the final TiO$_2$ materials. Final TiO$_2$ samples were also taken for analysis by SEM. Initial analysis of all the materials by SEM (**Figure 4.23**) was used to rapidly assess the success of the pattern transfer from triblock copolymer to inorganic material, before the lengthier full analysis.

SEM analysis showed that in the case of the TC1^{2P} and TC3 compositions, the resulting composites retained the microparticle structure of the original templates. Average particle sizes were shown to be slightly higher than the original polymers, owing to the additional TiO$_2$ inserted into the particles. High magnification images showed that for the TC1^{2P} composite, particles contained some surface porosity not seen in the original polymer particles. This new topography is likely a result of the previously reported "swelling induced porosity effect".[104]

Surface P4VP domains are selectively swollen by the ethanol sol-gel solvent, which then collapse to form pores once the solvent is evaporated. No such topography is seen in the TC3 composite microparticles, possibly due to the drastically different morphology of the P4VP in this polymer.
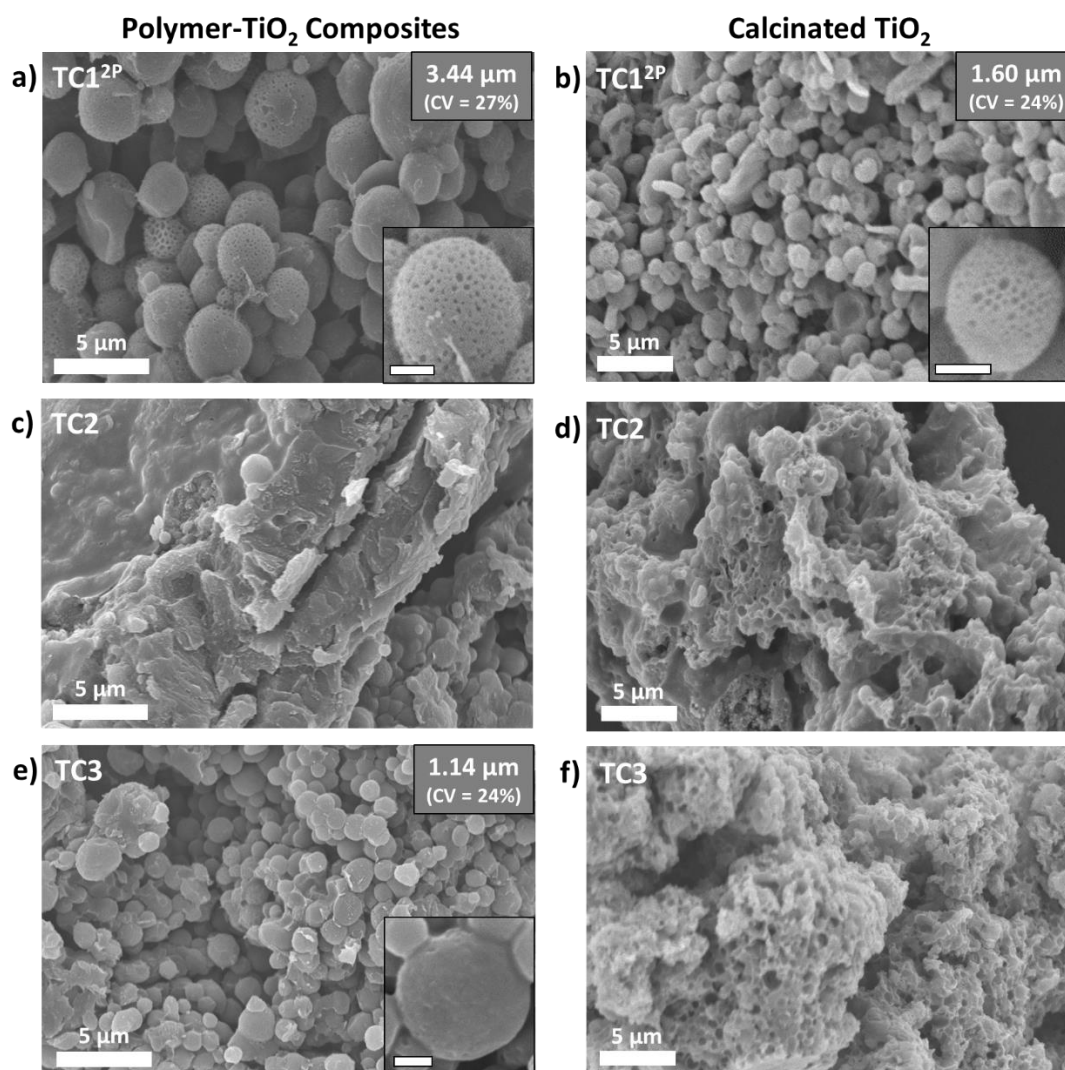
Figure 4.23: *SEM micrographs of the polymer-TiO₂ composites and resulting calcinated TiO₂, using PMMA-b-PS-b-P4VP triblock copolymer templates with the (a/b) TC1²ᴾ, (c/d) TC2 and (e/f) TC3 compositions. The scale bar on the high-resolution inserts is 1 μm.*

Very little microparticle structure was seen for the polymer-TiO₂ composite synthesised using the TC2 composition triblock copolymer. Instead, large amorphous aggregates were observed which may be due to formation of TiO₂ material around the polymer particles, rather than infusion of the inorganic material into the particles.

Upon calcination of the composite materials to form the pure TiO$_2$ products, only the TiO$_2$ synthesised using the TC1^{2P} template retained the microparticle structure. The surface porosity seen in the composite material was also retained. The average particle size was shown to be approximately half that of the original triblock copolymer (1.60 μm), caused by contraction of the TiO$_2$ regions in the composite to fill voids left by the combusted polymer.

TiO$_2$ formed using the TC2 and TC3 polymers did not show any microparticle morphology, though a large degree of microscale surface textures were visible. This may indicate that although the polymer morphologies were not fully translated to the final TiO$_2$, the templates did partially succeed in directing the formation of the TiO$_2$ and avoiding the formation of bulky monolith structures.

The initial analysis of the microscale structure of the products suggest that it may not be possible to employ a single sol-gel synthetic procedure for multiple different polymer morphologies. A more in-depth analysis is required to determine the rate at which the TTIP precursor is infiltrated into each of the triblock copolymer's microparticle structure. It is likely that changes in the nanostructured morphology of each template will alter the rate of infiltration of the solution into the polymer structure. Hence, longer gelation times, or an increased concentration of TTIP, may be required to ensure adequate templating fidelity, depending on how restrictive the morphology is to the movement of the inorganic precursor through the polymer matrix. The process of TTIP infiltration may have to be modelled by examining polymer particles at various timepoints during the sol-gel reaction, to determine their inorganic content.

Due to its desirable microscale features, only the TC1^{2P} sample was taken further for the more in-depth nanoscale morphological analysis. The internal nanoscale morphologies of the polymer-TiO$_2$ composite and final calcinated TiO$_2$ materials synthesised using the TC1^{2P} polymer were analysed by TEM of thin sample cross-sections (**Figure 4.24**). No staining agent was used prior to sample imaging as contrast in these samples was formed by the presence of the heavy titanium atoms.
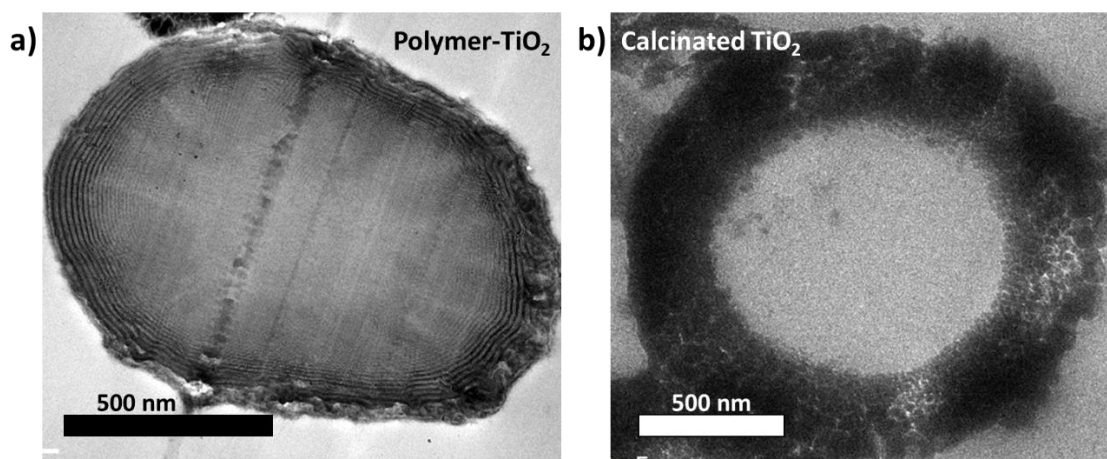
Figure 4.24: *TEM cross-sectional micrographs of the (a) polymer-TiO₂ composite and (b calcinated TiO₂ synthesised using the PMMA-b-PS-b-P4VP triblock copolymer with the TC1²ᴾ composition. Contrast is formed by the presence of the heavier titanium atoms.*

The internal morphology of the polymer-TiO₂ composite proved to be very similar to that of the original triblock copolymer. Dark lamellar rings were observed around the outer shell of the microparticles, with the lamellae slightly broken apart as in the earlier predicted L+S(II) polymer morphology. This proves that the TiO₂ material was selectively incorporated into the P4VP domains of the triblock copolymer. The concentration of TiO₂ was also shown to decrease dramatically towards the particle centres, as seen by the lighter image contrast. The presence of TiO₂ solely within the outer shell of the composite particles was further confirmed by *in-situ* TEM elemental mapping (**Figure 4.25**). The electron beam of the TEM causes excitation of the sample atoms and emission of characteristic X-rays that are then mapped across the sample.
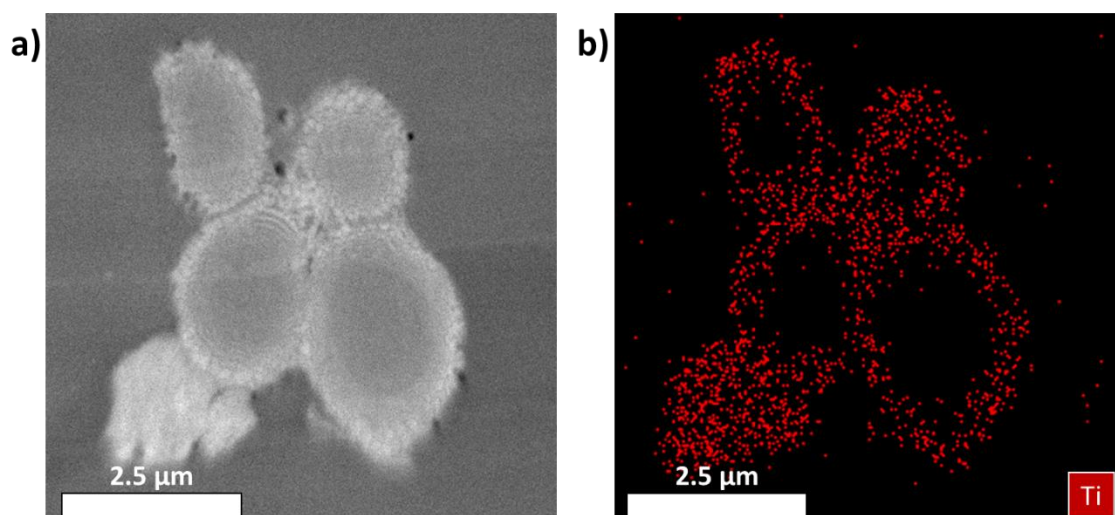
Figure 4.25: *TEM in-situ elemental mapping of TC1²ᴾ polymer-TiO₂ composite material. (a) dark-field micrograph and (b) corresponding elemental map with high concentration of elemental titanium highlighted as red pixels.*

The limited infusion of the TiO₂ through the polymer particles may be caused, in part, by the large microparticle diameters of the TC1²ᴾ polymer samples. However, it is more likely this is a direct result of the triblock copolymer morphology. The presence of the hydrophobic PS lamellae hinders the diffusion of the inorganic precursor into the central P4VP domains. This is clearly seen by the separate and well-defined dark layers of TiO₂ in the composite TEM image.

The internal morphology of the final calcined TiO₂ material was shown to be a rigid shell with a hollow core. The internal voids correlate to the central area of the polymer-TiO₂ composite which did not contain any inorganic material. Thus, the solid polymer core of the composite is fully combusted leading to a central void surrounded by an outer TiO₂ shell. The TEM image also confirms that the porosity seen on the particle surface persists throughout the shell. As the particles would have heated from the outside-inward during the calcination process, the rigid TiO₂ likely begins to form first. The added structure and porosity of the shell would then allow the remaining core polymer material to be extracted out of the particle without the microstructure collapsing. The overall result is a mesoporous hollow-cored microparticle.

4.4.6. Comparison to PMMA-*b*-P4VP diblock copolymer

The hollow-cored TiO₂ microparticles, fabricated using the L+S(II) type morphology of the TC1²ᴾ triblock copolymer, differs significantly with the fully mesoporous TiO₂ fabricated using

a PMMA-*b*-P4VP diblock copolymer (**Figure 4.26**).[69] It was hoped that this new TiO$_2$ morphology would be more advantageous over the previous structure, as hollow TiO$_2$ particles have already proven to be valuable in applications such as dye-sensitized solar cells, photocatalysis and energy storage.[105-107] As such, the remaining chemical and functional characterisation required for the hollow TiO$_2$ sample was performed in direct comparison with the previously synthesised diblock equivalent TiO$_2$ material. The study here focusses on application of the materials in photocatalysis.
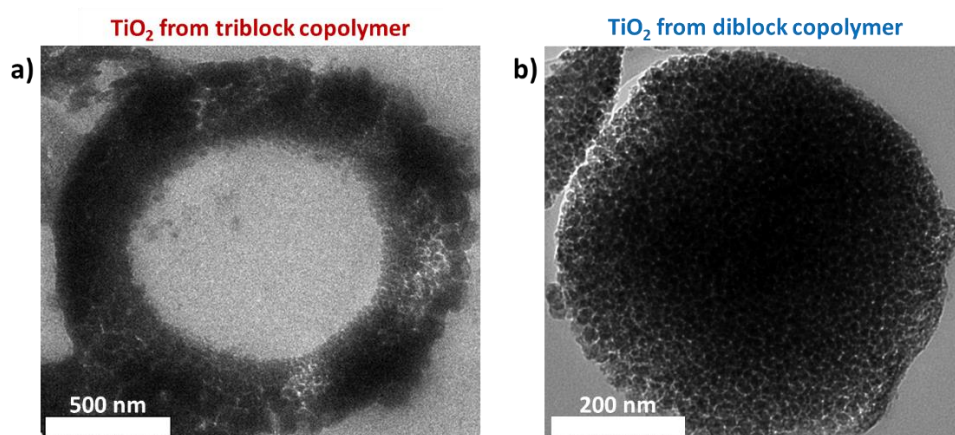
Figure 4.26: *TEM cross-sectional micrographs of the (a) hollow-cored TiO$_2$ synthesised using the TC1^{2P} composition triblock copolymer and (b) mesoporous TiO$_2$ synthesised using an equivalent diblock copolymer.*

Firstly, the purity of the triblock TiO$_2$ sample was assessed, to confirm all polymer had been removed as in the diblock equivalent material.[69] Complete removal of the triblock copolymer template was confirmed by TGA analysis (**Figure 4.27**). The polymer-TiO$_2$ composite was heated to 500 °C and held at this temperature for two hours, a direct comparison to the calcination conditions used to synthesise the final TiO$_2$ material. The final material weight was shown to be 25.2 wt% of the original composite (excluding volatiles), in good agreement with the target TiO$_2$ composition. This is good evidence that the polymer template is fully removed upon calcination, leaving a pure TiO$_2$ product.
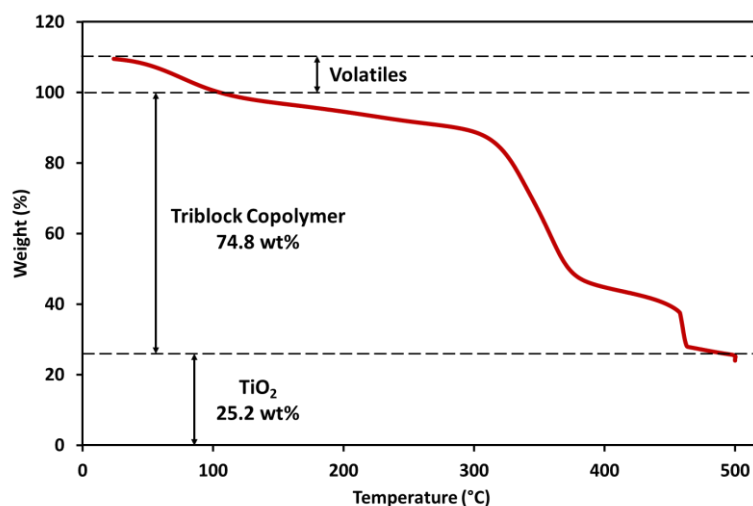
Figure 4.27: *TGA profile for calcination of the polymer-TiO₂ composite using the TC1²ᴾ composition copolymer. Weight percentage is scaled to exclude volatiles (<100 °C). The mass loss at 450 °C is attributed to degradation of the remaining PDMS-MA stabiliser.*

TiO_2 is a polymorphic material, existing in several different crystalline phases. The most common and naturally occurring minerals are known as rutile and anatase, both tetragonal crystal structures; as well as brookite, an orthorhombic structure.[108] Rutile is the most thermodynamically stable phase and can be formed when other metastable crystalline structures are annealed at temperatures above ~600 °C.[109] It is generally accepted that the anatase phase is more efficient as a photocatalyst in comparison to rutile or brookite.[110]

The phase composition of the TiO_2 samples was determined by powder XRD analysis (**Figure 4.28**). Measured diffraction peaks were compared to the known anatase and rutile phase patterns. The weight distribution of the anatase phase ($w_{anatase}$) was quantified using the empirical method of Spurr and Myers (**Equation 4.3**),[111] by comparing the intensities of the anatase (101) peak (I_{A101}) and the rutile (110) peak (I_{R110}). Calculated values are shown below (**Table 4.8**).

$$w_{anatase} = \frac{1}{1 + 1.265 \left(\frac{I_{R110}}{I_{A101}} \right)}$$

Equation (4.3)
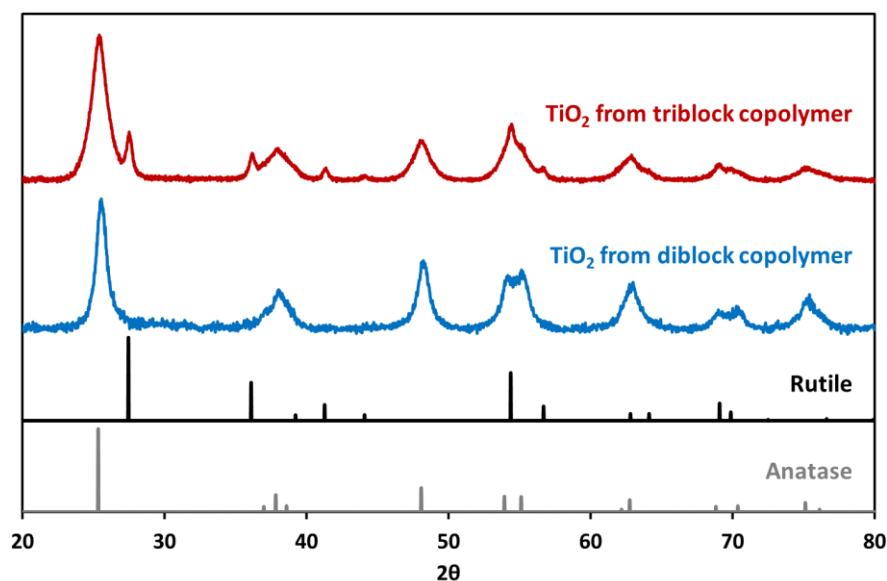
Figure 4.28*: Powder XRD diffractograms of the TiO₂ materials. Rutile and anatase reference patterns are plotted below.*

The XRD analysis showed that both materials were highly crystalline after annealing at 500 °C for 2 hours, giving clear and characteristic TiO₂ peaks. While the TiO₂ sample made using the diblock copolymer was shown to be a pure anatase material, the triblock TiO₂ sample contained significant rutile impurities. The rutile component was calculated to be approximately 29.5 wt% of the material. This was envisaged to be a result of the less uniform morphology for the triblock copolymer-TiO₂ composite, with a decreasing amount of TiO₂ seen towards the centre of the microparticles. This variable concentration of TiO₂ through the composite may have led to discrepancies in the crystallisation of TiO₂ during the annealing process, leading to formation of multiple crystal phases.

Table 4.8: *Summary of quantitative characterisation measurements for the TiO₂ materials synthesised using the diblock and triblock copolymers.*

Polymer Template Used	$w_{anatase}$ (wt%) [a]	Specific surface area ($m^2 \ g^{-1}$) [b]	Average pore size (nm) [c]	H₂ evolution [$\mu mol \ g^{-1} \ h^{-1}$] [d]
Diblock	100	26.4	17.9	30.3
Triblock	70.5	170.9	9.1	53.4

[a] Calculated from powder XRD measurements. [b] Calculated from nitrogen sorption isotherm using the BET method. [c] Calculated from nitrogen sorption profile using the BJH method. [d] Calculated from the gradient of the linear portion of the H₂ evolution plot.

Though not intended, the formation of rutile impurities may be beneficial for the photocatalytic activity of the triblock TiO_2 sample. As stated previously, the anatase crystal structure is widely accepted as the more efficient photocatalytic material, however, studies have shown the presence of rutile impurities can lead to even higher catalytic activities.[112, 113] A report demonstrates a synergistic effect between the phase mixture, leading to a lower recombination rate of photogenerated electron-hole pairs.[114]

Another important factor in determining photocatalytic activity is the total available surface area of the catalyst to adsorb substrates. Both TiO_2 materials are shown to possess the nanoscale structure of their polymer templates and should therefore have high specific surface areas. The surface area of each TiO_2 material was calculated by measuring the nitrogen sorption isotherm of each sample (**Figure 4.29**). The BET method was then applied to the recorded isotherms to give the available surface area of each sample (**Table 4.8**).
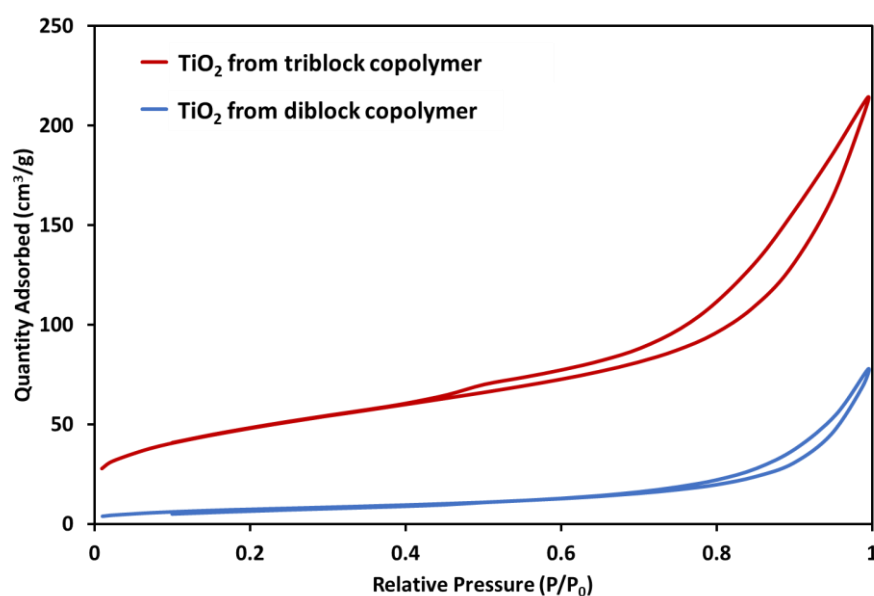
Figure 4.29: *N₂ sorption isotherms for the TiO₂ materials.*

The surface area of the TiO_2 material synthesised using the triblock copolymer was more than six times higher than that of the equivalent diblock copolymer TiO_2 sample (170.9 $m^2\,g^{-1}$). This may in large part be due to the extra internal surface of the hollow-cored triblock TiO_2 particles. The much higher surface area of this material is likely to make it a considerably more efficient photocatalyst than the diblock TiO_2. The extra surface area provided by the complex morphology of the triblock copolymer is also highly attractive for a wealth of other functional inorganic materials.

The shape of the nitrogen sorption isotherms can also yield valuable information about the samples. Both samples display type-II isotherms with H4-type hysteresis loops upon desorption of the nitrogen. This indicates both samples are highly mesoporous, in good agreement with the observations made in the SEM analysis. However, the larger hysteresis loop of the triblock copolymer TiO_2 indicates the sample has a higher degree of porosity, and therefore a smaller average pore diameter. The average pore size for each sample was calculated using the BJH method (**Table 4.8**).

The average pore size of the triblock TiO_2 material was calculated to be almost half that of the diblock TiO_2 equivalent material. This may be due to the more restrictive lamellar morphology present in the triblock copolymer, causing smaller TiO_2 nanostructures to form in the inner layer of the particle shells. Contributions of these smaller pores are also likely to be a reason for the much higher surface area of the triblock TiO_2 material. It should also be noted that the overall average molecular weight of the triblock copolymer is higher than that of the diblock copolymer. This increase in molecular weight of the P4VP polymer may also be a contributing factor in the higher degree of porosity seen in the resulting TiO_2.

Finally, the photocatalytic activity of the TiO_2 materials was assessed by measuring the rate of H_2 production under exposure to simulated solar radiation. The TiO_2 materials were dispersed in aqueous methanol solutions and exposed to a filtered Xe lamp light source. The amount of H_2 released was plotted cumulatively over time (**Figure 4.30**). The gradient of the linear portion of this plot was used to calculate the overall H_2 evolution rates (**Table 4.8**).

The photocatalytic activity of the triblock copolymer synthesised TiO_2 (53.4 µmol g^{-1} h^{-1}) was found to be considerably higher than the diblock counterpart (30.3 µmol g^{-1} h^{-1}). This is likely a direct result of the higher active surface area and the mixed phase composition of this material. The H_2 evolution rates for both of the synthesised TiO_2 materials and were higher than those reported in the literature for Degussa P25 commercial standards (nanoparticulate TiO_2), under near identical conditions (~20 µmol g^{-1} h^{-1}).[115]
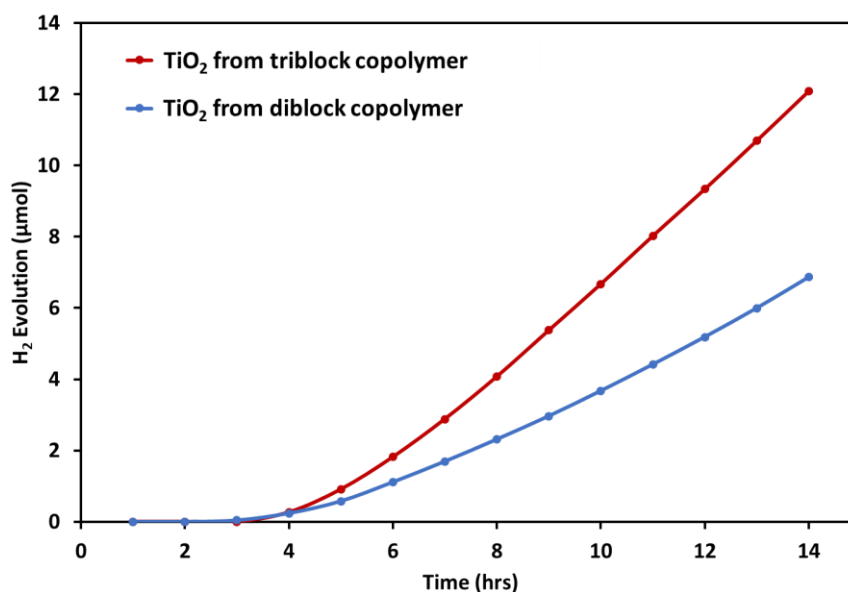
Figure 4.30: *Cumulative H₂ evolution profiles for the TiO₂ materials in aqueous methanol solutions when exposed to simulated solar radiation.*

Though this rate of hydrogen production measured is considerably lower than other values reported recently in the literature, it is nevertheless a meaningful result.[116-118] The TiO₂ samples synthesised here are undoped, highly abundant inorganic materials, tested under relatively low UV irradiation levels with no co-catalyst. The marked increase in photocatalytic activity over nanoparticulate TiO₂ serves as a valuable demonstration of the benefit gained when applying the triblock copolymer as a structural template to the functional material. It is hoped this triblock copolymer may also be applied to the synthesis of more exotic inorganic materials, leading to similar enhancement in their activities.

4.5. Conclusions

In this chapter, the synthesis and self-assembly of PMMA-*b*-PS-*b*-P4VP ABC triblock copolymers was demonstrated by RAFT-mediated scCO$_2$ dispersion, with variable success. Several PMMA-*b*-PS-*b*-P4VP triblock copolymers were synthesised with various block compositions by both one and two-pot dispersion methods. The P4VP block composition was kept consistent throughout.

Though the one-pot dispersion method initially proved triblock copolymers could be formed by sequential high-pressure addition of all monomers, limitations were identified in terms of the attainable block compositions. Sample collection at each stage of the polymerisation was also shown to be an issue, with high-pressure pipework seeming to be contaminated after the first sample collection.

A two-pot re-dispersion method was developed using pre-synthesised PMMA macro-RAFT seed particles to overcome the limitations of the one-pot method. Though this was shown to be highly successful for the lowest PMMA composition triblock copolymer, the method led to the formation of uncontrolled free-radical P4VP in other cases. SEM analysis shows this was caused by the secondary nucleation of nanosized P4VP particles, instead of incorporation into the seed particles. Therefore, the re-dispersion process requires optimisation depending on the final target composition of the copolymer. Visualisation through view-cell tests and a variable quantity of additional PDMS-MA surfactant may be required to achieve this.

A combination of DSC, TEM and SAXS analyses were used to study the internal morphologies of the three successfully synthesised triblock copolymer compositions, alongside approximate theoretical calculations. The resulting data proved to be insufficient to confidently assign a morphology in all cases. Only the TC1^{2P} composition (25 wt% PMMA, 50 wt% PS, 25 wt% P4VP) gave adequate enough results to tentatively assign a lamellar with spheres morphology, L+S(II). This was in part due to the inconclusive SAXS data, caused by lack of scattering contrast, and inability to visualise the 3D three-phase morphologies through TEM images.

A major issue with morphology assignment was the lack of morphological consistency between particles in each sample. This is certainly a result of the increased Đ values generated upon addition of the third polymer block. Due to the increased richness of possible morphologies in ABC triblock copolymer systems, only very small changes to the copolymer

composition are needed to change the preferred morphology. This is evident by the small regions in reported ternary phase diagrams and the use of living polymerisation techniques to study these materials in literature, where Đ is usually below 1.1.[119, 120] This may mean that RAFT-mediated scCO$_2$ dispersion is not an appropriate method to use in order to intricately study the triblock copolymer self-assembly. However, it has proved useful for generating some unique nano-morphologies not available through diblock copolymers, in an environmentally benign way at the gram scale.

The three synthesised triblock copolymers were utilised in the sol-gel synthesis of TiO$_2$. Only the TC1^{2P} composition copolymer was successful in translating the polymer microstructure to the final pure TiO$_2$ material without any aggregation. It was theorised that this may be because a different sol-gel procedure may be required based on the morphology of the polymer template. It may also be likely that the ability of the other two triblock copolymers to template the inorganic precursor was hindered by their large morphological diversity, seen in the polymer TEM analysis. Good consistency in the triblock copolymer nanostructure is expected to be crucial in templating the TiO$_2$ with high fidelity and avoiding aggregation.

The L+S(II) morphology of the TC1^{2P} triblock copolymer was found to produced pure mesoporous TiO$_2$ microparticles containing a large hollow core. The facile synthesis of this complex 3D architecture is useful for creating materials with enhanced properties for a myriad of applications.

Furthermore, this new structure provided by the triblock copolymer was found to be a superior when compared directly to the PMMA-*b*-P4VP diblock copolymer equivalent. Using identical synthetic procedures, the triblock TiO$_2$ product was found to have a far greater surface area and increased photocatalytic activity. This benchmark test highlights the potential benefits of applying complex ABC triblock copolymer morphologies to nanofabrication. It is anticipated that this new, more complex, 3D polymer template may provide opportunities to further enhance the properties of a variety of inorganic functional materials for a broad range of potential applications. However, it is important that the additional synthesis time required to form the triblock copolymers is adequately offset with any potential property enhancement when compared to diblock copolymers. This will be required to ensure economic and environmental viability of triblock systems.

4.6. References

1.   F. S. Bates, *Science*, 1991, **251**, 898-905.
2.   M. W. Matsen, *The Journal of Chemical Physics*, 2000, **113**, 5539-5544.
3.   W. Zheng and Z.-G. Wang, *Macromolecules*, 1995, **28**, 7215-7223.
4.   Y. Mogi, H. Kotsuji, Y. Kaneko, K. Mori, Y. Matsushita and I. Noda, *Macromolecules*, 1992, **25**, 5408-5411.
5.   S. P. Gido, D. W. Schwark, E. L. Thomas and M. do Carmo Goncalves, *Macromolecules*, 1993, **26**, 2636-2640.
6.   W. Xu, K. Jiang, P. Zhang and A.-C. Shi, *The Journal of Physical Chemistry B*, 2013, **117**, 5296-5305.
7.   F. S. Bates and G. Fredrickson, *Block Copolymers—Designer Soft Materials*, 1999.
8.   J. Beckmann, C. Auschra and R. Stadler, *Macromolecular Rapid Communications*, 1994, **15**, 67-72.
9.   C. Auschra and R. Stadler, *Macromolecules*, 1993, **26**, 2171-2174.
10. M. W. Matsen, *The Journal of Chemical Physics*, 1998, **108**, 785-796.
11. Y. Mogi, M. Nomura, H. Kotsuji, K. Ohnishi, Y. Matsushita and I. Noda, *Macromolecules*, 1994, **27**, 6755-6760.
12. V. Balsamo, G. Gil, C. Urbina de Navarro, I. W. Hamley, F. von Gyldenfeldt, V. Abetz and E. Cañizales, *Macromolecules*, 2003, **36**, 4515-4525.
13. T. H. Epps, E. W. Cochran, T. S. Bailey, R. S. Waletzko, C. M. Hardy and F. S. Bates, *Macromolecules*, 2004, **37**, 8325-8341.
14. S. Ludwigs, A. Böker, V. Abetz, A. H. E. Müller and G. Krausch, *Polymer*, 2003, **44**, 6815-6823.
15. R. Kumar, S. W. Sides, M. Goswami, B. G. Sumpter, K. Hong, X. Wu, T. P. Russell, S. P. Gido, K. Misichronis, S. Rangou, A. Avgeropoulos, T. Tsoukatos, N. Hadjichristidis, F. L. Beyer and J. W. Mays, *Langmuir*, 2013, **29**, 1995-2006.
16. T. Goldacker and V. Abetz, *Macromolecular Rapid Communications*, 1999, **20**, 415-418.
17. F. H. Schacher, H. Sugimori, S. Hong, H. Jinnai and A. H. E. Müller, *Macromolecules*, 2012, **45**, 7956-7963.
18. U. Krappe, R. Stadler and I. Voigt-Martin, *Macromolecules*, 1995, **28**, 4558-4561.
19. S. Li, W. Qiu, L. Zhang and H. Liang, *The Journal of Chemical Physics*, 2012, **136**, 124906.
20. C. A. Tyler, J. Qin, F. S. Bates and D. C. Morse, *Macromolecules*, 2007, **40**, 4654-4668.
21. Z. Guo, G. Zhang, F. Qiu, H. Zhang, Y. Yang and A.-C. Shi, *Physical Review Letters*, 2008, **101**, 028301.
22. R. Stadler, C. Auschra, J. Beckmann, U. Krappe, I. Voight-Martin and L. Leibler, *Macromolecules*, 1995, **28**, 3080-3097.
23. R. Ishige, T. Higuchi, X. Jiang, K. Mita, H. Ogawa, H. Yokoyama, A. Takahara and H. Jinnai, *Macromolecules*, 2015, **48**, 2697-2705.
24. S. Brinkmann, R. Stadler and E. L. Thomas, *Macromolecules*, 1998, **31**, 6566-6572.
25. V. Abetz and T. Goldacker, *Macromolecular Rapid Communications*, 2000, **21**, 16-34.
26. X. Qiang, R. Chakroun, N. Janoszka and A. H. Gröschel, *Isr. J. Chem.*, 2019, **59**, 945-958.
27. J. Gensel, I. Dewald, J. Erath, E. Betthausen, A. H. E. Müller and A. Fery, *Chemical Science*, 2013, **4**, 325-334.
28. T. I. Löbling, O. Borisov, J. S. Haataja, O. Ikkala, A. H. Gröschel and A. H. E. Müller, *Nature communications*, 2016, **7**, 12097.

29.	J. Zhu and W. Jiang, *Macromolecules*, 2005, **38**, 9315-9323.

30.	A. O. Moughton, M. A. Hillmyer and T. P. Lodge, *Macromolecules*, 2012, **45**, 2-19.

31.	A. H. Gröschel, F. H. Schacher, H. Schmalz, O. V. Borisov, E. B. Zhulina, A. Walther and A. H. E. Müller, *Nature communications*, 2012, **3**, 710.

32.	T. P. Lodge, A. Rasdal, Z. Li and M. A. Hillmyer, *Journal of the American Chemical Society*, 2005, **127**, 17608-17609.

33.	C. K. Wong, F. Chen, A. Walther and M. H. Stenzel, *Angew. Chem., Int. Ed.*, 2019, **131**, 7413-7418.

34.	S. Davaran, A. Ghamkhari, E. Alizadeh, B. Massoumi and M. Jaymand, *Journal of Colloid and Interface Science*, 2017, **488**, 282-293.

35.	A. Walther and A. H. E. Müller, *Chemical Reviews*, 2013, **113**, 5194-5261.

36.	A. Kirillova, C. Schliebe, G. Stoychev, A. Jakob, H. Lang and A. Synytska, *ACS applied materials & interfaces*, 2015, **7**, 21218-21225.

37.	J. W. Ma, X. Li, P. Tang and Y. Yang, *The Journal of Physical Chemistry B*, 2007, **111**, 1552-1558.

38.	Z. Li, E. Kesselman, Y. Talmon, M. A. Hillmyer and T. P. Lodge, *Science*, 2004, **306**, 98-101.

39.	Z. Li, M. A. Hillmyer and T. P. Lodge, *Langmuir*, 2006, **22**, 9409-9417.

40.	B. Yu, J. Deng, B. Li and A.-C. Shi, *Soft Matter*, 2014, **10**, 6831-6843.

41.	J. Bang, U. Jeong, D. Y. Ryu, T. P. Russell and C. J. Hawker, *Advanced Materials*, 2009, **21**, 4769-4792.

42.	H. Hu, M. Gopinadhan and C. O. Osuji, *Soft Matter*, 2014, **10**, 3867-3889.

43.	J. G. Son, J. Gwyther, J.-B. Chang, K. K. Berggren, I. Manners and C. A. Ross, *Nano Letters*, 2011, **11**, 2849-2855.

44.	V. P. Chuang, C. A. Ross, P. Bilalis and N. Hadjichristidis, *ACS Nano*, 2008, **2**, 2007-2014.

45.	J. Podbielski, F. Giesen and D. Grundler, *Physical Review Letters*, 2006, **96**, 167207.

46.	R. Ruiz, E. Dobisz and T. R. Albrecht, *ACS Nano*, 2011, **5**, 79-84.

47.	M. M. Miller, G. A. Prinz, S.-F. Cheng and S. Bounnak, *Appl. Phys. Lett.*, 2002, **81**, 2211-2213.

48.	L. W. Yu, K. J. Chen, J. Song, J. Xu, W. Li, X. F. Li, J. M. Wang and X. F. Huang, *Physical Review Letters*, 2007, **98**, 166102.

49.	H. K. Choi, J. Gwyther, I. Manners and C. A. Ross, *ACS Nano*, 2012, **6**, 8342-8348.

50.	Y. Li, B. P. Bastakoti and Y. Yamauchi, *APL Materials*, 2016, **4**, 040703.

51.	E. J. W. Crossland, M. Kamperman, M. Nedelcu, C. Ducati, U. Wiesner, D. M. Smilgies, G. E. S. Toombes, M. A. Hillmyer, S. Ludwigs, U. Steiner and H. J. Snaith, *Nano Letters*, 2009, **9**, 2807-2812.

52.	B.-K. Cho, A. Jain, S. M. Gruner and U. Wiesner, *Science*, 2004, **305**, 1598-1601.

53.	M. C. Orilall and U. Wiesner, *Chemical Society Reviews*, 2011, **40**, 520-535.

54.	T. S. Bailey, C. M. Hardy, T. H. Epps and F. S. Bates, *Macromolecules*, 2002, **35**, 7007-7017.

55.	F. S. Bates, M. F. Schulz, A. K. Khandpur, S. Förster, J. H. Rosedale, K. Almdal and K. Mortensen, *Faraday Discuss.*, 1994, **98**, 7-18.

56.	G. Floudas, B. Vazaiou, F. Schipper, R. Ulrich, U. Wiesner, H. Iatrou and N. Hadjichristidis, *Macromolecules*, 2001, **34**, 2947-2957.

57.	P. Docampo, M. Stefik, S. Guldin, R. Gunning, N. A. Yufa, N. Cai, P. Wang, U. Steiner, U. Wiesner and H. J. Snaith, *Advanced Energy Materials*, 2012, **2**, 676-682.

58. M. Stefik, S. Wang, R. Hovden, H. Sai, M. W. Tate, D. A. Muller, U. Steiner, S. M. Gruner and U. Wiesner, *Journal of Materials Chemistry*, 2012, **22**, 1078-1087.

59. M. Stefik, S. Mahajan, H. Sai, T. H. Epps, F. S. Bates, S. M. Gruner, F. J. DiSalvo and U. Wiesner, *Chemistry of Materials*, 2009, **21**, 5466-5473.

60. C. D. Cowman, E. Padgett, K. W. Tan, R. Hovden, Y. Gu, N. Andrejevic, D. Muller, G. W. Coates and U. Wiesner, *Journal of the American Chemical Society*, 2015, **137**, 6026-6033.

61. Z. Li, K. Hur, H. Sai, T. Higuchi, A. Takahara, H. Jinnai, S. M. Gruner and U. Wiesner, *Nature communications*, 2014, **5**, 3247.

62. H. Feng, X. Lu, W. Wang, N.-G. Kang and J. W. Mays, *Polymers*, 2017, **9**, 494.

63. Y. Zou, X. Zhou, J. Ma, X. Yang and Y. Deng, *Chemical Society Reviews*, 2020, **49**, 1173-1208.

64. M. Li and C. K. Ober, *Materials Today*, 2006, **9**, 30-39.

65. Z. Sun and J. S. Gutmann, *Physica A: Statistical Mechanics and its Applications*, 2004, **339**, 80-85.

66. M.-S. Seo, I. Jeong, J.-S. Park, J. Lee, I. K. Han, W. I. Lee, H. J. Son, B.-H. Sohn and M. J. Ko, *Nanoscale*, 2016, **8**, 11472-11479.

67. P. S. Chinthamanipeta, Q. Lou and D. A. Shipp, *ACS Nano*, 2011, **5**, 450-456.

68. X. Chen and S. S. Mao, *Chemical Reviews*, 2007, **107**, 2891-2959.

69. T. M. Bennett, G. He, R. R. Larder, M. G. Fischer, G. A. Rance, M. W. Fay, A. K. Pearce, C. D. J. Parmenter, U. Steiner and S. M. Howdle, *Nano Letters*, 2018, **18**, 7560-7569.

70. M. A. K. L. Diasanayake, G. K. R. Senadeera, H. N. M. Sarangika, P. M. P. C. Ekanayake, C. A. Thotawattage, H. K. D. W. M. N. R. Divarathne and J. M. K. W. Kumari, *Materials Today: Proceedings*, 2016, **3**, S40-S47.

71. Y. Bai, I. Mora-Seró, F. De Angelis, J. Bisquert and P. Wang, *Chemical Reviews*, 2014, **114**, 10095-10130.

72. J. Bai and B. Zhou, *Chemical Reviews*, 2014, **114**, 10131-10176.

73. S. Banerjee, D. D. Dionysiou and S. C. Pillai, *Applied Catalysis B: Environmental*, 2015, **176-177**, 396-428.

74. S.-Y. Lee and S.-J. Park, *Journal of Industrial and Engineering Chemistry*, 2013, **19**, 1761-1769.

75. G. L. Chiarello, M. V. Dozzi and E. Selli, *Journal of Energy Chemistry*, 2017, **26**, 250-258.

76. V. Bolis, C. Busco, M. Ciarletta, C. Distasi, J. Erriquez, I. Fenoglio, S. Livraghi and S. Morel, *Journal of Colloid and Interface Science*, 2012, **369**, 28-39.

77. Q. Guo, C. Zhou, Z. Ma and X. Yang, *Advanced Materials*, 2019, **31**, 1901997.

78. H. Dong, G. Zeng, L. Tang, C. Fan, C. Zhang, X. He and Y. He, *Water Res.*, 2015, **79**, 128-146.

79. V. Etacheri, C. Di Valentin, J. Schneider, D. Bahnemann and S. C. Pillai, *Journal of Photochemistry and Photobiology C: Photochemistry Reviews*, 2015, **25**, 1-29.

80. Y. Tang, G. Zhang, C. Liu, S. Luo, X. Xu, L. Chen and B. Wang, *J. Hazard. Mater.*, 2013, **252-253**, 115-122.

81. J. Low, B. Cheng and J. Yu, *Appl. Surf. Sci.*, 2017, **392**, 658-686.

82. M. R. Al-Mamun, S. Kader, M. S. Islam and M. Z. H. Khan, *Journal of Environmental Chemical Engineering*, 2019, **7**, 103248.

83. M. Humayun, F. Raziq, A. Khan and W. Luo, *Green Chemistry Letters and Reviews*, 2018, **11**, 86-102.

84. A. Khlyustova, N. Sirotkin, T. Kusova, A. Kraev, V. Titov and A. Agafonov, *Materials Advances*, 2020, **1**, 1193-1201.
85. J. Gomes, J. Lincho, E. Domingues, R. M. Quinta-Ferreira and R. C. Martins, *Water*, 2019, **11**, 373.
86. K. Lee, H. Yoon, C. Ahn, J. Park and S. Jeon, *Nanoscale*, 2019, **11**, 7025-7040.
87. W. Zhang, Y. Tian, H. He, L. Xu, W. Li and D. Zhao, *National Science Review*, 2020, **7**, 1702-1725.
88. S. Topcu, G. Jodhani and P. Gouma, *Frontiers in Materials*, 2016, **3**.
89. S. B. Khan, M. Hou, S. Shuang and Z. Zhang, *Appl. Surf. Sci.*, 2017, **400**, 184-193.
90. S. T. Kochuveedu, Y. J. Jang, Y. H. Jang, W. J. Lee, M.-A. Cha, H. Shin, S. Yoon, S.-S. Lee, S. O. Kim, K. Shin, M. Steinhart and D. H. Kim, *Green Chemistry*, 2011, **13**, 3397-3405.
91. J. H. Pan, X. S. Zhao and W. I. Lee, *Chem. Eng. J.*, 2011, **170**, 363-380.
92. J. Jennings, M. Beija, A. P. Richez, S. D. Cooper, P. E. Mignot, K. J. Thurecht, K. S. Jack and S. M. Howdle, *Journal of the American Chemical Society*, 2012, **134**, 4772-4781.
93. J. Jennings, S. P. Bassett, D. Hermida-Merino, G. Portale, W. Bras, L. Knight, J. J. Titman, T. Higuchi, H. Jinnai and S. M. Howdle, *Polymer Chemistry*, 2016, **7**, 905-916.
94. T. P. Russell, R. P. Hjelm and P. A. Seeger, *Macromolecules*, 1990, **23**, 890-893.
95. J. G. Kennemur, *Macromolecules*, 2019, **52**, 1354-1370.
96. M. Alauhdin, T. M. Bennett, G. He, S. P. Bassett, G. Portale, W. Bras, D. Hermida-Merino and S. M. Howdle, *Polymer Chemistry*, 2019, **10**, 860-871.
97. A. Rajendran, B. Bonavoglia, N. Forrer, G. Storti, M. Mazzotti and M. Morbidelli, *Industrial & Engineering Chemistry Research*, 2005, **44**, 2549-2560.
98. S. Hilic, S. A. E. Boyer, A. A. H. Pádua and J.-P. E. Grolier, *Journal of Polymer Science Part B: Polymer Physics*, 2001, **39**, 2063-2070.
99. Y. Zhang, K. K. Gangwani and R. M. Lemert, *The Journal of Supercritical Fluids*, 1997, **11**, 115-134.
100. D. F. Sunday, M. J. Maher, A. F. Hannon, C. D. Liman, S. Tein, G. Blachut, Y. Asano, C. J. Ellison, C. G. Willson and R. J. Kline, *Macromolecules*, 2018, **51**, 173-180.
101. I. M. Kalogeras and W. Brostow, *Journal of Polymer Science Part B: Polymer Physics*, 2009, **47**, 80-95.
102. J. E. C. Mark, *Polymer data handbook*, Oxford University Press, Oxford, UK, 2009.
103. L. Boldon, F. Laliberte and L. Liu, *Nano Reviews*, 2015, **6**, 25661.
104. G. He, T. M. Bennett, M. Alauhdin, M. W. Fay, X. Liu, S. T. Schwab, C.-g. Sun and S. M. Howdle, *Polymer Chemistry*, 2018, **9**, 3808-3819.
105. S. Dadgostar, F. Tajabadi and N. Taghavinia, *ACS applied materials & interfaces*, 2012, **4**, 2964-2968.
106. H. Li, Z. Bian, J. Zhu, D. Zhang, G. Li, Y. Huo, H. Li and Y. Lu, *Journal of the American Chemical Society*, 2007, **129**, 8406-8407.
107. Z. Wang, L. Zhou and X. W. Lou, *Advanced Materials*, 2012, **24**, 1903-1911.
108. D. A. H. Hanaor and C. C. Sorrell, *Journal of Materials Science*, 2011, **46**, 855-874.
109. M. Hirano, C. Nakahara, K. Ota, O. Tanaike and M. Inagaki, *J. Solid State Chem.*, 2003, **170**, 39-47.
110. N. Mahdjoub, N. Allen, P. Kelly and V. Vishnyakov, *Journal of Photochemistry and Photobiology A: Chemistry*, 2010, **210**, 125-129.
111. R. A. Spurr and H. Myers, *Anal. Chem.*, 1957, **29**, 760-762.
112. R. I. Bickley, T. Gonzalez-Carreno, J. S. Lees, L. Palmisano and R. J. D. Tilley, *J. Solid State Chem.*, 1991, **92**, 178-190.

113.   T. Ohno, K. Sarukawa, K. Tokieda and M. Matsumura, *J. Catal.*, 2001, **203**, 82-86.

114.   W. R. Siah, H. O. Lintang, M. Shamsuddin and L. Yuliati, *IOP Conference Series: Materials Science and Engineering*, 2016, **107**, 012005.

115.   V. Kumaravel, M. D. Imam, A. Badreldin, R. K. Chava, J. Y. Do, M. Kang and A. Abdel-Wahab, *Catalysts*, 2019, **9**, 276.

116.   P. Ganguly, M. Harb, Z. Cao, L. Cavallo, A. Breen, S. Dervin, D. D. Dionysiou and S. C. Pillai, *ACS Energy Letters*, 2019, **4**, 1687-1709.

117.   N. Fajrina and M. Tahir, *Int. J. Hydrogen Energy*, 2019, **44**, 540-577.

118.   J. Corredor, M. J. Rivero, C. M. Rangel, F. Gloaguen and I. Ortiz, *Journal of Chemical Technology & Biotechnology*, 2019, **94**, 3049-3063.

119.   S. Ludwigs, A. Böker, A. Voronov, N. Rehse, R. Magerle and G. Krausch, *Nature materials*, 2003, **2**, 744-747.

120.   Y. Tanaka, H. Hasegawa, T. Hashimoto, A. Ribbe, K. Sugiyama, A. Hirao and S. Nakahama, *Polym. J.*, 1999, **31**, 989-994.

Chapter 5 – Synthesis of Block Copolymer-Silver Nanoparticle Composite Materials in Supercritical CO$_2$

5.1. Overview

While previous chapters in this thesis employed a separate synthetic procedure to incorporate inorganic components into block copolymer templates, this chapter aims to integrate this step into scCO$_2$ alongside the polymer synthesis. Specifically, the synthesis of antimicrobial silver nanoparticles (AgNPs) was combined with the polymerisation of PMMA-*b*-P4VP in scCO$_2$ dispersion to yield homogeneous microparticulate composite products. A CO$_2$ cleaning process was also applied at the end of the synthesis in the hopes of producing clean and biocompatible materials without the need for any additional purification steps with non-renewable solvents.

Various quantities of a silver precursor complex were thermally degraded in scCO$_2$ to produce AgNPs that were co-assembled with the P4VP, utilising the complexation to the pyridinyl nitrogen moieties. The morphology of the resulting composites was thoroughly investigated by microscopy techniques to determine the distribution of the AgNPs in the polymers. The size of the formed AgNPs and their effect on the thermal properties of the copolymers was also examined. The controlled release of the AgNPs from the composites was then tested by dispersing the composite powder in different pH aqueous solutions. The biocompatibility of the composites was also tested against human intestinal cells, along with their antimicrobial activity against multiple strains of bacteria.

Finally, the resulting PMMA-*b*-P4VP-AgNPs composite was then tested for its feasibility as an antimicrobial 'ink' in additive manufacturing, commonly referred to as 3D printing. The composite powder was fabricated into small solid objects using selective laser sintering (SLS) to fuse the polymer microparticles. The resulting composition of the printed objects was investigated by surface elemental mapping and mass spectrometry analysis over the depth of the sample to confirm an even distribution of AgNPs was achieved in the final product.

5.2. introduction

This introduction expands on some of the general concepts outlined in **Chapter 1**. As the main research goal of this chapter is to incorporate inorganic components directly into block copolymers from scCO$_2$, the synthesis of inorganic compounds in scCO$_2$ is discussed. This is particularly focussed on the synthesis of metallic nanoparticles. Silver nanoparticles (AgNPs) are specifically highlighted as a useful and accessible inorganic product, with specific attention given to their application in the biomedical field. Finally, a brief review is given on the current 3D printing techniques exploited to manufacture products from AgNPs composites.

5.2.1. Inorganic Synthesis in scCO$_2$

In **Chapter 1** of this thesis, the beneficial use of scCO$_2$ in the synthesis of polymers was discussed. However, it is important to note that scCO$_2$ is also a well utilised solvent for a range of other chemical syntheses, including those containing inorganic components.[1] This includes but is not limited to metal-catalysed organic syntheses,[2] organometallic syntheses,[3] sol-gel reactions[4] and the formation of metal nanoparticles.[5] Though, conducting these reactions in scCO$_2$ can present some practical difficulties due to the high-pressures required, this solvent alternative generally offers several benefits to offset this. These include the environmental advantages, the ability to readily tune solubility, low gas-like viscosity and vanishing surface tension.[6]

The most relevant inorganic reactions for this thesis are the synthesis of metal nanoparticles and metal oxides in scCO$_2$, as these compounds stand to benefit the most from selective orientation in a block copolymer template. As has previously been discussed throughout this thesis, imparting periodic nanoarchitectures onto metal oxides offers a good scope to enhance the functional properties of the materials.[7] Whereas metal nanoparticles that are spatially well-ordered by a substrate can have unique and desirable magnetic, electronic and optical properties.[8]

Synthesis of metal oxides in scCO$_2$ is commonly achieved through the use of sol-gel chemistry. Typical sol-gel reactions involve the hydrolysis of metal alkoxides followed by their polycondensation to form a metal oxide gel, before finally removing the solvent.[9] Before its more recent use as the reaction solvent, scCO$_2$ was commonly used at the end of traditional

sol-gel reactions to replace the liquid solvent and dry the gel.[10] This is because conventional evaporation of the high surface tension liquid solvents can create large capillary force in the porous gel structure causing it to shrink dramatically. Drying with scCO$_2$ negates this effect and yields highly porous and low-density metal oxides known as aerogels.[4]

Loy et al. were the first to demonstrate the direct formation of a SiO$_2$ aerogel by using scCO$_2$ as the reaction solvent.[11] Water-free hydrolysis of tetramethoxysilane was achieved in scCO$_2$ with the addition of formic acid, followed by polycondensation of the resulting silanol and simply venting the solvent after sufficient gelation to yield the silica aerogel (**Figure 5.1**). Since then, a variety of other metal oxides have been produced directly in scCO$_2$. The Charpentier group has been particularly successful in this area, with reports detailing the successful sol-gel synthesis of TiO$_2$, [12, 13] Al$_2$O$_3$ [14] and ZrO$_2$ [15], all directly in scCO$_2$. These were all achieved simply by dissolving the desired metal alkoxide precursors in relatively high-pressure scCO$_2$ and conducting the sol-gel reaction with the aid of acetic acid. Modification of the reaction parameters were also studied to assert some control on to the resulting morphology of the metal oxides.[12] Beyond this, scCO$_2$ has also proven useful for synthesising mixed metal oxide materials via the sol-gel route, such as ZrO$_2$-TiO$_2$, with the high diffusivity of the solvent leading to excellent homogeneity in the materials.[16-18]
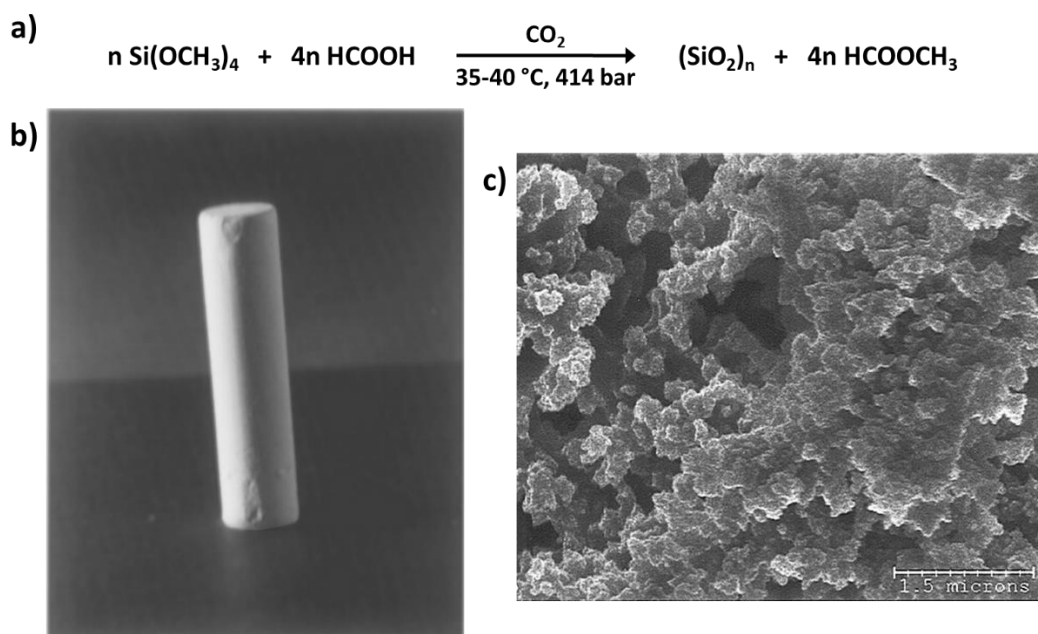
Figure 5.1: *Sol-gel synthesis of a SiO$_2$ aerogel directly in scCO$_2$. Showing (a) the details of the chemical reaction, (b) a picture of the resulting SiO$_2$ aerogel and (c) an SEM image of the aerogel.[11]*

Metal nanoparticles are a class of materials that have been intensively studied over the past few decades and are now becoming increasingly important for use in many different industrial sectors. This is particularly true of noble metal nanoparticles.[19, 20] They have proven to be valuable in applications such as catalysis,[21] optics,[22] electronics,[23] sensors,[24] medicine[25] and as inks for 3D printing.[26] Supercritical fluids, including scCO₂, have become a popular solvent choice for the preparation of metal nanoparticles and composites materials containing nanoparticles.[27] One of the main advantages being the high diffusivity and mass transport of the fluids to yield homogeneous and relatively monodisperse particles.[5] These properties, along with the zero-surface tension of the solvent, also allow metal nanoparticles to be deposited evenly on highly porous substrates.[28, 29] Their high production rate has also been utilised in supercritical continuous flow systems,[30-32] with nanoparticles now produced at the multi-ton scale in this way by companies such as Promethean Particles Ltd.

The general procedure employed for synthesising colloidal metal nanoparticles in scCO₂ is to dissolve a metal precursor compound in scCO₂ and then decomposed the compound to form the desired nanoparticles.[5] Decomposition is often achieved through either thermolysis[33, 34] or reductive reactions of the precursor,[35-37] which have been found to proceed at a much higher rate in scCO₂ compared to conventional solvents.[5, 30] The wide availability of scCO₂-souble precursor compounds has led to the successful synthesis of many different metal nanoparticles, including Ag,[38] Au,[39] Pt,[40] Pd,[41] and Ir.[40] The synthesis of these metal nanoparticles is commonly accompanied by depositing or embedding the particles on a target substrate to prevent agglomeration and to provide a support for the nanoparticles in their final applications. The literature in this field is extensive and is reviewed more thoroughly elsewhere.[5, 29, 42, 43]

From this brief review of the literature surrounding inorganic synthesis in scCO₂, it is clear that the synthesis of metal nanoparticles is by far the simplest to perform. Syntheses can be conducted in a single step and in some case using only a single reagent. As such, these materials will be the focus of this initial investigation into co-synthesis and co-assembly with block copolymers.

5.2.2. Synthesis of Silver Nanoparticles in scCO₂

Silver nanoparticles (AgNPs) are a highly desirable type of metal nanoparticle. Their unique properties make them particularly useful in catalysis[44], plasmonics[45], surface enhanced Raman scattering[46] and in the biomedical field,[47] which is discussed more thoroughly in the next section. This high demand for AgNPs means there is a host of literature available on different routes to syntheses AgNPs.[48-51] Synthesis in scCO₂ commonly features because of the various advantages outlined in the previous section, but also because of the ability to omit any chance of the final product containing solvent residues.[27, 52-54] This is particularly advantageous for medical applications to ensure good biocompatibility.[55]

ScCO₂ has been used to generate colloidal solutions of AgNPs. In particular, Ji et al. detailed a method utilising a rapid expansion of supercritical solution (RESS) technique of a water-in-scCO₂ microemulsion to rapidly yield AgNPs. Though, the particle size dispersity of the nanoparticles was found to be quite high (5-15 nm) due to some agglomeration of the collected powder.[56] Sun et al. later improved upon this method by modifying the RESS technique to spray into a liquid solution of sodium borohydride, with greater size control reported.[57] However, it has since been found that scCO₂ can be much more useful to simultaneously synthesise and impregnate AgNPs on a substrate to yield nanoparticle composites in a single step. These composites are generally more desirable than colloidal solutions to prevent any future agglomeration of the particles and for use in end applications.[53]

The Howdle group reported the first successful impregnation of porous substrates with silver coordination complexes, used as precursors to AgNPs.[55] ScCO₂ was used to solvate various silver complexes at 40 °C and then infuse them into silica aerogels and poly(styrene-divinylbenzene) beads, taking advantage of the high diffusivity of the solvent. The precursor complexes were then subsequently reduced under H₂ gas at 60 °C to yield AgNPs, with high homogeneity observed throughout the substrates. A final scCO₂ purge step was also applied to remove any precursor residues to ensure purity of the resulting composites. Control of the size and distribution of the AgNPs in the composite was also demonstrated, with precursor solubility found to be a crucial factor for determining these properties.[55] Subsequent reports in the literature also detail similar procedures to impregnate other supports with AgNPs, including polycarbonates and polyimides.[46, 53, 58-60]

Though these procedures have proven highly effective at producing polymer-AgNPs composites with homogeneous nanoparticle distributions, the methods lack any real definitive control as to exactly where the AgNPs will be deposited in the substrate or how they are arranged. Specific spatial control of nanoparticle arrangements on a substrate has the potential to yield properties that differ to those of either the bulk or individual nanoparticles.[61] These properties are attributed to coupling between individual nanoparticles and have potential to be useful for advanced applications such as selective catalysis[62] and nanophotonics.[63] The scCO$_2$ deposition process also requires multiple steps to obtain the end composite. The support material must first be synthesised, followed by impregnation with the precursor and a subsequent change in conditions to form the AgNPs.

The only example in the literature to attempt to overcome these limitations in scCO$_2$ is a report by Hasell et al. where a PMMA support is synthesised in scCO$_2$ along with AgNPs (**Figure 5.2**).[34] A RAFT agent with a PDMS end group is used as both the polymeric stabiliser in the dispersion polymerisation and the radical control agent for the reaction. As a result, the RAFT moieties were always positioned on the outer surface of the PMMA particles. The formed AgNPs are preferentially attracted to these RAFT moieties via favourable silver-sulfur interactions, to selectively decorate only the surface of the PMMA with the AgNPs. They note that this arrangement of AgNPs on a support is particularly attractive for catalytic applications.[34]
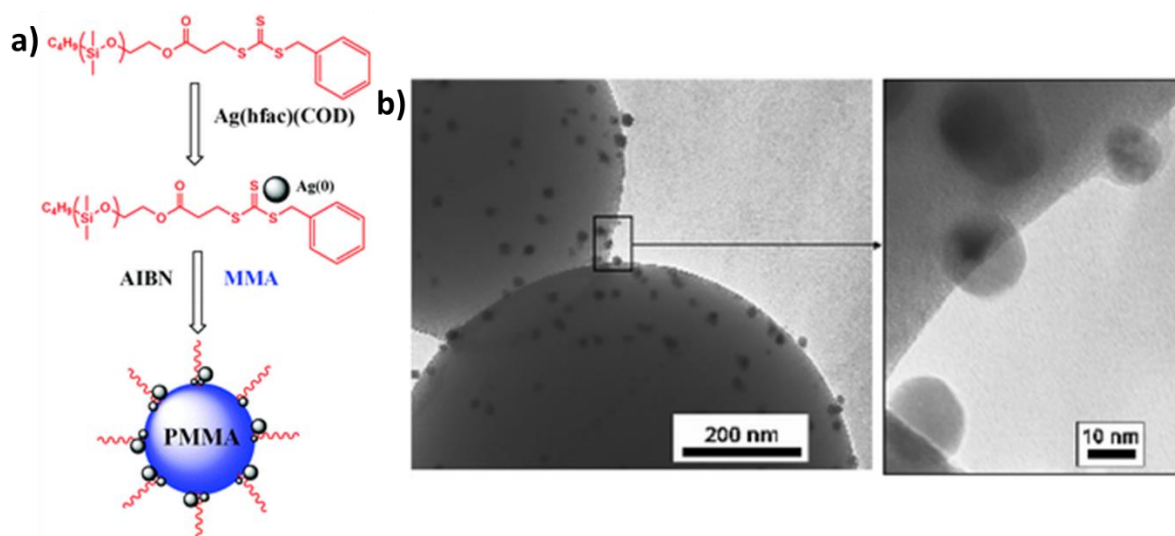
Figure 5.2: *(a) Schematic demonstrating the method to form AgNPs-decorated PMMA microparticles using a PDMS-based RAFT agent and (b) TEM images of the resulting composite.[34]*

5.2.3. Biomedical Applications of Silver Nanoparticles

As mentioned previously, AgNPs are of interest for use in a host of applications. Though, arguably the most popular of these is their use in the biomedical field.[47, 64] This is due to their high intrinsic antimicrobial activity towards a large range of pathogens, including bacteria, viruses, fungi and even protozoa.[65] In fact, the therapeutic activity of silver has been established for millennia, with the ancient Greeks and Romans known to preserve beverages for long periods of time in silver vessels to prevent festering. This empiric knowledge has also led to the custom of using silverware cutlery by the wealthy throughout the course of history.[66] In the modern era, silver is commonly employed in wound dressings and as coatings on medical devices to limit or combat infection.[67] However, in more recent years, superior antimicrobial activity of AgNPs has been demonstrated when compared to other silver compounds, shifting research focus to implement these more attractive nanomaterials in biotechnology.[68]

Despite the long-term knowledge of the antimicrobial effects of silver, the precise anti-pathogenic mechanism of AgNPs has not been entirely clarified and is only now beginning to be fully understood.[47] In bacteria, it is believed cell death occurs through multiple interaction pathways (**Figure 5.3**).[69] Firstly, AgNPs can accumulate on the cell wall of bacteria due to their affinity to the sulfur proteins. The build-up of AgNPs can lead to the perforation of the cell wall and denature the cell membrane due to their nanoscale size, leading to lysis and death of the bacterium. Moreover, AgNPs can continuously release silver ions that also contribute to the killing of bacteria. Silver ions that permeate the bacterium membrane can denature the respiratory enzymes and ribosomes present in the cytoplasm. This inhibits the production of proteins and adenosine triphosphate (ATP) while also generating harmful reactive oxygen species (ROS). The silver ions can also intercalate within the bacteria DNA, due to the sulfur and phosphorous components, leading to problems in DNA replication. All these effects can contribute to deactivation or death of the bacteria.[69] The overall antimicrobial activity of AgNPs has also proven to be dependent on the physiochemical parameters of the particles, for example, their size and shape.[70]
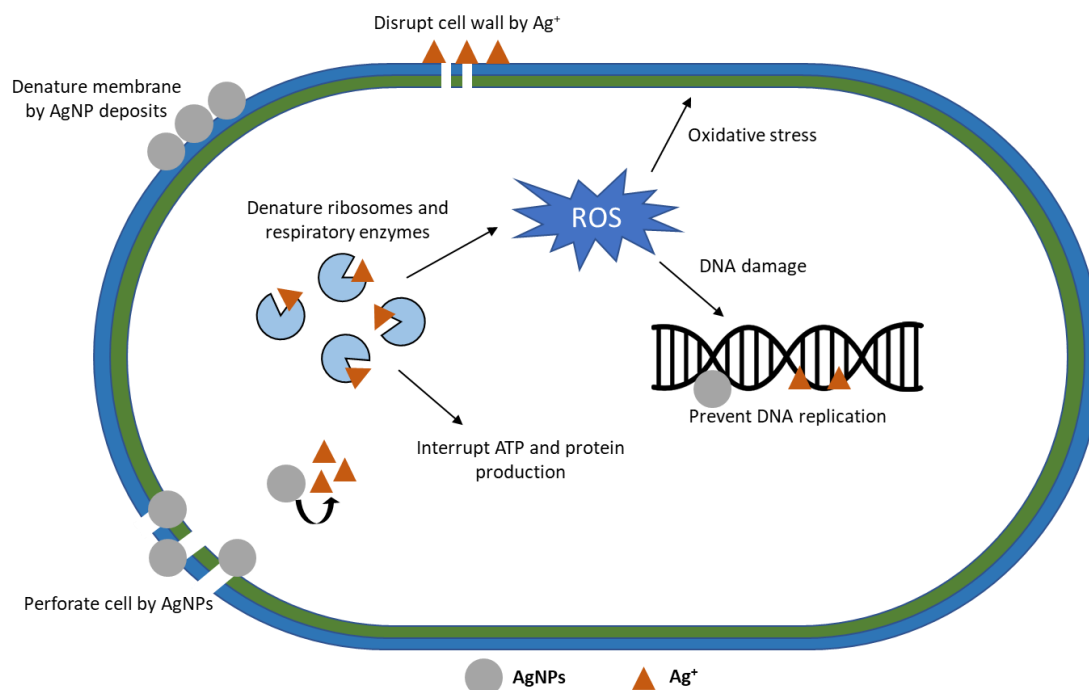
Figure 5.3: *Diagram summarising some of the key antibacterial actions of AgNPs. Figure adapted from literature.*[69]

The high effectiveness of AgNPs against a range of bacteria is thought to be because of this complex mode of action.[71] This is particularly advantageous as it is difficult for microorganisms to build an effective resistance against the effect of AgNPs, when compared to conventional antibiotics.[65] As a result, AgNPs have proven to be highly effective against known antibiotic-resistant strains of gram-positive and gram-negative bacteria, making them an attractive solution to help combat the emerging threat of drug-resistant pathogens.[72]

The global consumption of AgNPs is predicted to increase substantially in the near future due to their growing use in the medical field and other key consumer markets.[73] As such, recent literature is very concerned with developing new synthesis methods to meet the demands of this growing commodity.[73, 74] Efficient and scalable production methods are a core focus, however green and biosynthetic approaches also feature heavily in recent studies.[75, 76] This is a particularly appealing strategy not just for environmental reasons, but also to produce clean biocompatible AgNPs.[77] Other common concerns in the synthesis of biomedical AgNPs is control of the particle morphology to ensure high activity, as well as stability of the AgNPs to guarantee longevity in the product.[78-80]

5.2.4. Silver Nanoparticles in 3D Printing

3D printing, or additive manufacturing, is a manufacturing process that is quickly gaining popularity for producing an assortment of devices and objects. There are a number of different 3D printing methods, but their commonality lies in the ability to turn a digital design into a 3D object by printing a material additively layer by layer. The main advantages of this approach are the ability to manufacture complex parts autonomously with a great deal of customisability between builds. This has proven to be particularly useful for rapid prototyping of new designs without the need to reconfigure a whole manufacturing process.[81]

The advent of new technologies means there are now several approaches to additive manufacturing. Four popular 3D printing methods are stereolithography (SLA), fused deposition modelling (FDM), inkjet printing (IJP) and selective laser sintering (SLS). In brief, SLA works by solidifying a liquid resin using a laser that is positioned to produce the desired shape. FDM is easily the most common type of additive manufacturing and works by selectively depositing a melted plastic via a heated extruder. IJP works by jetting a material ink onto a build surface where it is cured or solidified by evaporation of the carrier solvent. SLS deposits a powder material onto a build platform where it is selectively sintered by a laser traced across the bed (**Figure 5.4**). The build is then gradually lowered with fresh powder being deposited for further sintering to build up the 3D structure. Each method comes with their own advantages, disadvantages and applicability for different classes of materials. A detailed review of all additive manufacturing techniques can be found elsewhere.[82, 83]

Academic research is often concerned with developing new materials that can be utilised in additive manufacturing processes, allowing new products to be produced.[84] Commercial 3D printing is dominated by simple polymer materials, with polylactic acid (PLA), acrylonitrile-butadiene-styrene (ABS) and polyamide (PA) widely available for use in FDM printing. However, products manufactured from these pure polymers are often only used for conceptual prototypes due to their inherent lack of functionality and durability.[85] Some printing techniques allow for additive manufacturing with stronger materials such as metals or ceramics. Though, there are still a relatively limited number of different printable materials available in these classes.[85] Another solution has been to develop polymer composite materials capable of being additively manufactured, to give various desirable physical properties to the end product.[86]
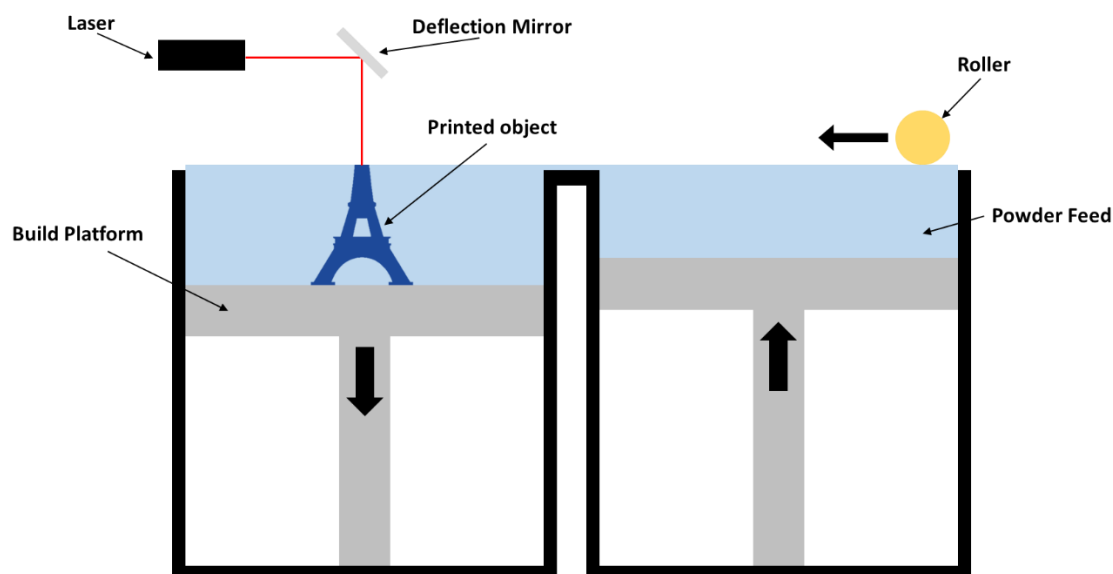
Figure 5.4: *Schematic illustrating the selective laser sintering (SLS) additive manufacturing method.*

AgNPs are becoming very popular for use in 3D printing, particularly in the form of free colloidal inks, with AgNPs inks now even commercially available.[26, 87] As a single component ink, AgNPs solutions are most commonly utilised in IJP methods to print high resolution patterns of closely packed AgNPs. This is because collections of AgNPs can be melted and sintered together at much lower temperatures than the bulk material, with the melting temperature shown to drop from 960 °C to around 100 °C.[88] This affords bulk metallic silver tracks after sintering, which are utilised heavily in the microelectronics industry due to the high electrical conductivity of silver.[89]

Composite materials of polymers containing AgNPs have also been developed for use in 3D printing.[90-92] Utilising nanocomposites, including those containing AgNPs, is becoming an attractive route to modify the properties of printed products. Printed composites with AgNPs are appealing primarily for their enhanced electrical conductivity, with Fantino et al. reporting an electrical conductivity of such a composite to be three orders of magnitude higher than that of the equivalent neat polymer.[93] There are also reports in the literature of printable polymer-AgNPs composites utilised specifically for biomedical applications, but these would appear to be far less common than utilising AgNPs for their electrical properties.[92, 94, 95]

A particular problem when 3D printing polymer-AgNPs composites is the high risk of aggregating the nanoparticles during printing, as the process typically involves heating. Though this is not of high concern for electronical applications, this does represent an issue if

the AgNPs are intended to be used for their antimicrobial ability. This agglomeration effect is known to be less prominent when AgNPs are dispersed homogeneously throughout the polymer matrix to limit their ability to fuse.[96, 97] Another way to circumvent this issue is to form the AgNPs either during the printing process or post-printing. For example, Vidakis et al. demonstrated that blends of PLA, $AgNO_3$, and nanoparticle capping agents could be printed directly using a melt extrusion technique. The $AgNO_3$ acted as a AgNPs precursor that formed the nanoparticles in the PLA during the heated printing process. The resulting printed composites were shown to have efficient antimicrobial activity against both gram-negative and gram-positive bacteria.[95]

A similar methodology has also been reported in SLA type 3D printing, with Taormina et al. demonstrating simultaneous generation of AgNPs during photocuring of a printable resin, yielding a highly uniform printed composite.[98] Fantino et al. also exploited a resin-based printing approach along with $AgNO_3$, followed by a subsequent heat treatment to form the AgNPs.[93] Thus far, no examples in the literature have been found that produce AgNPs composite materials for biomedical applications using the SLS printing method.

5.2.5. Summary and Research Objectives

A review of the literature has shown that scCO₂ is a suitable solvent for the synthesis of a range of inorganic compounds. The fabrication of metal nanoparticles in particular has been widely studied in scCO₂, with synthesis shown to be relatively simple. A range of different noble metal nanoparticles have been synthesised successfully in scCO₂ and show promise for an array of potential applications. AgNPs are a very desirable type of metal nanoparticle for a number of uses, but most prominent among these is their value in the biomedical field because of their high antimicrobial activity towards a range of pathogens. AgNPs can be synthesised readily in scCO₂ and methodologies already exist to prepare clean polymer-AgNPs composites, though these procedures lack any fine control over how these AgNPs are arranged in the substrate.

Self-assembled block copolymer templates offer a simple solution to organise the arrangement of AgNPs, in an identical manner to the other inorganic materials explored in previous chapters. In fact, P4VP block copolymers have already proven successful at controlling the spatial arrangement of AgNPs.[99] The ability to co-synthesise a block copolymer

template and AgNPs simultaneously in scCO$_2$ represents an advancement over current reports in the literature. Not only will this limit the number of synthetic steps required to yield an organised polymer-inorganic composite but will also completely eliminate the need for any conventional non-renewable solvents.

Furthermore, highly uniform polymer-AgNPs composite powders, like those that may be obtained from scCO$_2$, have good applicability for use in additive manufacturing. In particular, a composite powder will be highly suitable for use in SLS 3D printing, which has thus far been underutilised for fabricating biomedical components. While a few examples exist of 3D printed AgNPs composites through the SLA and FDM techniques, developing a material suitable for SLS unlocks the potential benefits of this technique. This includes the ability to print higher resolution 3D objects with more complex arrangements, as SLS has no need for support structures.[83]

To summarise, the aim of this chapter is to incorporate the synthesis of AgNPs into scCO$_2$ during the polymerisation of a PMMA-*b*-P4VP block copolymer. Co-assembly of the block copolymer with the formed AgNPs will be used to yield polymer particles containing a uniform distribution of AgNPs, all without the use of conventional organic solvents. The composites will then be tested for suitability in biomedical applications by assessing their biocompatibility and antimicrobial activity. Finally, the composite powders will be used in SLS 3D printing to prove their potential use as an antimicrobial ink for the manufacturing of biomedical devices.

5.3. Experimental

5.3.1. Materials

Methyl methacrylate (MMA, ProSciTech, 99%) and 4-vinylpyridine (4VP, Acros Organics, 95%) were purified by eluting through a basic alumina column to remove inhibitor. 2,2'-azobis(2-methylpropionitrile) (AIBN, Sigma Aldrich, 98%) was purified by recrystallisation from methanol. (1,5-Cyclooctadiene)(hexafluoroacetylacetonato)silver(I) (Ag(hfac)(COD), Sigma Aldrich, 99%), dry CO$_2$ (BOC, SFC grade, 99.99%), 2-(Dodecylthiocarbonothioylthio)-2-methylpropionic acid (DDMAT, Sigma Aldrich, 98%) and poly(dimethylsiloxane) monomethyl methacrylate (PDMS-MA, Fluorochem, M$_n$ ~10 kg mol^{-1}) were all used as received.

5.3.2. Synthesis of PMMA-*b*-P4VP-AgNPs Composite

All PMMA-*b*-P4VP-AgNPs composites in this chapter were synthesised using a two-pot dispersion method in scCO$_2$. All reactions were performed using the high-pressure equipment detailed in **Chapter 2** and operated following the standard operating procedure described in **Section 2.2.4**.

The following procedure describes the synthesis of a PMMA-*b*-P4VP-AgNPs block copolymer composite with target molecular weight of 67 kg mol^{-1} (25 wt% P4VP composition) and a AgNP loading equalling to 5 wt% Ag precursor with respect to the mass of 4VP monomer.

The 50 kg mol^{-1} PMMA macro-RAFT agent was first synthesised by preparing a solution of MMA (10 g, 99.9 mmol), AIBN (16.4 mg, 0.10 mmol), DDMAT (72.8 mg, 0.20 mmol) and PDMS-MA polymeric stabiliser (0.5 g). The solution was mixed in a sealed vial at 0 °C and degassed by purging with argon for 30 minutes. The monomer solution was then added to the degassed 60 mL high-pressure autoclave via syringe against a positive pressure of CO$_2$ to prevent the ingress of air. The autoclave was then sealed, heated to 65 °C and pressurised to 241 bar, following the standard operating procedure. After stirring at 300 rpm for 24 hours, the reaction was cooled to room temperature, slowly vented and the PMMA macro-RAFT agent product collected as a fine free-flowing powder (9.50 g, 89%).

In the second reaction stage, the PMMA macro-RAFT agent (7.5 g, M$_n$ ~50 kg mol^{-1}), additional PDMS-MA (0.125 g) and Ag(hfac)(COD) (0.125 g, 0.30 mmol) inorganic precursor were loaded into the 60 mL autoclave and degassed by flushing with CO$_2$ at 1-2 bar for 30 minutes. The autoclave was then sealed, heated to 65 °C and pressurised to 241 bar, following the standard

operating procedure. After stirring at 300 rpm for ~1 hour to re-disperse the polymer particles and dissolve the silver complex, a degassed solution of 4VP (2.5 g, 23.8 mmol) with AIBN (6.25 mg, 0.04 mmol) was added to the autoclave via a HPLC pump at a rate of 0.5 mL min^{-1}. After 24 hours the autoclave was cooled to 50 °C and the CO_2 inlet and outlet taps were opened slowly and simultaneously. A moderate flow of CO_2 was allowed to pass through the autoclave for 30 minutes, keeping the vessel pressure between approximately 138-201 bar, to fully remove any scCO₂ soluble impurities. After the CO_2 extraction, both inlet and outlet taps were closed simultaneously, and the autoclave was cooled to room temperature before slowly venting to atmospheric pressure. The PMMA-*b*-P4VP-AgNPs composite product was collected as a light brown, dry free-flowing powder (7.54 g, 74%).

5.3.3. AgNPs Release Study

The release of AgNPs from the polymer composite was tested in aqueous solutions. Samples of the PMMA-*b*-P4VP-AgNPs composites (25 mg) were dispersed in distilled water (5 mL) or 4.7 pH buffer (5 mL, 0.1 M, acetic acid/sodium acetate) solutions via rapid stirring. Mixtures were stirred constantly during the duration of the study. Small amounts (100 µL) of the mixture were removed at the desired timepoints and passed through a membrane filter (Millex, 0.45 µm) to remove any large polymer microparticles. AgNP content of the filtered samples was then measured using high throughput UV/vis spectrometry (see below). Larger samples (2 mL) of the mixtures were also taken at the end of the study (72 hours) and filtered in the same manner to assess the size of the released AgNPs.

5.3.4. Selective Laser Sintering of PMMA-*b*-P4VP-AgNPs

PMMA-*b*-P4VP-AgNPs composite powders were printed into solid objects using a SLS additive manufacturing printer. Thin square sections (0.5 x 20 x 20 mm) were printed, produced using Materialise Magics design software. The PMMA-*b*-P4VP-AgNPs powder was prepared by sieving through a 200 µm mesh filter and dried at 100 °C for an hour. The composite powder was then loaded onto the build platform and printed using an EOS Formiga P110 SLS printer equipped with a CO_2 laser (λ = 10.6 µm, spot size 200 µm). The powder was sintered using a bed temperature of 90 °C, hatching speed of 2500 mm s^{-1}, hatching distance of 0.25 mm, hatching laser power of 19 W and contour laser power of 19 W. Once printed, the sections were left to cool to room temperature in the powder bed before collecting.

5.3.5. Characterisation

Many of the characterisation techniques used in this chapter are described in **Section 2.3** of this thesis. Additional techniques used only in this chapter are described below.

5.3.5.1. UV/Vis Spectroscopy

UV/vis spectra for the PMMA-*b*-P4VP-AgNPs composites were obtained by dissolving the composites in dichloromethane at a concentration of 3 mg mL^{-1}. Solutions were then analysed using a Perkin Elmer Lambda 25 UV/vis spectrometer, scanning in the range of 250-600 nm.

High throughput UV/vis spectroscopy was used to analyse the AgNPs content of the filtered supernatants from the release study. Samples were analysed in a 96-well plate using a BioTek Epoch 2 microplate spectrophotometer, in the range of 300-600 nm at 5 nm intervals.

5.3.5.2. Dynamic Light Scattering

The size of the AgNPs in the dissolved composites and filtered solutions from the release studies was assessed by dynamic light scattering (DLS). A Zetasizer nano spectrometer (Malvern Instruments Ltd) equipped with a 633 nm laser at a fixed angle of 173° was used. Samples were equilibrated at 25 °C for 20 seconds prior to measuring. All measurements were an average of a total of 15 scans. The polydispersity index (PDI) was calculated from **Equation 5.1** rather than from the cumulant fit of the correlation function, as measured by the Zetasizer instrument. This was done to avoid the contribution of aggregate peaks. PDI was calculated using the mean average particle diameter (d_n) and standard deviation (σ) for each individual DLS peak.[100]

$$PDI = \frac{\sigma^2}{d_n{}^2}$$

(Equation 5.1)

5.3.5.3. Cytotoxicity Measurements

The biocompatibility of PMMA-*b*-P4VP-AgNPs composites was determined by cytotoxicity tests against caco-2 human intestinal epithelial cells. Cell were seeded in a 12-well plate at a density of 1.2 x10^5 cells per well in 1 mL Dulbecco's modified Eagle's medium (DMEM) with 10 vol% fetal bovine serum (FBS). Cells were cultured for 24 hours before exposure to 1 mg of the selected PMMA-*b*-P4VP-AgNPs composite for 48 hours. Metabolic activity was determined by exposure to PrestoBlue® (Thermo Fisher Scientific) and cell membrane

damage was assessed by a lactate dehydrogenase (LDH) release assay (Sigma-Aldrich, TOX7 kit). Triton X-100 (Sigma-Aldrich) applied at a concentration of 1 vol% was used as a positive control for cell death. Cells were exposed to no additional reagents for the negative control.

After exposure to the composite samples, 50 µL of supernatant was collected per well for LDH content analysis. Cells were then washed twice with phosphate-buffered saline (PBS) before adding 100 µL PrestoBlue® reagent solution (10 vol% in phenol red free medium) per well for 60 mins. The resulting fluorescence was measured at 560/600 nm ($\lambda_{ex}/\lambda_{em}$) on a Tecan Spark M10 multimode plate reader. Relative metabolic activity was calculated by setting measurements from the negative control as 100% activity and measurements from the positive control as 0% activity. LDH detection was performed according to the manufacturer's instructions, with 100 µL LDH reagent added to the collected supernatants before incubating in absence of light at room temperature for 25 min. Absorbance at 492 nm was then recorded. Relative LDH release was calculated with the negative control's absorbance taken as 0% and the positive control's taken as 100%, as it was assumed this caused total cell lysis.

All biocompatibility tests were performed in triplicate. This procedure was carried out by Dr Robert Cavanagh (School of Pharmacy, University of Nottingham).

5.3.5.4. Antimicrobial Tests

Antimicrobial activity of the synthesised composites was determined by exposing bacteria to the aqueous supernatants of the dispersed samples. Samples were prepared as suspensions in sterilised water at a concentration of 10 mg mL^{-1}. Small samples (10 µL) of the supernatants were withdrawn from the suspensions at 24-hour and 48-hour timepoints. These supernatants were placed on Muller Hinton agar plates previously seeded with either *Staphylococcus aureus* (*S.* aureus, ATCC 10850) or *Escherichia coli* (E. coli, ATCC 25922). Bacteria were seeded at an optical density of 0.05, corresponding to 1×10^9 colony forming units (CFU) per mL. Plates were incubated at 37 °C for 18 hours and the activity of the samples was determined by measuring the size of the bacterial inhibition halo of each sample drop. All antimicrobial tests were conducted by Dr Claudia Vuotto (IRCCS Fondazione Santa Lucia, Rome) and Prof. Iolanda Francolini (Sapienza University of Rome, Italy).

5.3.5.5. Surface Elemental Mapping

Elemental maps of the surface of printed PMMA-*b*-P4VP-AgNPs samples were obtained during SEM imaging (see **Section 2.3.3**) through energy-dispersive X-ray spectroscopy (EDXS). Elemental composition was determined by measuring the characteristic electron-induced X-ray emissions of the sample using an Oxford Instruments XMax 100TLE detector, controlled using an Aztec software package.

5.3.5.6. Time-of-Flight Secondary Ion Mass Spectrometry

Time-of-flight secondary ion mass spectrometry (ToF-SIMS) depth profile data were obtained using a ToF-SIMS IV instrument (ION-TOF GmbH., Münster, Germany). The measurements were acquired in a dual beam, non-interlaced mode with alternating analysis and sputtering cycles. The primary ion beam used for analysis was a bismuth liquid metal ion gun (Bi^{3+}) operated at 25 keV and an argon gas cluster (Ar_{1700}^{+}, 10 keV) was used as the sputter source for depth profiling. Sputtering was performed over an area of 500x500 μm, with the central 200x200 μm area analysed using the primary beam in a 256x256 pixel raster scan. The profiling data were analysed using SurfaceLab 7 software (IONTOF GmbH). All ToF-SIMS measurements were performed by Dr Long Jiang (School of Pharmacy, University of Nottingham).

5.4. Results and Discussion

5.4.1. Synthesis of PMMA-*b*-P4VP with AgNPs

In this study, AgNPs were intended to be synthesised simultaneously with the P4VP polymer block in the scCO$_2$ dispersion polymerisation. Hence, a AgNP precursor needed to be chosen that fit several crucial criteria to ensure compatibility with the polymer synthesis. Firstly, the silver precursor needed to be readily soluble in scCO$_2$, specifically, at the pressure used to conduct the dispersion polymerisation. Secondly, the precursor needed to be relatively stable at mild conditions but also degrade to form nanoparticles when required. Significant degradation of the precursor needed to occur at around the polymerisation temperature, ideally this would be 65 °C. An unstable precursor would form AgNPs before polymerisation of the 4VP had begun, while an overly stable precursor would require a higher temperature to induce degradation, which may compromise the polymer dispersion.

The silver complex Ag(hfac)(COD) (**Figure 5.5**) was chosen for this study. This particular complex has been used in previous studies in scCO$_2$ and has already proven to meet the above requirements.[34, 46, 101] The compound is demonstrated to have good solubility in scCO$_2$ above ~103 bar and decomposes to form nanoparticles at temperatures ranging from 60-180 °C.[101] A number of studies degrade this complex to AgNPs under an atmosphere of H$_2$ to aid in the reduction process.[55, 59] Though, other studies omit this and have still proven to yield AgNPs.[34]
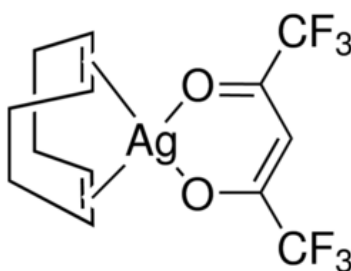
Figure 5.5: *Chemical structure for (1,5-Cyclooctadiene)(hexafluoroacetylacetonato)silver(I), (Ag(hfac)(COD)), the silver complex used for the formation of AgNPs in this chapter.*

Synthesis of the PMMA-*b*-P4VP-AgNPs hybrid materials was achieved using the procedure described in **Section 5.3.2**. Composites were synthesised using a two-pot approach, first creating 50 kg mol^{-1} PMMA macro-RAFT agent seed particles. Then, the polymer was re-dispersed in scCO$_2$ with additional PDMS-MA stabiliser and various quantities of the silver complex. This was followed by injection of the 4VP monomer and radical initiator once the

dispersion was reformed, to ensure microparticle structures were preserved (**Figure 5.6**). This approach was chosen over a one-pot synthetic strategy due to practical limitations. The solid Ag(hfac)(COD) compound could not be added directly to the autoclave after polymerisation of the MMA was complete, as the HPLC injection method was only suitable for addition of liquid compounds or solutions. Hence, the synthesis was divided into two steps to allow for addition of the silver complex. However, one-pot synthesis of these composites could be achieved using high-pressure solid addition apparatus, which have already been designed.[102]
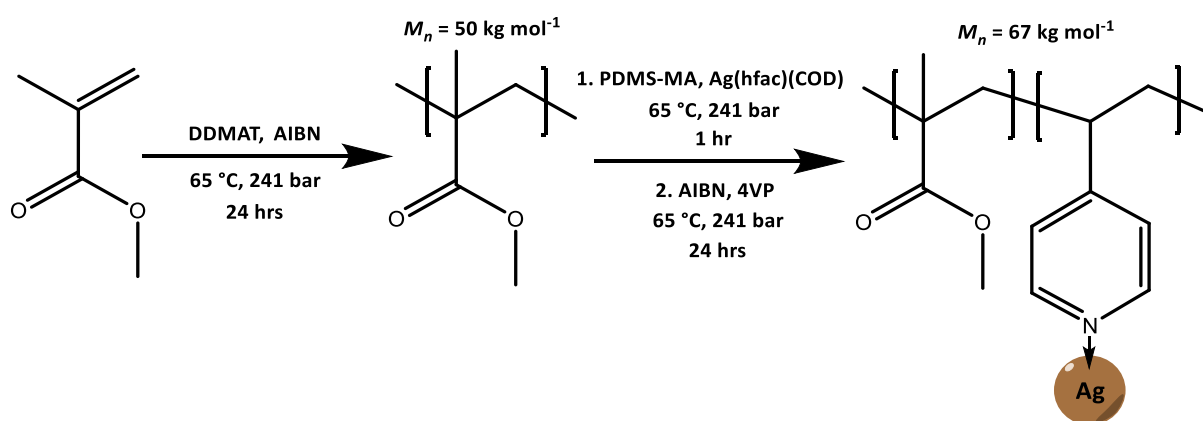
Figure 5.6: *Reaction scheme for the two-pot synthesis of PMMA-b-P4VP-AgNPs composites, using the Ag(hfac)(COD) complex. Polymer structures are simplified and do not include the RAFT or initiator end groups.*

The mass of Ag(hfac)(COD) added to the autoclave was varied from 62.5 mg to 250 mg. This equated to a loading of 2.5 to 10 wt% of silver precursor, relative to the mass of 4VP monomer being polymerised. In all cases, a total molecular weight of 67 kg mol^{-1} was targeted for the PMMA-*b*-P4VP block copolymer, with a w_{P4VP} of 25%, to mirror previous studies in this thesis. Polymerisations were performed for 24 hours to ensure high conversion of the 4VP monomer to block copolymer. Following this, the reaction mixtures were purified with a flow of CO_2 for 30 mins to remove any remaining scCO₂-soluble compounds. This included unreacted monomer and displaced ligands from the Ag(hfac)(COD) complex. Supercritical fluids are commonly employed in this manner to extract specific chemical components from a mixture.[103]

The final washed composite materials were obtained as dry, brown-coloured powders, with darker colour observed when more of the Ag(hfac)(COD) complex was added. This colour is

typical for silver nanoparticles, caused by absorption of visible light through excitation of the particle's surface plasmon resonance.[104] The composition of the materials was assessed by ^{1}H NMR (**Figure 5.7**). This was used to evaluate sample purity to ensure the CO_2 extraction step was successful and also to measure the P4VP block fraction and molecular weight (**Table 5.1**).

Table 5.1: *Summary of polymer characterisation data for the PMMA-b-P4VP-AgNPs block copolymer composite samples, synthesised with various amounts of Ag(hfac)(COD).* [a]

Ag(hfac)(COD) loading (mg)	PMMA		PMMA-*b*-P4VP		
	$M_{n\,exp}$ [b] (kg mol^{-1})	$Đ$ [b]	$M_{n\,exp}$ [c] (kg mol^{-1})	w_{P4VP} [c]	d_n (µm) [d]
62.5	53.3	1.23	65.8	16	2.34
125	54.0	1.22	67.6	20	2.13
250	55.5	1.21	65.1	15	2.06

[a] *Conditions: 7.5 g of PMMA macro-RAFT seed dispersed with 0.125 g PDMS-MA and Ag(hfac)(COD) at 65 °C and 241 bar for 1 hr, then 2.5 g of 4VP added for 24 hrs.* [b] *Obtained from GPC, eluting in a chloroform/ethanol/TEA mixture, measured with dRI detector calibrated against PMMA narrow standards.* [c] *Obtained from ^{1}H NMR integrations.* [d] *Measured from SEM images.*
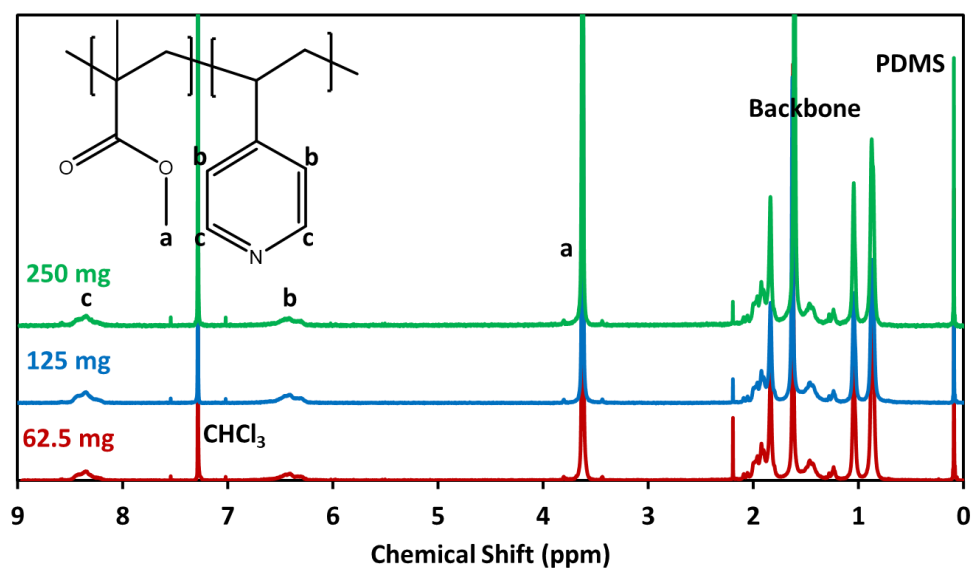
Figure 5.7: *^{1}H NMR spectra for the PMMA-b-P4VP-AgNPs composite materials, synthesised with different quantities of Ag(hfac)(COD) precursor.*

In this study the block copolymer molecular weights were only investigated using ^{1}H NMR, rather than GPC. It was a concern that the added AgNPs in the composite materials may damage the stationary phase columns of the GPC. Due to extensive previous study of this 4VP polymerisation in scCO₂, it was assumed that block copolymers were similarly formed in all cases for these syntheses. Molecular weight values for the P4VP blocks were extrapolated

using the $M_{n\,exp}$ values for the PMMA macro-RAFTs and the measured w_{P4VP} from the ^{1}H NMR, assuming 100% blocking efficiency.

For all the synthesised composites, the calculated w_{P4VP} values for the block copolymers was significantly lower than the target value of 25 wt%. This indicated that polymerisation of the 4VP monomer was not complete in the 24-hour time period it would normally take to reach high monomer conversion for this reaction. This is undoubtedly a consequence of the added silver precursor in these dispersion polymerisations. 4VP interaction with the silver complex, or AgNPs, may hinder the polymerisation kinetics. Alternately, decomposition of the silver precursor may lead to scavenging of radical species in the polymerisation, as the complex is reduced to elemental silver. This would be expected to increase the Đ in the block copolymer product, however, this cannot currently be assessed without the use of GPC.

The ^{1}H NMR spectra for the composites indicate the extraction step at the end of the synthesis was successful after only 30 mins of CO_2 flow. The spectra show no characteristic peaks for any expected impurities, including the silver complex and the unreacted 4VP monomer. No peaks were observed in the region of 4.0 - 6.0 ppm where signals would be expected for the vinyl 4VP protons, as well as protons for the cyclooctadiene and hexafluoroacetylacetone ligands. This provides good evidence that these composite materials should not present any toxic side effects as a result of residual monomer or silver complex.

The microstructure of the PMMA-*b*-P4VP-AgNPs composites was evaluated by SEM (**Figure 5.8**). Microparticle structure was expected to be maintained in the composites, provided by the PMMA macro-RAFT agent particles used to create them. Their d_n sizes (**Table 5.1**) were measured from SEM images using the method described in **Section 2.3.3**, with dispersity quoted as a coefficient of variation (CV) percentage.

SEM analysis for the composite with the lowest precursor loading (62.5 mg) revealed relatively well-defined microparticles with a d_n value of 2.34 µm. The slightly large average particle size is due to the two-pot re-dispersion method used to make the composites, whereby a fixed number of already formed PMMA seed particles are dispersed and increase in size by addition of the subsequent monomer into the particles. Particle size dispersity was also found to be relatively similar to that seen previously for block copolymer dispersion polymerisations in scCO₂.
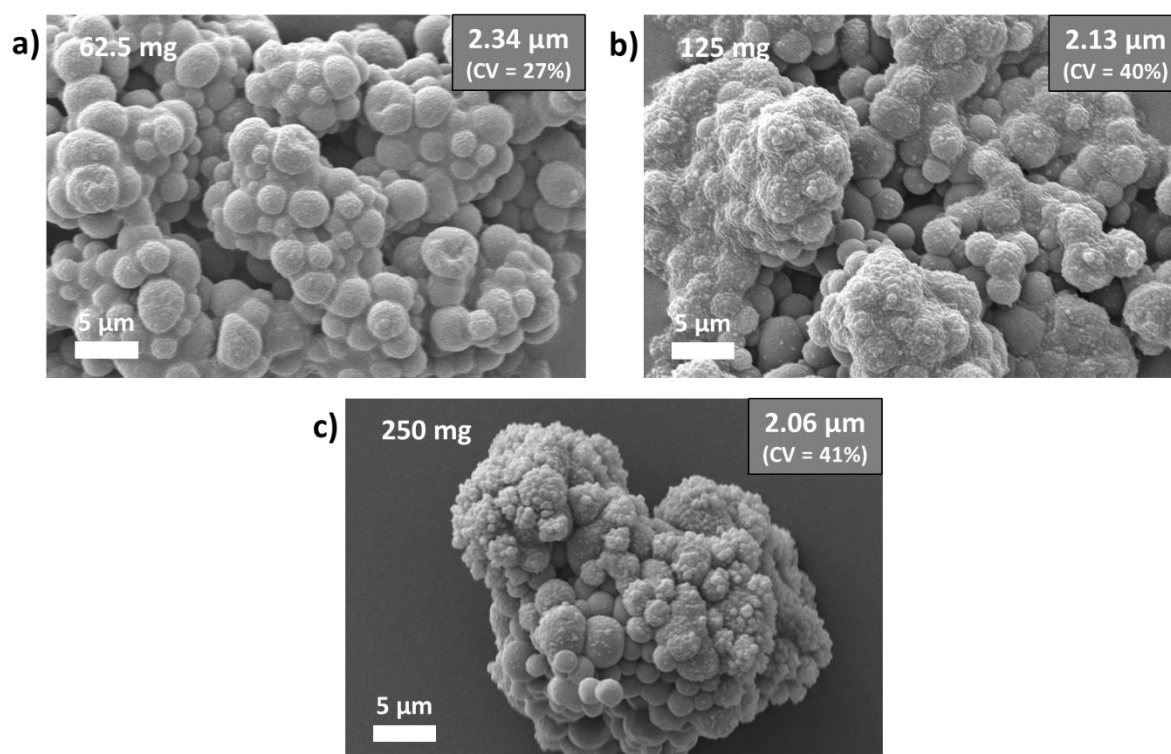
Figure 5.8: *SEM micrographs of the PMMA-b-P4VP-AgNPs composites synthesised with (a) 62.5 mg, (b) 125 mg and (c) 250 mg of Ag(hfac)(COD) precursor.*

At increased loadings of silver precursor (125 and 250 mg), the microparticle structures were found to be slightly less well-defined, with some areas of aggregation visible. Upon closer inspection, the aggregated material appeared to be a collection of smaller nanoscale particles. These smaller particles are likely comprised of P4VP homopolymer that nucleated into secondary particles rather than diffusing into the PMMA macro-RAFT particles. This would appear to be a direct result of the higher concentration of Ag(hfac)(COD) in these polymerisations. The added silver complex may have hindered the ability of the PMMA macro-RAFT particles to re-disperse in the second stage of the reaction. Alternately, excess Ag(hfac)(COD) may adversely affect the controlled polymerisation kinetics of the 4VP and favour the formation of new particles instead of diffusion into PMMA seed particles.

Regardless of the exact mechanism, it is clear that higher quantities of the silver complex can be detrimental to the success of the dispersion polymerisation. However, the amount of silver complex used in this study appear to form only small quantities of aggregated material with a significant amount of well-defined microparticles still visible. The high d_n values for all

samples also suggest a considerable amount of the 4VP monomer is added into the seed particles, likely forming the desired block copolymer composite.

5.4.2. Distribution of AgNPs Within Composites

It was expected that the association of silver to the 4VP monomer would allow the AgNPs to be distributed throughout the composite microparticles, rather than just on their surfaces. This being a result of the unique physical properties of scCO$_2$, with gas-like diffusivity allowing the monomer-inorganic mixture to diffuse into the PMMA particles and become trapped by polymerisation of the monomer onto the macro-RAFT agent.

To confirm the even distribution of AgNPs through the polymer microparticles, the composites were analysed by cross-sectional TEM (**Figure 5.9**). Composite particles were embedded in resin and cut using an ultramicrotome to give thin, electron-transparent particle cross-sections. No selective polymer staining agents were used to ensure maximum contrast between only the polymeric material and the AgNPs.

All TEM images revealed block copolymer microparticles with internal nanostructure. The nanostructures are shown to be the typical spherical-type block copolymer morphology, consistent with what would be expected for PMMA-*b*-P4VP copolymers with the $w_{P4VP} \approx$ 20%.[105] These spherical morphologies were slightly difficult to distinguish as no I$_2$ vapour staining agent was used prior to imaging. The identification of internal self-assembled nanostructures further confirms the successful synthesis of PMMA-*b*-P4VP block copolymers, despite the lack of available GPC data.

In addition to the polymer morphology, distinct dark dots can be seen for all the composite samples, distributed relatively evenly throughout the particles' cross-sections. These are undoubtedly the AgNPs formed within the block copolymer. Due to the omission of staining agents, only the silver atoms are heavy enough to give such a dark contrast in the TEM images. Though these AgNPs are large and easily visible in the 250 mg composite (**Figure 5.9 e, f**), the dots are much smaller in the lower precursor loaded samples, being only clearly noticeable in the higher magnification images (**Figure 5.9 b, d**). The large AgNP sizes in the highest precursor loaded composite is likely caused by a more significant degree of aggregation of the decomposed silver complex, due to its higher concentration in the reaction. This

concentration appears to be too high to lead to controlled formation of reasonably uniform AgNPs.
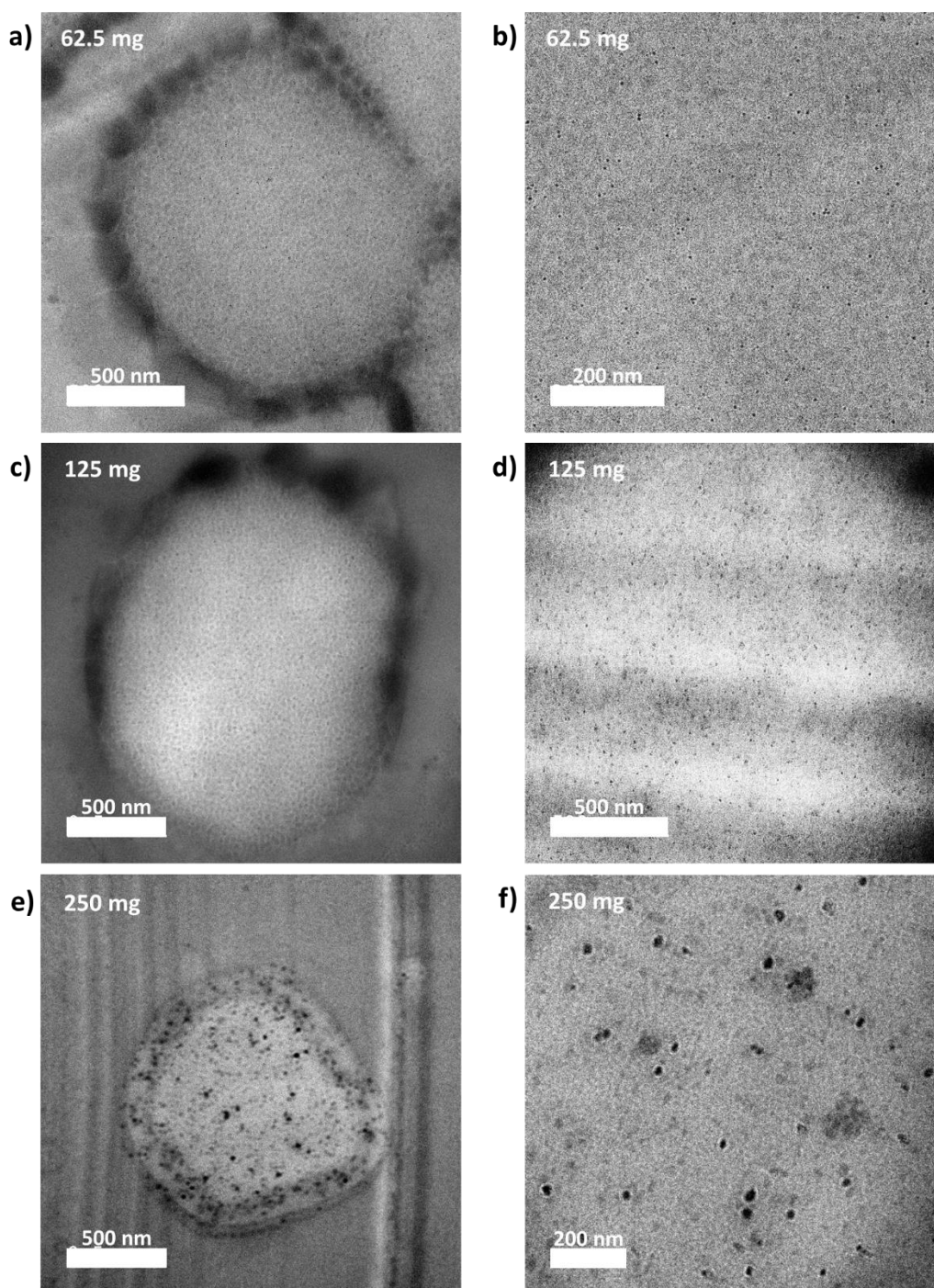
Figure 5.9: *TEM cross-sectional micrographs of the PMMA-b-P4VP-AgNPs composites, synthesised using (a, b) 62.5 mg, (c, d) 125 mg and (e, f) 250 mg of Ag(hfac)(COD) precursor.*

From the TEM images it was clear that the dispersion polymerisation was successful in infusing the silver precursor within the block copolymer particles. Inorganic material was effectively transported into the polymer particles, with aid of the 4VP monomer, and fixed

within the microparticles to give a uniform composite material. More specifically, it was likely that the silver precursor first began to degrade to form the AgNPs in the scCO$_2$ dispersion. These growing nanoparticles could then have adsorbed 4VP monomer to their surface and been carried into the PMMA seed particles, with high diffusivity of the AgNPs facilitated by the high solubility of the 4VP outer shell. Once within the polymer particles the monomer would polymerise with the PMMA macro-RAFT and fixate the AgNPs within the microparticles. However, a full kinetic investigation would be required prove this theory, by analysing the state of the product at various timepoints in the reaction.

Due to the extremely small sizes, it was difficult to conclusively determine whether the AgNPs reside solely within the slightly darker spherical P4VP domains, though this was the expectation. The AgNPs were also too small to accurately measure through TEM images but are certainly <20 nm in diameter for the lower precursor loaded composites. This is comparable to other reports of AgNPs synthesised in scCO$_2$.[34, 52, 56]

In order to prove that the distribution of AgNPs within the microparticles was a direct result of the polymerisation and co-assembly with 4VP, a control experiment was performed. PMMA macro-RAFT seed particles were dispersed in scCO$_2$ with additional PDMS-MA and 125 mg of Ag(hfac)(COD). The injection step of 4VP was omitted and after 24 hours the PMMA-AgNPs material was collected. The resulting material's morphology was analysed using the same SEM and TEM microscopy techniques used for the previous composites (**Figure 5.10**).
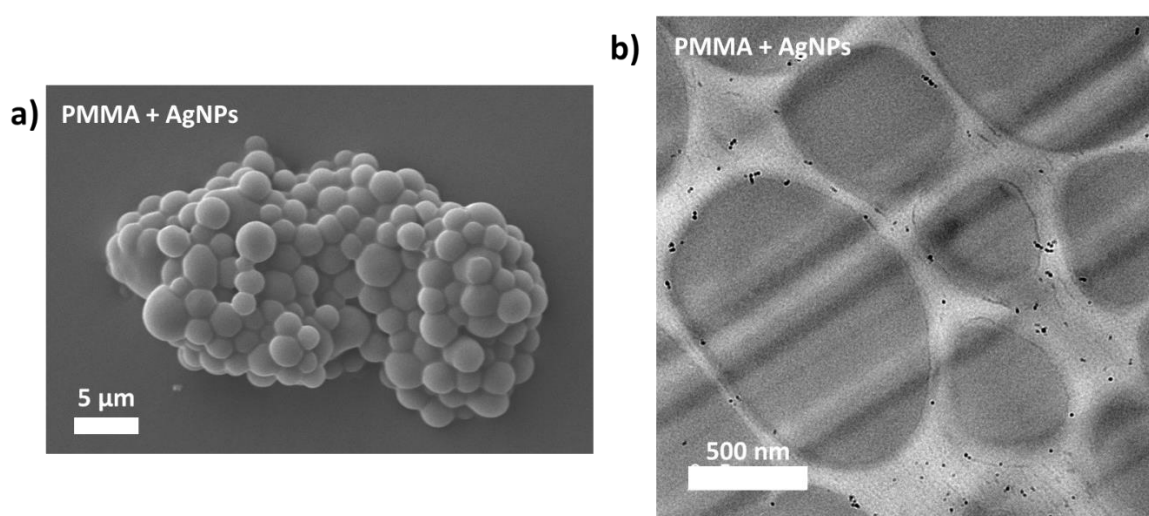
Figure 5.10: *(a) SEM and (b) cross-sectional TEM micrographs of PMMA microparticles dispersed in scCO₂ with only the Ag(hfac)(COD) complex.*

The PMMA-AgNPs composite was shown to consist of well-defined microparticles, unaffected by the addition of the silver precursor. Cross-sectional TEM analysis revealed the formation of AgNPs only on the surfaces of the PMMA microparticles or in the resin support. No AgNPs were observed within the polymer particles, proving that AgNPs could only be carried within the polymer by the addition of the 4VP monomer bound to the silver. Hence, only the block copolymer composite materials contain an even distribution of AgNPs throughout the material.

5.4.3. Characterisation of AgNPs composites

With the morphology of the composite samples confirmed to be block copolymer microparticles embedded with silver nanoparticles, as intended, further analysis was performed to fully characterise the composites. Firstly, DSC analysis was conducted on the three composite samples to determine their thermal properties (**Figure 5.11 a**). Properties such as the T_g of the polymer materials are important to ascertain for SLS printing. This is because an optimal temperature must be applied to encourage even spreading of the powdered polymer on the build platform, without causing inadvertent sintering of the particles. Measured values are also summarised below (**Table 5.2**).
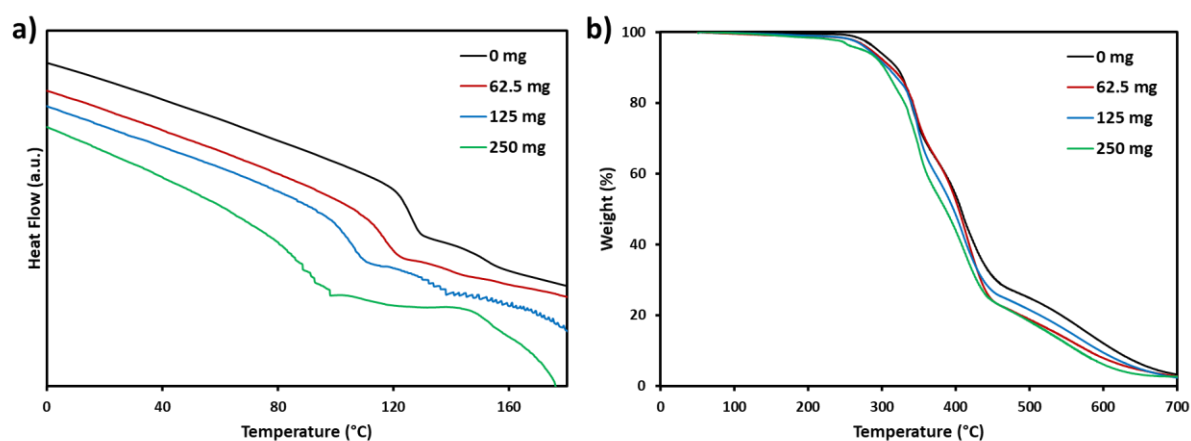
Figure 5.11: *(a) DSC and (b) TGA thermal characterisation data for all the polymer-AgNPs composites and a blank PMMA-b-P4VP copolymer.*

Step transitions in the DSC heat flow plots indicated the T_g values of the materials. For the original PMMA-*b*-P4VP block copolymer, a large step transition can be seen at 125 °C for the glass transition of the PMMA.[106] A smaller step was also observed at around 150 °C, relating to the T_g of the P4VP block, though the intensity of this transition is small due to the lower

abundance of P4VP in the copolymer ($w_{P4VP} \approx 25\%$). A single step transition was observed for all the polymer-AgNPs composites, likely relating to the PMMA block, with any T_g for the P4VP block remaining undetected, likely due to the very low w_{P4VP} values calculated for these polymers. A trend of decreasing PMMA T_g with increased loading of silver precursor was observed (**Table 5.2**). Such a trend is common in polymers loaded with a nanofiller, as the nanoparticles inhibit polymer chain packing and thus the energy needed to overcome polymer-polymer interactions.[107] A decrease in T_g is achieved when the polymer-nanoparticle interactions are weaker than the polymer-polymer interactions, which would appear to be the case for these AgNPs composites.

The increasing depression of the T_g is a good indication that AgNPs content is increasing with precursor loading in the composites. A depression of the PMMA T_g would indicate that the AgNPs are present in the PMMA block copolymer phase rather than exclusively in the P4VP domains. Though it should be noted that DSC data was obtained on the second heating cycle of the samples and the AgNPs may have migrated to the PMMA domains during the first heat cycle.

Table 5.2: *Summary of the characterisation data for the PMMA-b-P4VP-AgNPs block copolymer composite samples, synthesised with various quantities of Ag(hfac)(COD).*

Ag(hfac)(COD) loading (mg)	Expected weight after calcination (wt%) [a]	Actual weight after calcination (wt%) [b]	PMMA T_g (°C) [c]	AgNP size [d]		Relative absorbance at 410 nm [e]
				Average size (nm)	PDI	
0	0	2.28	125	N/A	N/A	0
62.5	0.16	2.17	117	8.2	0.016	0.19
125	0.31	1.97	107	14.8	0.038	0.38
250	0.63	2.63	89	20.2	0.015	0.36

[a] Calculated assuming no loss of monomer and full conversion of Ag(hfac)(COD) to AgNPs. [b] Obtained TGA measurements. [c] Obtained DSC measurements. [d] Obtained from DLS measurements. [e] Obtained from UV/vis spectra.

TGA analysis was performed on the AgNPs composites to determine their degradation temperature and silver loading (**Figure 5.11b**). Samples were heated to 700 °C and calcined for one hour to remove all polymeric components of the composites while leaving behind the more thermal stable AgNPs. The TGA profiles for all the composites were found to be near

identical to the blank PMMA-*b*-P4VP copolymer, with the onset of polymer degradation found to be at ~280 °C in all cases. This demonstrates that the addition of AgNPs does not alter the thermal degradability of the block copolymer.

The quantity of precursor used for each reaction was converted into the expected weight percentage of AgNPs in the composites (**Table 5.2**). This assumed all precursor formed AgNPs in the synthesis and that there was no loss of monomer during the extraction. These values were compared to the final weight values obtained from the TGA data. The values from the TGA were not found to be representative of the expected quantity of AgNPs in each composite. In fact, it was shown that even the PMMA-*b*-P4VP copolymer with no AgNPs contained a small quantity of uncombusted material. It is not clear what this may be but is likely some carbon-based material that did not have sufficient oxygen in the TGA to combust fully. As this is present for all materials, it is not possible to directly correlate the end TGA mass with the mass of AgNPs in the composite. Other more sophisticated analytical methods may be required to quantify this trace amount of silver, such as quantitative inductively coupled plasma mass spectrometry.

To further assess the quantity of AgNPs contained within the synthesised composites, UV/vis spectroscopy was performed on the material dissolved in dichloromethane (**Figure 5.12 a**). This was used to detect the surface plasmon absorbance of the AgNPs and the relative intensity of the absorbance was used as a means to compare the quantity of AgNPs in the composites. All samples contained a strong absorbance peak at ~310 nm, corresponding to the DDMAT RAFT agent used in the synthesis of the block copolymers.[108] All UV/vis spectra were scaled so as to overlap the intensity of all the RAFT peaks, as the quantity of RAFT agent remained constant through all syntheses.

The AgNPs composite samples all displayed a broad absorbance at around 390-410 nm. This was a relatively low wavelength absorption for the surface plasmon resonance of AgNPs, relating to a nanoparticle size of roughly <10 nm, as the energy of the surface plasmon is known to be particle size dependent.[109-110] The absorption peak also appeared to be bimodal, indicating that there may in fact be two distinct distributions of nanoparticle size. Though, this may also indicate the presence of multiple nanoparticle morphologies, as the plasmon absorption is also shape dependent.[111] However, due to its very low wavelength (~390 nm),

the less intense peak may relate to colloidal atomic silver or small atomic clusters.[112] The plasmon absorbance was shown to increase in intensity from a loading of 62.5 mg to 125 mg of silver precursor, indicating a higher concentration of AgNPs. However, the absorbance appeared to remain at a relatively similar intensity for the composite with 250 mg precursor. This may indicate that not all the excess precursor degraded during the polymer synthesis and may have instead been removed during the CO_2 extraction process.
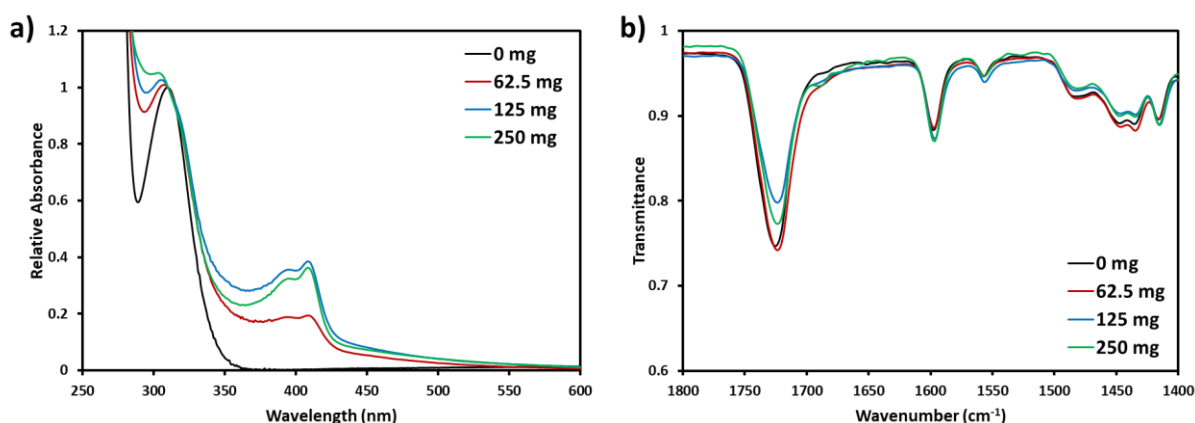
Figure 5.12: *(a) UV/vis spectra of the dissolved composite samples synthesised with increasing amount of silver precursor and (b) the corresponding IR spectra.*

The block copolymer and all composite samples were also analysed via FTIR spectroscopy (**Figure 5.12 b**). This was used to identify any bonding between the block copolymer and the AgNPs in the undissolved solid state. The IR spectra were found to be completely identical for all samples, regardless of amount of AgNPs. Notable absorbances are the peak at around 1725 cm^{-1} that relates to the $v(C=O)$ stretch of the carbonyl group in the PMMA and the peak at around 1600 cm^{-1} corresponding to the $v(CNC)$ aromatic stretch of the pyridine ring in the P4VP.[113, 114] If strong bonding of the pyridinyl nitrogen to the AgNPs was present, it would be expected that the $v(CNC)$ absorption peak would shift to higher wavenumber.[115] This was not observed for any of the composites and may be a sign that bonding to the P4VP is broken as the AgNPs are formed. However, this could also be because of the low quantity of AgNPs in comparison to the total number of pyridine groups, making the IR peak shift indetectable.

Finally, the AgNPs in the composites were assessed by dynamic light scattering (DLS) (**Figure 5.13**). DLS can be used to calculate the size of particles suspended in a solution and is used here to determine the size of the AgNPs once the polymer matrix is fully dissolved in

dichloromethane, as described in **Section 5.3.5.2**. The calculated average AgNPs size and the polydispersity index (PDI) of the nanoparticles is tabulated above (**Table 5.2**).
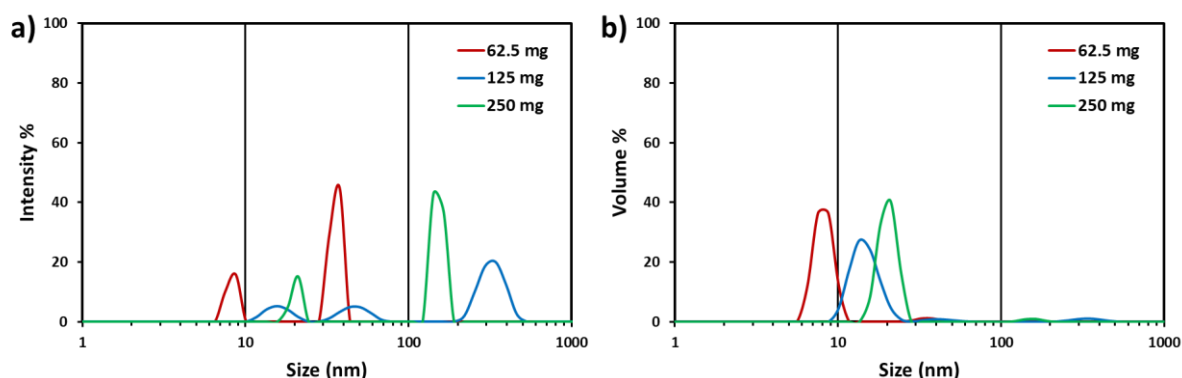
Figure 5.13: *DLS plots for the AgNPs composites samples dissolved in dichloromethane. The (a) scattering intensity and (b) particle volume percentage are plotted separately.*

DLS particle size data was first plotted as a function of the scattering intensity. This revealed several peaks for each composite sample, indicating the presence of multiple particle distributions in each sample. The larger particles seen in the scattering profile (>30 nm) were likely agglomerates of the original AgNPs. These would be expected to form to some extent as no stabilisers or capping agents were used to stabilise the AgNPs in the solutions. It could not be ruled out that these larger particles may also be block copolymer micelles that form through self-assembly in solution.

The particle size data was then converted and plotted as a function of particle volume (**Figure 5.13 b**). This data is much more relevant as Rayleigh scattering intensity is proportional to d^6, where d is the particle diameter. Though this does make it possible to detect even a miniscule number of larger particles in a solution, it does tend to overshadow the abundance of smaller particles. DLS data was replotted to indicate the average particle size of the smaller AgNPs, which were found to make up >90% of the total particle volume. AgNP size was shown to increase with the precursor loading, suggesting that a higher concentration of silver complex in the polymer dispersion did not necessarily nucleate a larger number of silver particles. A higher loading of silver precursor in the polymer instead encouraged greater growth of the AgNPs. This trend supported the observations made in the TEM analysis.

5.4.4. Biological activity of PMMA-*b*-P4VP-AgNPs Composites

The silver composites were tested for their potential use in biomedical applications, specifically as an antibacterial polymeric material. The first step in assessing viability in this application was to prove the composite materials' biocompatibility with human cells. The earlier ^{1}H NMR analysis suggested these composites contained no toxic components (monomer and precursor ligands) after the CO_2 extraction step of the synthesis. To substantiate this, the cytotoxicity of the composites was measured against caco-2 intestinal epithelial cells (**Figure 5.14**), following the procedure described in **Section 5.3.5.3**. This is a common cell line culture used to model the intestinal epithelial barrier.[116] Tests were conducted in triplicate, with the mean average result plotted and standard deviation represented by the error bars.
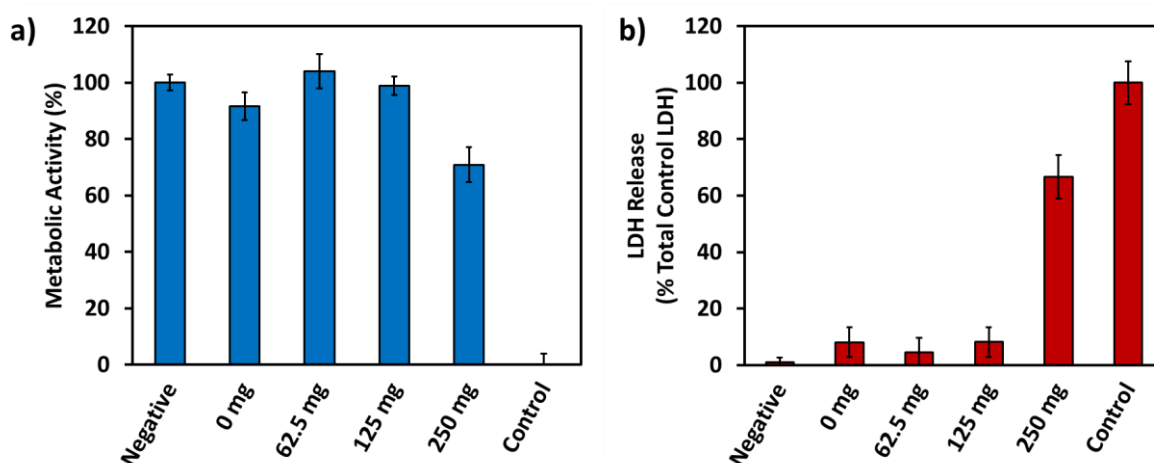
Figure 5.14: Biocompatibility tests of PMMA-b-P4VP-AgNPs samples with caco-2 intestinal epithelial cells. Measurement of cell (a) metabolic activity and (b) LDH release after exposure to samples. A negative cell line was run with only the caco-2 cells and a control cell line was also run containing Triton X-100 detergent to fully lyse the cells. Tests conducted in triplicate.

The composites synthesised with 62.5, 125 and 250 mg of precursor were all tested for their compatibility with the caco-2 cells. In addition, a blank PMMA-*b*-P4VP block copolymer, a positive control sample containing Triton X-100 detergent and a negative set of samples containing no additional reagents were also tested to reference the cell viability. After exposure to the materials for 48 hours, the cells were treated with PrestoBlue® to measure the cell's metabolic activity. Under the environment of normal living cells PrestoBlue® is reduced to a fluorescent red colour, indicating cell activity.[117] A secondary test was performed

to measure the concentration of lactate dehydrogenase (LDH) in the cell solutions. Damage to the cell membranes causes LDH to be released into the solution, with high concentrations being an indicator of cell necrosis.[118]

The high metabolic activity and low LDH release for the blank PMMA-*b*-P4VP and lower precursor loaded AgNPs composites indicated good compatibility with this cell line. This is good initial evidence that these composites may be safe to use directly in contact with human tissue without any short-term side effects. However, this was not true of the final composite with the highest concentration of AgNPs, synthesised using 250 mg of precursor. Decreased metabolic activity and much higher concentration of LDH suggests this composite caused significant damage to the cells and would therefore not be biocompatible in its current form.

As AgNPs have been demonstrated to be non-cytotoxic to this cell line in these concentrations,[119] it is expected that this composite contains trace amounts of some other hazardous compounds. A probable candidate being the ligands of the silver precursor complex, as these would have been present at a high concentration in this particular reaction. Hence, it was likely that the CO_2 extraction step used to purify the composite product was not rigorous enough when using the higher loading of 250 mg Ag(hfac)(COD) precursor.

With the majority of the materials showing good biocompatibility, the next test was to measure the release of the antibacterial AgNPs from the composites in aqueous solutions. Nanoparticle release studies were conducted over a period of 72 hours, following the procedure described in **Section 5.3.3**. The composites were suspended in distilled water (pH 7) and pH 4.7 buffer solutions to model different physiological environments. Mixtures were prepared at concentrations of 5 mg mL^{-1} and were exposed to constant agitation. Small samples of the supernatants were then collected at various timepoints and filtered to remove the larger polymer microparticles (>0.45 μm). AgNP content of the samples was then evaluated using high throughput UV/vis spectroscopy (**Figure 5.15**).

The UV/vis spectra for all sampled supernatants revealed a trend of increasing absorbance at higher loading of precursor in the composite, with a generally higher absorbance with increasing length of time as well. This represented promising initial evidence that the active component of the antimicrobial composites could be released in a controlled and sustained manner. No UV absorbance was seen for the lowest precursor loaded composite (62.5 mg),

except a very small peak at 72 hours in the pH 7 solution. The other two composites showed clear UV absorbance peaks at approximately 375 nm, with a moderate increase in absorbance intensity over the course of the study. For the highest precursor loaded composite, an absorbance maximum was observed at 24 hours with no further increase at 72 hours. This may indicate this material undergoes a rapid burst release of AgNPs rather than a sustained release.
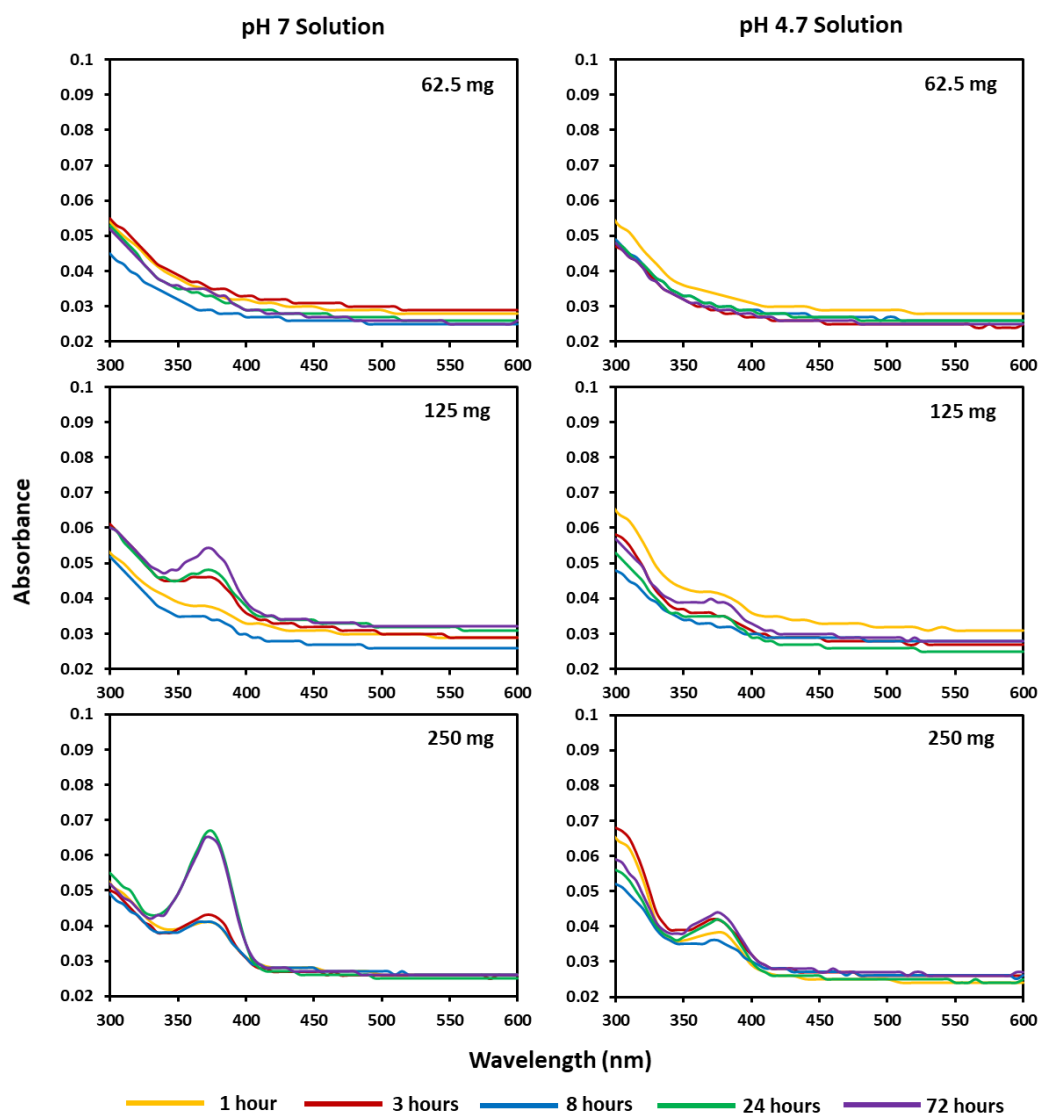
Figure 5.15: *UV/vis spectra of the sampled supernatants from the AgNP release study in distilled water (left) and pH 4.7 buffer solution (right) at various timepoints.*

These UV/vis absorbance peaks in this study were blue shifted to slightly lower wavelengths when compared to the AgNPs peaks previously observed for the composites fully dissolved in dichloromethane (**Figure 5.12 a**). In fact, the peaks observed in this release study did not

appear to correspond to the surface plasmon absorbance of AgNPs at all. Instead, these peaks would seem to relate more closely to the absorbance of either colloidal silver atoms or small clusters in solution.[112, 120] It is known from the literature that AgNPs can release a supply of Ag^+ in aqueous solutions, which may correspond to the observed UV/vis peak.[121, 122] The lack of detectable AgNPs may be caused by aggregation of the nanoparticles during their release into the solution phase, as no stabilising agent was added to the release medium.[123]

Another clear trend in this release study was a decrease in UV/vis absorbance in the pH 4.7 buffer solutions in comparison to the higher pH solutions. This lower absorbance was also accompanied by the appearance of a shoulder absorbance peak at around 310 nm, matching the position of the RAFT agent observed previously. It was expected that a lower pH environment would encourage swelling of the P4VP domains, as this is known to be soluble in acidic conditions.[124] This would explain the appearance of the RAFT absorbance peak as some of the copolymer is inadvertently released into the solution phase of the mixture. It was expected that this would also result in an increase in UV/vis absorbance of the silver as more was released from the dissolved polymer, which was not the case. However, it should be noted again here that this absorbance at ~375 nm likely relates only to small silver cluster rather than AgNPs and may not represent an overall decrease in released silver content.[112]

To aid in identifying the state of the silver in the release supernatants, DLS was performed on filtered supernatants at the end of the release study (72-hour timepoint) (**Figure 5.16**). The values calculated from these measurements are summarised below (**Table 5.3**). Measurements for the pH 7 solutions revealed a relatively high particle size diameter (>200 nm) for the two composites with lower silver precursor loading. This indicated the formation of large silver aggregate particles in the release supernatants, most likely formed due to the omission of any stabiliser molecules in the solutions.[123] These aggregates were too large to lead to a visible surface plasmon absorbance, meaning they were undetected in the UV/vis spectra.[125] Instead, the UV/vis analysis revealed the presence of smaller silver species in all samples, which would be too small to be detected by the DLS analysis.
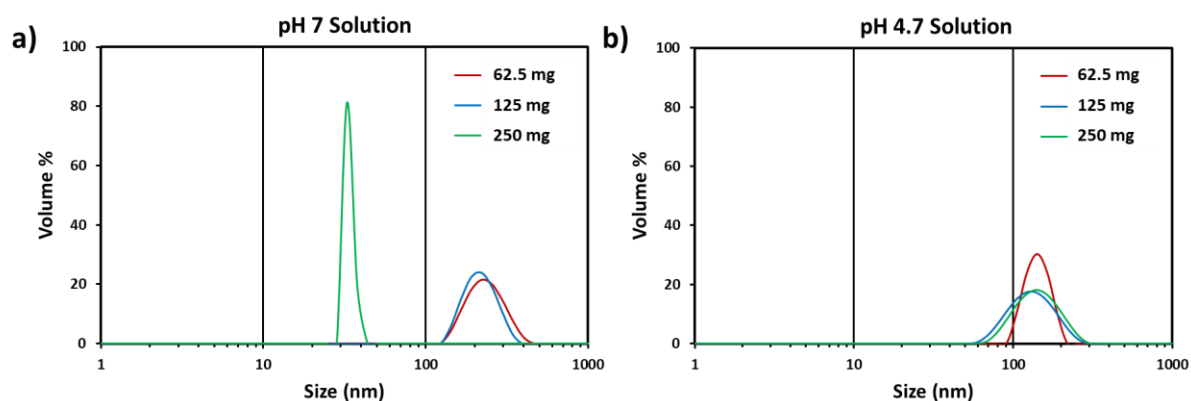
Figure 5.16: *DLS plots of the filtered supernatants at the end of the AgNPs release study in (a) distilled water and (b) pH 4.7 buffer solution.*

Table 5.3: *Summary of measured nanoparticle diameters for filter supernatants at the end of the AgNPs release study.* [a]

Ag(hfac)(COD) loading (mg)	pH 7 Solution		pH 4.7 Solution	
	Average particle diameter (nm)	PDI	Average particle diameter (nm)	PDI
62.5	262.5	0.069	147.2	0.042
125	237.9	0.057	135.1	0.093
250	33.5	0.013	151.3	0.130

[a] *All values calculated from DLS measurements.*

On the other hand, the higher loading composite (250 mg) was shown to release particles of much smaller diameter, closer to that calculated for the original AgNPs when the composite was dissolved in dichloromethane (20.2 nm). However, as AgNPs of this size would have produced a strong UV/vis absorption at >400 nm, it was envisaged that these particles may have been very dilute in the supernatant. It was also predicted that the same AgNPs agglomeration process occurred for this composite, but these aggregates were likely larger than the ones produced by the other composites. It was proposed that this was because of the larger size of the initial AgNPs in this composite, resulting in the formation of larger aggregates that would have been filtered out prior to analysis.

Particle diameters of released AgNPs from the composites in the pH 4.7 buffer solution were around 140 nm and were consistent across all the composites. This was notably smaller than the particle sizes measured for the pH 7 solutions but larger than the size of the AgNPs. In this case, it is possible that the added solvation of some of the block copolymer may have helped

limit AgNPs aggregation to some extent to give smaller silver aggregates. P4VP has been used frequently in the literature to stabilise or immobilise AgNPs.[126-128] However, the size of these silver aggregates is still quite large and may lack a strong surface plasmon absorbance.[125]

It is clear from both this release study and the characterisation of the dissolved AgNPs composites in dichloromethane, that when in the solution phase the AgNPs preside in several states. When solvated without a stabilising agent, the AgNPs appear to both aggregate into large clusters that are only visible in the DLS analysis and release atomic silver or very small silver clusters that are only detectable by UV/Vis spectroscopy. When the polymer is fully solvated in dichloromethane, the silver is detected predominantly in its original AgNPs form, whereas in the release study in aqueous media, the atomic silver and silver aggregates are more common. This is likely a result of the longer timescale of the release study. The diagram below (**Figure 5.17**) attempts to clarify and illustrate these experimental observations.
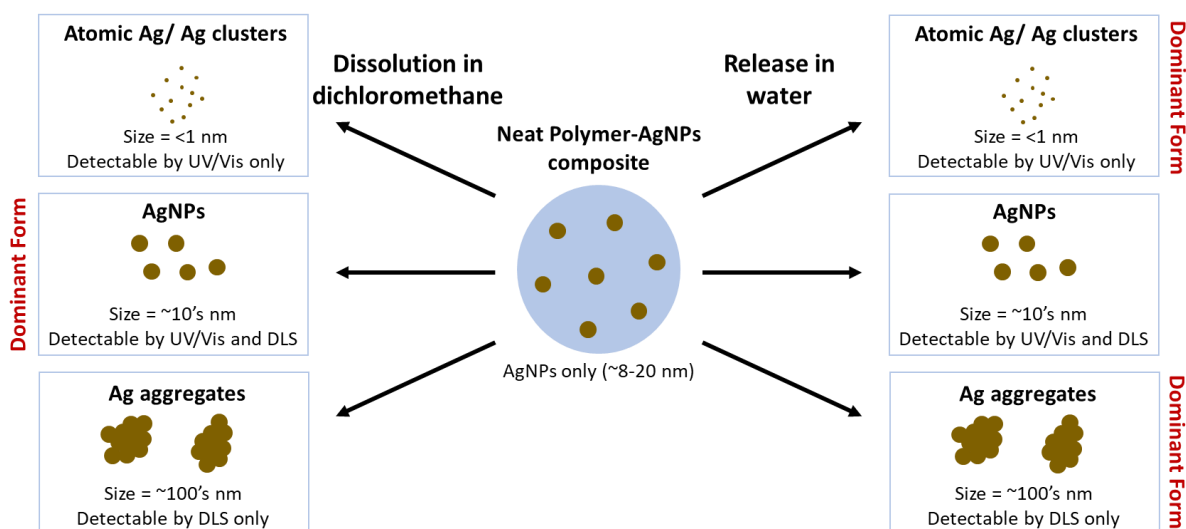
Figure 5.17: Schematic depicting the several forms of silver particles detected in the studies of this chapter when the composites were exposed to solvents.

From the release study it was clear that the AgNPs could be released from the block copolymers to some extent. Finally, the released AgNPs were tested for their antimicrobial activity against an antibiotic resistance gram-positive (*Staphylococcus Aureus*) and gram-negative (*Escherichia Coli*) bacterial strain (**Figure 5.18**). Composites were dispersed in sterilised distilled water and the supernatants were collected after 24 and 48-hour time periods. The release waters were applied directly to bacteria cultures and incubated to see if

any inhibition of bacteria growth could be achieved. Release waters from blank PMMA and PMMA-*b*-P4VP were also tested to ensure no false positive tests were produced from effects of the polymer. Antimicrobial activities were determined only by studying the release waters of composite samples rather than physical contact of the composite with the bacteria. This was to ensure that antimicrobial activity was a sole result of the AgNP content and not physical effects of the applied solids.
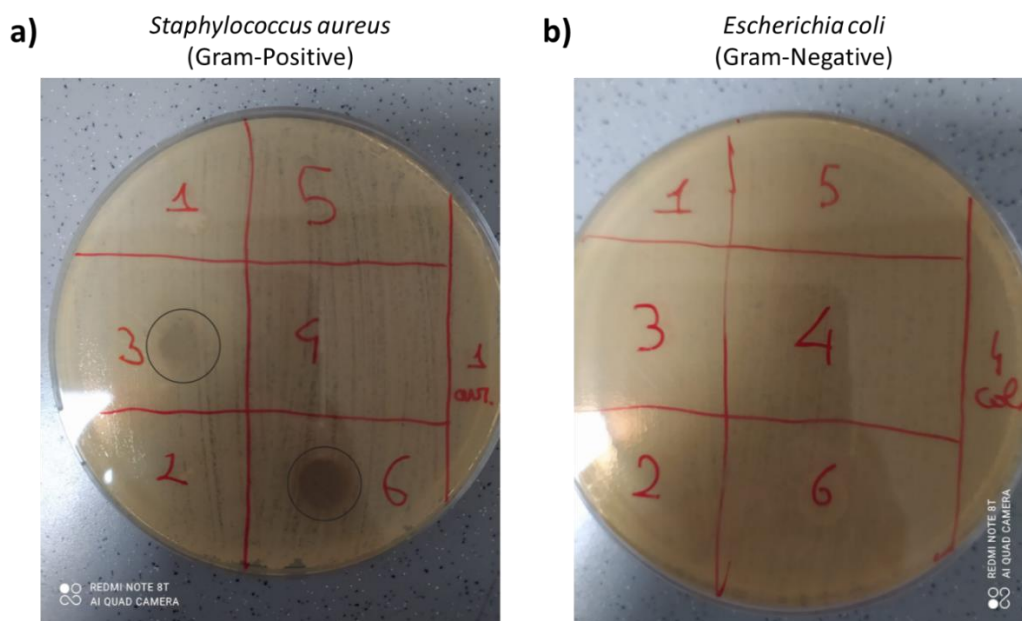
Figure 5.18: Images of agar plates seeded with (a) S. aureus and (b) E. coli exposed to release waters collected after dispersion for 48 hours. Number zones relate to the release waters from (1) blank PMMA, (2) blank PMMA-b-P4VP, (3) the 125 mg composite, (4) PMMA seeded with AgNPs, (5) the 250 mg composite and (6) the 62.5 mg composite.

All the release water taken after 24 hours dispersion time showed no visible inhibition of bacteria growth for either strain. However, after 48 hours, the release waters for the 62.5 and 125 mg precursor composite samples showed a clear 9mm halo of inhibition on the agar plate containing the gram-positive bacteria. The same samples also gave slightly discoloured halos on the agar plates containing the gram-negative bacteria, which indicates modified bacteria growth rather than a total inhibition. The lesser antimicrobial effect here was unexpected as AgNPs have proven to be more effective against gram-negative strains of bacteria rather than gram-positive.[129-131] Further testing will be needed to determine the cause of this enhanced effect against *S. aureus* in this study.

The release waters for the blank PMMA and PMMA-*b*-P4VP samples proved completely ineffective at inhibiting bacterial growth, hence antibacterial activity in the other samples is solely a product of the released AgNPs. No antibacterial activity was observed for the 250 mg precursor composite sample. As postulated in the release study, this may be due to the formation of large silver aggregates during the release of the AgNPs into the aqueous phase. These large aggregates are likely to be less effective at killing bacteria than the smaller particles produced in the other composites.[132, 133]

Overall, the PMMA-*b*-P4VP-AgNPs composites created using 62.5 mg and 125 mg of silver precursor proved to be biocompatible and antimicrobial against gram-positive bacteria. Though it was clear some AgNPs content of the composites was being release into aqueous solution, further investigation is needed to optimise and fully understand this process.

5.4.3. 3D printing of PMMA-*b*-P4VP-AgNPs

The final test in this study was to prove that the PMMA-*b*-P4VP-AgNPs composites could be successfully printed into solid structures using the SLS 3D printing technique. For this test, only the AgNPs composite synthesised with 125 mg precursor was used, due to its high performance in the antibacterial and biocompatibility tests. The powdered composite was loaded and spread onto a heated SLS build platform (90 °C). Small square structures (20x20 mm) were then sintered using a CO_2 laser following the operating parameters outlined in **Section 5.3.4 (Figure 5.19)**. The powder bed was heated to just below the polymer T_g to aid in even spreading of the composite across the bed and to prevent warping of the printed squares when laser sintered.

The printing parameters were optimised by gradually increasing the CO_2 laser powder until a solid object was formed. Though the printed squares did retain their shape after printing, the objects were still very fragile and could easily be broken. This may be due to the thinness of the object (0.5 mm) or may be an indication that printing parameters needed to be further investigated to ensure total sintering of the composite particles was achieved. Low viscosity of the selectively heated polymer needs to be achieved to ensure good coalescence of the particles and prevent brittleness.[134] The printed sections did preserve the brown colour of the original composite powder which was a good indication that AgNPs were still present in the printed objects and did not completely aggregate. Though this was only a rudimentary test,

to the author's knowledge, this may be the first successful example of an SLS printed antimicrobial polymer object.
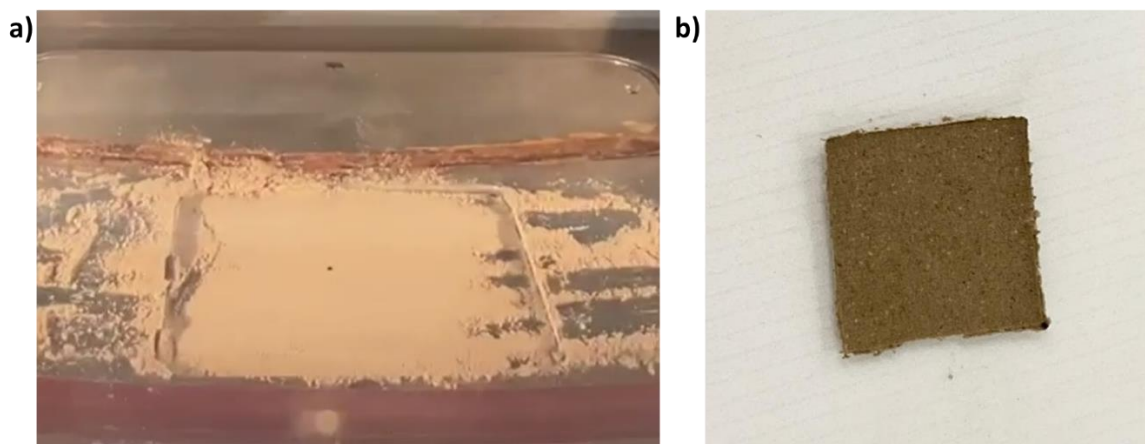
Figure 5.19: *Images of (a) the SLS printer powder bed loaded with PMMA-b-P4VP-AgNPs composite and (b) a 20x20 mm printed composite square.*

The surface morphology of the printed squares was investigated using SEM (**Figure 5.20**). Low magnification SEM images revealed the object's surface was reasonably smooth with the formation of a number of microfractures. This was likely the cause of the brittleness in the samples and was possibly caused by some incomplete sintering of the polymer powder. Higher magnification images showed that the surface was mostly sintered but did indeed contain visible evidence of some microparticles structures. Further study would be needed to assess whether the interior of the printed object also contained any unsintered material.
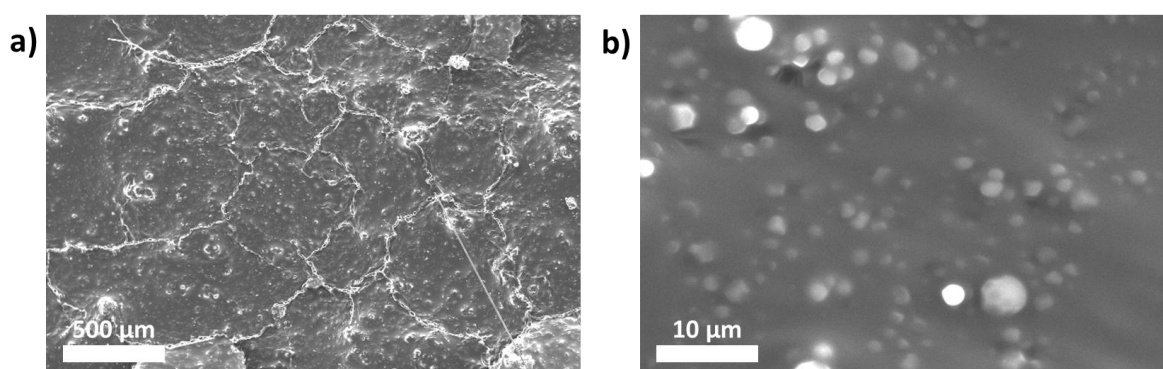
Figure 5.20: *(a) low and (b) high magnification SEM micrographs of the SLS printed PMMA-b-P4VP-AgNPs square.*

To confirm that an even distribution of AgNPs was achieved in the printed samples, an elemental map of the surface of the sample was produced (**Figure 5.21**). The elemental

distributions were mapped using *in-situ* energy-dispersive X-ray spectroscopy (EDXS) during the SEM imaging process. An SEM raster scan was used to produce an image of the printed sample surface while simultaneously measuring the characteristic X-ray emissions for each pixel of the image. Strong characteristic X-ray emissions for a particular element were represented as a coloured pixel.
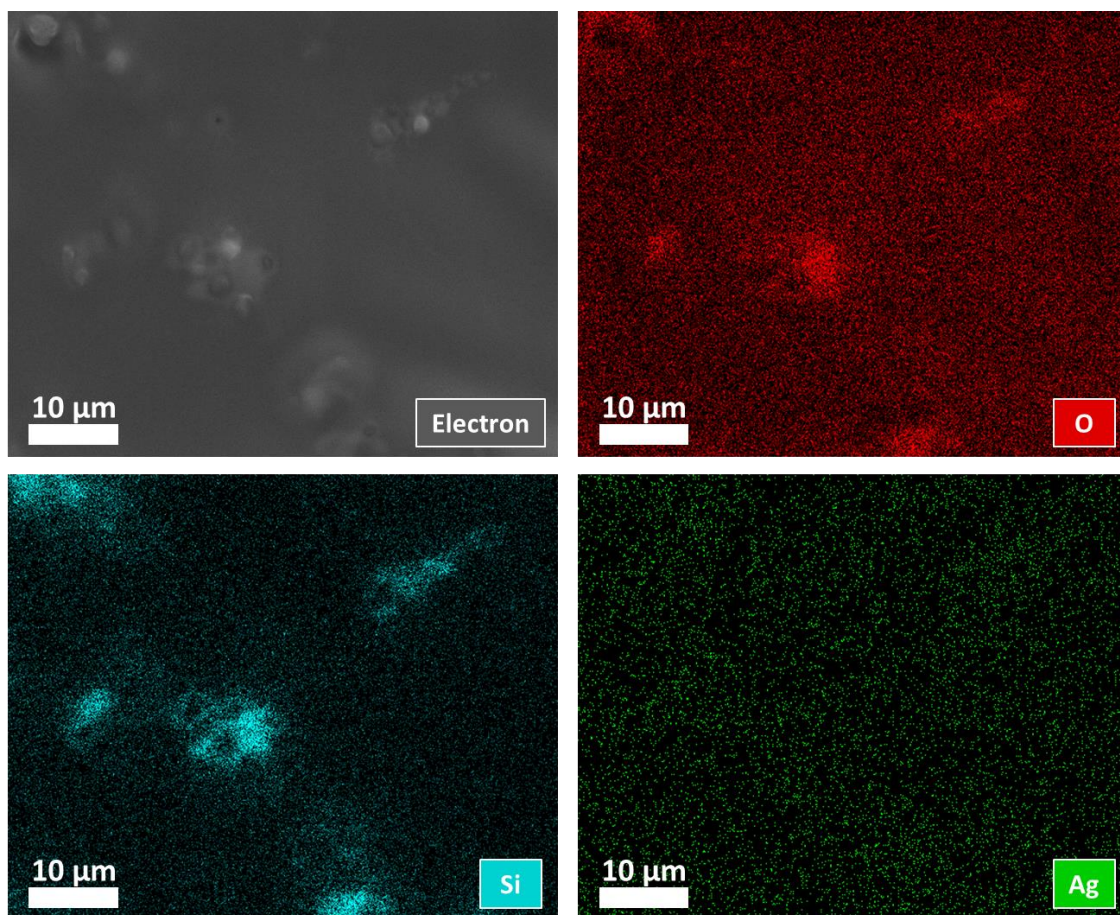
Figure 5.21: *EDXS elemental maps for the SLS printed PMMA-b-P4VP-AgNPs square, obtained during SEM imaging. Oxygen (red), silicon (blue) and silver (green) maps are displayed separately.*

The SEM image used as a reference for the elemental map shows a very smooth highly sintered surface, with a few small areas of aggregated material resembling unsintered microparticles. A highly uniform distribution of silver (green dots) was observed across the sample surface, indicating that AgNPs were fully dispersed throughout the printed sample. The aggregated material was found to contain a relatively large concentration of both silicon and oxygen, though these elements are found all over the material surface. This high elemental concentration no doubt relates to high quantities of the PDMS-MA polymeric stabiliser that would be present on the surface of synthesised microparticles. This polymeric

stabiliser appears to be more evenly dispersed in the sintered material but remains highly concentrated on the surface of unsintered areas.

To confirm that the even distribution of AgNPs persisted throughout the sample depth, time-of-flight secondary ion mass spectrometry (ToF-SIMS) was performed on the square section and compared to the unprocessed powdered material (**Figure 5.22**). ToF-SIMS utilises a high energy ion beam source to impact the sample surface, generating secondary ion fragments from the top few monolayers of the sample. These fragments can then be collected and analysed through mass spectrometry. Here, the technique is also coupled with a sputtering source which is used to slowly etch away the sample surface. This allows the composition to be analysed as a function of sample depth, with increased sputtering time relating to a deeper depth in the sample.

For both the printed and powdered samples, various mass fragments were detected that related to the individual components of the composite. Notable fragments were plotted, including the chain ends of the PDMS-MA ($SiC_3H_9^+$, $Si_2C_5H_{15}O^+$), the monomer units and pendent groups for the PMMA ($C_6H_{11}O_2^+$, $C_5H_9O_2^+$, $C_4H_5O^+$) and P4VP ($C_7H_9N^+$, $C_5H_5N^+$) and silver ions (Ag^+) from the AgNPs.

The powdered sample produced a strong intensity for the PDMS-MA fragments at the beginning of the measurement that then quickly diminished with increased sputtering time. This is to be expected as the PDMS-MA resides primarily on the surface of the composite particles, with its relative concentration expected to reduce as the interior of the microparticles is analysed with increased sputtering time. P4VP mass fragments show the reverse trend in the powdered sample with relative intensity quickly increasing with sample depth. On the other hand, PMMA mass fragments showed only a marginal increase in intensity. This indicates that the PMMA block of the copolymer is more concentrated towards the outer surface of the microparticles when compared to the amount of P4VP block. This corresponds to the observed nanoscale morphology of the PMMA-*b*-P4VP self-assembled within the microparticles. P4VP spheres are contained within a PMMA matrix, meaning the outermost layer of the particles will consist of PMMA. Relative intensity for the Ag^+ ions produced by the AgNPs was shown to increase relatively linearly with sample depth, confirming that AgNPs exist predominantly within the interior of the microparticles.
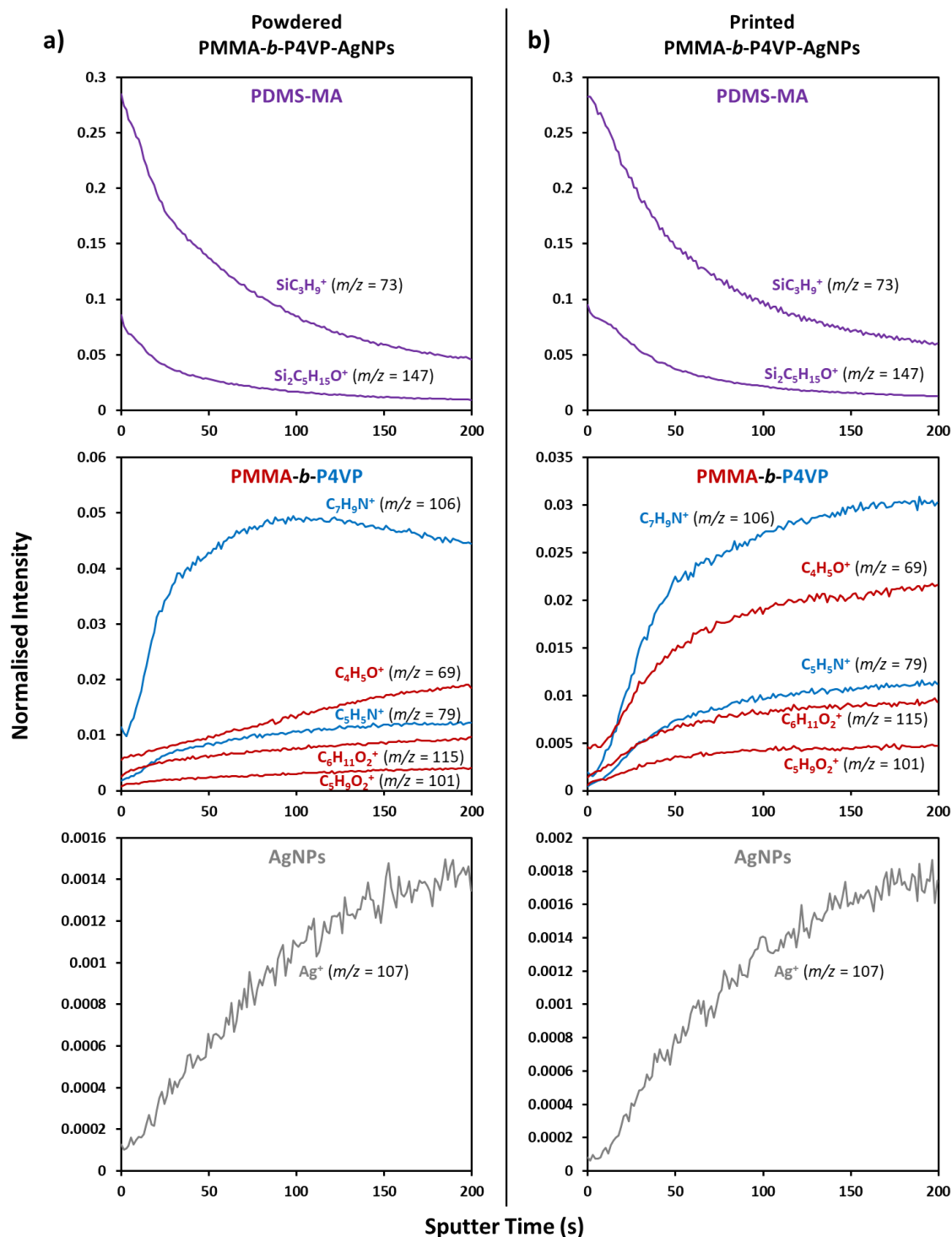
Figure 5.22: *ToF-SIMS intensity profiles for the (a) powdered and (b) printed PMMA-b-P4VP-AgNPs composite as a function of sputtering time. Mass fragments are labelled with their relevant mass to charge ratios (m/z). Individual components of the composite are plotted separately for clarity.*

The printed PMMA-*b*-P4VP-AgNPs composite revealed essentially the same trends as the non-printed powdered sample. The only difference being the matching trends of increasing intensity for both the PMMA and P4VP mass fragments. This may be a sign that the nanoscale

214

morphology is no longer present in the sintered material and the two blocks are blended during printing. It may also be that the morphology of the block copolymer has been altered to produce a pattern that no longer favours a PMMA surface topography. Other than this, the compositional tomography of the printed composite appeared to be the same as the original powder.

Finally, the nature of the silver in the printed sample was investigated through UV/vis spectroscopy and DLS measurements of the printed section dissolved in dichloromethane (**Figure 5.23**). Elemental mapping and ToF-SIMS proved the printed material contained an even distribution of silver; however, it was not clear from this whether the AgNPs had aggregated during the printing process.
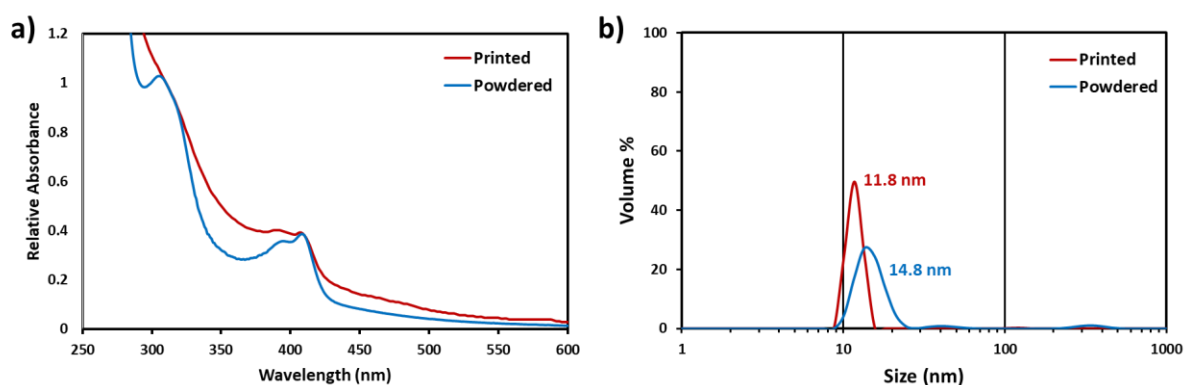
Figure 5.23: *(a) UV/vis spectra and (b) DLS measurements comparing the AgNPs present in the printed composite (red) and the unprinted powdered material (blue).*

A UV/vis absorbance was observed at roughly the same position and intensity as the original dissolved composite. The presence of this surface plasmon absorbance in the printed material confirmed that the printed section did indeed contain AgNPs. The DLS measurement also showed the presence of particles roughly the same size as those found in the original powder composite (11.8 nm). The AgNPs in the printed sample proved to be slightly smaller and of a narrower dispersity than those of the original powder, though this difference was fairly negligible. From this it can be concluded that the AgNPs of the composite were unaffected by the SLS printing process and remained intact and evenly dispersed in the printed material. Thus, it would be expected that the printed material would display very similar antimicrobial effect to the original powdered material. Though, further study will be required to confirm that this is true.

5.5. Conclusions

In this chapter, the synthesis and self-assembly of PMMA-*b*-P4VP via RAFT-mediated dispersion in scCO$_2$ was successfully combined with the formation of AgNPs. The loading of silver precursor used to prepare the AgNPs was varied between 62.5 and 250 mg per 10 g total monomer to yield three different composite materials, produced in a single environmentally benign process. All composites were found to be highly pure with little to no trace of monomer or precursor ligands after a 30-minute CO$_2$ extraction process was applied post-synthesis. However, it was discovered that the well-defined microparticle structure of the product appeared to deteriorate more as silver precursor concentration was increased, with formation of some additional smaller nanoscale particles observed.

Cross-sectional TEM images of the microparticles showed that all the composite materials contained AgNPs dispersed evenly through the block copolymer particles. These AgNPs were found to increase in size as the precursor loading was increased (~8-20 nm) with the AgNPs appearing significantly more aggregated in the composite synthesised with the highest quantity of the precursor (250 mg). The block copolymer composites were directly compared to an equivalent PMMA microparticulate material used alongside the synthesis of AgNPs in scCO$_2$. This PMMA material was found to contain AgNPs only on the surface of the polymer microparticles. This proved that the formation of AgNPs within the PMMA-*b*-P4VP microparticles was a direct result of the interaction of silver with the 4VP monomer. This allowed the transport of AgNPs into the PMMA particles to give the homogeneous composites. Were another block copolymer morphology to be targeted, this could lead to the formation of unique spatial arrangements of the AgNPs.

The two composites with the lowest silver precursor loading were proven to be biocompatible through exposure to a caco-2 intestinal cell line. However, the highest loaded composite was shown to be mildly cytotoxic, likely due to the presence of the residual silver complex. The release of the AgNPs from the composites in aqueous solutions was then modelled through a 72-hour release study. UV/vis spectroscopy showed an increase in absorbance with both release time and AgNPs loading in the composite, providing initial evidence that the release profile could be controlled. Still, the exact nature of this released silver requires further study, as both sub-nanometre silver and larger silver aggregates seemed to be present in the supernatants. It was predicted that this was primarily due to a lack of nanoparticle stabilising

agent in the release solutions. The release water obtained after 48 hours were found to possess good antimicrobial activity against *S. aureus* (gram-positive) bacteria but only a mild effect against *E. coli* (gram negative) bacteria.

Finally, the antimicrobial PMMA-*b*-P4VP-AgNPs composite powder was printed into small solid objects using SLS printing, a commonly used additive manufacturing technique. Overall, the printed sections were able to be manufactured from base chemicals without the need for any non-renewable or toxic solvents. SEM analysis revealed that the sections were highly sintered with only limited evidence of the original microparticle structures found. A combination of surface elemental mapping and depth-profiling ToF-SIMS confirmed that the composition of the printed sections remained almost identical to the original microparticulate material. An even distribution of silver was observed across the surface with UV/vis and DLS analysis confirming this to be AgNPs. This initial characterisation provided encouraging evidence that the antimicrobial activity of the printed objects should be comparable to the original composite powder.

Overall, this study has outlined a promising route to produce clean, homogeneous antimicrobial polymer composites through co-synthesis and co-assembly of block copolymers with AgNPs in scCO$_2$. These composites show great promise to be used in SLS 3D printing of biomedical devices. However, intense further study is still required to fully understand and optimise the release of AgNPs from the composites and to produce objects with excellent mechanical properties. Also, this work signifies a good precedence that other nanostructured polymer-inorganic composites could be synthesised directly in scCO$_2$, including other noble metal nanoparticles and potentially even functional metal oxides.

5.6. References

1.   J. A. Darr and M. Poliakoff, *Chemical Reviews*, 1999, **99**, 495-542.
2.   R. Skouta, *Green Chemistry Letters and Reviews*, 2009, **2**, 121-156.
3.   M. Poliakoff, M. W. George and S. M. Howdle, in *Chemistry Under Extreme and Non-Classical Conditions*, eds. R. V. Eldik and C. M. Hubbard, Wiley, Heidelberg, 1996, ch. 5, pp. 189-218.
4.   Y. Tao and P. P. Pescarmona, *Catalysts*, 2018, **8**, 212.
5.   Y. Xu, V. Musumeci and C. Aymonier, *Reaction Chemistry & Engineering*, 2019, **4**, 2030-2054.
6.   X. Zhang, S. Heinonen and E. Levänen, *RSC Advances*, 2014, **4**, 61137-61152.
7.   G. Cao and Y. Wang, *Nanostructures and Nanomaterials: Synthesis, Properties, and Applications*, World Scientific, 2011.
8.   Z. Nie, A. Petukhova and E. Kumacheva, *Nature Nanotechnology*, 2010, **5**, 15-25.
9.   J. Livage, *Curr. Opin. Solid State Mater. Sci.*, 1997, **2**, 132-138.
10.   J. Fricke, *Aerogels: Proceedings of the First International Symposium, Würzburg, Fed. Rep. of Germany September 23–25, 1985*, Springer Berlin Heidelberg, 2012.
11.   D. A. Loy, E. M. Russick, S. A. Yamanaka, B. M. Baugher and K. J. Shea, *Chemistry of Materials*, 1997, **9**, 2264-2268.
12.   R. Sui, A. Rizkalla and P. A. Charpentier, *Microporous Mesoporous Mater.*, 2011, **142**, 688-695.
13.   R. Sui, A. S. Rizkalla and P. A. Charpentier, *Langmuir*, 2005, **21**, 6150-6153.
14.   M. B. I. Chowdhury, R. Sui, R. A. Lucky and P. A. Charpentier, *Langmuir*, 2010, **26**, 2707-2713.
15.   R. Sui, A. S. Rizkalla and P. A. Charpentier, *Crystal Growth & Design*, 2008, **8**, 3024-3031.
16.   R. A. Lucky and P. A. Charpentier, *Advanced Materials*, 2008, **20**, 1755-1759.
17.   R. A. Lucky, Y. Medina-Gonzalez and P. A. Charpentier, *Langmuir*, 2010, **26**, 19014-19021.
18.   R. A. Lucky and P. A. Charpentier, *Nanotechnology*, 2009, **20**, 195601.
19.   G. Vinci and M. Rapa, *Bioengineering (Basel)*, 2019, **6**, 10.
20.   A. Saravanan, P. S. Kumar, S. Karishma, D.-V. N. Vo, S. Jeevanantham, P. R. Yaashikaa and C. S. George, *Chemosphere*, 2021, **264**, 128580.
21.   M. J. Ndolomingo, N. Bingwa and R. Meijboom, *Journal of Materials Science*, 2020, **55**, 6195-6241.
22.   Y.-x. Zhang and Y.-h. Wang, *RSC Advances*, 2017, **7**, 45129-45144.
23.   I. Matsui, *J. Chem. Eng. Jpn.*, 2005, **38**, 535-546.
24.   E. Priyadarshini and N. Pradhan, *Sensors and Actuators B: Chemical*, 2017, **238**, 888-902.
25.   V. V. Mody, R. Siwale, A. Singh and H. R. Mody, *J Pharm Bioallied Sci*, 2010, **2**, 282-289.
26.   H. W. Tan, J. An, C. K. Chua and T. Tran, *Advanced Electronic Materials*, 2019, **5**, 1800831.
27.   Y. Zhang and C. Erkey, *The Journal of Supercritical Fluids*, 2006, **38**, 252-267.
28.   A. O'Neil and J. J. Watkins, *MRS Bulletin*, 2005, **30**, 967-975.
29.   M. Türk and C. Erkey, *The Journal of Supercritical Fluids*, 2018, **134**, 176-183.
30.   C. Aymonier, G. Philippot, A. Erriguible and S. Marre, *The Journal of Supercritical Fluids*, 2018, **134**, 184-196.

31.   T. Adschiri, K. Kanazawa and K. Arai, *J. Am. Ceram. Soc.*, 1992, **75**, 1019-1022.
32.   P. W. Dunne, A. S. Munn, C. L. Starkey, T. A. Huddle and E. H. Lester, *Philosophical Transactions of the Royal Society A: Mathematical, Physical and Engineering Sciences*, 2015, **373**, 20150015.
33.   J. J. Watkins and T. J. McCarthy, *Chemistry of Materials*, 1995, **7**, 1991-1994.
34.   T. Hasell, K. J. Thurecht, R. D. W. Jones, P. D. Brown and S. M. Howdle, *Chem. Commun.*, 2007, DOI: 10.1039/B710503G, 3933-3935.
35.   Y.-W. Chih and W.-T. Cheng, *Materials Science and Engineering: B*, 2007, **145**, 67-75.
36.   T. Gendrineau, S. Marre, M. Vaultier, M. Pucheault and C. Aymonier, *Angewandte Chemie International Edition*, 2012, **51**, 8525-8528.
37.   X. Fan, M. C. McLeod, R. M. Enick and C. B. Roberts, *Industrial & Engineering Chemistry Research*, 2006, **45**, 3343-3347.
38.   A. Kameo, T. Yoshimura and K. Esumi, *Colloids and Surfaces A: Physicochemical and Engineering Aspects*, 2003, **215**, 181-189.
39.   K. Esumi, S. Sarashina and T. Yoshimura, *Langmuir*, 2004, **20**, 5189-5191.
40.   P. S. Shah, S. Husain, K. P. Johnston and B. A. Korgel, *The Journal of Physical Chemistry B*, 2001, **105**, 9433-9440.
41.   M. C. McLeod, W. F. Gale and C. B. Roberts, *Langmuir*, 2004, **20**, 7078-7082.
42.   J. A. Darr, J. Zhang, N. M. Makwana and X. Weng, *Chemical Reviews*, 2017, **117**, 11125-11238.
43.   S. E. Bozbağ and C. Erkey, *The Journal of Supercritical Fluids*, 2015, **96**, 298-312.
44.   Z.-J. Jiang, C.-Y. Liu and L.-W. Sun, *The Journal of Physical Chemistry B*, 2005, **109**, 1730-1735.
45.   N. Kalfagiannis, P. G. Karagiannidis, C. Pitsalidis, N. T. Panagiotopoulos, C. Gravalidis, S. Kassavetis, P. Patsalas and S. Logothetidis, *Sol. Energy Mater. Sol. Cells*, 2012, **104**, 165-174.
46.   T. Hasell, L. Lagonigro, A. C. Peacock, S. Yoda, P. D. Brown, P. J. A. Sazio and S. M. Howdle, *Adv. Funct. Mater.*, 2008, **18**, 1265-1271.
47.   A.-C. Burduşel, O. Gherasim, A. M. Grumezescu, L. Mogoantă, A. Ficai and E. Andronescu, *Nanomaterials (Basel)*, 2018, **8**, 681.
48.   K. S. Siddiqi, A. Husen and R. A. K. Rao, *Journal of Nanobiotechnology*, 2018, **16**, 14.
49.   H. D. Beyene, A. A. Werkneh, H. K. Bezabh and T. G. Ambaye, *Sustainable Materials and Technologies*, 2017, **13**, 18-23.
50.   S. H. Lee and B.-H. Jun, *International journal of molecular sciences*, 2019, **20**, 865.
51.   N. Tarannum, Divya and Y. K. Gautam, *RSC Advances*, 2019, **9**, 34926-34948.
52.   L. Lu and X. An, *The Journal of Supercritical Fluids*, 2015, **99**, 29-37.
53.   J. Yang, T. Hasell, D. C. Smith and S. M. Howdle, *Journal of Materials Chemistry*, 2009, **19**, 8560-8570.
54.   V. Arakcheev, V. Bagratashvili, A. Bekin, D. Khmelenin, N. Minaev, V. Morozov and A. Rybaltovsky, *The Journal of Supercritical Fluids*, 2018, **140**, 159-164.
55.   K. S. Morley, P. C. Marr, P. B. Webb, A. R. Berry, F. J. Allison, G. Moldovan, P. D. Brown and S. M. Howdle, *Journal of Materials Chemistry*, 2002, **12**, 1898-1905.
56.   M. Ji, X. Chen, C. M. Wai and J. L. Fulton, *Journal of the American Chemical Society*, 1999, **121**, 2631-2632.
57.   Y.-P. Sun, P. Atorngitjawat and M. J. Meziani, *Langmuir*, 2001, **17**, 5707-5710.
58.   J. Rosolovsky, R. K. Boggess, A. F. Rubira, L. T. Taylor, D. M. Stoakley and A. K. St. Clair, *J. Mater. Res.*, 1997, **12**, 3127-3133.

59.   J. Yang, T. Hasell, W. Wang and S. M. Howdle, *European Polymer Journal*, 2008, **44**, 1331-1336.

60.   N. Nazem, L. T. Taylor and A. F. Rubira, *The Journal of Supercritical Fluids*, 2002, **23**, 43-57.

61.   C. Huang, X. Chen, Z. Xue and T. Wang, *Science Advances*, 2020, **6**, eaba1321.

62.   Q. Yang, W. Liu, B. Wang, W. Zhang, X. Zeng, C. Zhang, Y. Qin, X. Sun, T. Wu, J. Liu, F. Huo and J. Lu, *Nature communications*, 2017, **8**, 14429.

63.   B. Shen, M. A. Kostiainen and V. Linko, *Langmuir*, 2018, **34**, 14911-14920.

64.   O. Gherasim, R. A. Puiu, A. C. Bîrcă, A.-C. Burduşel and A. M. Grumezescu, *Nanomaterials (Basel)*, 2020, **10**, 2318.

65.   N. R. Chowdhury, M. MacGregor-Ramiasa, P. Zilm, P. Majewski and K. Vasilev, *Journal of Colloid and Interface Science*, 2016, **482**, 151-158.

66.   S. Medici, M. Peana, V. M. Nurchi and M. A. Zoroddu, *J. Med. Chem.*, 2019, **62**, 5923-5943.

67.   W. Sim, R. T. Barnard, M. A. T. Blaskovich and Z. M. Ziora, *Antibiotics (Basel)*, 2018, **7**, 93.

68.   M. Konop, T. Damps, A. Misicka and L. Rudnicka, *Journal of Nanomaterials*, 2016, **2016**, 7614753.

69.   I. X. Yin, J. Zhang, I. S. Zhao, M. L. Mei, Q. Li and C. H. Chu, *Int J Nanomedicine*, 2020, **15**, 2555-2562.

70.   N. Durán, M. Durán, M. B. de Jesus, A. B. Seabra, W. J. Fávaro and G. Nakazato, *Nanomedicine: Nanotechnology, Biology and Medicine*, 2016, **12**, 789-799.

71.   G. Franci, A. Falanga, S. Galdiero, L. Palomba, M. Rai, G. Morelli and M. Galdiero, *Molecules*, 2015, **20**.

72.   M. K. Rai, S. D. Deshmukh, A. P. Ingle and A. K. Gade, *Journal of Applied Microbiology*, 2012, **112**, 841-852.

73.   A. Syafiuddin, Salmiati, M. R. Salim, A. Beng Hong Kueh, T. Hadibarata and H. Nur, *J. Chin. Chem. Soc.*, 2017, **64**, 732-756.

74.   A. A. Yaqoob, K. Umar and M. N. M. Ibrahim, *Applied Nanoscience*, 2020, **10**, 1369-1378.

75.   S. Iravani, H. Korbekandi, S. V. Mirmohammadi and B. Zolfaghari, *Res Pharm Sci*, 2014, **9**, 385-406.

76.   P. Rauwel, S. Küünal, S. Ferdov and E. Rauwel, *Advances in Materials Science and Engineering*, 2015, **2015**, 682749.

77.   G. Von White, P. Kerscher, R. M. Brown, J. D. Morella, W. McAllister, D. Dean and C. L. Kitchens, *Journal of Nanomaterials*, 2012, **2012**, 730746.

78.   S. Ali, S. Perveen, M. Ali, T. Jiao, A. S. Sharma, H. Hassan, S. Devaraj, H. Li and Q. Chen, *Materials Science and Engineering: C*, 2020, **108**, 110421.

79.   M. A. Shenashen, S. A. El-Safty and E. A. Elshehy, *Particle & Particle Systems Characterization*, 2014, **31**, 293-316.

80.   F. Khan, S. Iqbal, N. Khalid, I. Hussain, Z. Hussain, R. Szmigielski and H. A. Janjua, *Applied Nanoscience*, 2020, **10**, 1941-1956.

81.   B. Berman, *Business Horizons*, 2012, **55**, 155-162.

82.   J.-Y. Lee, J. An and C. K. Chua, *Applied Materials Today*, 2017, **7**, 120-133.

83.   V. Gupta, P. Nesterenko and B. Paull, *3D Printing in Chemical Sciences: Applications Across Chemistry*, Royal Society of Chemistry, Croydon, 2019.

84.   S. A. M. Tofail, E. P. Koumoulos, A. Bandyopadhyay, S. Bose, L. O'Donoghue and C. Charitidis, *Materials Today*, 2018, **21**, 22-37.

85.   T. D. Ngo, A. Kashani, G. Imbalzano, K. T. Q. Nguyen and D. Hui, *Composites Part B: Engineering*, 2018, **143**, 172-196.

86.   X. Wang, M. Jiang, Z. Zhou, J. Gou and D. Hui, *Composites Part B: Engineering*, 2017, **110**, 442-458.

87.   C. Y. Lai, C. F. Cheong, J. S. Mandeep, H. B. Abdullah, N. Amin and K. W. Lai, *J. Mater. Eng. Perform.*, 2014, **23**, 3541-3550.

88.   I. Theodorakos, F. Zacharatos, R. Geremia, D. Karnakis and I. Zergioti, *Appl. Surf. Sci.*, 2015, **336**, 157-162.

89.   L. Nayak, S. Mohanty, S. K. Nayak and A. Ramadoss, *Journal of Materials Chemistry C*, 2019, **7**, 8771-8795.

90.   S. Almohammed, M. Alruwaili, E. G. Reynaud, G. Redmond, J. H. Rice and B. J. Rodriguez, *ACS Applied Nano Materials*, 2019, **2**, 5029-5034.

91.   S.-N. Kwon, S.-W. Kim, I.-G. Kim, Y. K. Hong and S.-I. Na, *Advanced Materials Technologies*, 2019, **4**, 1800500.

92.   M. S. Mannoor, Z. Jiang, T. James, Y. L. Kong, K. A. Malatesta, W. O. Soboyejo, N. Verma, D. H. Gracias and M. C. McAlpine, *Nano Letters*, 2013, **13**, 2634-2639.

93.   E. Fantino, A. Chiappone, F. Calignano, M. Fontana, F. Pirri and I. Roppolo, *Materials*, 2016, **9**, 589.

94.   S. Calamak and M. Ermis, *J. Mater. Res.*, 2021, **36**, 166-175.

95.   N. Vidakis, M. Petousis, E. Velidakis, M. Liebscher and L. Tzounis, *Biomimetics*, 2020, **5**, 42.

96.   H. C. Kim, H. T. Hahn and Y. S. Yang, *J. Compos. Mater.*, 2013, **47**, 501-509.

97.   T. Hupfeld, A. Sommereyns, T. Schuffenhauer, E. Zhuravlev, M. Krebs, S. Gann, O. Keßler, M. Schmidt, B. Gökce and S. Barcikowski, *Additive Manufacturing*, 2020, **36**, 101419.

98.   G. Taormina, C. Sciancalepore, F. Bondioli and M. Messori, *Polymers*, 2018, **10**, 212.

99.   H. Acharya, J. Sung, B.-H. Sohn, D. H. Kim, K. Tamada and C. Park, *Chemistry of Materials*, 2009, **21**, 4248-4255.

100.   L. J. Duffus, J. E. Norton, P. Smith, I. T. Norton and F. Spyropoulos, *Journal of Colloid and Interface Science*, 2016, **473**, 9-21.

101.   M. J. Casciato, G. Levitin, D. W. Hess and M. A. Grover, *Journal of Nanoparticle Research*, 2012, **14**, 836.

102.   *US Pat.,* 3 547 809A, 1970.

103.   S. D. Manjare and K. Dhingra, *Materials Science for Energy Technologies*, 2019, **2**, 463-484.

104.   P. Mulvaney, *Langmuir*, 1996, **12**, 788-800.

105.   J. Jennings, S. P. Bassett, D. Hermida-Merino, G. Portale, W. Bras, L. Knight, J. J. Titman, T. Higuchi, H. Jinnai and S. M. Howdle, *Polymer Chemistry*, 2016, **7**, 905-916.

106.   J. E. C. Mark, *Polymer data handbook*, Oxford University Press, Oxford, UK, 2009.

107.   A. Bansal, H. Yang, C. Li, K. Cho, B. C. Benicewicz, S. K. Kumar and L. S. Schadler, *Nature materials*, 2005, **4**, 693-698.

108.   J. Jennings, M. Beija, J. T. Kennon, H. Willcock, R. K. O'Reilly, S. Rimmer and S. M. Howdle, *Macromolecules*, 2013, **46**, 6843-6851.

109.   I. De Leersnyder, H. Rijckaert, L. De Gelder, I. Van Driessche and P. Vermeir, *Nanomaterials (Basel)*, 2020, **10**, 1394.

110. R. Desai, V. Mankad, S. Gupta and P. Jha, *Nanoscience and Nanotechnology Letters*, 2012, **4**, 30-34.

111. J. J. Mock, M. Barbic, D. R. Smith, D. A. Schultz and S. Schultz, *J. Chem. Phys.*, 2002, **116**, 6755-6759.

112. B. G. Ershov, E. Janata, A. Henglein and A. Fojtik, *The Journal of Physical Chemistry*, 1993, **97**, 4589-4594.

113. G. Duan, C. Zhang, A. Li, X. Yang, L. Lu and X. Wang, *Nanoscale research letters*, 2008, **3**, 118-122.

114. Y. Xue and H. Xiao, *Polymers*, 2015, **7**, 2290-2303.

115. R. Ferwerda, J. H. van der Maas and F. B. van Duijneveldt, *J. Mol. Catal. A: Chem.*, 1996, **104**, 319-328.

116. T. Lea, in *The Impact of Food Bioactives on Health*, eds. K. Verhoeckx, P. Cotter, I. López-Expósito, C. Kleiveland, T. Lea, A. Mackie, T. Requena, D. Swiatecka and H. Wichers, Springer, Cham, Switzerland, 2015, ch. 10, pp. 103-111.

117. N. Lall, C. J. Henley-Smith, M. N. De Canha, C. B. Oosthuizen and D. Berrington, *Int J Microbiol*, 2013, **2013**, 420601-420601.

118. F. K.-M. Chan, K. Moriwaki and M. J. De Rosa, *Methods Mol Biol*, 2013, **979**, 65-70.

119. Y. Song, R. Guan, F. Lyu, T. Kang, Y. Wu and X. Chen, *Mutation Research/Fundamental and Molecular Mechanisms of Mutagenesis*, 2014, **769**, 113-118.

120. A. A. Ahmed and E. W. A. Allah, *J. Am. Ceram. Soc.*, 1995, **78**, 2777-2784.

121. S. Kittler, C. Greulich, J. Diendorf, M. Köller and M. Epple, *Chemistry of Materials*, 2010, **22**, 4548-4554.

122. J. Dobias and R. Bernier-Latmani, *Environmental Science & Technology*, 2013, **47**, 4140-4146.

123. K. Patel, B. Bharatiya, T. Mukherjee, T. Soni, A. Shukla and B. N. Suhagia, *J. Dispersion Sci. Technol.*, 2017, **38**, 626-631.

124. J. G. Kennemur, *Macromolecules*, 2019, **52**, 1354-1370.

125. N. G. Bastús, F. Merkoçi, J. Piella and V. Puntes, *Chemistry of Materials*, 2014, **26**, 2836-2846.

126. D. Eli, M. Y. Onimisi, S. Garba and J. Tasiu, *SN Applied Sciences*, 2020, **2**, 1769.

127. A. Pasche, B. Grohe, S. Mittler and P. Charpentier, *Journal of Photonics for Energy*, 2017, **7**, 035504.

128. R. Keunen, N. Cathcart and V. Kitaev, *Nanoscale*, 2014, **6**, 8045-8051.

129. J. S. Kim, E. Kuk, K. N. Yu, J.-H. Kim, S. J. Park, H. J. Lee, S. H. Kim, Y. K. Park, Y. H. Park, C.-Y. Hwang, Y.-K. Kim, Y.-S. Lee, D. H. Jeong and M.-H. Cho, *Nanomedicine: Nanotechnology, Biology and Medicine*, 2007, **3**, 95-101.

130. S. Shrivastava, T. Bera, A. Roy, G. Singh, P. Ramachandrarao and D. Dash, *Nanotechnology*, 2007, **18**, 225103.

131. A. M. Fayaz, K. Balaji, M. Girilal, R. Yadav, P. T. Kalaichelvan and R. Venketesan, *Nanomedicine: Nanotechnology, Biology and Medicine*, 2010, **6**, 103-109.

132. Y. Jeong, D. W. Lim and J. Choi, *Advances in Materials Science and Engineering*, 2014, **2014**, 763807.

133. F. J. Osonga, A. Akgul, I. Yazgan, A. Akgul, G. B. Eshun, L. Sakhaee and O. A. Sadik, *Molecules*, 2020, **25**, 2682.

134. M. Schmid, A. Amado and K. Wegener, *AIP Conference Proceedings*, 2015, **1664**, 160009.

Chapter 6 – Conclusions and Future Work

6.1. Overview

This final chapter summarises the key outcomes and conclusions of this thesis. Proposals for potential future work are also given. The main aim of this thesis, as stated in the introduction chapter, is reiterated below for reference:

"This thesis aims to demonstrate the versatility of P4VP block copolymer templates from scCO$_2$ in nanofabrication. This will be achieved by investigating synthetic strategies to control the size and shape of the templates, as well as utilising them for several end applications in the energy and healthcare sectors."

6.2. Conclusions

In this thesis, multiple strategies were employed to demonstrate the versatility of scCO$_2$ synthesised P4VP block copolymers for nanofabrication applications. Firstly, the tuneable size of the block copolymer templates over multiple length scales was demonstrated in **Chapter 3**. The amount of polymeric stabiliser in the scCO$_2$ dispersion was altered to achieve control of the microparticle size of the PMMA-*b*-P4VP templates, in the range of around 0.5–2.5 µm. Control of the internal nanoscale P4VP domain sizes was also demonstrated in the range of 22-35 nm by varying the overall polymer molecular weight. However, control over the nanoscale dimensions proved difficult using only the RAFT-mediated dispersion technique, with the polymer dispersity increasing as higher molecular weights were targeted. This led to a large distribution in P4VP domain sizes and therefore a more tenuous control of the exact size of the nanoscale features of the polymer templates.

The shape of the P4VP morphology in the templates was also altered in **Chapter 4** by producing new triblock copolymers in scCO$_2$. PMMA-*b*-PS-*b*-P4VP copolymers were synthesised with various volume ratios of the PMMA and PS blocks, while the P4VP block was kept reasonably constant for consistent nanofabrication properties. To achieve the synthesis of triblock copolymers in scCO$_2$ with low PMMA content, a two-pot re-dispersion method was developed, demonstrating that a wide range of triblock copolymer compositions could be formulated.

A number of new and complex P4VP morphologies were identified through TEM imaging, however, most of these arrangements could not be definitively assigned due to the lack of supporting SAXS data. Assignment also proved difficult due to slight irregularities in the morphologies, with notable morphological differences observed between some microparticles. This was undoubtedly a result of the dispersity in the polymer chains, as very consistent polymer chains are needed to self-assembly into regular three-phase morphologies. This is due to the variety of possible morphologies that can be achieved in triblock systems.[1] Despite these issues, one PMMA-*b*-PS-*b*-P4VP copolymer was tentatively assigned to possess a lamellar with spheres, or L+S(II) type morphology. This demonstrated that shape modification of the P4VP template was possible without the need to alter the volume fraction of P4VP.

While modifications to the polymer synthesis proved the size and shape of the P4VP templates could be altered, this thesis also demonstrates the versatility in the potential end applications of these materials. **Chapter 3** detailed the use of the PMMA-*b*-P4VP templates to produce nanostructured $LiFePO_4$/C for use in rechargeable batteries. Highly crystalline $LiFePO_4$ was synthesised by a simple sol-gel procedure followed by calcination under inert atmosphere. A study using the templates with various microparticle dimensions showed that only the PMMA-*b*-P4VP copolymers with the largest particle sizes (> 1.0 μm) were able to produce battery materials with very high surfaces areas (> 150 m^2 g^{-1}). These $LiFePO_4$/C materials were also the only ones to show high fidelity in the transfer of morphology from the polymer template to the final calcined materials. Unfortunately, preliminary electrochemical tests did not show that these high surface area materials possessed any enhanced battery performance. Though, as this was only an initial study, it was possible that the low performances were a result of ineffective fabrication of the cell electrodes.

Chapter 4 demonstrated the fabrication of TiO_2 from the PMMA-*b*-PS-*b*-P4VP triblock copolymers for photocatalytic applications. Though this simple metal oxide is already well-studied, the results showed a strong dependence of the final TiO_2 structure on the type of P4VP morphology used to create it. While some of the triblock compositions yielded highly aggregated TiO_2 from a sol-gel templating procedure, the P4VP template with the L+S(II) morphology was found to produce mesoporous TiO_2 microparticles with a large hollow core. When compared to the TiO_2 fabricated using the spherical diblock copolymer morphology, the triblock templated counterpart was found to possess greatly increased surface area and higher photocatalytic activity towards H_2 production. The study highlighted the possible increase in functionality that may be achieved when applying different template morphologies to photocatalysts. Applying this new triblock template to the synthesis of more reactive or chemically doped photocatalysts may produce materials with unparalleled activities.

In **Chapter 5**, the synthesis of the polymeric template and inorganic component was combined into a single synthetic procedure in $scCO_2$. Composites of PMMA-*b*-P4VP with AgNPs were produced by simultaneous polymerisation of the P4VP and thermal degradation of a silver precursor complex. The result was microparticulate composites containing a homogeneous distribution of AgNPs within the polymer. By specifically being able to deposit

the AgNPs inside the polymer particles, this demonstrated a promising ability to control the distribution of inorganic particles within a block copolymer template, all in a single synthetic step. This methodology is sure to be highly transferable to other metal nanoparticles that can be synthesised in $scCO_2$.

Furthermore, by incorporating a CO_2 extraction step post-synthesis, the composites could be obtained as clean synthetic products, with no evidence of residual unreacted monomer or silver precursor found. This gave promise that the composites could be utilised in biomedical applications, with the majority of the materials showing good biocompatibility, a long-lived release of silver and good antimicrobial activity against gram-positive bacteria. Finally, the microparticulate consistency of the composite products allowed them to be utilised in SLS 3D printing to manufacture small solid sections. Through multiple complementary analytical techniques, these printed objects were found to contain the same homogeneous distribution of AgNPs as found in the original powdered material. This provided good initial evidence that the powders could be printed into custom objects and still maintain the same level of antimicrobial activity.

To summarise, several new approaches are presented to modify the dimensions and morphology of P4VP based block copolymer in $scCO_2$. These polymer templates were also used as structural templates to facilitate the nanofabrication of several inorganic functional materials, with a wide range of possible applications investigated. Additionally, this thesis presents an approach to combine template synthesis and structure direction into a single green synthetic process. The work presented demonstrate that these P4VP templates are a highly versatile solution to fabricate a vast array of functional materials. Furthermore, the results also highlight the large dependence of template design on both the templating success and the end properties of the desired inorganic materials. As such, an adaptable polymeric template system is sure to be extremely advantageous to optimise the functionality of future nanomaterials.

6.3. Future Work

The work presented in this thesis discusses a few avenues to synthesise P4VP block copolymers in scCO$_2$ with influence over the size and shape of the template morphology. For the microparticle size changes, excellent control was exhibited over a reasonably large size range. However, control over the P4VP domain size and the resulting triblock copolymer morphologies was shown to be slightly less well-defined. In both cases, this was thought to be due to polymer dispersity being too large in the products, either through targeting too high a molecular weight, or by addition of another unique polymer block.

As such, to truly take advantage of precise tuneability of the P4VP templates, it may be necessary to further optimise the controlled polymerisations, particularly when targeting high molecular weights. Other controlled polymerisations methods such as ATRP and cationic polymerisation have already been studied in scCO$_2$ and may offer a route to achieve greater control.[2, 3] Though, these methods will need significant optimisation in scCO$_2$ to produce the desired P4VP block copolymer products. Alternatively, the RAFT polymerisation technique may need further adjustments to limit termination reactions and reduce polymer chain dispersity. This could be achieved by exploring other RAFT agents with different end groups or by quenching the reaction before full conversion is reached and extracting the remaining monomer. The recent development of new on-line monitoring equipment for scCO$_2$ reactions will certainly aid in optimising these controlled polymerisations.[4]

The successful synthesis of ABC triblock copolymers in scCO$_2$ represents a significant advancement to the other diblock copolymers reported. In **Chapter 4**, only a few possible compositions are studied and with only the same three constituent blocks. The synthesis method present in this thesis may be applied to synthesise a much larger variety of chemical formulations. Though this, a wider array of three-phase polymer morphologies could be created such as the complex knitting patterns and network structures presented in the literature.[5, 6] This may be particularly useful to model the unique block copolymer phase behaviour exhibited in scCO$_2$, in a similar way to work already performed on diblock copolymers.[7] New characterisation methodologies would also need to be developed to accurately study these complex morphologies. Performing SAXS measurements on thin particle sections may be used to achieve this, in order to limit microparticle scattering.

Additional chemical functionality could also be incorporated into these triblock copolymers to allow multiple inorganic species to be templated independently.

The sol-gel synthesis presented in **Chapter 3** demonstrated a route to produce high surface area LiFePO$_4$/C with hierarchical morphology. The initial electrochemical characterisation of these materials did not prove to be very successful and needs to be explored further to determine if the cathodes possess any significantly enhanced charge capacities. The carbon coating of these battery materials also needs to be studied further. The allotropic composition should be determined, and a fabrication strategy should also be utilised to tune the final quantity of carbon in the materials, for optimal electrochemical performance. For instance, calcination under an argon atmosphere containing H$_2$ gas could help to remove some carbon without oxidising the LiFePO$_4$.[8]

The simultaneous synthesis of P4VP block copolymers and AgNPs in scCO$_2$, presented in **Chapter 5**, opens up the possibility to create a range of nanostructured polymer-inorganic composites in a simple and environmentally benign way. This may be achieved by substituting in other CO$_2$-soluble inorganic precursors, of which many already exist.[9] Interchanging the silver precursor for other metal complexes is sure to provide a route to synthesis block copolymer composites containing other noble metal nanoparticle. Other metal oxide composites may also be achievable; however, the polymerisation may have to be adapted slightly to accommodate the other synthetic processes taking place.

The AgNPs composites proved to be readily printable using SLS and demonstrated a reasonable level of antimicrobial activity, along with good biocompatibility. All these properties make them highly desirable for use in manufacturing bespoke medical devices. Future work in this area should focus on improving the mechanical properties of the printed objects. This may be accomplished by altering the printing parameters or by incorporating an additive to reduce the brittleness of the object. Afterwards, the antimicrobial activity of these final printed products should also be assessed.

6.4. References

1.   F. S. Bates and G. Fredrickson, *Block Copolymers—Designer Soft Materials*, 1999.
2.   J. L. Kendall, D. A. Canelas, J. L. Young and J. M. DeSimone, *Chemical Reviews*, 1999, **99**, 543-564.
3.   P. B. Zetterlund, F. Aldabbagh and M. Okubo, *Journal of Polymer Science Part A: Polymer Chemistry*, 2009, **47**, 3711-3728.
4.   K. Kortsen, A. A. C. Pacheco, J. C. Lentz, V. Taresco and S. M. Howdle, *The Journal of Supercritical Fluids*, 2021, **167**, 105047.
5.   T. Goldacker and V. Abetz, *Macromolecular Rapid Communications*, 1999, **20**, 415-418.
6.   Y. Mogi, M. Nomura, H. Kotsuji, K. Ohnishi, Y. Matsushita and I. Noda, *Macromolecules*, 1994, **27**, 6755-6760.
7.   J. Jennings, S. P. Bassett, D. Hermida-Merino, G. Portale, W. Bras, L. Knight, J. J. Titman, T. Higuchi, H. Jinnai and S. M. Howdle, *Polymer Chemistry*, 2016, **7**, 905-916.
8.   M. M. Doeff, J. D. Wilcox, R. Yu, A. Aumentado, M. Marcinek and R. Kostecki, *J. Solid State Electrochem.*, 2008, **12**, 995-1001.
9.   S. E. Bozbağ and C. Erkey, *The Journal of Supercritical Fluids*, 2015, **96**, 298-312.